İÇİNDEKİLER / CONTENTS
Sayfa / Page

Amaç/Objective
Isı bilimi ve tekniğinin geliştirilmesini teşvik etmek, ısı bilimi ve tekniği alanında özgün, teorik, sayısal ve deneysel çalışmaların yayınlanmasına olanak sağlamaktır.
To contribute to the improvement of thermal sciences and technology and publication of original, theoretical, numerical, and experimental studies in thermal sciences and technology.

İçerik/Content
Isı bilimi ve tekniği alanındaki özgün ve derleme makaleler.
Original and review articles in thermal sciences and technology.

Değerlendirme/Evaluation
Dergi hakemli bir dergi olup, her bir makale konusunda uzman en az iki hakem tarafından değerlendirilir.
Each article published in this journal is evaluated by at least two referees.

Türk Isı Bilimi ve Tekniği Derneği'nin Saygıdeğer Üyeleri,

2023 yılı Cumhuriyetimizin kuruluşunun 100. yılı olup, şanlı Türk tarihine işlenen bir mihenk taşıdır. Atatürk'ün önderliğinde büyük Türk Milleti'nin kanı, canı ve sonsuz emekleriyle kurulan Cumhuriyetimizi, tüm değerleriyle sonsuza kadar yaşatmak hepimizin vazgeçilmez ortak sorumluluğudur. Öncelikle, Büyük Önderimiz Atatürk'ü, silah arkadaşlarını, aziz şehitlerimizi ve gazilerimizi saygı ve rahmetle anıyorum.

Cumhuriyetimizin 100. yılı olması sebebiyle, Uluslararası Katılımlı 24. Isı Bilimi ve Tekniği Kongresini, başkentimizde Başkent Üniversitesi'nde gerçekleştirdik. Türk Isı Bilimi ve Tekniği Derneği Yönetim Kurulu Üyeleri ve kongre katılımcıları ile birlikte; Atamıza ve ilkelerine bağlılığımızı arz etmek için Anıtkabir'de Atamızın huzuruna çıktık. 1976 yılında kurulan Derneğimiz, ısı bilimi ve tekniğinin gelişmesine katkı sağlamayı amaçlayan bir dernektir. Her iki yılda bir kongre düzenlemekte olup yılda iki sayı olmak üzere uluslararası saygınlığa sahip bilimsel bir dergi çıkarılmaktadır. Cumhuriyetimizin ilkelerini düstur edinerek, Atamızın bizlere göstermiş olduğu çağdaş yoldan ilerlemeye ve Türk'ün çalışma azmi ve zekâsını tüm dünyaya gösterebilmek için "*En hakiki mürşit ilimdir*" demeye devam ediyoruz. "*Cumhuriyet; fikren, ilmen ve bedenen kuvvetli ve yüksek karakterli koruyucular ister.*" Ey büyük Atatürk; bize armağan ettiğin Cumhuriyet'e sahip çıkarak, "*fikri hür, vicdanı hür, irfanı hür nesiller*" yetiştirmeye devam edeceğimize söz veriyoruz.

Bizlere emanet edilen Cumhuriyetimizi nice 100 yıllara taşımak dileğiyle, hepinizin Cumhuriyet Bayramı'nı kutlarım.

Saygılarımla,

Prof. Dr. Nuri Yücel
Türk Isı Bilimi ve Tekniği Derneği (TIBTD) Başkanı

ASSESSMENT AND COMPARISON OF THE GAMMA AND BC TRANSITION MODELS FOR EXTERNAL FLOWS

Sami KARABAY*, Özgür Uğraş BARAN**
* ROKETSAN A.Ş.06780 Elmadağ, Ankara,
sami.karabay@metu.edu.tr ORCID: 0000-0001-9325-1172
**Orta Doğu Teknik Üniversitesi Makina Mühendisliği Bölümü06800, Ankara,
ubaran@metu.edu.tr ORCID: 0000-0002-8437-7862

Abstract: Modelling of transition from the laminar to turbulent flow became a hot topic due to recent developments in renewable energy, UAV technologies and similar aerospace applications. The transition from laminar flow to turbulence is challenging to model in CFD analysis. The drag is overestimated if the transition is neglected in CFD solutions by assuming the flow is fully turbulent. This results in missing the fundamental characteristics of the flow and inaccurate predictions of the flow field. The most popular transition models are Menter's models applied to the SST turbulence model and the Baş-Çakmakçıoğlu (BC) transition model applied to the Spalart-Almaras model. We have focused on Menter's simpler but more popular γ model and Baş Çakmakçıoğlu models. The γ model relies on the local turbulence intensity, which makes applying the model challenging in external flows. This difficulty stems from the complex relationship between turbulence decay and transition onset. BC transition model utilizes the free stream turbulence intensity. Both models are verified using the Klebanoff and ERCOFTAC flat plate cases and several 2D external flow cases. Skin friction coefficient results are compared to experimental data. Results show that both models predict transition very similarly. BC model is computationally cheaper and easier to implement than the γ model. Also, γ model suffers from boundary conditions ambiguity.
Keywords: Transition Flow, Transition Model, Intermittency, CFD, Flat Plate.

GAMMA VE BC GEÇİŞ MODELLERİNİN DIŞ AKIŞLAR İÇİN DEĞERLENDİRİLMESİ VE KARŞILAŞTIRILMASI

Özet: Laminer akıştan türbülanslı akışa geçişin modelleri, yenilenebilir enerji, İHA teknolojileri ve benzeri havacılık uygulamaları alanındaki son gelişmeler nedeniyle yeniden popüler haline gelmiştir. Laminer akıştan türbülansa geçişin HAD analizlerinde modellenmesi oldukça zor bir konudur. Geçiş bölgesi ihmal edilerek HAD çözümlerinde akışın tamamen türbülanslı olduğu varsayılırsa sürükleme kuvveti gerçeğinden fazla tahmin edilir. Bu durum, akışın temel özelliklerinin gözden kaçırılmasına ve akış alanının yanlış tahmin edilmesine neden olmaktadır. En popüler geçiş modelleri SST türbülans modeline uygulanan Menter modelleri ve Spalart-Almaras modeline uygulanan Baş-Çakmakçıoğlu (BC) modelidir. Bu çalışmada, Menter'in daha sade ama daha popüler olan γ modeli ve Baş Çakmakçıoğlu modellerinin dış akışlaradaki performansına odaklanılmıştır. γ modeli, harici akışlarda uygulanmasını zorlaştıran yerel türbülans yoğunluğuna dayanmaktadır. Bu zorluk, türbülans azalması ile geçiş başlangıcı arasındaki karmaşık ilişkiden kaynaklanmaktadır. BC geçiş modeli ise serbest akış türbülans yoğunluğunu kullanmaktadır. Her iki model de Klebanoff ve ERCOFTAC düz levha deney verileri ve iki boyutlu harici akış deney verisi kullanılarak doğrulanmıştır. Yüzey sürtünme katsayısı sonuçları deneysel verilerle karşılaştırılır. Sonuçlar, her iki modelin de türbülans geçişini çok benzer şekilde tahmin ettiğini göstermektedir. BC geçiş modeli hesaplama açısından γ modelinden daha ucuz ve uygulaması daha kolaydır. Ayrıca, γ modeli sınır koşullarının pratik olarak belirlenmesindeki belirsizlikten muzdariptir.

Anahtar Kelimler: Geçişli Akış, Geçiş Modeli, Kesiklilik, HAD, Düz Levha.

INTRODUCTION

The transition from laminar to turbulent regime called laminar-to-turbulent transition, is a complex and compelling phenomenon in engineering studies. Because of its significant impact on the performance of many real-life applications, including aircraft, wind turbine, and

turbomachinery applications, the laminar-turbulent transition has been the subject of theoretical, experimental, and computational studies. A laminar flow with an ordinary, streamlined velocity profile evolves into a turbulent flow characterized by unpredictable variations in several flow variables. The leap between these very different flow regimes is called turbulence transition. One of the main differences between the laminar and turbulent flows is their very different skin friction. Therefore, transition onset should be modeled to separate these regions for an accurate drag prediction of real-life applications.

The complex nature of transition hinders obtaining accurate predictions of transient flows with an analytic approach. This difficulty leads to new solution methods for turbulence transition using computational fluid dynamics. With the increasing availability of high-performance computing (HPC) resources, there has been a movement in modeling trends toward computations using Large Eddy Simulation (LES) and Direct Numerical Simulation (DNS). Although these numerical approaches have been proven to attain high accuracy, they need a large amount of computing power seldom accessible in everyday simulations. As a result, less resource-intensive techniques, like the RANS methods, remain feasible for general-industrial CFD simulations.

Much effort has been made into numerical modeling of the transition during the last twenty years, resulting in a wide range of methodologies for RANS-based simulations. A family of transition models based on nonlocal variables has been developed in the last two decades. Although they were promising, implementing the nonlocal transition models into general-purpose CFD codes is not practical. Lately, transition models based on local variables have been introduced (Menter et al. (2002), Menter, Langtry et al. (2006), Langtry (2006), Langtry (2006b)).

Transition models use the local variables to attract attention as they can give reasonably accurate solutions. The Langtry-Menter $\gamma - Re_\theta$ model (Langtry 2009)) is the first approach to modeling transition based on the local variables. The general functionality of the Langtry-Menter $\gamma - Re_\theta$ model has increased with additional model modifications to accommodate the effects of surface roughness and crossflow situations. However, this complex model makes it challenging to implement and fine-tune different turbulence models for specific flow scenarios. The Langtry-Menter transition model

also lacks Galilean invariance, an essential property for generic CFD simulations.

Lately, Menter et al. (2015) proposed a new local correlation-based transition model based on a single transport equation and may be thought of as an improved version of the $\gamma - Re_\theta$ model. The new model benefits from the simpler formulation. Also, this model is Galilean invariant.

Transition Phenomena

The boundary layer is the flow region adjacent to a bounding surface where viscous effects are significant. The boundary layer has two flow regimes, each with distinct characteristics: laminar and turbulent. Figure 1 depicts a boundary layer development across a plate.
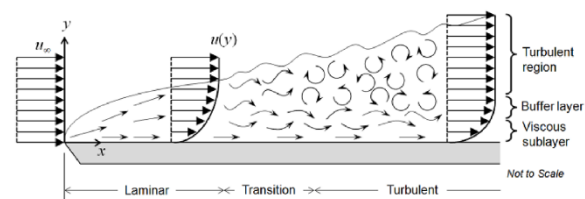
Figure 1. Transition Phenomena Frei, (2013)

When uniform velocity fluid reaches the upstream of the plate, a laminar boundary layer begins to form. The laminar region has a streamlined and smooth velocity profile near the surface. Disturbances in the flow field appear after a certain distance, indicating the onset of the transition zone. The whole flow field ultimately breaks down into a completely turbulent flow characterized by random changes in flow.

The fundamental governing parameter separating viscous flow regions is the Reynolds number that indicates the flow state. It is defined as the ratio of inertial forces to viscous forces. Threshold Reynolds numbers that separate whether the flow is laminar, turbulent, or transition are determined empirically. The point of transition influences the overall properties of the flow. The high velocity gradient in the turbulent boundary layer results in high skin friction than that of the laminar boundary layer. Hence, the total drag of the surface increases. Moreover, laminar and turbulent flows have different heat transfer characteristics besides drag force. Due to the increased mixing in the turbulent flow, significantly higher heat between the fluid and the bounding surface is observed.

On the other hand, determining if the flow is in the transition zone is not straightforward. Unlike the

laminar or fully turbulent zones, the transition flow is unstable. Transitional flow measurements show that a laminar flow is interrupted by turbulent bursts in this zone. Therefore, the flow is split into laminar and turbulent moments. When the Reynolds number is lower, the time spent in laminar periods is larger than in turbulent periods. As the local Reynolds number increases, the time spent in turbulent flow progressively increases, yielding a fully turbulent flow. The percentage of turbulent bursts in total time is called intermittency. The intermittency (γ) is zero when the flow is laminar and one if the flow is fully turbulent. Therefore, intermittency is a key factor in many transition models.

Transition Mechanisms

The transition can occur through different mechanisms due to a variety of reasons. Freestream conditions, turbulence intensity, and surface roughness are examples. Generally, the primary modes are natural, bypass, and separation-induced transitions. Wake-induced and shock-induced transitions are secondary transition modes (Mayle (1991)). In this part, different modes of transition are explained.

Natural Transition: The natural transition is the most common mechanism in low turbulence intensity freestream conditions, as given in Figure 2. In this mechanism, laminar freestream flow reaches critical Reynolds Number Tolmien-Schlichting waves are formed. Then turbulent spots are followed by full turbulent flow (Mayle (1991)). The intermittency increases in the process.
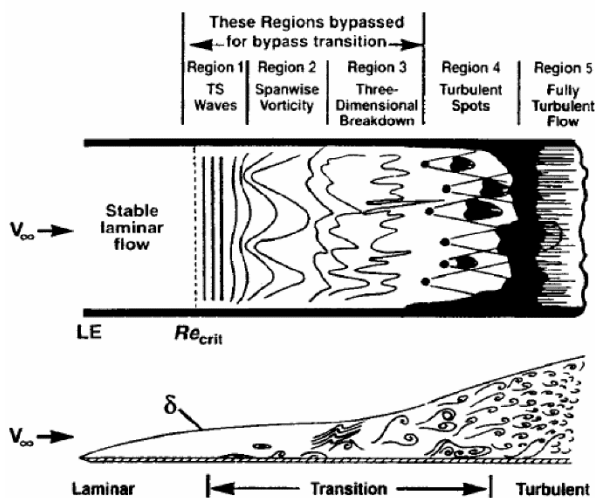
Figure 2. Natural Transition Mode Frei, (2013)

Bypass Transition: If the freestream turbulence level is larger than 1%, natural transition stages are

bypassed, and turbulent spots are produced directly. In this mode, linear stability theory fails, and no Tollmien-Schlichting waves are formed. Freestream turbulence level, rough surface, and favorable pressure gradients can also be reasons for the bypass transition mode.

Separation-Induced Transition: The transition may occur in the shear layer when the flow separates. In this mode, a laminar separation bubble can be formed on the surface, resulting in the flow reattachment. This mode contains all stages of the natural transition. According to the freestream turbulence level, the size of the separation bubble changes.

Wake-Induced Transition: This transition mode can be observed on periodic unsteady turbulent wakes passing over blades or airfoils (Langtry (2006), Wang (2021)). Turbulent wakes disrupt the laminar boundary layer when they impinge the wakes, and turbulent spots propagate downstream.

Reverse Transition: Reverse transition or relaminarization refers to the transition from turbulent to laminar

Transition Modelling

It is possible to consider transition models according to their level of sophistication. The most basic model is the e^N model from Smith (1956). The model is applied to a 2D steady flow by Nichols (2010), and it is based on the linear stability theory and is often used for low-turbulence flows. A velocity profile is required a priori.

More advanced low Reynolds Number turbulence models were introduced by Jones (1973). These models modify wall-damping functions to capture the transition effects. These models rely on turbulence diffusion from the freestream into the boundary layer to anticipate the transition onset. Low Reynolds Number turbulence models are generally used for bypass transition flows. However, they are unreliable since they are not sensitive to pressure gradients and flow separations (Dhawan (1958)].

Next, a group of more advanced and complex transition models called correlation-based transition models were formulated by Kaynak et al. (2019). The main idea is to blend the laminar and turbulent regions by introducing a new variable, intermittency (Langrtry (2009)). Intermittency could be defined as the probability that the flow is

turbulent. These models try to model the intermittent character of turbulence resulting from the fluctuations in the flow field. A new set of algebraic or partial differential equations are coupled with existing turbulence models Such as Langtry (2009), Suzen (2006), Walters (2008) and Çakmakçıoğlu (2018). In those equations, constants derived from experiments and observations are used. It is convenient to group these models according to whether they use local or nonlocal flow variables.

Models Depending on Nonlocal Flow Variables

The transition mechanism and the Momentum Reynolds number are proven experimentally correlated. The momentum thickness Reynolds number is the Reynolds number based on the momentum thickness, θ.

$$Re_\theta = \frac{\rho U_e \theta}{\mu} \qquad (1)$$

Experimental correlations reveal that the transition onset is observed at a critical momentum thickness Reynolds number, $Re_{\theta c}$. Many models are based on this correlation. Note that $Re_{\theta c}$ is not a local parameter and should be calculated starting from the wall. Therefore these models need to use an exhausting search algorithm to calculate the momentum thickness Reynolds number for complex flows. For example, The Dhawan and Narasimha (1958) model is the first attempt at correlation-based transition models. They proposed an algebraic intermittency function (γ) assuming the transition onset, (x_t), is known as apriori.

Steelant and Dick (2001) proposed a set of transport equations called the conditional Navier- Stokes equations. Their transport equation is derived from the intermittency function proposed by Dhawan and Narasimha. The model can predict intermittency in the streamwise direction by assuming uniform intermittency distribution in the cross-stream direction. However, their approach is not consistent with experimental data.

Cho and Chung (1992) proposed a new transport equation coupled with the $k - \varepsilon$ turbulence model. The model itself cannot predict the onset of transition. However, intermittency profiles agree with the experimental results for various flow conditions.

Suzen and Huang (2000) improved the intermittency equation approach significantly.

Their intermittency transport equation includes source terms from the Steelant and Dick and Cho-Chung models. The transport equation is coupled with Menter's (1994) shear stress transport turbulence model. The model's superiority is that the intermittency profile along the cross-stream direction can be predicted, which was the shortcoming of the previous models.

Models Depending on Local Flow Variables

These models use constants derived from observations and experiments in transport equations. A prominent feature of these models is that they are compatible with modern CFD codes as vorticity Reynolds Number is used. Re_V is calculated as follows;

$$Re_V = \frac{\rho d_w^2}{\mu} \Omega \qquad (2)$$

In Equation (2), d_w denotes the distance from the nearest wall. Since all variables used are local, Re_V is also a local variable that can be computed in CFD codes. The Blasius theory shows that the local vorticity Reynolds Number, Re_V, is proportional to the momentum thickness Reynolds Number, Re_θ, which is a fundamental parameter for transition. Thus, local correlation transition models can be used to model transition in CFD simulations.

The first of these models proposed by Langtry (2009) and Menter is the $\gamma - (Re_{\theta t})$ model. Two additional scalar transport equations (3)-(4) are solved besides the SST model transport equations.

$$\frac{\partial(\rho\gamma)}{\partial t} + \frac{\partial(\rho u_{j\gamma})}{\partial x_j} =$$
$$P_\gamma - E_\gamma + \frac{\partial}{\partial x_j}\left[\left(\mu + \frac{\mu_t}{\sigma_f}\right)\frac{\partial\gamma}{\partial x_j}\right] \qquad (3)$$

$$\frac{\partial(\rho\hat{Re}_{\theta t})}{\partial t} + \frac{\partial(\rho u_j \hat{Re}_{\theta t})}{\partial x_j} =$$
$$P_{\theta t} + \frac{\partial}{\partial x_j}\left[\sigma_{\theta t}(\mu + \mu_t)\frac{\partial Re_{\theta t}}{\partial x_j}\right] \qquad (4)$$

The first of these two equations is for intermittency (γ). The second one solves for transition momentum thickness Reynolds Number ($Re_{\theta t}$), which refers to a local Re_θ. Menter's $\gamma - (Re_{\theta t})$ model formulation consists of local variables. Hence, it can be used for complex flows with any grid type.

Menter (2015) proposed the simplified version of the $\gamma - (Re_{\theta t})$ model. In the new model, called

Menter's one equation γ model, the $(Re_{\theta t})$ transport equation is removed, and experimental correlations are embedded into the intermittency equation. The transport equation is the same as the $\gamma - (Re_{\theta t})$ model transport equation, as given in (5). However, source terms are slightly modified, and some constants differ.

$$\frac{\partial(\rho\gamma)}{\partial t} + \frac{\partial(\rho\,u_j\gamma)}{\partial x_j} = \\ P_\gamma - E_\gamma + \frac{\partial}{\partial x_j}\left[\left(\mu + \frac{\mu_t}{\sigma_f}\right)\frac{\partial\gamma}{\partial x_j}\right] \quad (5)$$

Although one of the equations is removed, the new model provides good predictions. The main advantage of the γ model is that it solves one less equation than the previous model.

Another local correlation-based transition model is the Walters-Cokljat (2008) $k_T - k_L - \omega$ model. This model is based on the concept that the cause of the bypass transition is very high amplitude streamwise fluctuations. These fluctuations differ from turbulent fluctuations and can be modeled separately. Mayle and Schulz (1996) proposed a second kinetic energy equation to describe these fluctuations. This kinetic energy was called laminar kinetic energy k_L. In this model, total kinetic energy is assumed to be the sum of the energy of large-scale and small-scale eddies. Large-scale eddies contribute to laminar kinetic energy, and small-scale eddies contribute to turbulent kinetic energy production. Thus, the transition can be modeled by calculating the k_L, with the transport equation given in (6). Besides the merely changed $k - \omega$ transport equations, one more transport equation is solved to calculate laminar kinetic energy.

$$\frac{Dk_L}{Dt} = P_{k_L} - R_{BP} - R_{NAT} - D_L \\ + \frac{\partial}{\partial x_j}\left[\nu\frac{\partial k_L}{\partial x_j}\right] \quad (6)$$

Since this model uses local formulation, it can be used in CFD codes.

The last model mentioned is Bas-Cakmakcioglu (2018) (BC) algebraic transition model. This model solves one algebraic equation instead of a partial differential equation for intermittency. Therefore, the computational cost of CFD simulations reduces significantly. BC transition model damps the turbulent production term of the Spalart-Allmaras (S-A) turbulence mode until the transition onset threshold is reached. Lately, the model has become

Galilean invariant with modification in the formulation (2013, Çakmakçıoğlu (2020)). Also, the local Reynolds number, hence the reference length, dependency of the original method is corrected. Thus, the BC algebraic transition model can be used for various flows with any grid type without the reliance on reference length selection.

The recent years Menter's γ model has gained significant popularity due to its popularity in commercial solvers. On the other hand, the BC transition model became available on open-source CFD code SU^2 solver. No widely available open-source solver allows the comparison of these models. Such comparison is necessary to eliminate the effects of the flow solver scheme. In this study, we aim to implement both models in the same solver and clearly compare these transition models.

METHODOLOGY

This section describes the implemented transition models. Also, the mesh domain used in simulations is elaborated on in this section.

Transition Prediction

A transition model should predict the onset and length of the transition. Transition length and characteristics are controlled by the intermittency concept, which refers to the probability of a point being in a turbulent region Emmons (1951))
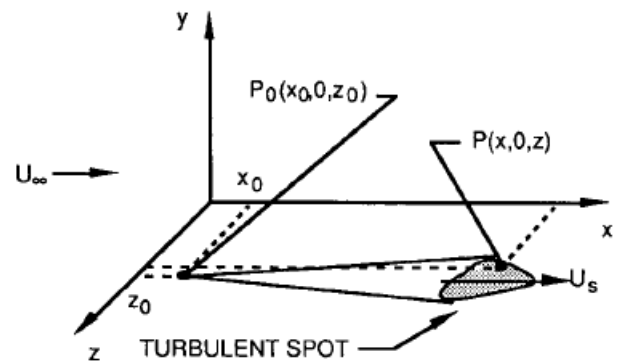
Figure 3: Intermittency in Space, Mayle (1991)

Intermittency equals one if in the fully turbulent boundary. If the flow is laminar, the intermittency is zero. Intermittency can be modeled with an algebraic function or with a transport equation. Source terms of the transport equations are responsible for the algebraic transition models in these equations. Modeling intermittency with the transport equation provides the modeling transition across the boundary layer and in the streamwise

direction. Thus, this approach gives more accurate solutions than the algebraic approaches.

The task of intermittency is to control the transition characteristics and length of the transition. As the boundary layer develops, intermittency, γ , increases and eventually, it becomes equal to unity. From this point on, the transition phase is completed, and the flow becomes fully turbulent. The underlying turbulence model is employed for turbulent flow. However, another mechanism besides intermittency is required to predict the onset of the transition.

Prediction of Transition Onset

Momentum thickness Reynolds number is a flow parameter that is calculated using the momentum given in the previous section. Transition onset momentum thickness Reynolds number, $Re_{\theta t}$, is the momentum thickness Reynolds number calculated at transition onset.

Studies and experiments show that transition onset is strongly related to the free stream turbulence intensity and pressure gradient. Experiments have shown that transition onset is earlier as turbulent intensity increases and transition onset momentum thickness Reynolds Number, $Re_{\theta t}$, gets smaller, as shown in Figure 4.
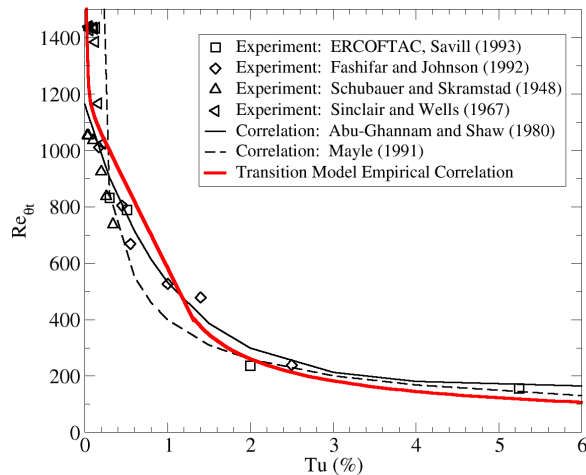
Figure 4: Relation between the Turbulence Intensity and Transition Onset Momentum Thickness Reynolds Number (Menter (2006b))

Thus, a transition model should include the effect of turbulence intensity. Menter's (2015) one-equation γ model utilizes the local turbulence intensity to provide a measure of intermittency. Then the term $(1 - \gamma)$ is multiplied by the turbulence production term to prevent or limit turbulence production near the wall.

The pressure gradient is decisive for the transition onset, similar to turbulence intensity. As shown in Figure 5, the transition onset momentum thickness Reynolds number decreases with increasing turbulence intensity. In other words, transition onset delays with a larger pressure gradient in the boundary layer.
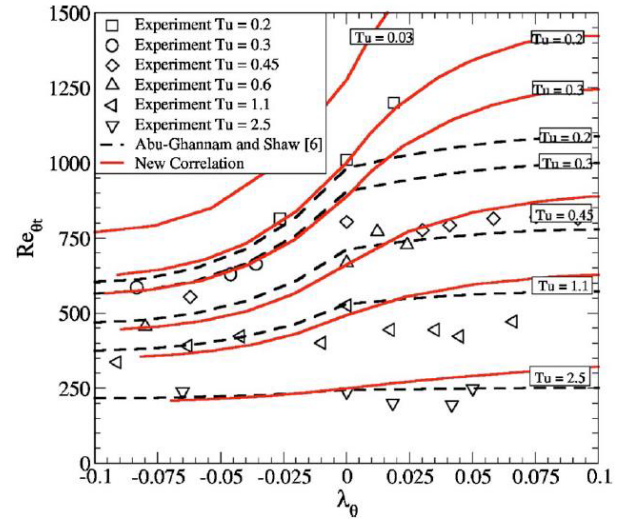
Figure 5: Relation between the Pressure Gradient Parameter and Transition Onset Momentum Thickness Reynolds Number (Menter (2006b))

To include the effect of the pressure gradient, the transition onset is calculated using the pressure gradient parameter term, λ_θ, besides the turbulent intensity. This term is also calculated from the local streamwise acceleration.

MENTER ONE-EQUATION γ MODEL

Menter's one-equation γ model is a simplified version of their γ-($Re_{\theta t}$) model. The difference is that the former does not solve any transport equation for momentum thickness Reynolds number, ($Re_{\theta t}$), but it is computed algebraically using local variables in the intermittency transport equation.

Menter (1994) implemented one equation γ model on the $k-\omega$ SST. The new model is calibrated with available experimental data. Calibration is done for self-similar flows, Falkner-Skan family flows and some non-equilibrium flows, mainly with separation. The adjustment of the model coefficients conducted according to self-similar flows and separation results with some differences with experimental data for different transition mechanisms.

The novelty of the Menter one-equation γ model is that, unlike turbulence models, this model does not seek to represent the physics of the transition process but rather provides a framework for incorporating correlation-based models into general-purpose CFD codes. The physics of the transition phenomenon is contained in the model's empirical correlations. As a result, this formulation is not confined to a single transition mechanism, such as natural transition or bypass transition. The formulation can be applied to any transition mode as long as modifications of the correlations are embedded into the model coefficients.

Menter's Transition Model

The intermittency transport equation of the Menter one equation γ model is presented in Equation (7).

$$\frac{\partial(\rho\gamma)}{\partial t} + \frac{\partial(\rho\, U_j\gamma)}{\partial x_j} =$$
$$P_\gamma - E_\gamma + \frac{\partial}{\partial x_j}\left[\left(\mu + \frac{\mu_t}{\sigma_f}\right)\frac{\partial\gamma}{\partial x_j}\right] \quad (7)$$

The γ production term is defined as:

$$P_\gamma = F_{length}\,\rho\,S\gamma(1-\gamma)F_{onset} \quad (8)$$

In equation 4-(8), S refers to the strain rate magnitude. It is included in the production term as a multiplier, as strain rate is the driving factor of the transition process. F_{length} is a calibration constant. F_{onset} is the term that triggers the onset of the transition. This term involves the ratio of vorticity Reynolds number to critical Reynolds number, between which a strong relationship is shown experimentally.

Before the onset of the transition, where flow is laminar, the production term is equal to zero, as expected. The destruction term in the transport equation is as follows:

$$E_\gamma = c_{a2}\rho\Omega\gamma F_{turb}(c_{e2}\gamma - 1) \quad (9)$$

Constants used in the production and destruction terms are given below.

$$F_{length} = 100, c_{e2} = 50, c_{a2} = 0.06,$$
$$\sigma_\gamma = 1.0, \quad (10)$$

Functions used in calculating the production and destruction terms are given below.

$$F_{onset1} = \frac{Re_V}{2.2Re_{\theta c}},$$
$$F_{onset2} = \min(F_{onset1}, 2.0),$$
$$F_{onset3} = \max\left(1 - \left[\frac{R_T}{3.5}\right]^3, 0\right),$$
$$F_{onset} = \max(F_{onset2} - F_{onset3}, 0), \quad (11)$$
$$F_{turb} = e^{-\left(R_T\frac{1}{4}\right)^2}, R_T = \frac{\rho k}{\mu\omega},$$
$$Re_V = \frac{\rho d_\omega^2 S}{\mu}, Re_{\theta c} = f(Tu_L, \lambda_\theta L,)$$

The boundary conditions of the transport γ-model are that flux of the γ through the wall is zero, and γ equals unity at the inlet to preserve the freestream turbulence decay rate of the underlying turbulence model (Langtry (2009)).

The critical momentum thickness Reynolds number, $Re_{\theta c}$, is defined as a function of the local turbulent intensity and pressure gradient parameter. Thus, to calculate $Re_{\theta c}$, local turbulent intensity and local pressure gradient parameters are calculated. Local turbulent intensity, Tu_L, is defined as:

$$Tu_L = \min\left(\frac{100\sqrt{2k/3}}{\omega d_\omega}, 100\right) \quad (12)$$

This formulation allows the local turbulent intensity to equal the freestream turbulent intensity in the middle of the boundary layer. The pressure gradient parameter is defined as follows:

$$\lambda_{\theta L} = -7.57x10^{-3}\frac{dV}{dy}\frac{d_\omega^2}{\nu} + 0.0128 \quad (13)$$

Coefficients in this formula are selected considering the self-similar flows. To achieve numerical robustness, Menter bounded $\lambda_{\theta L}$ as follows:

$$\lambda_{\theta L} = \min\left(\max(\lambda_{\theta L}, -1.0), 1.0\right) \quad (14)$$

Coupling with SST Turbulence Model

The coupling of the Menter one equation γ model with the SST turbulence model is done by slightly modifying the transport original transport equations of turbulent kinetic energy (Menter (2015)

$$\frac{\partial}{\partial t}(\rho k) + \frac{\partial}{\partial x_j}(\rho u_j k) =$$

$$\tilde{P}_k + P_k^{\lim} - \tilde{D}_k + \frac{\partial}{\partial x_j}\left[(\mu + \sigma_k \mu_t)\frac{\partial k}{\partial x_j}\right]$$

$$\frac{\partial}{\partial t}(\rho \omega) + \frac{\partial}{\partial x_j}(\rho u_j \omega) = \alpha \frac{P_k}{v_t} - D_\omega$$

$$+ CD_\omega + \frac{\partial}{\partial x_j}\left[(\mu + \sigma_\omega \mu_t)\frac{\partial \omega}{\partial x_j}\right]$$

$$(15)$$

Also:

$$\tilde{P}_\gamma = \gamma P_k$$
$$\tilde{D}_\gamma = \max(\gamma, 0.1) D_k \qquad (16)$$

Where P_k and D_k are the production and destruction terms of the original turbulent kinetic energy of the equation of SST. The updated k equation includes the term $P_k^{\lim}$ to provide the generation of k at the transition phase for small turbulence intensity values.

$$P_k^{\lim} = 5 C_k \max(\gamma - 0.2, 0)$$
$$(1 - \gamma) F_{on}^{\lim} \max(3 C_{sep}\mu - \mu_t, 0) S\Omega$$
$$F_{on}^{\lim} = \min\left(\max\left(\frac{Re_V}{2.2 Re_C^{\lim}} - 1, 0\right), 3\right) \qquad (17)$$
$$Re_{\theta c}^{\lim} = 1100, c_k = 1.0, c_{sep} = 1.0$$

BC Transition Model

The BC transition model relies on the experimental correlation of the transition location and the theoretical relation between $Re_{\theta c}$ and $Re_{v,max}$. The critical momentum thickness is given in equation (18) based on experimental data.

$$Re_{\theta c} = 803.73(Tu_\infty + 0.6067)^{-1.2027} \qquad (18)$$

The above equation provides an excellent theoretical basis for the transition onset. Equation (18) correlates the free stream turbulence intensity and the transition onset rather than the local turbulence intensity as Menter's model does. Indeed, no correlation for the latter case is available in the literature.

The parameter $Re_{\theta c}$ is utilized to determine the intermittency.

$$\gamma_{BC} = 1 - \exp(-\sqrt{Term1} - \sqrt{Term2})$$
$$Term1 = \frac{\max(Re_\theta - Re_{\theta c}, 0.0)}{\chi_1 Re_{\theta c}} \qquad (19)$$
$$Term1 = \frac{\max(v_{BC} - \chi_2, 0.0)}{\chi_2}$$

Finally, the Spalart-Almaras turbulence model is modified to Equation (20). The only difference from the original equation is the multiplication of the production term with γ_{BC}, as indicated by the boldface. Therefore, the turbulence equation does not alter where the intermittency is equal to one.

$$\frac{\partial}{\partial t}(v_T) + \frac{\partial}{\partial x_j}(u_j v_T) =$$
$$\boldsymbol{\gamma_{BC}} C_{b1} s v_T - c_{w1} f_w \left(\frac{v_T}{d_w}\right)^2 \qquad (20)$$
$$+ \frac{1}{\sigma}\left\{\frac{\partial}{\partial x_j}\left[(v_L + v_T)\frac{\partial v_T}{\partial x_j}\right] - C_{b2}\frac{\partial v_T}{\partial x_j}\frac{\partial v_T}{\partial x_j}\right\}$$

COMPUTATIONAL SETUP VALIDATION

In this section, we have validated our solver and our γ model implementations. The transition model verification is conducted by comparing our results with the reference (Menter (2015)) implementations. Also, we have shown the mesh study in this section. The validated meshing strategy is repeated for flat plate verification studies.

CFD Solver

All developments are implemented in our cell-based finite volume solver. The current $k - \omega - \gamma$ development is applied as a new turbulent solver library starting from the $k - \omega$ model. All the necessary modifications are done, and changes to the SST model are implemented. The Baş-Çakmakçıoğlu model, however, is added directly to the SA solver. We have utilized their (2020) model, as this model provides the Galilean invariance and Reynolds number independence. The applied flux scheme is the second-order accurate implicit HLLC with Venkatakrishnan limiter. The solver and turbulence models are validated in previous studies (Dikbaş (2022), Duru (2021)).

Experimental Data for Transition

The number of available test cases utilized for transition modeling is somewhat limited. We have used the standard flat plate test cases and some 2D test cases.

Flat Plate Cases

Standard benchmark cases to test the development and implementation of transition models are available in the literature. Those are Schubauer-

Klebanoff (1955) and ERCOFTAC series experiments.

The Schubauer-Klebanoff (1955) flat plate test case is one of the most well-known flat plate cases used to validate transition models. This test is a natural transition on a flat plate with low freestream turbulence intensity. This test case

The T3 experiments were conducted by Rolls Royce in the 1990s and have become benchmark cases for transition model validation by Savill et al. (1993). The bypass transition mode dominates the transition in all T3 cases due to high freestream turbulence intensities. Freestream velocity profiles, freestream turbulence intensity profiles and skin friction coefficients are measured and reported in the T3 series. T3A, T3B and T3A- are zero-pressure gradient flat plate cases. T3C series are nonzero pressure gradient cases.

All flat plate test conditions are given in Table 1. Note that turbulent viscosity is taken from Menter's study. BC transition model does not require this ratio.

One notable difference between Menter's study and experimental data appears in the Schbauer Klebanoff test case. Schubauer and Klebanoff conducted their experiments at a free stream velocity of 80 ft/s, which is changed to 50.1 m/s in Menter's study. S&K experiment reports that the transition occurs at x-locations between 5 to 8 inches. Menter reported wall shear stress results, first as local Reynolds number, then x locations. Both results are consistent with the experiments in terms of Reynolds numbers, where the transition Reynolds number is around 3×10^6. There s an ambiguity in the free stream turbulence level, too. SChubauer reports the free stream turbulence as 0.03%. Menter reports this value at 0.3% in Table 1 and 0.18% in Figure 4 in their 2009 study, and 0.03% in their 2015 study. Indeed, the free stream turbulence level is very low, and either selection has no significant effect on the results.

Table 1: Inlet Conditions of Different Test Cases

Case	U in [m/s]	Tu(%)	μ_t/μ	ρ ,kg/ m 3	μ,kg/ms
S&K	50.1	0.18	1	1.2	$1.8 \times 1 0$ -5
T3A	5.18	4.5	8	1.2	$1.8 \times 1 0$ -5
T3B	9.4	7.8	80	1.2	$1.8 \times 1 0$ -5
T3A-	19.8	1.1	6	1.2	$1.8 \times 1 0$ -5

T3C2	5.4	3	9	1.2	$1.8 \times 1 0^{-5}$
T3C3	4.0	3	5	1.2	$1.8 \times 1 0^{-5}$
T3C4	1.4	3	2	1.2	$1.8 \times 1 0^{-5}$
T3C5	9.1	7	12	1.2	$1.8 \times 1 0^{-5}$

Mesh Generation

It is shown that the $(\gamma - Re_{\theta t})$ and Menter one equation γ model is sensitive to mesh properties both streamwise and normal to wall directions. Menter et al. (2015) recommend following practice rules in mesh generation for Menter one equation γ model;

- Dimensionless wall distance y^+ should be less than one,
- The expansion ratio in the normal wall direction should be less than 1.1,
- At least 30 cells normal to wall direction,
- At least 100 cells in a streamwise direction.

The grid convergence studies for all cases are conducted, and one study is presented for the Schubauer-Klebanoff case. Five different meshes with different numbers of cells are created, considering the guidelines mentioned above. The convergence plot based on the drag is given in Figure 6. The x-axis represents the $(1/N)^{1/2}$, which is proportional to average grid spacing, h. Labels indicate the normal to wall mesh and ($\times$) streamwise mesh counts.
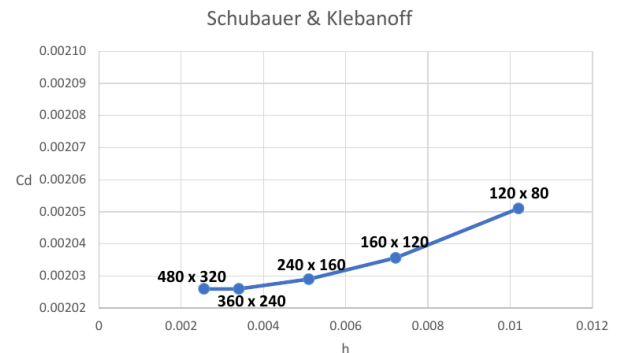

Figure 6: Convergence of Drag coefficient

Skin friction coefficients obtained using five grids are reported in Figure 7. Computational skin frictions are calculated the wall boundaries that are shown in red in Figure 8. The experimental data is taken from Schubauer Klebanoff study. The experimental measurement locations are correlated through Reynolds similarity.
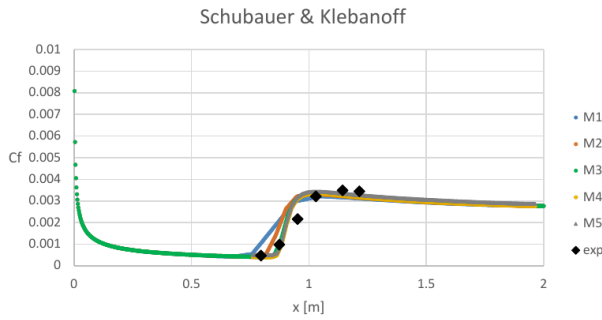
Figure 7: Skin friction coefficients obtained using five meshes

Similar to the drag coefficient, skin friction coefficients converge as the element size in the streamwise direction decreases. We have followed a similar approach for all test cases. The mesh independence studies of the other cases are not involved in this study.

The properties of the meshes used are presented in Table 2.

Table 2: Mesh Properties

Case	Cells	Expansion Ratio	First Cell Thickness	y^+
Zero Pressure Gradient	240×160×1	1.08	2x1 0 -5	0.8
Nonzero Pressure Gradient	255×150×1	1.05	1x1 0 -5	0.7

Computational Domain

Boundary conditions assigned to mesh obtained at the end of the mesh generation process are shown in Figure 8.
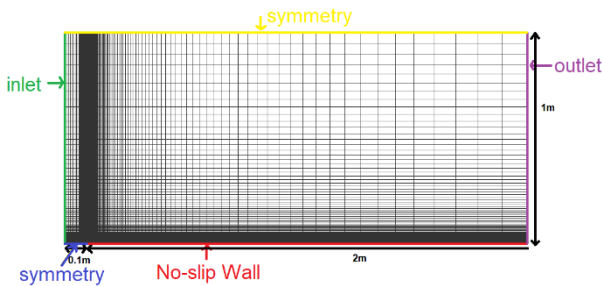
Figure 8: Computational Domain for Zero Pressure Gradient Cases

At the inlet, velocity, pressure and density are specified with turbulent kinetic energy k and dissipation rate, ω. Very high-quality and dense mesh is defined at the leading edge of the flat plate to resolve the stagnation point with reasonable accuracy. y+ is kept close to unity. The Klebanoff, T3A, T3B and T3A- test cases are solved using the mesh explained.

T3C series are the cases with pressure gradients. The computational domain of T3C cases is generated in the converging-diverging duct form to simulate the pressure gradient.
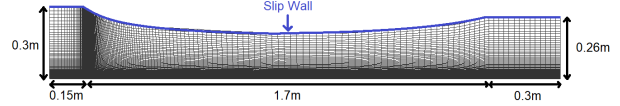
Figure 9: Mesh Domain for Cases with Pressure Gradient

RESULTS

Simulation results are compared with experimental data in this section, and comments are given. We have verified our flat plate solutions with Menter's solutions (2015) to eliminate implementation errors in our conclusions. Therefore, the flat plate cases serve for both implementation validation and model comparison purposes.

Flat plate results

Schubauer-Klebanoff Test Case

Results of the Schubauer-Klebanoff test case show that Menter one equation γ model and the Bas-Cakmakcioglu model can predict natural transition accurately. Bas-Cakmakcioglu model predicts skin friction coefficient better than the Menter one-equation γ model after the flow becomes fully turbulent for the Schubauer-Klebanoff test case. Menter's reported solution taken from the 2015 study is also given in Figure 10. The turbulence decay is not reported for this experiment. The experimental data shows the transition onset is around $Re_x = 3 \times 10^6$ ($x = 0.8$ in our case). The transition length extends the transition zone until x=1.2. The BC transition model is an abrupt transition model that does not incorporate the transition length. The sudden jump from the laminar to turbulent flow is visible in Figure 10. The γ model claimed to be calibrated for the transition length. However, the γ solution shows abrupt (or short-length) transitions like BC Model. This observation was repeated for other flat plate test cases.
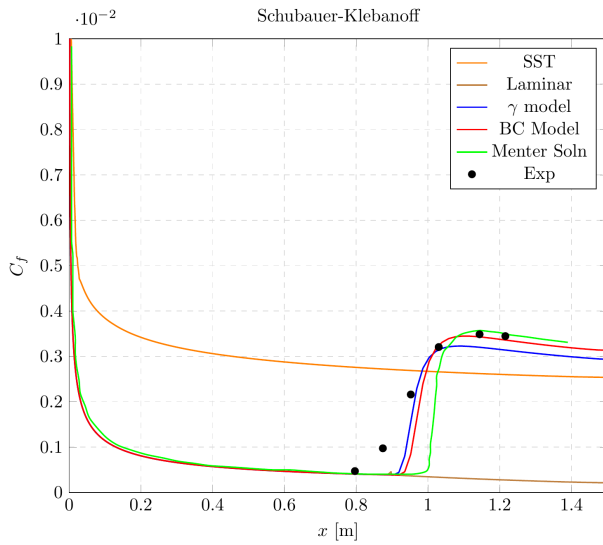
Figure 10: Comparison of Skin Friction Coefficients obtained with Different Models, including Menter's (2015) results for S&K Case

ERCOFTAC Zero Pressure Gradient Cases

T3A, T3B and T3A- zero pressure gradient cases are examined with the studied transition models. These cases are more challenging than the S&K case since they are bypass transition cases as turbulent intensities are larger than 1% or close to 1%. Thus, resolving the transition in these cases is more challenging than in the S&K case. The inlet freestream turbulence intensity and viscosity ratio are adjusted according to experimental turbulence intensity data. Turbulence intensity profiles and skin friction coefficients are given in the following figures. We have compared our results with the Menter (2015) study in these figures. Other solutions are obtained from our solver.

Figure 11: Turbulence intensity profile of T3A simulation

Figure 12: Comparison of Skin Friction Coefficients obtained with Different Models for T3A Case

Figure 13: Turbulence intensity profile of T3B simulation
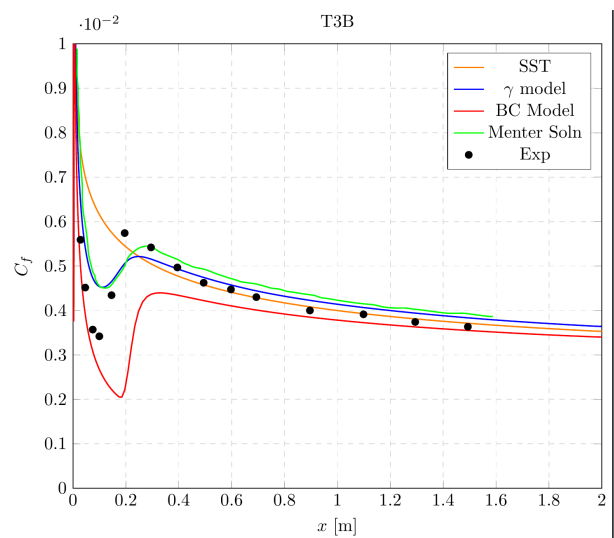
Figure 14: Comparison of Skin Friction Coefficients obtained with Different Models for T3B Case

145
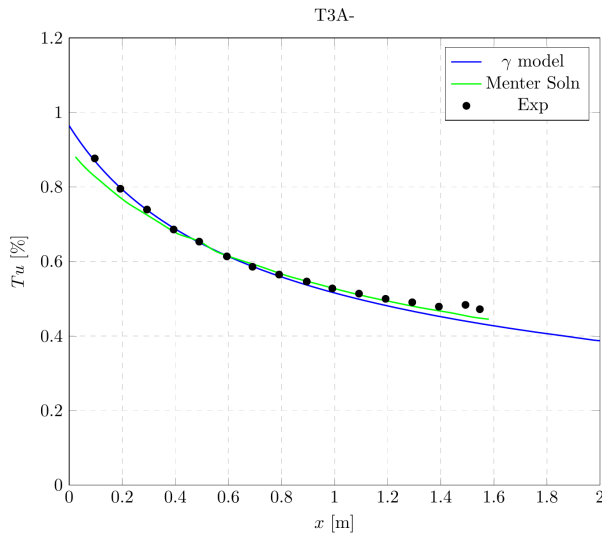
Figure 15: Turbulence intensity profile of T3A-simulation

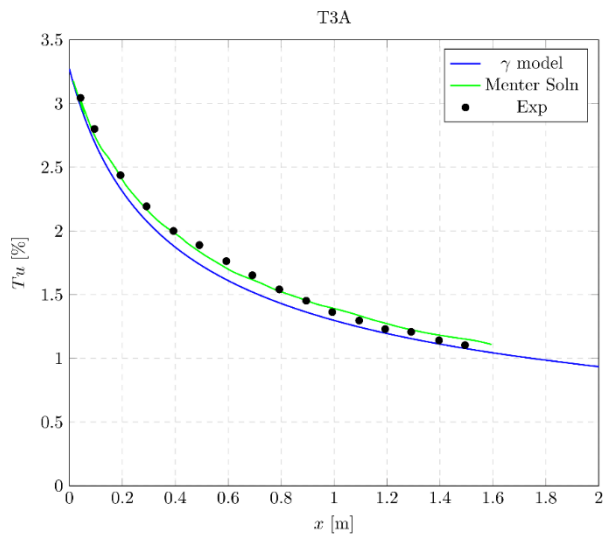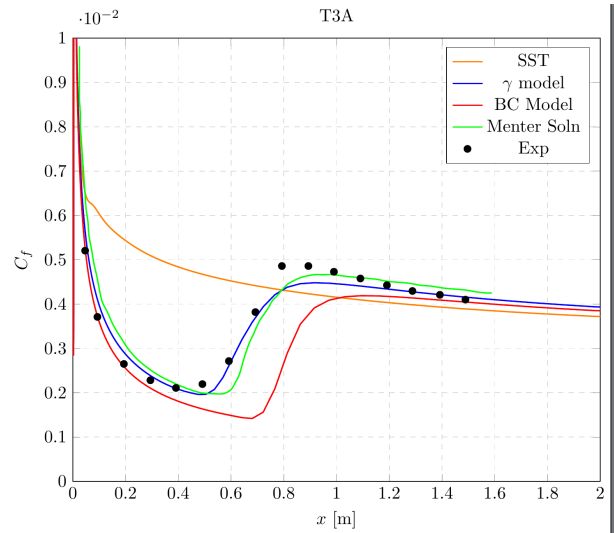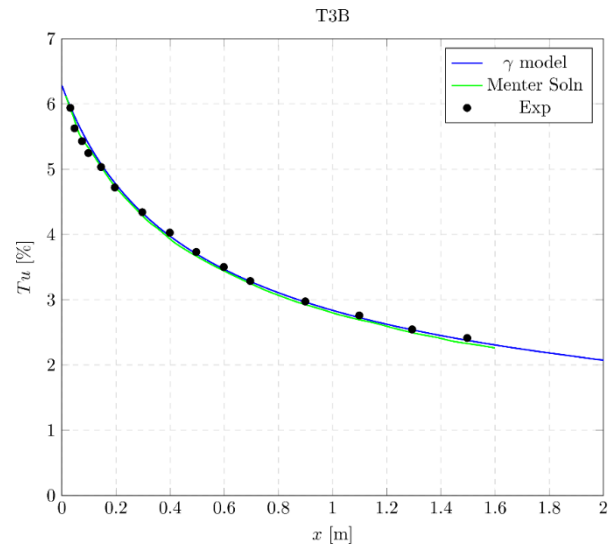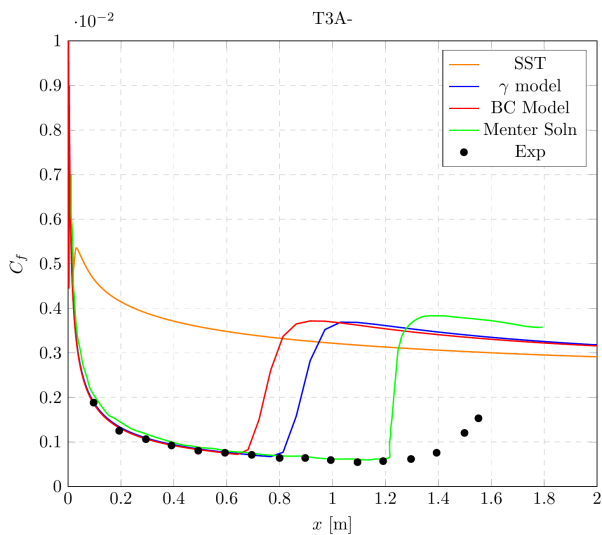**Figure 16:** Comparison of Skin Friction Coefficients obtained with Different Models for T3A- Case

Menter's solutions are digitized from the original (2015) paper and added to T3A and T3B plots to show that the model is implemented correctly. The small discrepancy between Menter's results and obtained results during this study could be the difference in flux schemes between the two codes. Nevertheless, the results match well.

Menter's one-equation γ model performed better than the BC transition model for the T3A case. The flow becomes fully turbulent in the T3B case immediately after interacting with the flat plate. The γ and BC transition models have captured transition with reasonable accuracy. The challenging aspect of T3A- is that transition onset occurs at the end of the plate. None of the transition models could predict transition onset correctly.

We should highlight a few important points in some ERCOFTAC cases. The validation cases involve some extreme conditions that make the model validation challenging. The T3B case features extremely high freestream turbulence intensity. Therefore, the transition occurs almost immediately. This feature makes the tuning of the γ model very difficult for this extreme case. A similar observation is valid for the BC transition model. This extreme case is particularly important in practice since the laminar flow section is short, and drag estimations are not affected significantly by the application of a transition model. In practice, this test case is very close to fully turbulent flows and a classical turbulence model can be utilized.

Finally, the shortcomings of a transition-free turbulence model should also be mentioned. We have employed $k - \omega - SST$ turbulence model for this purpose since it constitutes the basis of γ model. As seen from Figures 10, 12, 14 and 16, the original $k - \omega - SST$ model underestimates the skin friction at the fully turbulent zone. The mismatch is more significant when the free stream turbulence is low and the transition length is short. A similar observation is reported between SA and SA-BC models.

Results for ERCOFTAC Nonzero Pressure Gradient Cases

The ERCOFTAC test cases T3C2, T3C3, T3C4 and T3C5 are used to validate the model in the scenario of a transitional boundary layer with the influence of a pressure gradient. The favorable pressure gradients impact the transition onsets of T3C2, T3C3, T3C4 and T3C5 under various freestream velocity changes. Analyses are done using The Menter one-equation γ and BC transition models. The results obtained in this section are highly dependent on computational domains. As mentioned, the pressure gradient is implemented using the converging-diverging duct shape domain. The upper boundary should be generated to satisfy the experimental data of local free stream flow velocity. The computational domain is obtained iteratively. The same domain is used for all T3C simulations. Inlet turbulence intensity and viscosity ratios are assigned considering turbulence intensity profiles of experimental data. Velocity profiles obtained using the inlet conditions in Table 1 are given in Figure 17 for T3C cases.
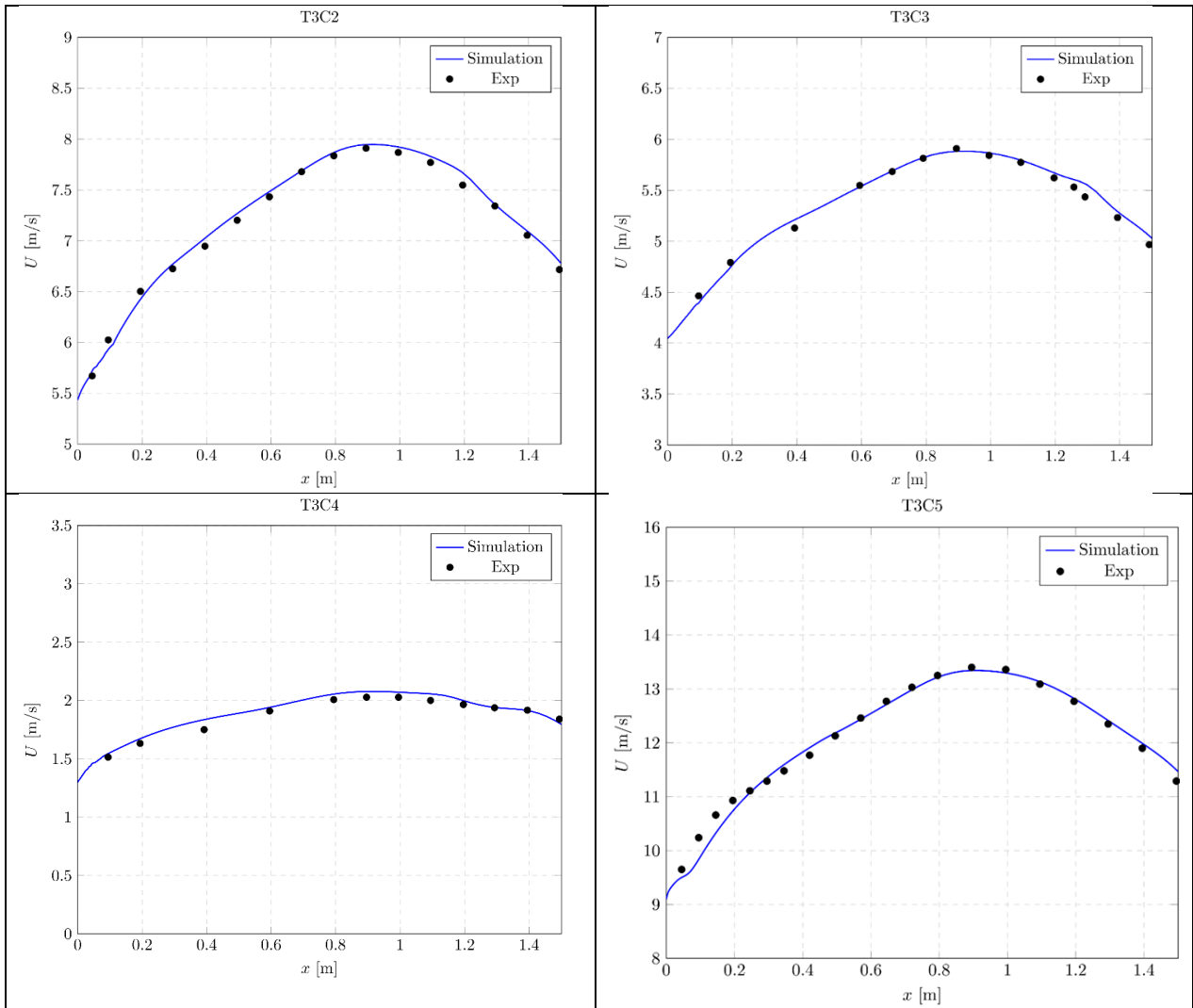
Figure 17: Distributions of freestream velocity for T3C cases. The freestream velocities are taken from the last velocity readings at each x-stations from experimental data. The numerical data is taken through a curve passing the same (x,y) locations and obtained with the γ model.

Velocity profiles reasonably agree with the experimental data. Turbulence intensity profiles of the simulations are presented in Figure 18. This proves that the geometry generated for turbulence dat work reasonably well.
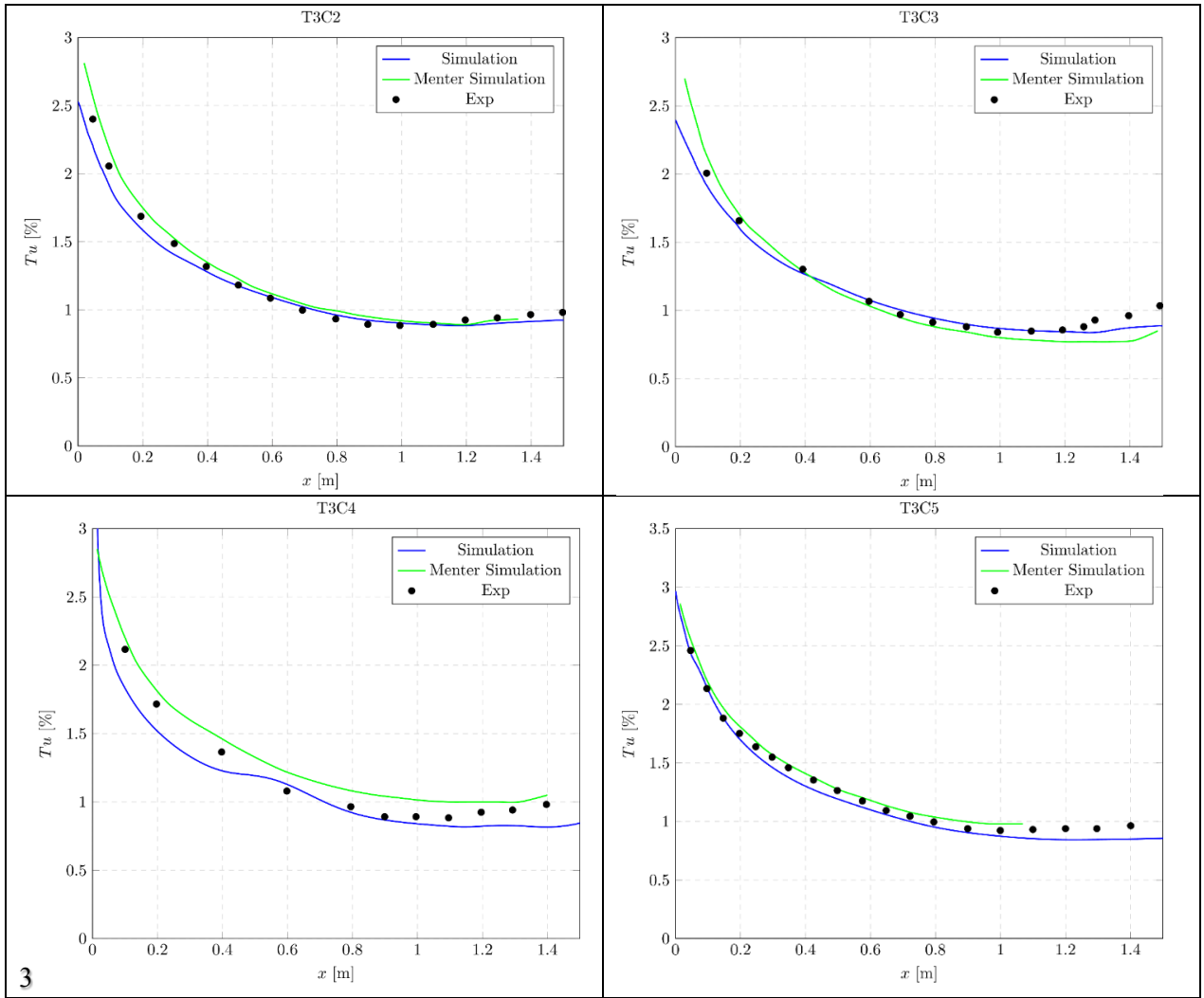
Figure 18: Turbulence intensity of T3C simulations. The numerical data is taken through a curve passing the centerline locations and obtained with the γ model.

Turbulence intensity profiles of T3C cases seem to be quite good. Skin friction coefficients for T3C2, T3C3, T3C4 and T3C5 cases are presented in Figures 19-22.
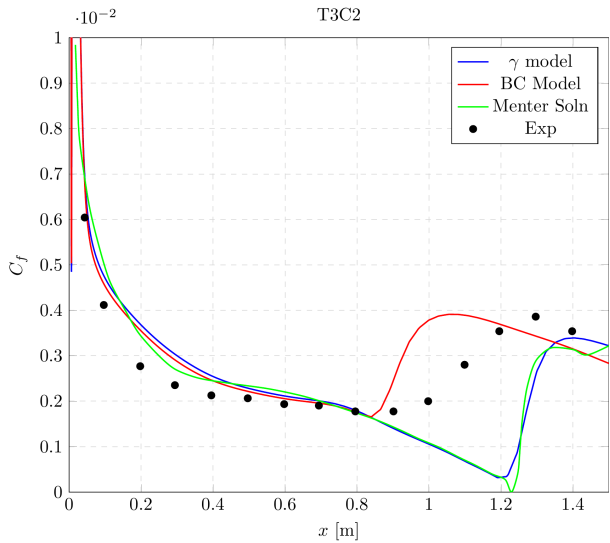
Figure 19: Skin friction coefficients obtained with Different Models for T3C2 Case
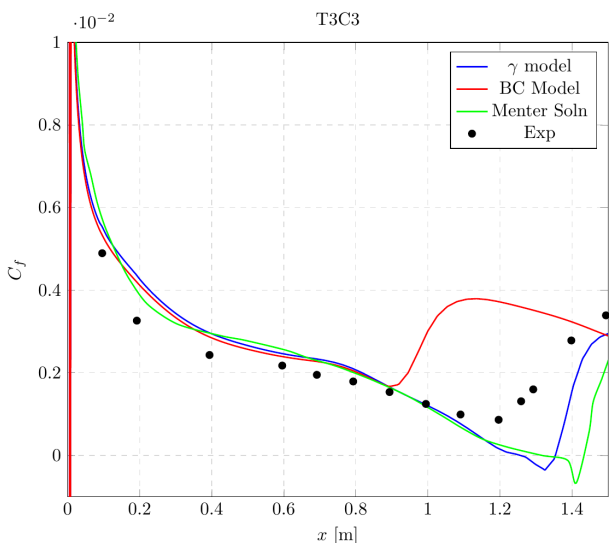
Figure 20: Skin friction coefficients obtained with Different Models for T3C3 Case
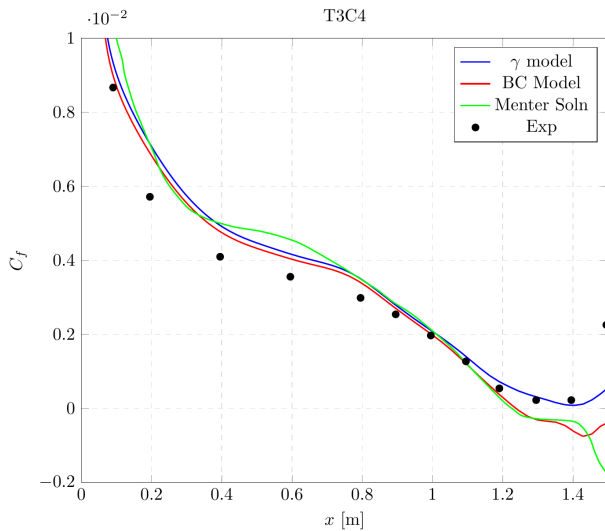
Figure 21: Skin friction coefficients obtained with Different Models for T3C4 Case
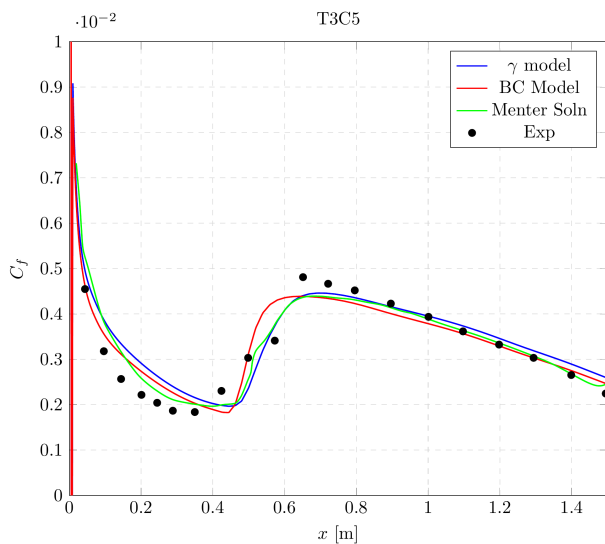
Figure 22: Skin friction coefficients obtained with Different Models for T3C5 Case

In the T3C2 case, both transition models capture transition onset with some errors. Both models predict a good enough skin friction coefficient after flow becomes fully turbulent. The Menter one-equation γ model and Bas-Cakmakciglu Model predict transition reasonably accurately in T3C3, similar to T3C2. T3C4 is the case with the smallest velocity. Although both models overpredict skin friction in the laminar region, they resolve transition onset accurately. Finally, in the T3C5 case, both transition models accurately resolve the laminar region, transition onset and length and flow after the transition. To sum up, the Menter one-equation γ model and the Bas-Cakmakciglu model predict transition onset and length similarly, and results

were reasonably accurate in favorable pressure gradient test cases.

Once again, T3C4 is the test case that is not well-suited for validation studies as in T3B. The transition onset is at the exit of the flat plate. Therefore, the results are open to experimental errors. The transition length is indefinite. Any differences in the transition onset estimations by the model may result in fully laminar flow results. Therefore, this test case is not a good test case for the evaluation of transition model performance.

2D Airfoil Cases

E387 Airfoil

Eppler E387 airfoil was tested to assess the γ model performance on 2D airfoil cases. Figure 23 shows the airfoil profile, which allows for a substantial amount of laminar flow before the transition on the suction side. Experimental data was taken from the study conducted at Langley low-turbulence pressure tunnel (LTPT) (McGhee (1988)) at Reynolds number 2×10^5. Lift and drag coefficients at different angles of attack obtained in the experiments are available. The importance of this airfoil is that the laminar separation bubble is formed at the suction side, and flow re-attaches as turbulent. In other words, a separation-induced transition is observed at the E387 airfoil.

A 699×179 O-type grid with a 1.075 growth ratio is generated for simulations. The first layer thickness is assigned 1×10^{-5} units to the first cell to maintain $y^+ < 1$ and resolve the boundary layer accurately. Freestream turbulence intensity is specified as 0.18, and the viscosity ratio was chosen as 2. The computational grid used around the airfoil is given in Figure 24.
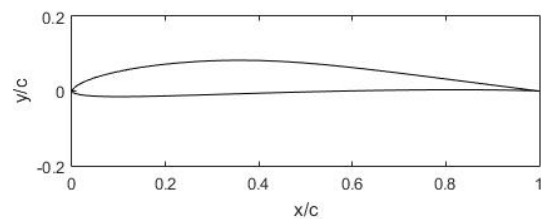
Figure 23: E387 airfoil profile
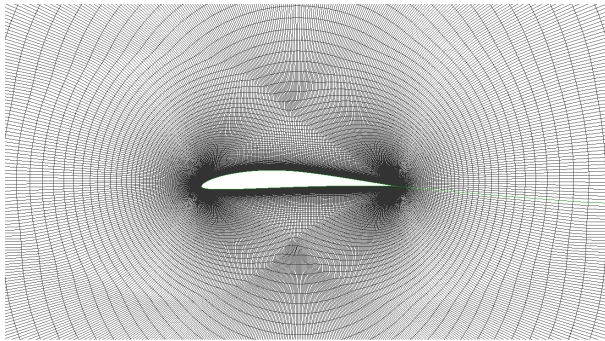
Figure 24: Computational domain around the E387 airfoil

In Figure 25, numerical results obtained with the γ model are compared with experimental data. This figure shows that the lift and drag coefficients obtained agree with experimental data, whereas a fully turbulent solution overpredicts the drag coefficients. The difference between the experimental data and simulation results at high angles of attack could be solver-based.
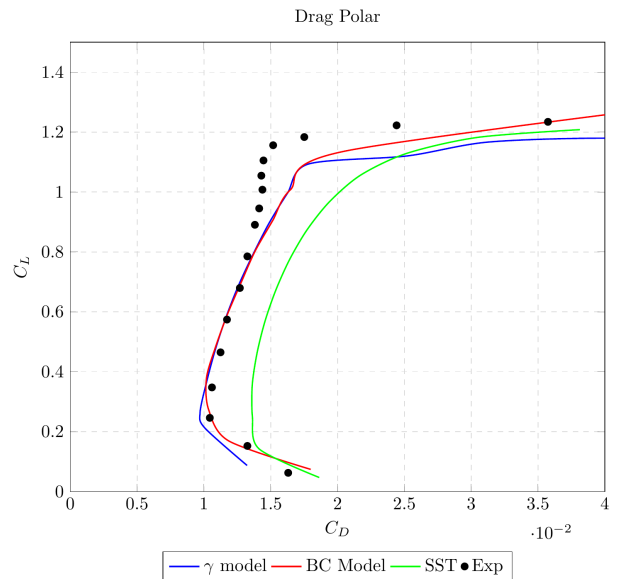
Figure 25: Drag polar of E387 airfoil

The importance of the E387 airfoil is that separation-induced transition occurs at the suction side of the airfoil. As expected, a fully turbulent solution misses the separation bubble. Both models predict that the flow separates to the laminar and re-attaches as fully turbulent after the separation bubble.
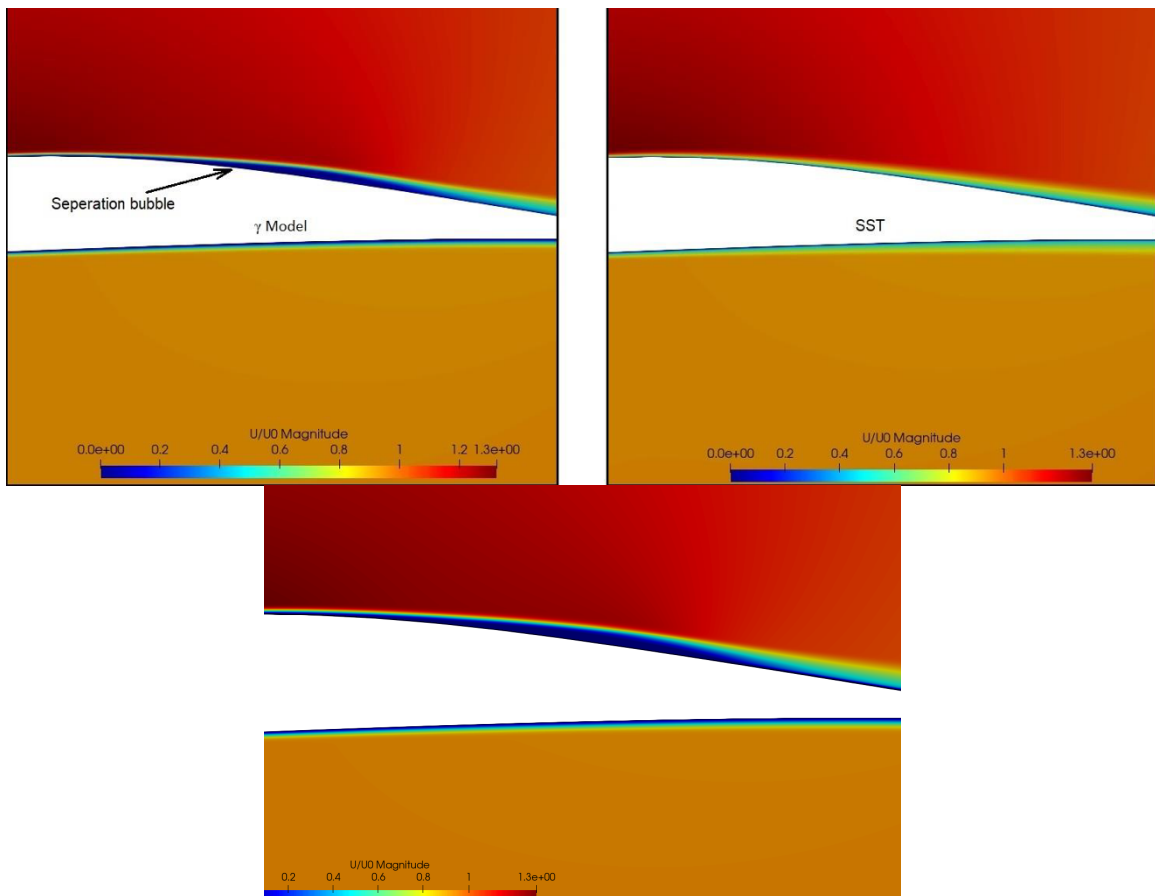
Figure 26: Flow field around the E387 airfoil top left: γ model, top right: SST, bottom: SA-BC model
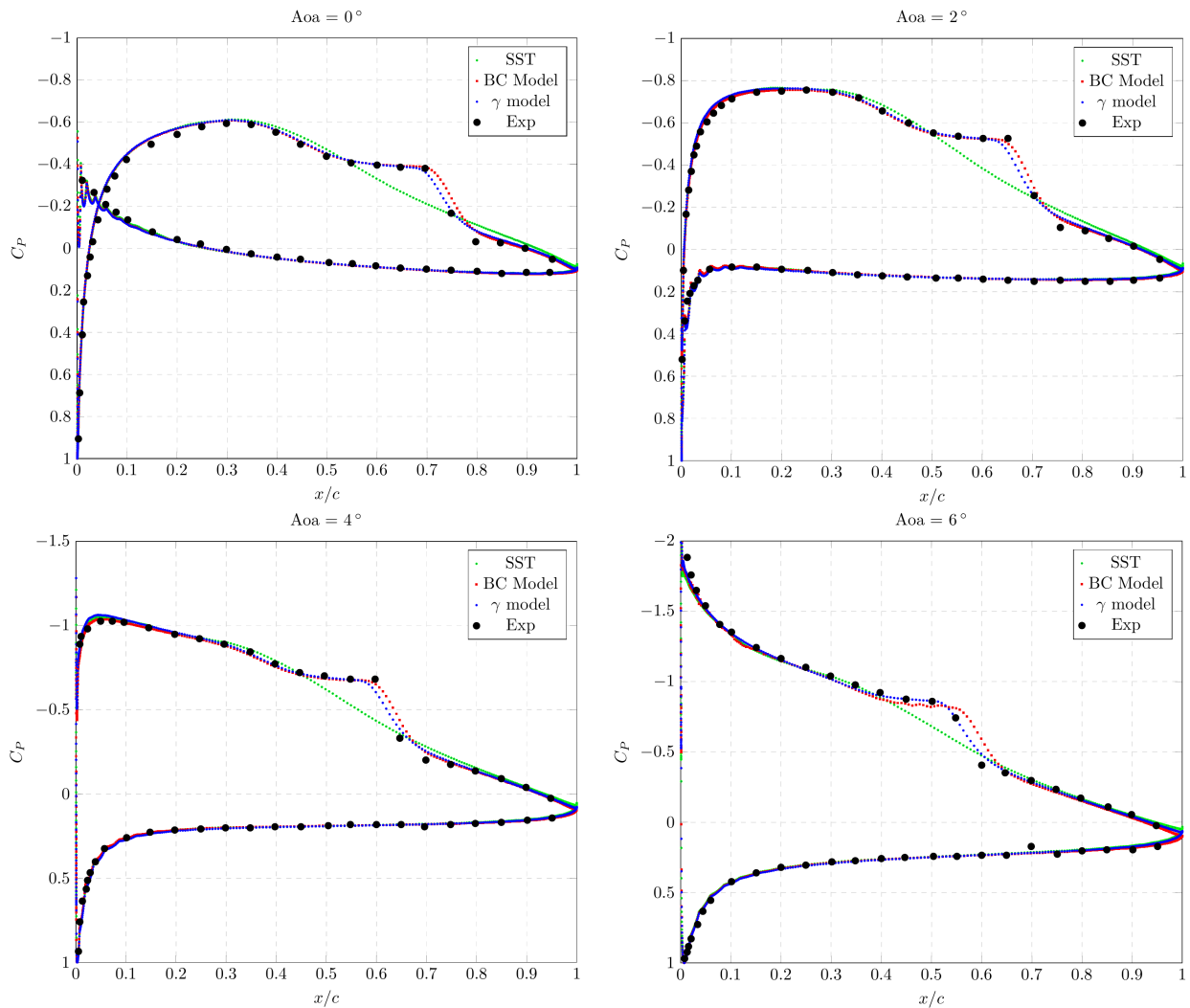
Figure 27: Comparison of Pressure Coefficients obtained with different models at different angles of attack

It can be inferred from Figure 26 that the γ model captures the separation bubble, whereas the fully turbulent solution based on the same model foundation (SST) misses it. The BC model also predicts a separation bubble at the same location with similar size. The same fact can be seen in Figure 27. The pressure coefficients obtained with the γ model, Bas- Cakmakcioglu model and SST are presented. Both transition models capture the separation-induced transition well enough, whereas a fully turbulent solution cannot. The reason for this difference stems from the lower skin friction estimations at the laminar forward part of the suction side. The adverse pressure gradient on the pressure side result in flow separation, according to von karmans momentum integral theory. The $k - \omega - SST$, on the other hand, model provide a higher fully turbulent skin friction that prevents the separation.

S809 Airfoil

The S809 airfoil is a laminar flow profile airfoil designed for horizontal axis wind turbine applications. Detailed experimental data, including drag coefficient, lift coefficient and pressure distribution of S809 airfoil, is available by Somers (1997). The airfoil profile is shown in Figure 28.
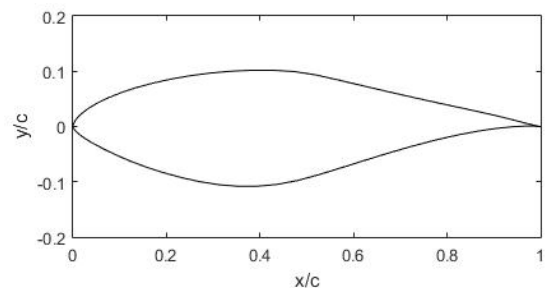
Figure 28: S809 airfoil profile
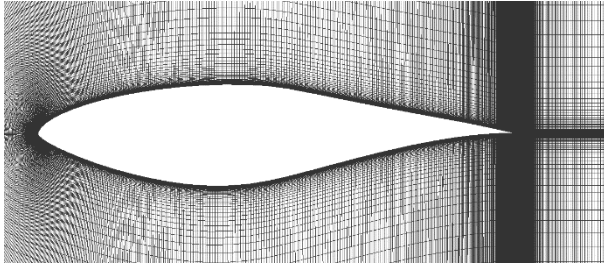
Figure 29: Computational domain around the S809 airfoil

C-type grid mesh is generated around the S809 airfoil with approximately 900 nodes (450 nodes on each side) around the airfoil. 100 nodes are created normal to airfoil profile with first layer thickness equal to 1×10^{-5} units to obtain $y^+ < 1$. The farfield boundary was located ten chord lengths from the airfoil. The computational domain used can be seen in Figure 29. Inlet conditions are given in Table 3.

Table 3: Inlet Conditions for the S809 Simulations

Case	Re_x	Mach	Chord (m)	FSTI(%)	μ_t/μ	α
S809	2×10^6	0.1	1	0.05	10	0° to 14°
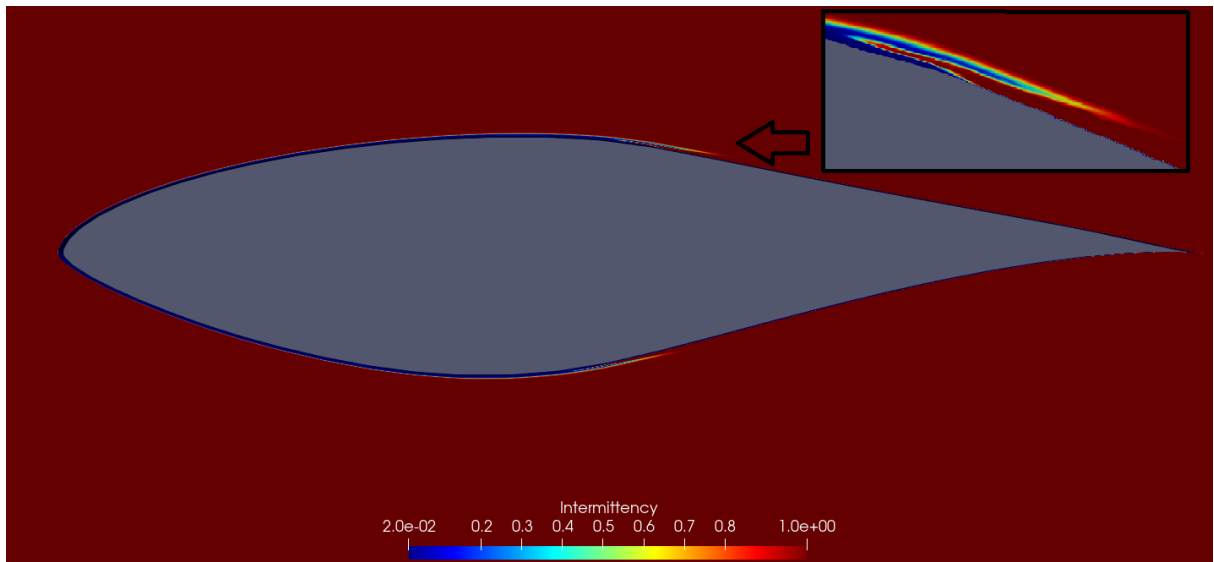
Figure 30: Intermittency at the angle of attack of $\alpha = 1°$ obtained with the γ model.

The drag polar plots of the S809 airfoil at various angles of attacks are given in Figure 31. Transition models significantly improve the drag coefficient prediction since the effect of laminar flow over the airfoil surface is captured. Menter's one-equation γ model and the Bas-Cakmakcioglu model make similar predictions.
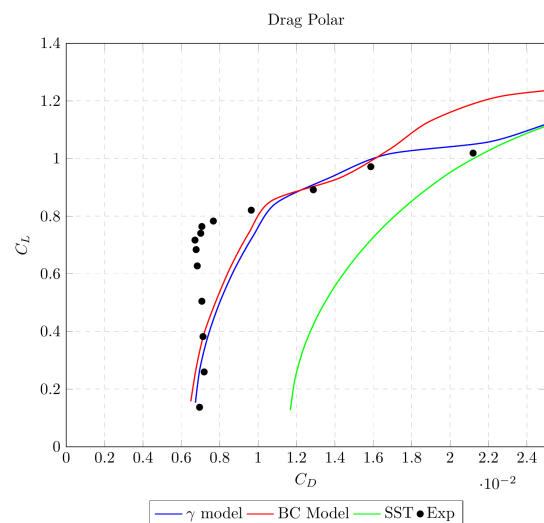
Figure 31: Drag polar of S809 Airfoil

152

Importance of Freestream Turbulence Properties

The most critical drawback of Menter's one equation γ model is its sensitivity to the inlet turbulence intensity and viscosity ratio, whose determination is the source of uncertainty. The model can predict different transition characteristics in transition onset and length for different inlet turbulence intensity and viscosity ratios.

The reasons for this behavior are the underlying turbulence model, $k - \omega - SST$, and the use of the local turbulence intensity in the implementation. The intermittency γ is coupled with the turbulent kinetic energy, hence the **local** turbulence intensity. Therefore γ model is affected by local turbulence characteristics. However, the success of the BC transition model shows that the turbulence intensity at the leading edge of the plate is the critical factor for the transition onset. Notice that the underlying turbulence model of the BC transition model, Spalart-Allmaras, does not provide any turbulence intensity information.

On the other hand, in external flow simulations, a user must provide appropriate k and ω boundary conditions at the freestream to solve transitions accurately. The k can be determined relatively easily. However, it is challenging to determine ω in engineering problems. Moreover, the freestream parameters decay until the leading edge, making applying these parameters even more difficult. To show this dependence on freestream conditions, the Menter one-equation γ model is tested for different freestream turbulence properties T3A test case.

Note that the freestream turbulence intensity alters the transition onset, and this parameter is measured and reported for all test cases. Therefore, the freestream turbulence intensity is kept the same with the experimental data while the viscosity ratio changes. Applied freestream turbulence properties are presented in Table 4.

Table 4: Inlet viscosity ratio applied in tests

	μ_t/μ						
Setup	1	4	9	12	30	60	120

The response of Menter one equation γ model to different viscosity ratios is given in Figure 32.
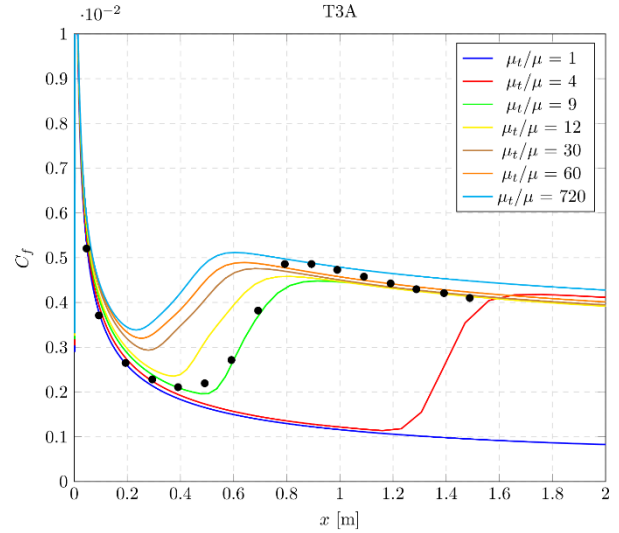
Figure 32: Effect of the viscosity ratio of freestream inlet conditions

Figure 32 shows that the freestream viscosity ratio significantly affects the results. For $\mu_t/\mu = 1$, flow behaves completely laminar. An increase in the viscosity ratio results in the transition onset location moving closer to the leading edge of the plate.

Discussion

In this study, we have tested two transition models a natural transition, bypass transition with and without pressure gradient and separation-induced transition. Both models can predict natural transition accurately and bypass transition with reasonable accuracy. Zero pressure gradient test case simulations show that the success of the γ model is highly dependent on the freestream turbulence properties. It should be noted that some of the freestream turbulence characteristics are difficult to determine in real-life applications. The study showed that transition prediction could change significantly for different viscosity ratio specifications. Mentioned deficiency complicates the simulation preparation and, as a result, the applicability of the γ model to general flow cases. BC transition model does not suffer such a shortcoming.

Zero-equation Bas-Cakmakcioglu transition model predicts transition effects similar to the γ model for different transition modes. On the other hand, the BC transition model does not suffer excessive turbulence boundary conditions requirements as it only requires the freestream turbulence intensity. In addition to that, as it does not solve additional differential equations, solutions are obtained faster

compared to the γ model. It should be noted that both models predict the transition onset accurately, and both of them can be applied depending on the selection of the underlying turbulence model.

CONCLUSIONS

In this study, we have studied the Menter one-equation γ and Baş-Çakmakçıoğlu models for transitional flows. The models are implemented in our open-source CFD solver. Then, the transition model is tested on different well-known benchmark transitional cases. Results show that both transition models give similar predictions as long as freestream turbulence properties are specified accurately. The performance of both transition models used in this study depends on the freestream turbulence intensity. BC transition model stands out as it does not suffer from the freestream viscosity ratio.

Both models are tested in this study on several flat-plate and two-dimensional airfoil cases. None of the test cases were decisive for the model performance for relaminarization problems. We recommend Baş-Çakmakçıoğlu model for external aerospace applications since it is simpler to implement, cheaper to run, and easier to apply than γ model.

As discussed previously, the transition onset depends on the freestream turbulence. This fact is shown by various experiments, including Schubauer, ERCOFTAC, Sinclair, and Fashifar experiments, as shown in Figure 3. The turbulence intensity is a local parameter in k-based turbulence models. Therefore, such models use local k as the transition trigger measure. These models include Menter's γ and $\gamma - Re_{\theta c}$ model and Walter and Colkjat's $k_L - k_T - \omega$ models.

However, this selection brings about a disadvantage to k-based methods. The freestream k that is supplied as a boundary condition decays significantly in the free stream. The decay rate of the k in all $k - \omega$ models is given as

$$D_k = -\beta^* \rho \omega k \qquad (21)$$

This indicates that the decay rate of k (hence Tu) depends on both k and ω. Therefore, local turbulence intensity is affected by both parameters. This is also true for γ model since the modified decay rate given in Equation 16 allows the decay of k even within the laminar region.

On the other hand, the experiments do not indicate any correlation between the local turbulence intensity and the transition onset. We have tested two different transition models for this purpose. The first one is $k - \omega$-based Menter's γ model, in which the turbulent decay is an issue. The other one is the SA-based BC transition model, where local turbulence intensity (hence decay of Tu) is not available, and the freestream Turbulence intensity is supplied as a parameter.

The numerical experiments show that for a wide range of freestream turbulence, the SA-BC transition model provides excellent results without any Tu-decay. The γ models also exhibit good results, provided that the free stream ω is supplied as μ_t such that k-decay is also fit. However, ω is not available for the free stream. Most CFD codes assign a small default ω at the free stream boundaries. Therefore, the decay rate at the freestream becomes small.

The requirement of the ω Boundary condition brings a couple of problems. If the flow is external, the user should adjust the freestream k at the leading edge of the solid boundary to fit the freestream k. For internal flows, such as turbomachinery flows, the decay rate of the high-turbulence intensity flows becomes important in k-based model.

Similar problems are implied in Menter's original work. ERCOFTAC cases (which are more akin to internal flow due to the pressure change) provide the turbulence decay data. Therefore, the freestream ω is adjusted for all test cases. The γ model is calibrated with these test cases with both freestream k and ω. Therefore simulation results on these calibration test cases are suitable.

On the other hand, The BC transition model fits the results comparably without turbulence decay and using only the freestream turbulence intensity. Therefore, we can argue that the local turbulence intensity has little to no effect on the transition onset, as the experiments suggest. Therefore utilization of the local turbulence feature in k-based transition models brings unjustified complexity.

We have demonstrated the dependency of the k-based models in the freestream turbulence parameters. As seen in the results, we have altered the freestream turbulent viscosity within the range of flat plate μ_t of Menter's simulations. It is seen that this parameter has a significant effect on the transition onset calculations. Although it is not given in this study, the W&C model shows similar

results. We can conclude that available $k - \omega$-based transition models have a similar shortcoming.

Another feature of the γ model is that the transition length is also calibrated in the models. The BC transition model is an abrupt transition model. However, the tests show that both models show similar transition lengths in all flat plate tests. We can conclude that all available transition experiments transition is abrupt, and transition length calibrations require more experimental data.

As the second claim of Menter was that the γ model could also be used in relaminarization problems and separation-induced transition problems. We could not find experimental data for relaminarization to test the former. For the latter, we have tested two airfoils. Both γ and BC transition models exhibit similar results. Drag polars show that the BC transition model has a small edge over the γ model without adjusting the free stream turbulent viscosity. Therefore we can argue that the BC transition model is ready for the external transient flow conditions without adjustment.

It should be noted that it is relatively easy to apply the γ model in external flow calculations. The difficulties mentioned above may arise in internal flow transition problems. We left the internal flow simulations as future work.

LIST OF SYMBOLS

BC	Bas Cakmakcioglu (Transition Model)
CFD	Computational Fluid Dynamics
DNS	Direct Numerical Simulation
FVM	Finite Volume Method
LES	Large Eddy Simulation
RANS	Reynolds Averaged Navier Stokes
SA	Spallart Allmaras
SST	Shear Stress Transport
WCM	Walters Cokljat Model
E	Destruction Term
ν	Kinematic Viscosity
μ	Dynamic Viscosity
P	Production Term
Re_ν	Vorticity Reynolds Number
$Re_{\theta c}$	Critical Momentum Thickness Reynolds Number
$Re_{\theta t}$	Transition Onset Momentum Thickness Reynolds Number
Re_θ	Momentum Thickness Reynolds Number
Re	Reynolds Number
S	Strain Rate Magnitude
μ_T	Turbulent viscosity
Tu	Turbulence Intensity
Ω	Vorticity Magnitude
γ	Intermittency
k_L	Laminar Kinetic Energy
k	Turbulent Kinetic Energy
λ	Pressure Gradient Parameter
ω	Specific Turbulence Dissipation Rate
ρ	Density

REFERENCES

Bas, Onur, Cakmakcioglu, Samet C, & Kaynak, Unver. 2013. A novel intermittency distribution-based transition model for low-re number airfoils.

Page 2531 of: 31st AIAA applied aerodynamics conference.

Cakmakcioglu, Samet C, Bas, Onur, Mura, Riccardo, & Kaynak, Unver. 2020. A revised one-equation transitional model for external aerodynamics. Page 2706 of: AIAA Aviation 2020 Forum.

Cakmakcioglu, Samet Caka, Bas, Onur, & Kaynak, Un- ver. 2018. A correlation-based algebraic transition model. Proceedings of the Institution of Mechanical Engineers, Part C: Journal of Mechanical Engineering Science, 232(21), 3915–3929.

Cho, Ji Ryong, & Chung, Myung Kyoon. 1992. A k—ε—γ equation turbulence model. Journal of Fluid Mechanics, 237, 301–322.

Dhawan, SJ, & Narasimha, R. 1958. Some properties of boundary layer flow during the transition from laminar to turbulent motion. Journal of Fluid Mechanics, 3(4), 418–436.

Dikbaş, E, and Baran ÖU. 2022, Implementation, verification and assessment of vortex capturing capabilities of k-kl turbulence model., Isı Bilimi ve Tekniği Dergisi 42 (1), 113-122.

Duru, C, Alemdar H, and Baran ÖU. 2021 CNNFOIL: Convolutional encoder decoder modeling for pressure fields around airfoils., Neural Computing and Applications 33 (12) 6835-6849.

Emmons, Howard W. 1951. The laminar-turbulent transition in a boundary layer-Part I. Journal of the Aeronautical Sciences, 18(7), 490–498.

Frei, Walter. 2013. Which Turbulence Model Should I Choose for My CFD Application? URL https://www. comsol. com/blogs/which-turbulence-model-should-choose-cfd-application/. accessed (2023): 03-20.

Jones, W Poo, & Launder, BrnE. 1973. The calculation of low-Reynolds-number phenomena with a two-equation model of turbulence. International Journal of Heat and Mass Transfer, 16(6), 1119–1130.

Kaynak, Unver, Bas, Onur, Cakmakcioglu, Samet Caka, & Tuncer, Ismail Hakki. 2019. Transition modeling for low to high speed boundary layer flows with CFD applications. In: Boundary layer flows-theory, applications and numerical methods. intechopen.

Langtry, Robin B, & Menter, Florian R. 2009. Correlation-based transition modeling for unstructured parallelized computational fluid dynamics codes. AIAA journal, 47(12), 2894–2906.

Langtry, Robin Blair. 2006. A correlation-based transition model using local variables for unstructured parallelized CFD codes.

Langtry, Robin Blair, Menter, FR, Likki, SR, Suzen, YB, Huang, PG, & Völker, S. 2006b. A correlation-based transition model using local variables—part II: test cases and industrial applications.

Mayle, RE, & Schulz, A. 1996. The path to predicting bypass transition. Page V001T01A065 of: Turbo Expo: Power for Land, Sea, and Air, vol. 78729. American Society of Mechanical Engineers.

Mayle, Robert Edward. 1991. The 1991 IGTI scholar lecture: the role of laminar-turbulent transition in gas turbine engines.

McGhee, Robert J. 1988. Experimental results for the Eppler 387 airfoil at low Reynolds numbers in the Langley low-turbulence pressure tunnel. Vol. 4062. National Aeronautics and Space Administration, Scientific and Technical. 55

Menter, Florian R. 1994. Two-equation eddy-viscosity turbulence models for engineering applications. AIAA journal, 32(8), 1598–1605.

Menter, Florian R, Kuntz, Martin, & Langtry, Robin. 2003. Ten years of industrial experience with the SST turbulence model. Turbulence, heat and mass transfer, 4(1), 625–632.

Menter, Florian R, Langtry, Robin Blair, Likki, SR, Suzen, YB, Huang, PG, & Völker, S. 2006a. A correlation-based transition model using local variables—part I: model formulation.

Menter, Florian R, Smirnov, Pavel E, Liu, Tao, & Avancha, Ravikanth. 2015. A one-equation local correlation-based transition model. Flow, Turbulence and Combustion, 95(4), 583–619.

Menter, FR, & Langtry, RB. 2012. Transition Modelling for Turbomachinery Flows. Low Reynolds Number Aerodynamics and Transition, 31–58.

Menter, FR, Esch, T, & Kubacki, S. 2002. Transition modelling based on local variables. Pages 555–564 of: Engineering Turbulence Modelling and Experiments 5. Elsevier.

Menter, FR, Langtry, R, & Völker, S. 2006b. Transition modelling for general purpose CFD codes. Flow, turbulence and combustion, 77(1), 277–303.

Nichols, Robert H. 2010. Turbulence models and their application to complex flows. University of Alabama at Birmingham, Revision, 4, 89.

Savill, AM. 1993. Some recent progress in the turbulence modelling of bypass transition. Near-wall turbulent flows, 829–848.

Schubauer, Galen B, & Klebanoff, Philip S. 1955. Contributions on the mechanics of boundary-layer transition. Tech. rept.

Smith, Apollo Milton Olin. 1956. Transition, pressure gradient and stability theory. Douglas Aircraft Co., Report ES 26388.

Somers, Dan M. 1997. Design and experimental results for the S809 airfoil. Tech. rept. National Renewable Energy Lab.(NREL), Golden, CO (United States).

Steelant, Johan, & Dick, Erik. 2001. Modeling of laminar- turbulent transition for high freestream turbulence. J. Fluids Eng., 123(1), 22–30.

Suzen, Y, & Huang, P. 2000. An intermittency transport equation for modeling flow transition.

Page 287 of: 38th Aerospace Sciences Meeting and Exhibit. 57

Walters, D Keith, & Cokljat, Davor. 2008. A three-equation eddy-viscosity model for Reynolds-averaged Navier–Stokes simulations of transitional flow. Journal of fluids engineering, 130(12).

Wang, Jiang-Sheng, & Wang, Jin-Jun. 2021. Wake-induced transition in the low-Reynolds-number flow over a multi-element airfoil. Journal of Fluid Mechanics, 915.

EFFECT OF INLET VELOCITY PROFILE AND ENTRANCE LENGTH ON ABDOMINAL AORTIC ANEURYSM HEMODYNAMICS SIMULATIONS

Burcu RAMAZANLI*, Cüneyt SERT**, Mehmet Metin YAVUZ***
*Middle East Technical University, Mechanical Engineering Department
06800, Çankaya, Ankara, karburcu@metu.edu.tr
**Middle East Technical University, Mechanical Engineering Department
06800, Çankaya, Ankara, csert@metu.edu.tr
***Middle East Technical University, Mechanical Engineering Department
06800, Çankaya, Ankara, ymetin@metu.edu.tr

Abstract: In computational Abdominal Aortic Aneurysm (AAA) hemodynamics studies, along with adjusting the problem geometry, mesh, transport, turbulence and rheology models; setting up boundary conditions (BC) is also a very important step which affect the reliability and accuracy of the hemodynamic assessment. The transient effects of physiological flow are well described by the *Womersley* profile, though its application might be difficult due to the complex nature of functions involved. Conversely, in literature, studies utilizing *Plug* or *Parabolic* profiles as inlet boundary conditions generally requires large entrance lengths to obtain the exact characteristics of the *Womersley* profile. In the current study, the differences arising between those boundary conditions, *Womersley*, *Parabolic* and *Plug*, with different entrance lengths, $L_{ent} = D, 3D$ and $11D$, are examined by comparing the results with a Base condition, which is a solution obtained with ensured fully-developed flow before entering the aneurysm sac at two physiological flow conditions with mean Reynolds numbers, $Re_m = 340$ and 1160. The results reveal that with increasing mean flow rate, applying the complex Womersley equation might not be necessary. For the inlet flow waveform with $Re_m = 1160$, the *Parabolic* profile can be used instead of the *Womersley* profile by supplying an entrance length $L_{ent} = 3D$. On the other hand, the *Plug* profile requires an entrance length at least $L_{ent} = 11D$ to replicate the Base condition for waveform with $Re_m = 340$.
Keywords: Abdominal aortic aneurysm hemodynamics, Womersley profile, Wall shear stress parameters, Vortex identification methods

GİRİŞ HIZ PROFİLİ VE GİRİŞ UZUNLUĞUNUN ABDOMİNAL AORT ANEVRİZMASI HEMODİNAMİĞİ SİMÜLASYONLARINA ETKİSİ

Öz: Hesaplamalı Abdominal Aort Anevrizması (AAA) hemodinamiği çalışmalarında problem geometrisi, ağ, taşıma, türbülans ve reoloji modellerinin ayarlanması ile birlikte; sınır koşullarının (BC) belirlenmesi de hemodinamik değerlendirmenin güvenilirliğini ve doğruluğunu etkileyen çok önemli bir adımdır. Fizyolojik akışın geçici etkileri, *Womersley* profili tarafından iyi bir şekilde tarif edilir, ancak ilgili fonksiyonların karmaşık doğası nedeniyle bu profilin uygulanması zor olabilir. Öte yandan, giriş sınır koşulu olarak *Plug* veya *Parabolik* hız profilleri kullanan çalışmalar, *Womersley* profilinin tam özelliklerini elde etmek için genellikle büyük giriş uzunlukları kullanırlar. Bu çalışmada, *Womersley*, *Parabolik* ve *Plug* hız profilleri ve üç ayrı giriş uzunluğu kullanılarak ($L_{ent} = D, 3D$ and $11D$) anevrizma içerisinde hemodinamik parametreler elde edilmiş ve sonuçlar Base koşul ile karşılaştırılarak incelenmiştir. Base koşulu, ortalama Reynolds sayıları $Re_m = 340$ ve 1160 olan iki fizyolojik akış koşulunda, anevrizma içine girmeden önce sağlanan tam gelişmiş akışla elde edilen bir çözümdür. Sonuçlar, ortalama debi arttıkça, karmaşık Womersley denkleminin uygulanmasının gerekli olmayabileceğini ortaya koymaktadır. $Re_m = 1160$ olan giriş debi profili için, en az $L_{ent} = 3D$ olan bir giriş uzunluğu sağlanarak *Womersley* profili yerine *Parabolik* profil kullanılabilir. Öte yandan, $Re_m = 340$ olan debi profil için, *Plug* profilinin *Womersley* profili yerine kullanılması için en az $L_{ent} = 11D$ olan bir giriş uzunluğu gereklidir.
Anahtar Kelimeler: Abdominal aort anevrizması hemodinamiği, Womersley profili, Duvar kayma gerilmesi parametreleri, Girdap tanımlama yöntemleri

NOMENCLATURE

AAA	=	abdominal aortic aneurysm
ILT	=	intraluminal thrombus
WSS	=	wall shear stress [Pa]
$TAWSS$	=	time-averaged wall shear stress [Pa]
$ECAP$	=	endothelial cell activation potential [1/Pa]
OSI	=	oscillatory shear index
L_B	=	bulge length [m]
L_{ent}	=	entrance length [m]
L_{ex}	=	exit length [m]
R_B	=	bulge radius [m]
u_x	=	axial velocity component [m/s]
u_r	=	radial velocity component [m/s]
U_m	=	mean velocity [m/s]
T	=	period of cardiac cycle [s]
ω	=	frequency of cardiac cycle [1/s]
ν	=	kinematic viscosity [m²/s]
Re_m	=	mean Reynolds number $[= U_m D/\nu]$
α	=	Womersley number $[= 0.5D\sqrt{\omega/\nu}]$
τ_w	=	wall shear stress [Pa]
λ_{ci}	=	λ_{ci}-criterion, swirling strength [1/s]
$\overline{\lambda_{ci}}$	=	time – averaged λ_{ci}-criterion [1/s]

INTRODUCTION

Over several decades, intense research on physiologic flow inside the abdominal aortic aneurysms (AAA) have been performed. In order to investigate the hemodynamics inside the abdominal aneurysms, a vast amount of numerical studies is performed (Arzani et al., 2014; Arzani and Shadden, 2016; Drewe et al., 2017; Finol and Amon, 2001). Computational models enable researchers to approximate behavior of blood flow hemodynamics under realistic conditions. The models are generated by defining the conditions on the boundaries and numerically solving governing equations in the fluid domain. Generation of the problem geometry and an appropriate mesh, setting up fluid flow models by adjusting boundary conditions, transport and turbulence properties are important steps which affect the reliability and accuracy of the hemodynamic assessments (Janiga et al., 2015; Salman et al., 2019). Since exact replication of human cardiovascular system is a challenging issue, researchers simplify the problem variables by making different assumptions on their computational models in order to decrease the cost of the solution procedure, which may lead the solutions to be far from the realistic hemodynamics. Indeed, the effect of those assumptions on the solution, and the degree of discrepancy should be examined to guide the researchers during the decision making period of their computational model.

One of the most commonly used assumptions is related to the inlet velocity profile. The most accurate application is utilizing PC-MRI measured patient-specific velocity profiles as an inlet velocity BC, obtained from the human aorta (Chandra et al., 2013;

Youssefi et al., 2018). However, accessing complete high quality patient-specific geometry and inlet profile data is not always possible due to lack of imaging facilities (Armour et al., 2021). Furthermore, directly measuring in vivo inflow conditions is still challenging because of the cardiac motion and resolution (Lodi Rizzini et al., 2020; Markl et al., 2016). Indeed, in several studies it is reported that there is no significant difference between profiles obtained from PC-MRI and artificial ones (Morris et al., 2006; Wei et al., 2019). Therefore, many studies in literature frequently use idealized profiles such as *Plug* (Drewe et al., 2017; Chen et al, 2020), *Parabolic* (Bit et al., 2020; Boyd et al., 2016; Li and Kleinstreuer, 2005; Bilgi and Atalık, 2020) and *Womersley* (Arzani et al., 2014; San and Staples, 2012).

The *Plug* profile is the uniform velocity at the inlet, while the *Parabolic* profile obtained from Poiseuille's equation, and therefore, they cannot present all the characteristics generated due to transitional effects. Although the *Womersley* profile (Womersley, 1955) is necessary to present transient effects especially for large α values, applicability and implementation of the Womersley equation as an inlet boundary condition can be difficult because of the Bessel functions and imaginary numbers that it contains (Campbell et al., 2012; Impiombato et al., 2021). Therefore, in literature, most of the studies utilize *Plug* or *Parabolic* profile with long entrance lengths to obtain fully developed condition (Stamatopoulos et al., 2010), rather than the *Womersley* profile, which increases the computation time. Indeed, the necessary entrance length to obtain fully developed conditions is also a controversial issue. In general, researchers concerned about the inlet velocity boundary conditions and to be on the safe side, they tend to extend the entrance region to ensure fully developed conditions (Madhavan and Kemmerling, 2018). In literature, recommended entrance length values to reach the fully developed state are significantly large (Durst et al., 2005; Salman et al., 2019). On the other hand, Hoi et al. (2010) reported that an entrance length at least three diameters of the artery is sufficient to avoid negligible errors in the hemodynamics of the carotid arteries. However, from a different point of view, Madhavan and Kemmerling (2018) stated that in the actual human arterial system, obtaining the fully developed hemodynamic conditions is not realistic due to the orientation of the vasculature, such as the thoracic aorta is located immediately distal to the heart.

Because the *Womersley* profile resembles the *Parabolic* form at the systole and nearly *Plug* patterns at the diastole (Womersley, 1955), it might be interesting to observe the differences arising from using these three different inlet boundary conditions. In 2012, Campbell et al. hypothesized that the *Womersley* and *Parabolic* inlet velocity boundary conditions give nearly the same result in carotid bifurcation, where $\alpha = 4.1$ and the average radius is 3 mm. However, they highlighted that the results are not applicable for large arteries like the aorta, in

which α is larger than 10, and they require further studies. In 2019, Wei et al. stated that no significant difference between realistic, *Womersley* and *Parabolic* inlet profiles while the *Plug* is notably different that the others for Fontan hemodynamics. However, to the author's best knowledge, there is a deficiency in literature to compare the effect of ideal velocity profiles on abdominal aortic aneurysm hemodynamics, where Womersley number is larger than 10, with different entrance lengths. Also, comparing the profiles at different Reynolds numbers might also be important because the *Womersley* profile shows different patterns for different flow rate values, which can be observed in cardiac conditions such as exercise and rest. Therefore, the aim of the current study is to characterize the behavior of idealized inlet velocity profiles at different entrance lengths and mean flow rates. For that purpose, *Plug*, *Parabolic* and *Womersley* velocity profiles obtained from two mean Reynolds number values, $Re_m = 340$ and 1160, for the same flow waveform pattern for the abdominal aorta are applied as inlet velocity BC to an aneurysm geometry with different entrance lengths, $L_{ent} = $ D, 3D and 11D, where D is the aorta diameter. The results are compared with a fully-developed Base case to check their applicability.

METHODS

The idealized axisymmetric abdominal aortic aneurysm models used in this study are given in Figure 1. Geometries are two dimensional axisymmetric, and created based on those used in Stamatopoulos et. al.'s study (2010). The inlet and exit parts are straight and cylindrical, while the aneurysm bulge is elliptical with a major radius of 0.034 m. The artery and bulge radii are, $R = 9$ mm and $R_B = 22$ mm. The lengths of the bulge and exit part are $L_B = 62$ mm and $L_{ex} = 206$ mm, while entrance lengths, L_{ent}, are different. As presented in Figure 1.b, entrance lengths are equal to $L_{ent} = $ D, 3D, 11D and 50D, from top to bottom and left to right, respectively. At the inlet of the models with $L_{ent} = $ D, 3D and 11D, all the velocity profiles, *Womersley*, *Parabolic* and *Plug*, are applied. To compare the results obtained with three different entrance lengths and velocity profiles, a Base condition is generated with the model having an entrance length $L_{ent} = $ 50D with only the *Plug* velocity profile at the inlet. The Base condition is checked to ensure the fully developed condition at each time steps before entering the aneurysm sac. In Table 1, the models with applied inlet velocity profiles are also presented. The vessel and bulge dimensions of all models are consistent with realistic arteries and aneurysms (Brewster et al., 2003). Actually, the idealization of the aneurysm bulge rather than utilizing patient-specific geometry may fail to simulate exact aneurysm hemodynamics. However, an idealized axisymmetric geometry is sufficient for a comparative parametric study to compare the behavior of different inlet velocity profiles, which is actually independent of geometric details.

Table 1. Aneurysm models with respect to entrance lengths, L_{ent}, and applied inlet velocity profiles.

L_{ent} (m)	Inlet Velocity Profile	
D, 3D, 11D	Womersley	
	Parabolic	
	Plug	
50D	Plug	**Base Case**

At the inlet, *Womersley*, *Parabolic*, and *Plug* profiles are specified according to the waveform which is considered to be physiologic, as presented in Figure 2a. *Plug* profile is actually the uniform velocity at the inlet, while *Parabolic* and *Womersley* velocity profiles are defined by Eqn. (1) and (2) (Wei et al., 2019, Womersley, 1955), respectively

$$u(r,t) = \frac{2Q(t)}{\pi R^2}\left(1 - \left(\frac{r}{R}\right)^2\right) \tag{1}$$

$$u(r,t) = \frac{2C_0}{\pi R^2}\left(1 - \left(\frac{r}{R}\right)^2\right) + \sum_{n=1}^{N}\frac{C_n}{\pi R^2\left(1 - \frac{2J_1\left(i^{\frac{3}{2}}\alpha_n\right)}{i^{\frac{3}{2}}\alpha_n J_0\left(i^{\frac{3}{2}}\alpha_n\right)}\right)}\left[1 - \frac{J_0\left(\alpha_n\frac{r}{R}i^{3/2}\right)}{J_0(\alpha_n i^{3/2})}\right]e^{i\omega_n t} \tag{2}$$

where α_n is the nth term of Womersley number, ω_n is the nth term of frequency, J_0 and J_1 are the Bessel function of the first kind of order zero and first, respectively (Womersley, 1955). Q is the physiologic flow rate, which is presented in Figure 2a. To obtain the Womersley profile, it is necessary to write the flow rate, $Q(t)$, in the harmonic form as in Eqn. (3)

$$Q(t) = \sum_{n=0}^{N} C_n e^{i\omega_n t} \tag{3}$$
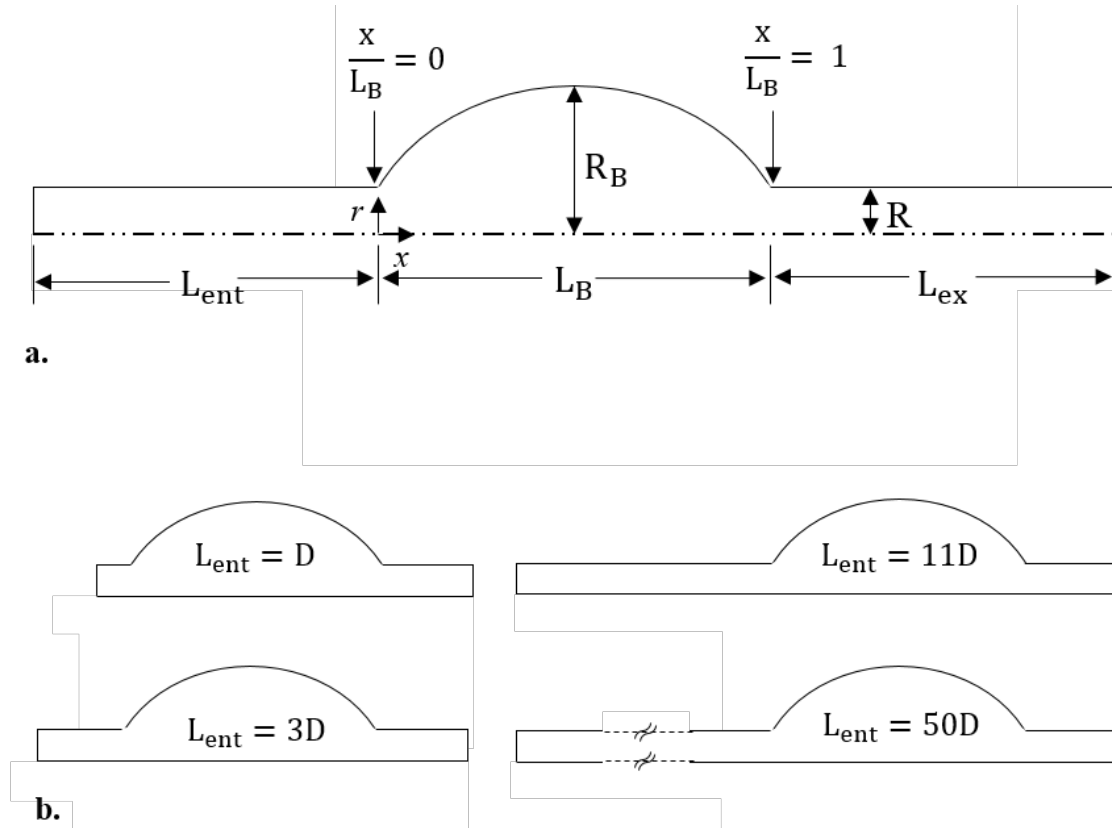
Figure 1. Sectional views of flow domains for aneurysm models, which is out of scale. Flow is from left to right.

where N is the total number of harmonic coefficients, which is equal to 70 in this study (Wei et al., 2019).A Fourier series decomposition of the flow waveform should be performed to obtain Fourier coefficients, C_n, and Fast Fourier Transforms (FFT) of the flow rates in Figure 2a are used. For that purpose, Fast Fourier Transform (FFT) method is applied to the available flow rate data, as presented in Figure 2a. C_0 and C_n's are the Finite Fourier Transform (FFT) coefficients of that flow rate, while the term n = 0 corresponds to a steady pressure gradient (Wei et al., 2019). Therefore, in Eqn. (2), the first term on the right hand side of the equation is equal to the steady Poiseuille equation (Womersley, 1955), while the second term is obtained from harmonic contribution.

In the current study, simulations are performed at two mean flow rates with Reynolds numbers, $Re_m = U_m D/\nu = 340$ and 1160, based on the mean flow velocity, where $U_m = 0.065$ and 0.22 m/s are the time averaged velocities over one period and $\nu = 3.14 \times 10^{-5}\ m/s^2$ is the kinematic viscosity. The period of all waveform patterns is the same and equal to $T = 1$ s, yielding a Womersley number of $\alpha = 0.5D\sqrt{\omega/\nu} = 12.14$, where D is the artery diameter, ω is the frequency and equals to $2\pi/T$. The waveform pattern for two flows is adapted from the study of Finol and Amon (2001) and is the same for both flow patterns as presented in Figure 2a; however, diastolic flow rate for $Re_m = 1160$ is higher. The reason for using two waveforms is to investigate the effect of increasing mean flow rate on the

applicability of *Parabolic* and *Plug* inlet velocity boundary conditions, rather than the *Womersley* profile. In Figure 2b, Womersley profiles obtained by corresponding waveforms at specified time instants are demonstrated. As can be seen from figure, with increasing flow rate, profiles obtained by Womersley formula are very similar to Parabolic form. The cardiac cycle is divided into six phases, which are early/mid/late systole and diastole. The location of each phase in the cardiac cycle is shown in Figure 2a, while time ranges for these phases are presented in Table 2.

The wall boundaries are taken as rigid and no-slip boundary condition is applied. Excluding the compliance effect with utilizing the walls as rigid is quite common common (Arzani et al., 2014; Finol and Amon, 2001). Reference pressure at the outlet is set to zero, which is a frequently utilized approach in literature for hemodynamics studies (Qiu et al., 2018; Reza and Arzani, 2019). Flow is considered to be laminar (Scotti et al., 2008) due to Reynolds number is not sufficient to reach turbulent conditions even at peak systolic phase, $Re_{peak} = 2000$. In general, blood has non-Newtonian characteristics where the viscosity decreases with increasing shear rate. However, at shear rates higher than $100\ s^{-1}$, blood shows Newtonian characteristics, and for large arteries, such as the one used in this study, it can be assumed as Newtonian (Reza and Arzani, 2019) with a kinematic viscosity of $3.45 \times 10^{-6}\ m^2/s$, and density of 1000 kg/m^3.
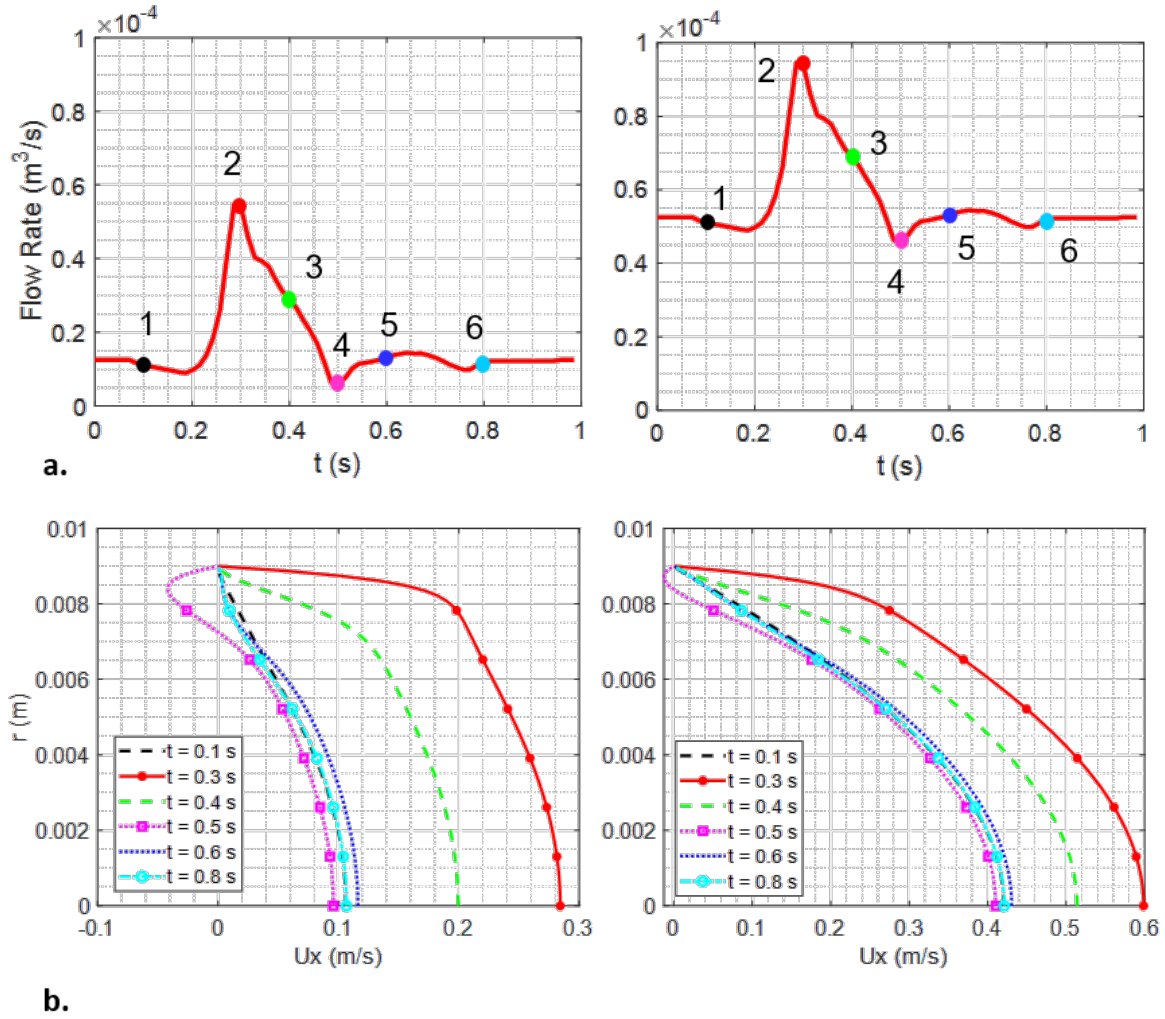
Figure 2. a. Physiological inlet flow rate waveforms and mean Reynolds numbers, $Re_m = 340$ and 1160, from left to right, respectively, with period $T = 1$ s, **b.** Womersley velocity profiles for those waveforms at selected time instants (Finol and Amon, 2001).

Table 2. Phases of cardiac cycle with period T = 1 sec.

Number	Phase	Time interval
1	Late Diastole	0 – 0.18
2	Early Systole	0.18 – 0.3
3	Mid Systole	0.3 – 0.4
4	Late Systole	0.4 – 0.5
5	Early Diastole	0.5 – 0.76
6	Mid Diastole	0.76 - 1

Numerical simulations are conducted by using OpenFOAM version 8 (openfoam.org). The governing equations are discretized using second order implicit discretization in time and second order central discretization in space. pimpleFoam solver is selected because of enabling automatic control of the time step to achieve a given maximum Courant number (C_{max}) for each case. To select an appropriate C_{max} that can provide

accurate solutions, five different Courant numbers, which are $C = 0.25, 0.5, 1, 2,$ and 4 were tested, and higher Courant numbers failed to provide stable solutions. For all Courant numbers, the same velocity profile was obtained, meaning that solutions until $C_{max} = 4$ give accurate results for the current study. However, C_{max} was taken as 1 to be on the safe side. 30 iterations are performed at each time step, and the solution is considered to be converged when residuals for axial velocity component and pressure are less than 10^{-4}. To ensure convergence, calculations are repeated for six cardiac cycles.

To select a suitable mesh, a mesh independence study is performed using four structured meshes created, as shown in Fig. 3. Figure 4a shows axial velocity profiles at the mid-plane of the aneurysm and swirling strength, λ_{ci} contours obtained by using these meshes at the peak systole and early diastole. In Figure 4b, OSI and ECAP distributions obtained by those meshes are provided. As from those figures, the axial velocity profiles are identical and swirling strength contours are very similar

for Mesh 3 and 4. Albeit OSI and ECAP distributions are very sensitive to the mesh selection, Mesh 3 and 4 obtain very similar OSI and ECAP distribution. Therefore, Mesh 3 is evaluated to be suitable and used to perform the simulations in the present study.
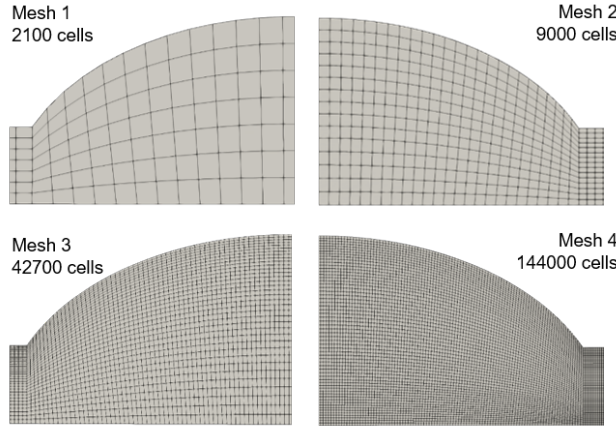
Figure 3. Four meshes generated for mesh independency check.

Stamatopoulos et al. (2010) have performed an experimental and numerical study in axisymmetric bulges similar to the ones used in the current study with a steady inlet flow. In Fig. 5a, axial velocity profiles obtained by Stamatopoulos et al. (2010) are compared with those obtained in the current study with a steady inlet flow. The validation study is performed using the Base case, and the match in the profiles is considered to be satisfactory. Ohtaroglu (2020) performed experiments with physiological, unsteady inlets using Stamatopoulos et al.'s geometry. Figure 5c compares the streamlines obtained in those experiments with the current simulation results at four different time instants of the physiological cycle. Progression of focus points in streamlines which are the indication of vortex core movement shows good agreement. Considering both spatial and the temporal evolution during the cycle, the model predictions are considered to be satisfactory. In addition, simulations are performed to ensure the validity of 2D axisymmetric simplification by comparing results with those of 3D simulations. This simplification aims to decrease the computation time and is justified by performing a sample 3D simulation to see whether there are any 3D effects altering the overall flow structure inside the aneurysm bulge. Considering the velocity profiles plotted at the mid plane of the bulge as demonstrated in Fig. 5c, 2D axisymmetric and 3D results turn out to be almost identical.

WSS Parameters and Swirling Strength

In literature, researchers utilize several physical phenomena to predict aneurysm development, thrombosis formation and rupture. Generally, wall shear stress (WSS) distribution and different WSS descriptors are used for this purpose. TAWSS descriptor evaluates the total shear stress exerted on the wall throughout a cardiac cycle and OSI highlights zones where WSS

shows directional changes over the cardiac cycle (Pinto and Campos, 2016). Mathematical definitions of these descriptors are given below (Salman et al., 2019).

$$TAWSS = \frac{1}{T}\int_0^T |\tau_w|\,dt \tag{4}$$

$$OSI = 0.5\left(1 - \frac{\left|\frac{1}{T}\int_0^T \tau_w\,dt\right|}{\frac{1}{T}\int_0^T |\tau_w|\,dt}\right) \tag{5}$$

$$ECAP = \frac{OSI}{TAWSS} \tag{6}$$

where T and τ_w are the cardiac cycle period and the wall shear stress, respectively.

Inside the aneurysm sac, there is a vortex ring, which evolves throughout the cardiac cycle. λ_{ci}-criterion is a velocity gradient based vortex identification criteria, which uses discriminant of characteristic equation to define a vortex and can be defined as follows (Chen et al., 2015)

$$\lambda_{ci} = \frac{1}{2}\sqrt{-4\frac{\partial u_r}{\partial x}\frac{\partial u_x}{\partial r} - \left(\frac{\partial u_x}{\partial x} - \frac{\partial u_r}{\partial r}\right)^2} \tag{7}$$

where u_r and u_x are radial and axial velocity components, respectively. Around a vortex region, λ_{ci} is larger than zero (Chen et al., 2015).

RESULTS AND DISCUSSIONS

In Figure 6, time-averaged axial velocity profiles obtained with *Womersley*, *Parabolic*, and *Plug* inlet velocity profiles at different entrance lengths for mean Reynolds number, $Re_m = 340$, are presented and compared with the Base condition. The profiles are plotted at proximal, mid, distal and exit sections of the models, where $x/L_B = 0.25, 0.5, 0.75$ and 1. At each section, results obtained with different inlet conditions at different entrance lengths, $L_{ent} = D, 3D,$ and $11D$, are plotted. For each section and entrance length, the time-averaged axial velocity profiles for *Womersley* are the same as in the Base case. For *Parabolic* and *Plug*, the general pattern of time-averaged axial velocity profiles is also very close to *Womersley* and the Base condition for $L_{ent} = 11D$. However, for $L_{ent} = D$ and $3D$, the shape of the time-averaged velocity profiles and maximum velocity values that they obtained are very different from the Base condition. In addition, the backflow region, which is an important characteristic of the aneurysm hemodynamics, is obtained inside the bulge by the *Womersley* and the Base case for all L_{ent} values. Especially for $L_{ent} = D$, *Plug* and *Parabolic* fail to have an accurate backflow region at those sections.
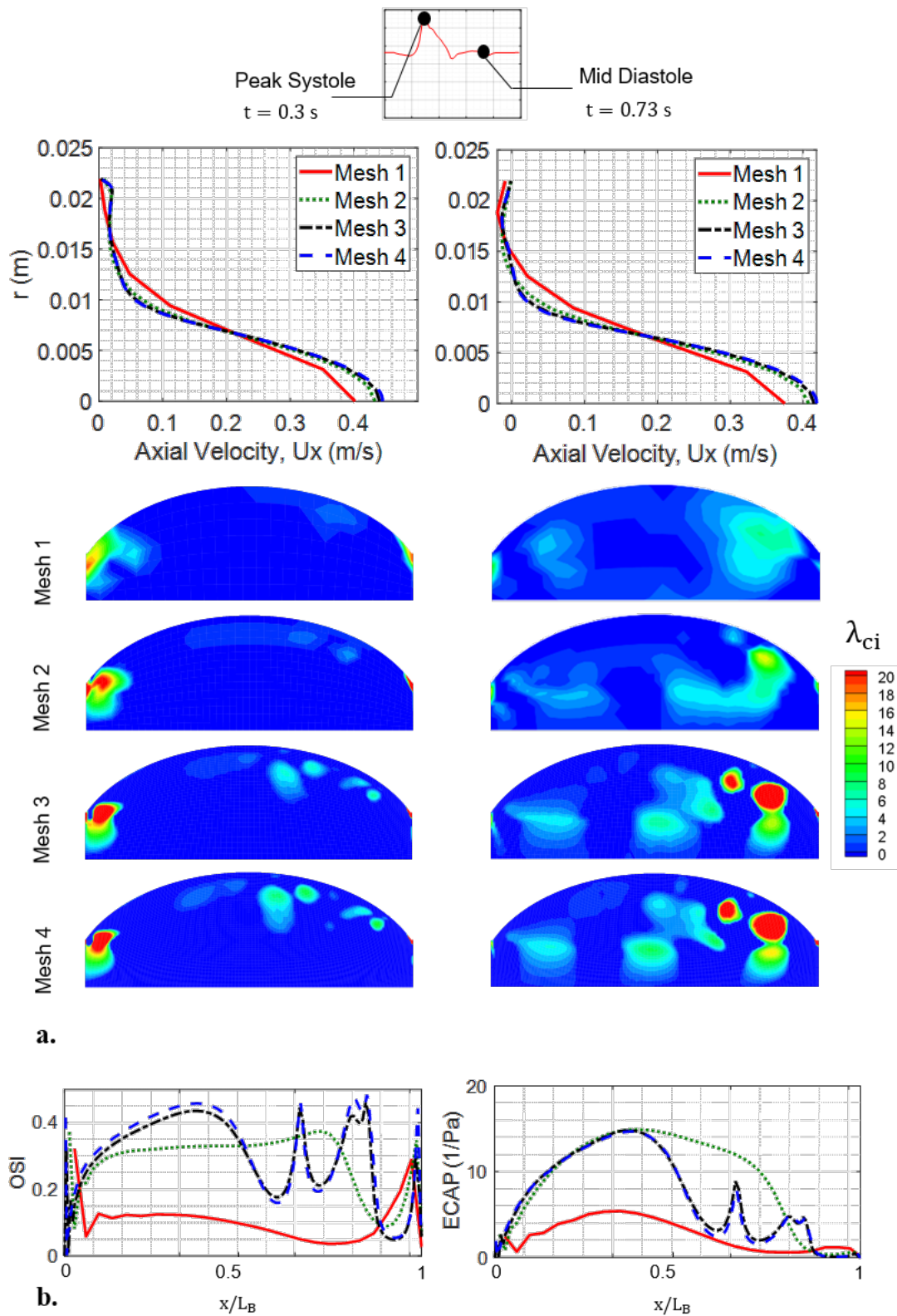
Figure 4. a. Axial velocity profiles, U_x, obtained with four different meshes at the mid-plane of the aneurysm, $x/L_B = 0.5$, and swirling strength (λ_{ci}) contours through the bulge at the peak systole and mid diastole, **b.** OSI and ECAP distributions of four meshes for mean Reynolds number, $Re_m = 1160$.
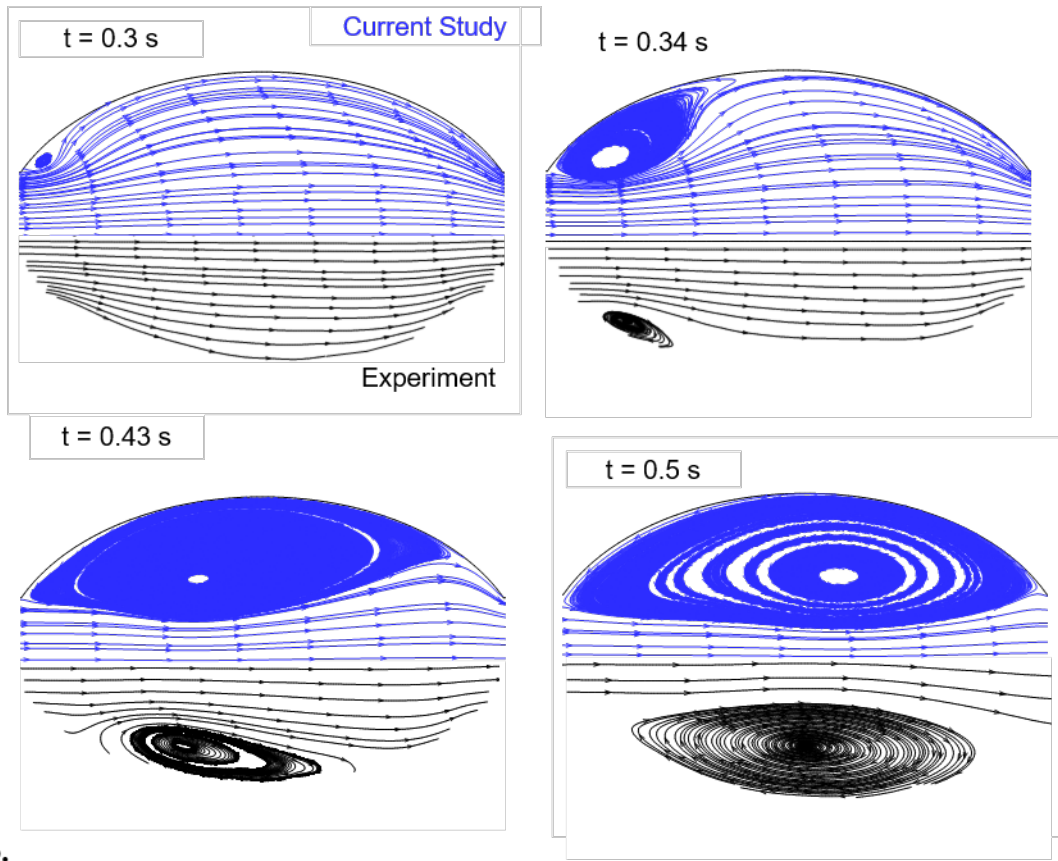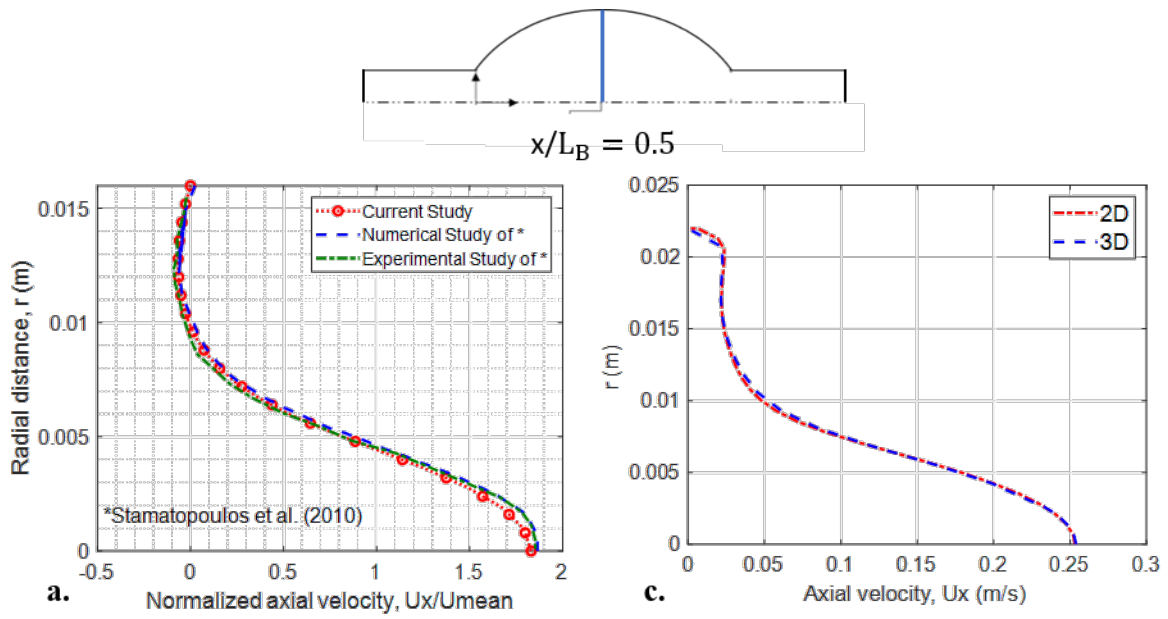
Figure 5. a. Comparison of the normalized axial velocity profile, U_x/U_{mean}, of the current study at the mid-plane of the aneurysm, $x/L_B = 0.5$, with results of Stamatopoulos et al. (2010) for a steady inlet velocity, **b.** Comparison of the streamline patterns of different time instants for a cardiac cycle; upper halves show the current results and lower halves are from Ohtaroglu (2020), **c.** Comparison of the axial velocity profiles, U_x, of 2D axisymmetric and 3D geometries at $x/L_B = 0.5$ at $t = 0.3$ sec.

Figure 6. Comparison of time-averaged axial velocity profiles, U_x, obtained by different inlet velocity profiles and entrance lengths for mean Reynolds number, $Re_m = 340$.

Figure 7 shows the time-averaged axial velocity profiles for $Re_m = 1160$ in the same orientation as the Figure 6. For this waveform, similar with the previous case, time-averaged axial velocity profiles for *Womersley* are nearly identical with the Base condition for all entrance lengths. Different from the results for $Re_m = 340$, *Parabolic* also obtains nearly the same velocity profile with *Womersley* and the Base condition for each sections and entrance length, even for $L_{ent} = D$, for $Re_m = 1160$. On the other hand, *Plug* fails to obtain a similar maximum velocity and backflow region with the Base case for both $L_{ent} = D$ and 3D. For $L_{ent} = 11D$, although the maximum velocity value is different, it can capture the backflow region. In addition, time-averaged axial velocity profiles for *Womersley* and *Parabolic* demonstrate a parabolic pattern, while *Plug* has a velocity profile with a flat central part, implying that even $L_{ent} = 11D$ is not sufficient for the *Plug* profile to achieve a fully developed condition for $Re_m = 1160$. For $Re_m = 340$, general pattern obtained by *Plug* is very similar to the *Womersley* and Base condition, while for $Re_m = 1160$, velocity profiles of *Parabolic* are nearly the same with them, even with $L_{ent} = D$. For physiological flows with a high Womersley number, especially $\alpha > 10$, transient inertia forces start to dominate the flow; therefore, velocity profiles resemble plug-like forms with a flattened central profile, and flow reversal areas are also observed due to harmonic contributions coming from transient inertial effects (Womersley, 1955). Indeed, this phenomenon is not governed only by the Womersley number, velocity profiles are also affected by the Reynolds number. For small Reynolds number flows, profiles have a plug-like form with a flattened central profile. With increasing Reynolds number, the effect of steady inertial forces starts to be more dominant, resulting in velocity profiles that are no longer plug-like, but instead more parabolic. Therefore, for $Re_m = 340$, general pattern obtained by *Plug* is very similar to the *Womersley* and Base condition, while for $Re_m = 1160$, velocity profiles of *Parabolic* are exactly the same with them.

In Figures 8 and 9, oscillatory shear index (OSI) and endothelial cell activation potential (ECAP) distributions obtained with *Womersley*, *Parabolic,* and *Plug* inlet velocity profiles at different entrance lengths throughout the aneurysm sac are plotted and compared with the Base case. For $Re_m = 340$ and $L_{ent} = 11D$, OSI and ECAP distributions for all inlet velocity profiles are the same with the Base condition. For $L_{ent} = D$ and 3D, *Womersley* gives the same OSI and ECAP distributions with Base condition. Although the maximum velocity values obtained by *Parabolic* at each section inside the aneurysm are very different for $L_{ent} = 3D$, OSI and ECAP distributions of *Parabolic* are very similar with Base condition because their backflow regions are similar, which affects the WSS parameters considerably. Similarly, for $L_{ent} = D$, in which the backflow region of *Parabolic* and *Plug* are completely different than the Base condition, the WSS parameters are also very

different. For $Re_m = 1160$, *Parabolic* and *Womersley* obtain nearly the same OSI and ECAP distributions with the Base case for $L_{ent} = 3D$ and 11D. Although their results are very similar with each other for $L_{ent} = D$, a deviation from the Base condition is observed. *Plug* fails to provide an accurate OSI and ECAP distribution for $Re_m = 1160$, even with a longer entrance length, $L_{ent} = 11D$.

In Figure 10, for $Re_m = 1160$, instantaneous wall shear stress distributions and contours of swirl strength, λ_{ci}, are presented for late systole and early diastole phases, t = 0.49 and 0.73 sec, through the aneurysm bulge. The top part of the figure shows the results for $L_{ent} = 3D$, while the mid part is for $L_{ent} = 11D$. For the top and mid parts, contours of swirl strength for *Womersley*, *Parabolic* and *Plug* inlet velocity profiles are located, under the instantaneous WSS distributions, from top to bottom, respectively. Contours of λ_{ci} and streamline patterns of the Base condition are located at the bottom part of the figure to compare the results obtained with idealized inlet velocity profiles. From the contours of λ_{ci} for the Base case, at the late systole, t = 0.49 sec, the primary vortex structure is translated to distal end, and a new vortex is originated from the primary vortex structure, which might be labeled as second primary vortex structure. The primary and second primary vortex structures are enclosed by a closed streamline pattern, but they have different vortex cores. At the early diastole, t = 0.73 sec, the primary vortex structure still stays the distal end of the bulge, but its intensity decreases due to viscous diffusion. An additional secondary vortex is generated and located between those two vortex cores, which is very near the wall and has a smaller swirl strength magnitude than the primary vortex.

At each time instant, the contours of swirl strength and instantaneous WSS distributions obtained by *Womersley* and *Parabolic* inlet velocity profiles with $L_{ent} = 11D$ are identical with the Base condition. The vortical structures obtained by *Plug* are also similar in terms of location of cores of the primary vortex structure and the general swirl strength pattern, but the intensity of the contours is significantly different especially in the late systolic and early diastolic phases, for t = 0.49 and 0.73 sec. Also, WSS distributions obtained by the *Plug* case are different than the others at the specified time instants, which is in accordance with swirl strength patterns. For $L_{ent} = 3D$, *Womersley* obtains nearly the same λ_{ci} patterns and WSS distributions as in the Base case. Although the WSS patterns of *Parabolic* are also the same with them, there is a negligible discrepancy in the intensity of the swirl strength contours for t = 0.49 and 0.73 sec. On the other hand, *Plug* obtains completely different results with $L_{ent} = 3D$, which is convenient with the differences observed in time-averaged axial velocity profiles and OSI and ECAP distributions for that inlet condition.
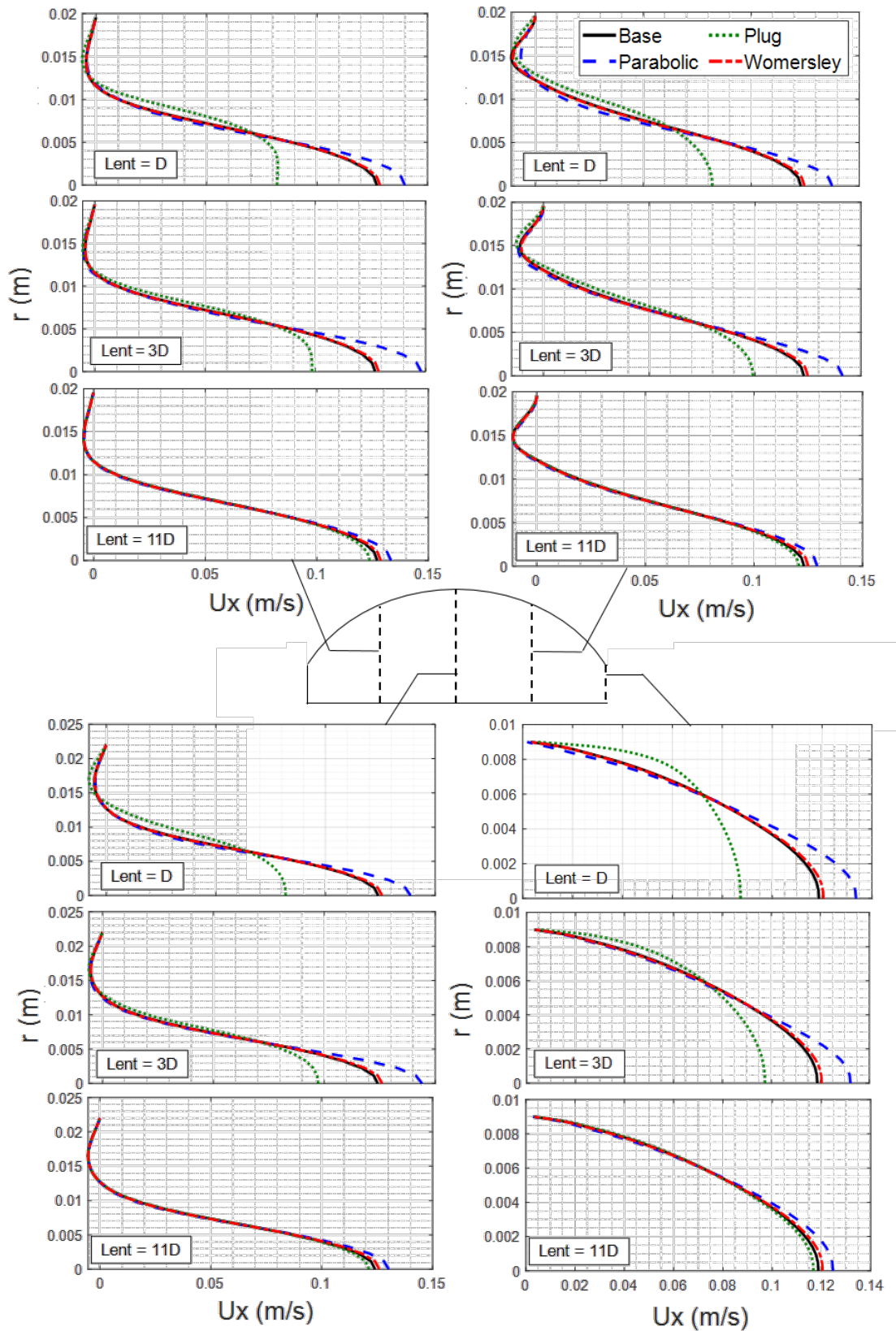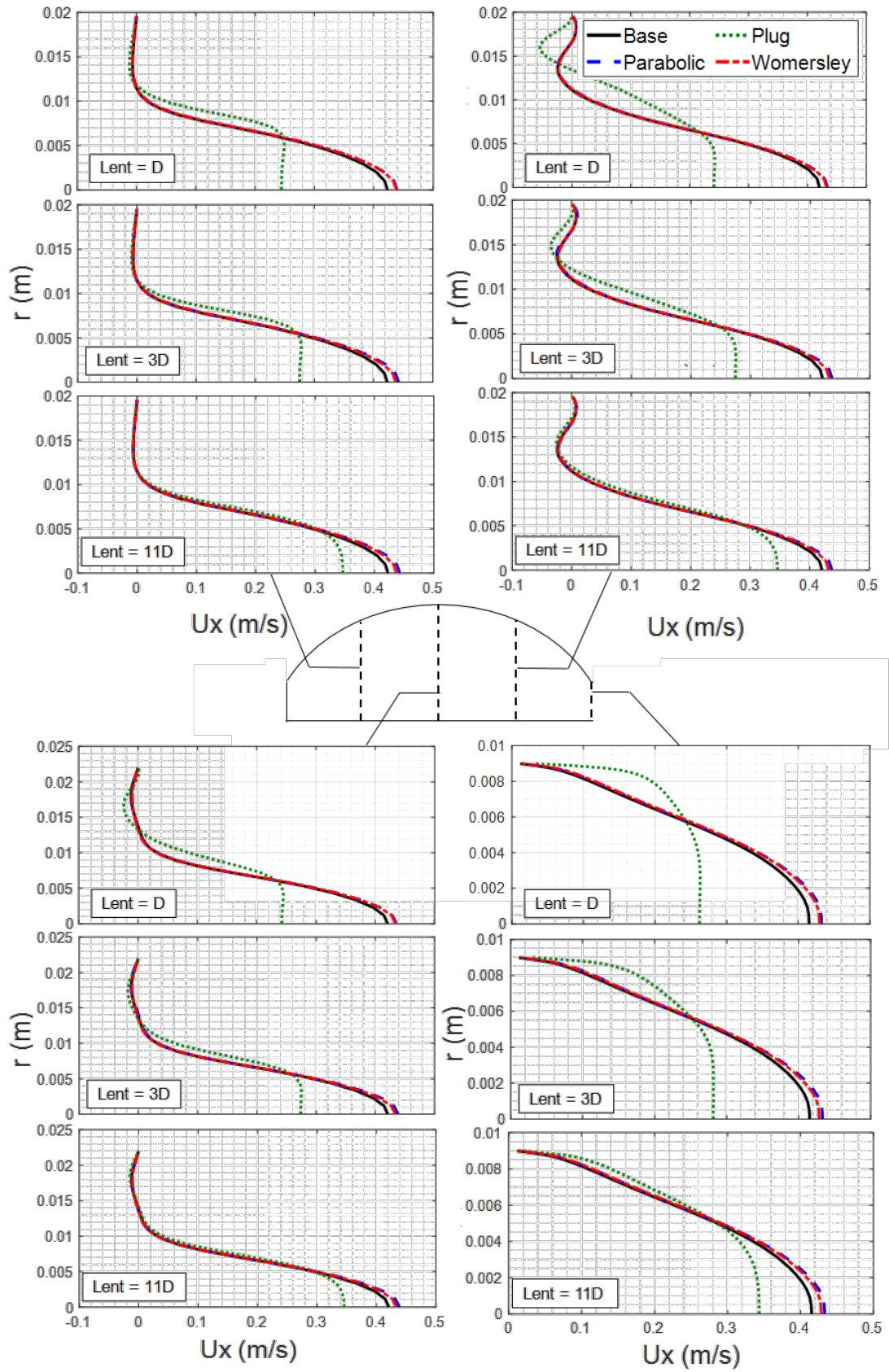
Figure 7. Comparison of time-averaged axial velocity profiles, U_x, obtained by different inlet velocity profiles and entrance lengths for mean Reynolds number, $Re_m = 1160$.
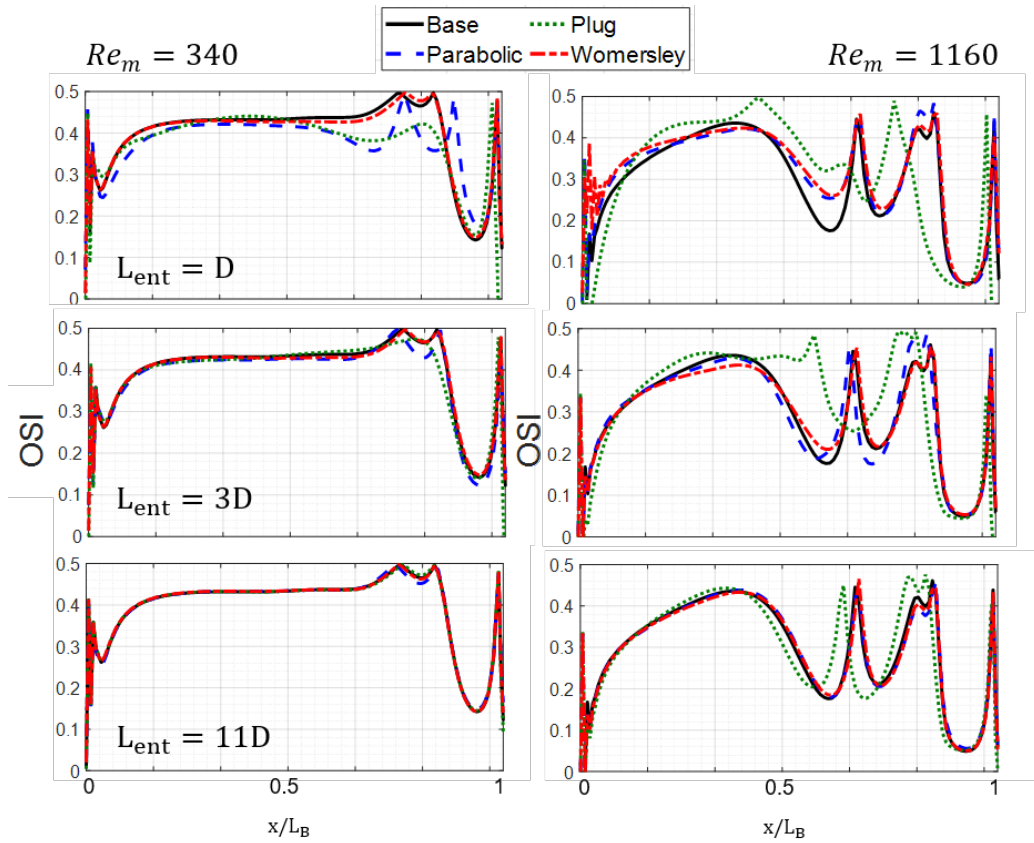
Figure 8. Comparison of oscillatory shear index (OSI) distributions obtained by different inlet velocity profiles and entrance lengths for mean Reynolds numbers, $Re_m = 340$ and 1160, from left to right, respectively.
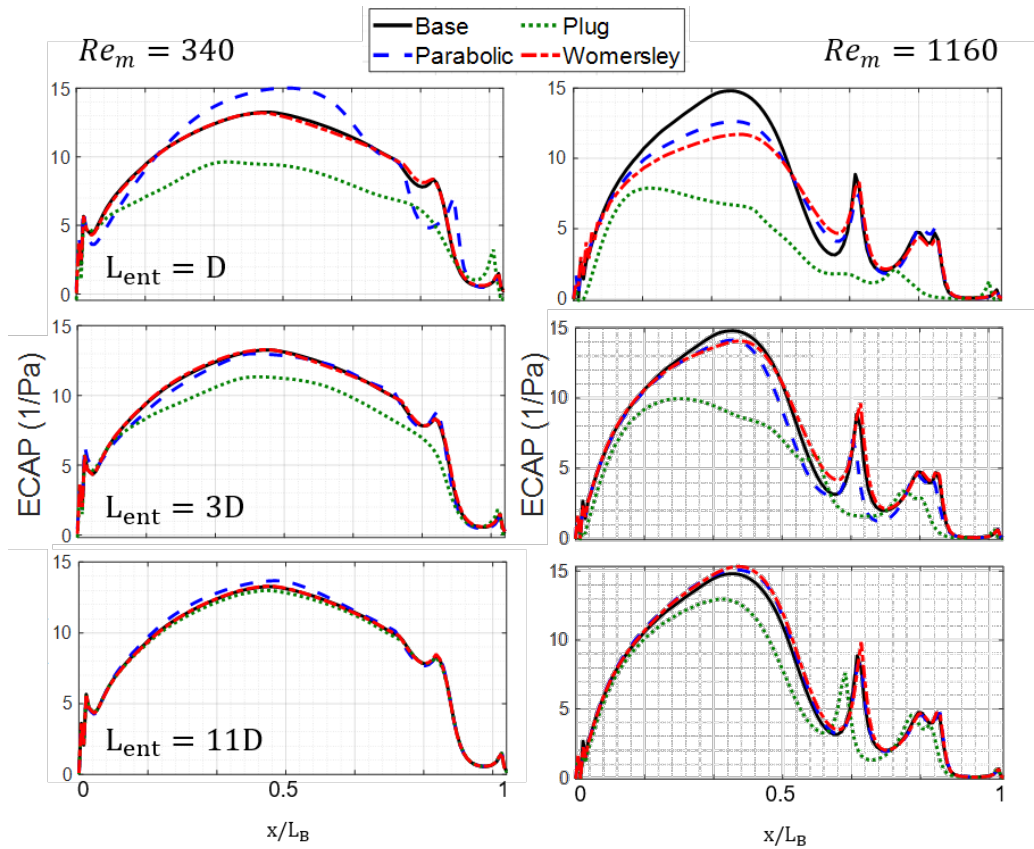
Figure 9. Comparison of endothelial cell activation potential (ECAP) distributions obtained by different inlet velocity profiles and entrance lengths for mean Reynolds numbers, $Re_m = 340$ and 1160, from left to right, respectively.

Figure 10. Comparison of instantaneous wall shear stress (WSS) distributions, contours of swirling strength, λ_{ci}, and streamline patterns obtained by different inlet velocity profiles and entrance lengths for mean Reynolds number, $Re_m = 1160$ at t = 0.49 and 0.73 sec.

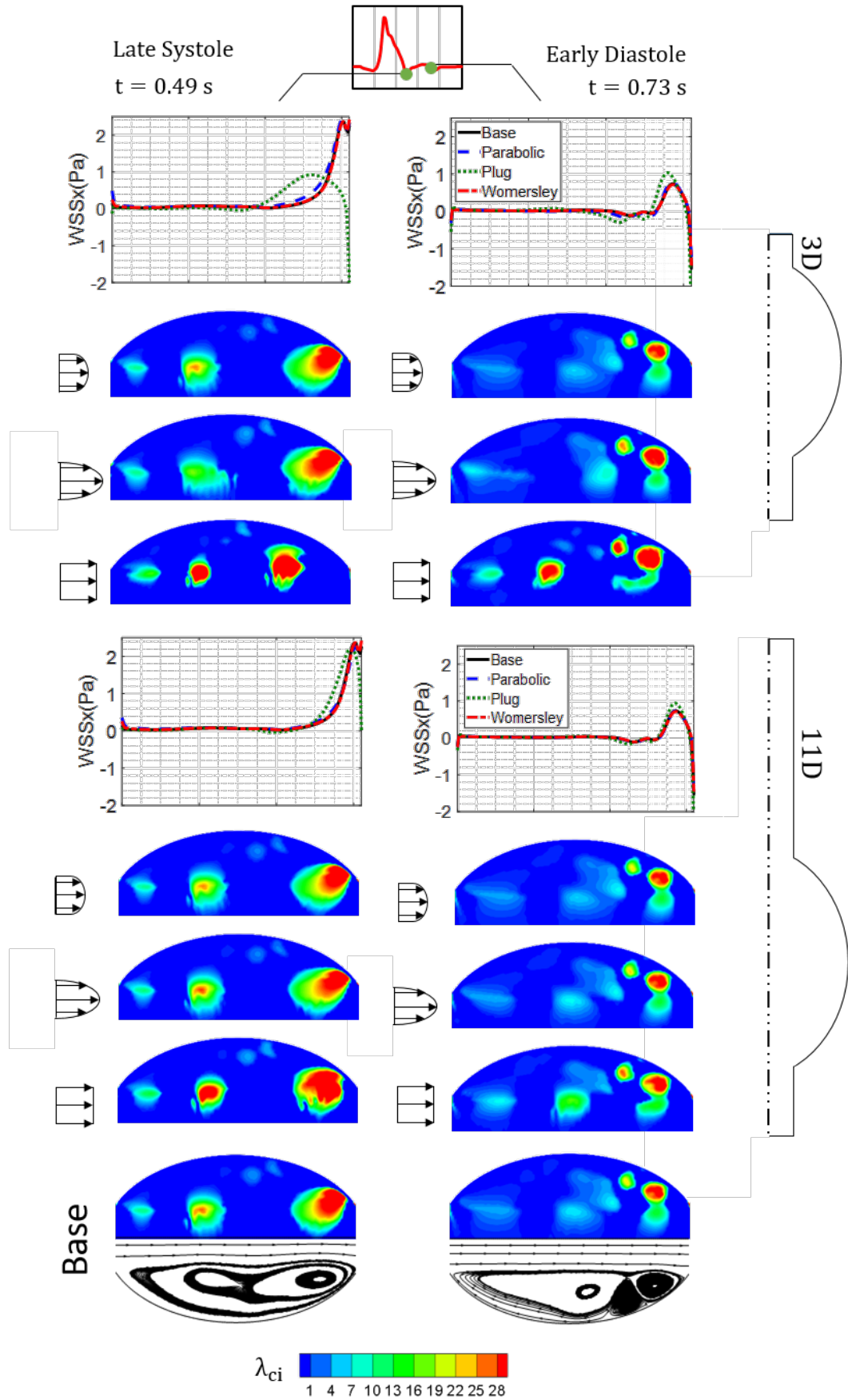WSS distributions at different time instants have a correlation with vortex structure movement and swirl strength magnitude, which is also observed by Biasetti et al. (2011). As can be seen in Figure 10, there is a WSS peak around the primary vortex structure which is near the wall at each time instants. With increasing the intensity and magnitude of λ_{ci} of the near-wall vortex structure, the magnitude of the WSS peak also increases. This phenomenon can also be observed in the WSS distribution and λ_{ci} contour of *Plug* at t = 0.49 sec with L_{ent} = 3D. For that time instant, primary vortex structure with a large $|\lambda_{ci}|$ of the *Plug* case is not located in proximity of the wall at the distal area, and its WSS distribution shows a very small peak at that region. Moreover, at t = 0.73 sec, primary vortex structure of *Plug* is not dissipated as much as in the Base condition, and it shows a high swirl strength intensity and WSS magnitude in the distal area, for L_{ent} = 3D. Despite the correlation between the primary vortex structure and WSS magnitude, the second primary vortex structure has no effect on WSS distribution due to the large distance between the vortex and aneurysm wall. However, at t = 0.73 sec, the secondary vortex structure is observed. It has an effect on WSS distribution since it is located in close proximity to the wall. Because the swirling strength magnitude is smaller for the secondary vortex structure, its effect on WSS distribution is also small.

In literature, Wei et al. (2019) have reported that there is no significant difference observed between the realistic, *Womersley*, and *Parabolic* inlet velocity profiles, whereas the *Plug* shows significant variations from the others for Fontan hemodynamics. Moreover, Campbell et al. (2012) have proposed that, in the case of carotid bifurcation with α = 4.1 and an average radius of 3 mm, the *Womersley* and *Parabolic* inlet velocity profiles yield nearly the same results. However, they have emphasized that such findings are not generalizable to larger arteries, such as the aorta, where the value of α exceeds 10, and further investigations are required. In this context, the current study compares the *Womersley*, *Parabolic* and *Plug* profiles for AAA hemodynamics, where the Womersley number is high, α = 12.41. The results demonstrate that, for large mean Reynolds numbers, the hemodynamic parameters obtained by the *Womersley* and *Parabolic* inlet profiles are identical for each entrance length. This might be attributed to the phenomenon that the steady inertial forces become increasingly dominant with increasing Reynolds number, leading to the *Womersley* profile no longer being plug-like and assuming more of a parabolic shape, even for large Womersley numbers. For carotid arteries, Hoi et al. (2010) have reported that an entrance length of L_{ent} = 3D is sufficient to avoid negligible errors. According to the present study, for AAA hemodynamics with a large mean Reynolds number, Re_m = 1160, L_{ent} = 3D might be adequate for the *Womersley* and *Parabolic* profiles to obtain similar results as in the Base case.

CONCLUSIONS

In the current study, the effect of inlet velocity profiles, which are *Womersley*, *Parabolic,* and *Plug*, on predicting hemodynamics by using different entrance lengths is discussed at two different Re_m using the same physiologic flow waveform pattern. Results are compared with the Base condition, which has a very long entrance length with a uniform flow at the inlet to ensure the flow entering the aneurysm sac is fully developed. According to the comparisons of time-averaged axial velocity profiles at different sections inside the sac, OSI and ECAP distributions, instantaneous WSS distributions and swirl strength contours, *Womersley* and *Parabolic* profiles give the same results with Base condition, even with a very small entrance length, L_{ent} = 3D. However, for Re_m = 1160, even the *Womersley* profile could not achieve the same OSI and ECAP distributions as the Base case with L_{ent} = D. With increasing Reynolds number, entrance length requirement of *Womersley* profile becomes nearly the same with *Parabolic* profile. Therefore, especially for high mean flow rates, utilization of *Womersley* profile might not be necessary, which is applicable for the physiological flow waveforms having diastolic flow rates larger than zero. Therefore, rather than applying complex Womersley formulation, utilization of *Parabolic* profile with an entrance length at least L_{ent} = 3D might be appropriate. On the other hand, *Plug* profile cannot obtain similar results with Base condition even L_{ent} = 11D for higher mean flow rates, albeit for R_m = 340, using an entrance length L_{ent} = 11D with *Plug* profile can yield the same results as the Base condition.

The present study, being a comparative parametric analysis, is subject to several limitations that could potentially influence the obtained results. The idealization of aneurysm bulge rather than utilizing patient-specific geometry may lead to inadequate simulation of the exact aneurysm hemodynamics, together with omitting the wall compliance, Windkessel boundary conditions and shear-thinning behavior of actual blood. Therefore, future studies will aim to incorporate patient-specific geometries with elastic walls, along with Windkessel boundary conditions and shear-thinning rheology models to reduce such limitations.

REFERENCES

Armour C. H., Guo B., Pirola, S., Saitta S., Liu Y., Dong Z. and Xu X. Y, 2021, The influence of inlet velocity profile on predicted flow in type B aortic dissection, *Biomech. Model. Mechanobiol.,* 20(2), pp. 481–490, doi: 10.1007/s10237-020-01395-4.

Arzani A., and Shadden S. C., 2015, Characterizations and Correlations of Wall Shear Stress in Aneurysmal Flow, *J. Biomech. Eng.,* 138(1), 014503-014503-014510, doi: 10.1115/1.4032056.

Arzani A., Suh G. Y., Dalman R. L., and Shadden S. C., 2014, A longitudinal comparison of hemodynamics and intraluminal thrombus deposition in abdominal aortic aneurysms, *American Journal of Physiology-Heart and Circulatory Physiology,* 307(12), H1786-H1795, doi: 10.1152/ajpheart.00461.2014.

Biasetti J., Hussain F., and Gasser T. C., 2011, Blood flow and coherent vortices in the normal and aneurysmatic aortas: a fluid dynamical approach to intra-luminal thrombus formation, *J. R. Soc. Interface*., 8(63), 1449-61, doi: 10.1098/rsif.2011.0041.

Biasetti J., Spazzini P. G., Swedenborg J. and Christian Gasser T., 2012, An integrated fluid-chemical model toward modeling the formation of intra-luminal thrombus in abdominal aortic aneurysms, *Front. Physiol.,* 3, no. July, pp. 1–16, doi: 10.3389/fphys.2012.00266.

Bilgi C. and Atalık K., 2020, Effects of blood viscoelasticity on pulsatile hemodynamics in arterial aneurysms, *J. Nonnewton. Fluid Mech.,* 279, no. July 2019, doi: 10.1016/j.jnnfm.2020.104263.

Bit A., Alblawi A., Chattopadhyay H., Quais Q. A., Benim A. C., Rahimi-Gorji M., and Do H. T, 2020, Three dimensional numerical analysis of hemodynamic of stenosed artery considering realistic outlet boundary conditions, *Comput. Methods Programs Biomed.,* 185, p. 105163, doi: 10.1016/j.cmpb.2019.105163.

Boyd A. J., Kuhn D. C. S., Lozowy R. J. and Kulbisky G. P., 2016, Low wall shear stress predominates at sites of abdominal aortic aneurysm rupture, *J. Vasc. Surg.,* 63(6), pp. 1613–1619, doi: 10.1016/j.jvs.2015.01.040.

Brewster D. C., Cronenwett J. L., Hallett J. W., Johnston K. W., Krupski W. C. and Matsumura J. S., 2003, Guidelines for the treatment of abdominal aortic aneurysms: Report of a subcommittee of the Joint Council of the American Association for Vascular Surgery and Society for Vascular Surgery, *J. Vasc. Surg.,* 37(5), pp. 1106–1117, doi: 10.1067/mva.2003.363.

Campbell I. C., Ries J., Dhawan S. S., Quyyumi A. A., Taylor W. R. and Oshinski J. N., 2012, Effect of inlet velocity profiles on patient-specific computational fluid dynamics simulations of the carotid bifurcation, *J. Biomech. Eng.,* 134(5), pp. 1–8, doi: 10.1115/1.4006681.

Chandra S., Raut S. S., Jana A., Biederman R. W., Doyle M., Muluk S. C., et al., 2013, Fluid-Structure Interaction Modeling of Abdominal Aortic Aneurysms: The Impact of Patient-Specific Inflow Conditions and Fluid/Solid Coupling, *J. Biomech. Eng.*, 135(8), 081001-081001-081014, doi: 10.1115/1.4024275.

Chen X., Zhuang J., and Wu Y., 2020, The effect of Womersley number and particle radius on the accumulation of lipoproteins in the human aorta, *Comput. Methods Biomech. Biomed. Engin.,* 23(10), pp.

571–584, doi: 10.1080/10255842.2020.1752681.

Chen Q., Zhong Q., Qi M. and Wang X. 2015. Comparison of vortex identification criteria for planar velocity fields in wall turbulence, *Phys. Fluids,* 27(8), doi: 10.1063/1.4927647.

Di Achille P., Tellides G., Figueroa C. A., Humphrey J. D., A haemodynamic predictor of intraluminal thrombus formation in abdominal aortic aneurysms, *Proc. R. Soc. A Math. Phys. Eng. Sci.,* 470(2172), 2014, doi: 10.1098/rspa.2014.0163.

Drewe C. J., Parker L. P., Kelsey L. J., Norman P. E., Powell J. T., and Doyle B. J., 2017, Haemodynamics and stresses in abdominal aortic aneurysms: A fluid-structure interaction study into the effect of proximal neck and iliac bifurcation angle, *J. Biomech.,* 60, 150-156, doi: https://doi.org/10.1016/j.jbiomech.2017.06.029.

Durst F., Ray S., Ünsal B., Bayoumi O. A., 2005, The Development Lengths of Laminar Pipe and Channel, *J. Fluids Eng.,* 127, November 2005, 1154–1160, doi: 10.1115/1.2063088.

Finol E. A. and Amon C. H., 2001, Blood flow in abdominal aortic aneurysms: Pulsatile flow hemodynamics, *J. Biomech. Eng.,* 123(5), pp. 474–484, doi: 10.1115/1.1395573.

Hoi Y., Wasserman B. A., Lakatta E. G. and Steinman D. A., 2010, Effect of common carotid artery inlet length on normal carotid bifurcation hemodynamics, *J. Biomech. Eng.,* 132(12), pp. 1–14, doi: 10.1115/1.4002800.

Impiombato A. N., La Civita G., Orlandi F., Franceschini Zinani F. S., Oliveira Rocha L. A. and Biserni, C., 2021, A Simple Transient Poiseuille-Based Approach to Mimic the Womersley Function and to Model Pulsatile Blood Flow, *Dynamics*, 1(1), pp. 9–17, doi: 10.3390/dynamics1010002.

Janiga G., Berg P., Sugiyama S., Kono K., and Steinman D. A., 2015, The computational fluid dynamics rupture challenge 2013 - Phase I: Prediction of rupture status in intracranial aneurysms, *Am. J. Neuroradiol.,* 36(3), pp. 530–536, doi: 10.3174/ajnr.A4157.

Li Z. and Kleinstreuer C., 2005, Blood flow and structure interactions in a stented abdominal aortic aneurysm model, *Med. Eng. Phys.,* 27(5), pp. 369–382, doi: 10.1016/j.medengphy.2004.12.003.

Lodi Rizzini M., Gallo D., De Nisco G., D'ascenzo F., Chiastra C., Bocchino P. P., Piroli F., De Ferrari G. and Morbiducci U., 2020, Does the inflow velocity profile influence physiologically relevant flow patterns in computational hemodynamic models of left anterior descending coronary artery?, *Med. Eng. Phys.,* 82, pp. 58–69, doi: 10.1016/j.medengphy.2020.07.001.

Madhavan S. and Kemmerling E. M. C., 2018, The effect

of inlet and outlet boundary conditions in image-based CFD modeling of aortic flow, *Biomed. Eng. Online,* 17(1), pp. 1–20, doi: 10.1186/s12938-018-0497-1.

Markl M., Schnell S., Wu C., Bollache E., Jarvis K., Barker A. J., Robinson J. D., Rigsby C. K., 2016, Advanced flow MRI: emerging techniques and applications, *Clin Radiol.,* 71(8):779-95, doi: 10.1016/j.crad.2016.01.011.

Morris L., Delassus P., Grace P., Wallis F., Walsh M. and McGloughlin T., 2006, Effects of flat, parabolic and realistic steady flow inlet profiles on idealised and realistic stent graft fits through Abdominal Aortic Aneurysms (AAA), *Med. Eng. Phys.,* 28(1), SPEC. ISS., pp. 19–26, doi: 10.1016/j.medengphy.2005.04.012.

Ohtaroglu O., 2020, Experimental investigation of physiological flow in abdominal aortic aneurysm. METU.

"OpenFOAM 8," OpenFOAM, 01-Sep-2020. [Online]. Available: https://openfoam.org/version/8/. [Accessed: 07-Jun-2022].

Pinto S. I. S. and Campos J. B. L. M., 2016, Numerical study of wall shear stress-based descriptors in the human left coronary artery, *Comput. Methods Biomech. Biomed. Engin.,* 19(13), pp. 1443–1455, doi: 10.1080/10255842.2016.1149575.

Qiu Y., Yuan D., Wen J., Fan Y., and Zheng T., 2018, Numerical identification of the rupture locations in patient-specific abdominal aortic aneurysmsusing hemodynamic parameters, *Comput. Methods Biomech. Biomed. Engin.,* 21(1), 1-12. doi: 10.1080/10255842.2017.1410796.

Reza M. M. S. and Arzani A., 2019, A critical comparison of different residence time measures in aneurysms, *J. Biomech.,* 88:122–9.

Salman H. E., Ramazanli B., Yavuz M. M. and Yalcin H. C., 2019, Biomechanical Investigation of Disturbed Hemodynamics-Induced Tissue Degeneration in Abdominal Aortic Aneurysms Using Computational and Experimental Techniques, *Front. in Biotech and Bioeng.,* 7, no. May, pp. 1–27, doi: 10.3389/fbioe.2019.00111.

San O. and Staples A. E., 2012, An improved model for reduced-order physiological fluid flows, *J. Mech. Med. Biol.,* vol. 12(3), doi: 10.1142/S0219519411004666.

Scotti C. M., Jimenez J., Muluk S. C., and Finol E. A., 2008, Wall stress and flow dynamics in abdominal aortic aneurysms: finite element analysis vs. fluid–structure interaction, *Comput. Methods Biomech. Biomed. Engin.,* 11(3), 301-322. doi: 10.1080/10255840701827412.

Stamatopoulos C., Papaharilaou Y., Mathioulakis D. S., and Katsamouris A., 2010, Steady and unsteady flow within an axisymmetric tube dilatation. *Experimental Thermal and Fluid Science,* 34(7), 915-927. doi: https://doi.org/10.1016/j.expthermflusci.2010.02.008.

Wei Z.A., Huddleston C., Trusty P.M., Singh-Gryzbon S., Fogel M.A., Veneziani A. and Yoganathan A. P., 2019, Analysis of Inlet Velocity Profiles in Numerical Assessment of Fontan Hemodynamics, *Ann. Biomed. Eng.,* 47(11), pp. 2258–2270, doi: 10.1007/s10439-019-02307-z.

Womersley J. R., 1955, Method for the calculation of velocity, rate of flow and viscous drag in arteries when the pressure gradient is known, *The Journal of Physiology,* 127(3), 553-563. doi: 10.1113/jphysiol.1955.sp005276.

Youssefi P., Gomez A., Arthurs C., Sharma R., Jahangiri, M. and Figueroa C. A., 2018, Impact of patient-specific inflow velocity profile on hemodynamics of the thoracic aorta, *J. Biomech. Eng.,* 140(1), doi: 10.1115/1.4037857.

AUTHORS

Dr. Burcu Ramazanlı*

B.Sc. METU, Mechanical Engineering, 2014
M.Sc. METU, Mechanical Engineering, 2017
Ph.D. METU, Mechanical Engineering, 2022

Prof. Dr. Cüneyt Sert**

B.Sc. METU, Mechanical Engineering, 1996
M.Sc. METU, Mechanical Engineering, 1998
Ph.D. Texas A&M University, Mechanical Engineering, 2003

Prof. Dr. Mehmet Metin Yavuz***

B.Sc. METU, Mechanical Engineering, 2001
M.Sc. Lehigh University, Mechanical Engineering, 2004
Ph.D. Lehigh University, Mechanical Engineering, 2006

NUMERICAL AND EXPERIMENTAL INVESTIGATION OF TUBE BUNDLE HEAT EXCHANGER ARRANGEMENT EFFECT ON HEAT TRANSFER PERFORMANCE IN TURBULENT FLOWS

Erman ASLAN*, Imdat TAYMAZ**, Kemal CAKIR*** and Elif EKER KAHVECI****
* Kocaeli University, Engineering Faculty, Department of Mechanical Engineering
41380, Kocaeli, erman.aslan@kocaeli.edu.tr, ORCID: 0000-0001-8595-6092
** Sakarya University, Engineering Faculty, Department of Mechanical Engineering
54050, Sakarya, taymaz@sakarya.edu.tr, ORCID: 0000-0001-5025-5480
*** Sakarya University, Engineering Faculty, Department of Mechanical Engineering
54050, Sakarya, cakir@sakarya.edu.tr, ORCID: 0000-0003-2194-5567
**** Sakarya University, Engineering Faculty, Department of Mechanical Engineering
54050, Sakarya, eeker@sakarya.edu.tr, ORCID: 0000-0001-6822-8296

Abstract: This study examines the friction factor, convective heat transfer, and area goodness factor of both inline and staggered tube bundles. The Finite Volume Method (FVM) is used for numerical simulations. Experimental and numerical approaches are utilized. Both 18.0 mm and 21.6 mm longitudinal distances are investigated. It is recommended to use ratio coefficients to reduce computation time. The proportion coefficients are used to obtain predictions for the three-dimensional cases based on the two-dimensional results or to transfer the 2D results to 3D. In addition, three turbulence models were utilized and compared within an Unsteady Reynolds Averaged Navier-Stokes (URANS) formulation. Experimental results validated numerical predictions. The thermal boundary conditions consist of a constant inlet temperature and a uniform heat flux on the support plate. Reynolds number is changed from 989 to 6352, while the Prandtl number remains at 0.70. Nusselt number and friction factor values have been observed to increase with increasing Reynolds number in all geometric configurations. The staggered configurations result in greater Nusselt number and friction factor values compared to inline configurations. The Nusselt number and pressure drop experience negative and positive effects, respectively, as the distance between rows decreases. SST turbulence models typically predict reasonable outcomes for all geometric configurations.
Keywords: Friction factor, Convective heat transfer, Tube bundle, Unsteady Reynolds averaged numerical simulations, Finite volume method.

TÜRBÜLANSLI AKIŞLARDA ISI TRANSFER PERFORMANSI ÜZERİNDEKİ BORU DEMETLİ ISI DEĞİŞTİRİCİ SIRALAMA ETKİSİNİN SAYISAL VE DENEYSEL İNCELENMESİ

Özet: Düzgün ve kaydırılmış sıralı hatlara sahip boru demetlerinin sürtünme faktörü, taşınımla ısı geçişi ve alan uyum faktörü özellikleri deneysel ve sayısal olarak incelenmiştir. Sonlu Hacim Yöntemi (FVM) kullanılmıştır. 18.0 mm ve 21.6 mm olmak üzere iki farklı uzunlamasına mesafe incelenmiştir. Daha az hesaplama için oran katsayılarının kullanılması önerilir. Orantı katsayıları, iki boyutta elde edilen sonuçlara dayanarak üç boyutlu durumlar için tahminler elde etmek, başka bir deyişle 2B sonuçları 3B'ye aktarmak için uygulanır. Bir URANS (farklı Kararsız Reynolds Ortalama Navier-Stokes) formülasyonunda üç türbülans modeli kullanıldı ve birbirleriyle karşılaştırıldı. Sayısal tahminler deneysel sonuçlarla doğrulandı. Isıl sınır koşulu olarak, girişte sabit sıcaklık uygulanır ve destek plakasında üniform ısı akışı gerçekleşir. Reynolds sayısı 989'dan 6352'ye değiştirilmiş ve Prandtl sayısı 0.70'de tutulmuştur. Nusselt sayısı ve sürtünme faktörü değerleri tüm geometrik konfigürasyonlar için Reynolds sayısı ile artmıştır. Kaydırılmış sıralamalar, düzgün düzenlemeye kıyasla daha büyük Nusselt sayısı ve sürtünme faktörü değerlerine yol açmıştır. Nusselt sayısı ve basınç düşüşü, sıralar arasındaki boyuna mesafenin azalmasıyla sırasıyla negatif ve pozitif etkiye sahiptir. Genel olarak, SST türbülans modelleri, tüm geometrik konfigürasyonlar için makul sonuçlar vermiştir.
Anahtar Kelimeler: Sürtünme faktörü, Taşınımla ısı geçişi, Boru demeti, Zamana bağlı Reynolds ortalamalı sayısal benzeşim, Sonlu hacimler yöntemi.

T_i	inlet temperature, K
T_0	outlet temperature, K
T_w	average wall temperature, K
F_{WA}	heat transfer area, m²
A_{GF}	area goodness factor
ΔP	pressure drop, N m⁻²
Nu	Nusselt number, dimensionless
Re	Reynolds number, dimensionless
Pr	Prandtl number, dimensionless
f	Friction factor
ρ	fluid density, kg m⁻³
Q	heat flow rate, J s⁻¹
k	fluid (air) thermal conductivity, W m⁻¹K⁻¹
h	convective heat transfer coefficient, W m⁻²K⁻¹
D	tube diameter, m
U	inlet velocity, m s⁻¹
ω	specific dissipation rate
SST	Shear Stress Transport
$\dot{m}$	mass flow rate, kg m s⁻²

INTRODUCTION

Understanding and accurately determining the convective heat transfer coefficient on the tube bundle support plate is crucial for analysing different tube bundle arrangements in heat exchangers and similar systems. With the development of nuclear power plants, steam generators have assumed a crucial role. There are four distinct heating arrangements: helical steam generators, meander steam generators, straight-flow heat exchangers, and U-tube heat exchangers. The most prevalent design for steam generators is the spiral configuration. Different-sized spiral-wound tubes are nested within one another to create a compact cylindrical tube bundle. The tube bundle is positioned on the support plates, where thermal stresses occur. A precise understanding of the convective heat transfer coefficient between the gas and the plate is necessary for determining the structural integrity of supporting plates through stress analysis. In addition, precise knowledge of the fluid and thermal areas is required for the analysis of thermal/hydraulic and thermal/structural unit designs in large-scale heat exchangers for nuclear applications (Aburoma et al., 1975).

It is extremely difficult to locate expansive experimental areas. Consequently, during thermal and hydraulic experiments, a single geometric arrangement of a single tube or tube bundle has replaced large-scale heat exchangers. Experiments have provided valuable insights into the behaviour of the tube; however, obtaining a precise temperature profile is still difficult due to data limitations. The temperature field is affected by the configuration of the tube bundle and the flow distribution (Dagsoz, 1975). The model has been evaluated in order to determine the convective heat transfer coefficient between the support plate and the medium through which the gaseous fluid flows. Formation and separation of the boundary layer have a substantial impact on heat transfer processes. By altering the flow patterns and thermal gradients at the surface, these phenomena have a significant effect on the efficiency of heat transfer. Cross-flow single-tube heat exchangers are rarely used in practise. Pipe bundles are utilised. Experiments are costly and time-consuming, so it is more practical to use numerical methods to calculate heat transfer coefficients than to conduct experiments (Aburoma et al., 1975).

In large heat exchangers, determining the pressure drop is equally as important as determining the convective heat transfer coefficient, as the pressure drop value affects directly the operating costs (Aburoma et al., 1975). When constructing a heat exchanger, a low pressure drop and a high heat transfer rate are considered ideal. In addition, reasonable operating costs are taken into account.

The tube bundle is arranged in a row and triangular shape, and the heat transfer coefficient is affected by these arrays. Hilpert (1933) devised a method for calculating the tube bundles' heat transfer coefficient. Grimison (1937) provides the constants formulated by Hilpert (1933). Brandt (1985) created an alternative method. This technique is the ratio of the volume between the tube bundles to the total volume of the bundle. In this research, both experimental and numerical studies are conducted. The literature review is therefore divided in half. Following a review of the experimental work, a review of the numerical research is provided. Kwak et al. (2003) investigated experimentally the convective heat transfer and penalty of pressure drop for an arbitrary number of transverse rows in a staggered finned tube with a single transverse row of the winglet pairs beside the front row of the tube bundles. In the experiments, two, three, four, and five rows of staggered tubes were used. The pair of wings used to improve heat transfer and reduce pressure loss were positioned in a manner that had not been used previously. Heat transfer increased by 30-10% in front of three rows of tubes along a single transverse row, while pressure loss decreased by 55-34%. Matos et al. (2004) conducted an experimental and numerical study to increase the total heat transfer rate between a finned tube bundle with staggered circular and elliptical tube arrangements. The optimal geometry for circular and elliptic tubes has been identified. The heat transfer gain in the ideal elliptical configurations was 19% greater than in the circular configurations. Kukulka and Smith (2014) conducted experimental research on tube bundles with staggered configurations. The use of Vipertex 1EHT enhanced heat transfer surface as opposed to smooth tubes, in conjunction with the use of various fluids such as n-Pentane, p-Xylene, and water, has resulted in a significant improvement in heat transfer capabilities. The Vipertex 1EHT tubes have been shown to increase heat transfer rates in comparison to conventional smooth tubes, making them a viable option for optimising heat transfer performance in a variety of applications. Ozturk et al. (2016) investigated the flow characteristics of a staggered array of multiple circular cylinders in a rectangular channel with close spacing.

PIV (laser particle image velocimetry) was utilised for this experiment. In experiments, a turbulent flow regime was identified. Distribution of velocity vector, streamline, vorticity and Reynolds stress, turbulent kinetic energy fields, and results from a single point spectral analysis were used to analyse flow characteristics in depth. Zhao et al. (2016) conducted an experiment to determine the pressure drop and friction factor values in the circular, elliptical, square, triangular, and diamond-shaped staggered array mini pins and the rectangular channel. Experiments were conducted with respect to three distinct flow regimes: laminar, transitional, and turbulent. It was observed that the friction factor correlation values could not accurately identify the entire flow region, including the laminar transition and turbulent regions, but correlations were still required. In additional experimental investigations, researchers have investigated a variety of variables in an effort to increase heat convection and reduce pressure drop. The utilisation of various tube shapes, such as elliptic (Khan et al., 2004; Ibrahim and Goma, 2009), twisted oval (Liu et al., 2018), and cam-shaped (Lavasani et al., 2014), has been investigated. These studies aim to optimise heat transfer performance by manipulating the tube geometry, resulting in enhanced convective heat transfer while minimising pressure drop within the system.

In addition, researchers have investigated the use of spherical turbulence promoters as an alternative configuration to improve heat transfer and reduce friction factor. Maithani et al. (2020) conducted a study on the application of spherical-shaped turbulence promoters, which revealed enhanced heat transfer performance and decreased friction factor. Utilising the unique flow characteristics induced by spherical turbulence promoters, this configuration maximises convective heat transfer while minimising energy losses due to friction within the system. They conducted experiments with Reynolds numbers ranging from 4500 to 16500. Various geometric parameters are defined, including the dimensionless spherical-shaped diameter, the stream-wise spacing parameter, and the span-wise spacing parameter.

Numerous instances exist in the literature for the numerical computation of heat convection on various configurations, without necessarily referring to the pressure drop. Some of these investigate laminar flow, including flow around a bluff body (Taymaz et al., 2015) and flow in a micro heat exchanger (Maqableh et al., 2011). Turbulent flow was considered for pipe flow (Benim et al,2004; You et al,2017), impinging jets (Chattopadhyay a Benim,2011; Benim et al,2007), flow around bluff bodies (Benim et al,2011) and elliptic tubes (Oclon et al,2015), gas turbine cooling (Benim et al,2004) and exhaust hood of steam turbines (Benim et al,1995). Launder and Massey (1978) conducted the first research on viscous laminar flow and heat transfer, referring to the pressure drop in the pipe bundle. To discretize the applied stream function-vorticity formulation, the finite difference method (FDM) was used. Barmasian and Hassan (1997) investigated flow characteristics in non-staggered and staggered tube bundles for turbulent flow numerically using the Large Eddy Simulation (LES) method and two different sub grid scale closure models. Their findings were consistent with the experimental data (Oengoeren and Ziada, 1992). Beale and Spaulding (1999) utilised the Finite Volume Method (FVM) to examine the heat transfer and flow characteristics of unsteady fluid flow. In tube bundles, the ratio of pitch (range) to diameter was determined to be 2:1. The staggered calculation of Strouhal numbers was consistent with experimental data. Mizushima and Suehiro (2005) performed an analysis of the flow through two consecutive circular cylinders. FDM is utilised for numerical research. When the constant and symmetrical flow at low Reynolds numbers exceeds the critical Reynolds number, it becomes unstable and changes to the released flow. For time discretization, the Runge-Kutta method of the fourth order was used. On drag and lift coefficients, it was discovered that the distance between two consecutive cylinders is significant. Horvat et al. (2006) examined transition numerical simulations for flow and heat transfer analysis in cylindrical, ellipsoidal, and winged different shapes of staggered arrangements. Ansys commercial code (FVM) Ansys-CFD was used to simulate unsteady three-dimensional numerical simulations. The shear stress transport (SST) model was used to model turbulence. To prevent large mesh sizes, periodic boundary conditions were employed. Estimates were made for heat transfer, drag coefficients, and Stanton numbers. Experimental data are compatible with numerical results for all Re and tube shapes. Bouris et al. (2001) compared numerically the flow and heat transfer characteristics of three different tube configurations, namely elliptic-shaped tubes in inline arrangements, circular-shaped tubes in inline arrangements, and circular-shaped tubes in staggered arrangements. They demonstrated that inline arrangements with elliptical tubes produced high heat transfer values and low pressure drop values. Hamid et al. (2014) created a two-dimensional model of a pre-heater using CFD by analysing fluid flow and heat transfer in a circular and elliptical tube bundle. Lin et al. (2008) created a three-dimensional turbulence model to improve the heat transfer performance of plate-fin heat exchangers utilising two distinct vortex generators. After comparing annular and inclined blocks, the best heat transfer performance was observed in vortex generators with an inclined block shape. Mavridou and Bouris (2012) discussed a new cross-flow tube heat exchanger for investigating properties such as fluid flow and heat transfer and inline-ordered tubes of varying diameters. There were a total of three arrangements, and they were compared. The first was a bundle of tubes with a common row of equal-diameter cylinders; the others are two different arrangements with two different transverse spacing and a ratio of 0.5 between the diameters of the small and large cylinders. FVM was employed as the numerical technique. LES was used to model the turbulent flow regime. Utilising alternately positioned cylinders with a diameter of 0.5 increased heat transfer and decreased pressure drop. A CFD study of the flow and heat transfer quantities in the inline bundle of tubes was examined by Abed and Afgan (2017), using URANS

turbulence models, namely, a standard k-ε model, SST k-ω, v2-f model, and EB k-ε model. Two configurations, square and non-square inline, with variable vertical and horizontal aspect ratios, were used. The closest results were achieved by the EB k-ε model, whereas the v2-f model also provided good results. Yahiaoui et al. (2016) investigated the change of flow characteristics around staggered tube bundles by the use of the grooved cylinders by using FVM with a Reynolds number of 9300, free stream velocity of 3.5 m/s, and pitch-to-diameter ratio of 3.8. Spalart–Allmaras, k–ε realizable, and k–ω SST, turbulence models were used. After the numerical analysis, it was in good agreement with the experimental results.

Another numerical investigation is done by Pourdel et al. (2019) for determining fluid flow and heat transfer in a flat tube under constant heat flux. In the numerical study Finite Volume method with SIMPLEC was used. The considered range of Reynolds numbers is 5000-20000, the range of dimensionless pitch is 1-2.33, and the range of dimensionless depth is 0.233-0.433. They observed that the presence of dimples inside of the channel changes the flow physics, temperature field, and heat transfer enhancement significantly in a good manner. For turbulence modeling, SST k-ω was used. Zheng et al. (2020) investigated the effects of morphology variation, wall temperature, transverse pitch, and longitude pitch of the tube bundle on ash deposition and heat transfer performance under high-temperature conditions by using a dynamic simulation method based on ANSYS FLUENT.

This paper investigates experimentally and numerically the effect of longitudinal distance between tubes on convective heat transfer friction factor and area goodness factor for flow over tube bundle arrangements (inline and staggered) on the support plate. In numerical calculations, the commercial code Ansys-Fluent (2009) based on FVM is utilised. To reduce computational effort, proportion coefficients are proposed for Nusselt number and pressure drop for all geometric configurations (inline and staggered arrangements, and two longitudinal distances between tubes). Consequently, two-dimensional numerical calculations represent three-dimensional numerical calculations. The URans method is used to model turbulence. Consequently, three distinct types of turbulence models are employed. There are comparisons between three distinct turbulence models and experimental data.

PROBLEM DEFINITION

Figure 1 depicts the experimental configuration. The test section's channel is made of Plexiglas material. It has an inner rectangular cross section with dimensions of 90 mm by 100 mm and a wall thickness of 5 mm. The length of the channel inlet is determined to be 1410 mm in order to provide a fully developed flow zone for the Reynolds numbers considered. At the channel inlet, four pressure sockets are used. Air is used as a fluid, and it enters the channel at speeds ranging from 0.26 to 1.31 metres per second.

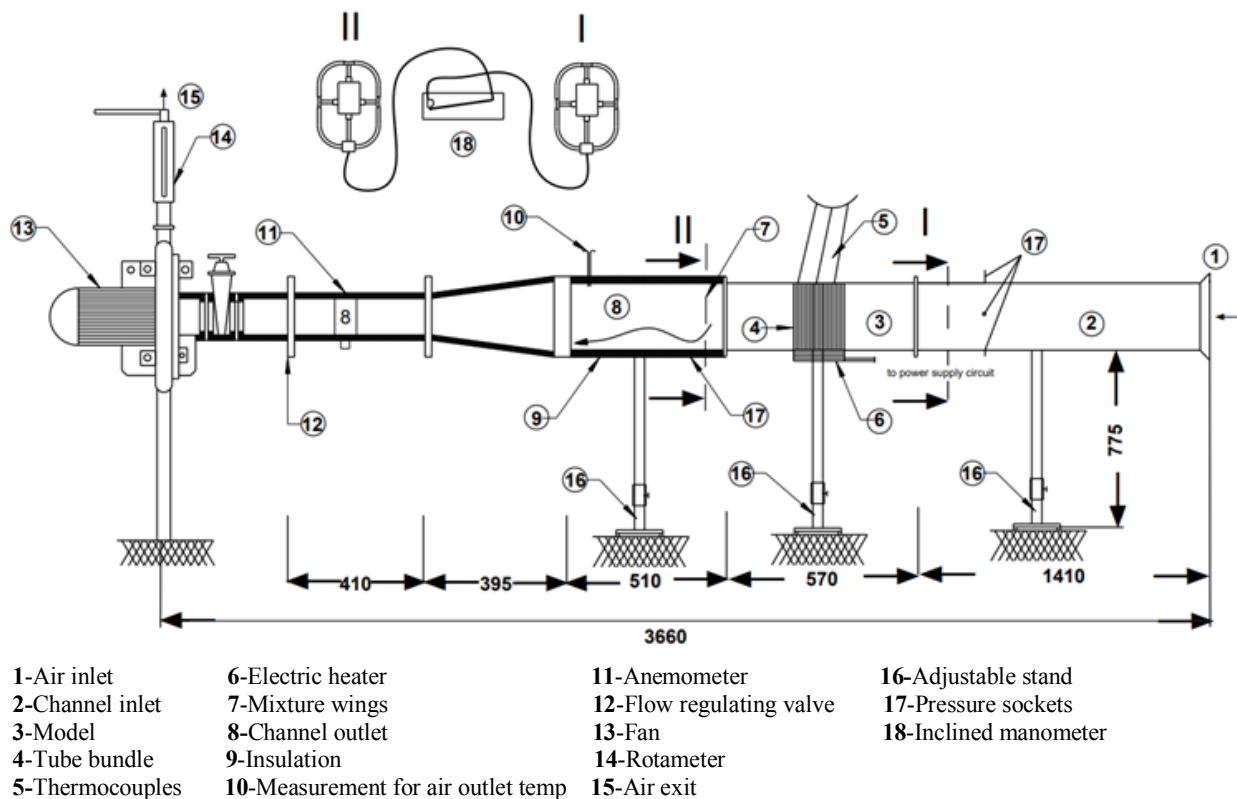|			
1-Air inlet	**6**-Electric heater	**11**-Anemometer	**16**-Adjustable stand
2-Channel inlet	**7**-Mixture wings	**12**-Flow regulating valve	**17**-Pressure sockets
3-Model	**8**-Channel outlet	**13**-Fan	**18**-Inclined manometer
4-Tube bundle	**9**-Insulation	**14**-Rotameter	
5-Thermocouples	**10**-Measurement for air outlet temp	**15**-Air exit	

Figure 1. Schematic diagram of the experimental setup.

The tubes are 140 mm in length and constructed from mahogany, which has a low thermal conductivity. The tubes are hollow, and thermocouples are located within the tube walls to measure the temperature of the fluid. As was previously stated, steel support plates are utilised at the base of the model. Using different voltage and current values, the steel support plate is heated unilaterally by the electric resistance method, ensuring a primarily constant heat flux. Since mahogany is deformed at higher heat fluxes, values of 96 for heat flux indicate deformation.

It is applied W/m^2, 88.5 W/m^2, and 86.25 W/m^2. To homogenise the heat flux, an aluminium plate with a perforation is used.

Under a steel plate is an aluminium plate with a thickness of 2 mm; the heaters are attached to this aluminium plate. As a heater, copper–nickel wires are utilised. Ceramic fibre with a thickness of 3 mm and aluminum-coated glass wool with a thickness of 50 mm were used, respectively, to prevent heat loss from heaters.

The 570 mm long test section containing the tube bundles is positioned in the middle of the channel. Over the support plate, the tube bundle can be arranged inline or staggered. A support plate is fabricated from steel. In this diagram, inline and staggered tube bundles are depicted.

Fig 2. 5 x 11 rows (transverse x longitudinal) were used to construct the tube arrays. 90 millimetres was the height of the support plate. The arrangement is defined by the tube diameter (D), the transverse distance (ST), the longitudinal distance (SL), and the length of the support plate (L). The diameter of the tube is 14.4 mm. The tube has a height-to-diameter ratio of 9.72. While the transverse distance is assumed to be 18 mm, two different longitudinal distances of 18 mm and 21.6 mm are used. The length of the support plate varies with the distance between the rows along its longitudinal axis. For the 18 mm and 21.6 mm longitudinal distances, support plate lengths of 196.4 mm and 232.4 mm are used, respectively. Table 1 lists the Reynolds number based on inlet velocity and hydraulic diameter. Keeping the Prandtl number at 0.7.

Following the section containing the tube bundles is a 510-mm-long outlet section with four pressure sockets, similar to the channel's inlet section. To achieve a uniform temperature at the channel outlet, a combination of wings is utilised.

Temperature is measured via Nickel chromium – Nickel (NiCr-Ni) thermocouples at eighteen points. In Fig 2, a mark "A", "B", and "x" represent the fluid and support plate temperature points, respectively. The distances between the temperature markings on the support plate and the nearest tube surface were 2 mm. The thermocouples' diameter was 0.2 mm. Three millimetres outside of the tubes, thermocouples are passed through the tubes to measure fluid temperature. All thermocouples are positioned so as not to impede fluid flow. Using a two-channel scanner, the temperature of eighteen points is measured. The reference temperature is 0 degrees Celsius, which is maintained by ice water in a thermos bottle. A digital thermometer with high sensitivity between -50°C and 50°C is used to control the temperature of ice water. Two rotameters are utilised for flow measurement. Both ends of the fan outlet are equipped with rotameters. It is assumed that two rotameters pass identical amounts of air.
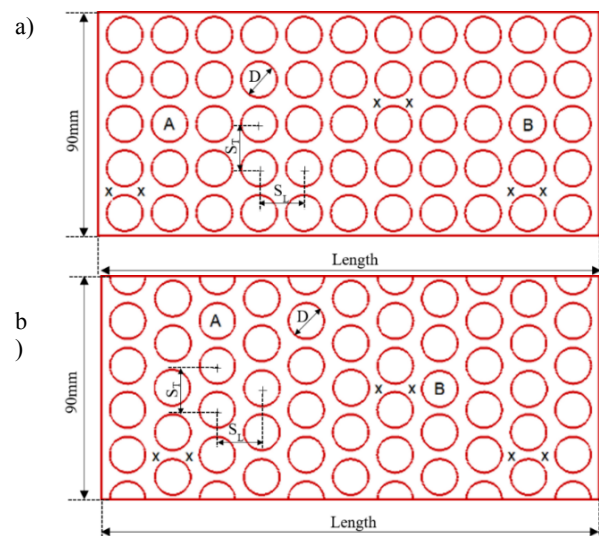
Figure 2. Tube bundle arrangements over the steel support plate (a) inline (b) staggered

A rotameter's measuring lines were calibrated with reference to 760 mmHg pressure and 20°C temperature. Flow velocity is measured with an anemometer, and the resulting flow rate is compared to rotameter readings. Flow regulating valves are installed to control the flow rate and, consequently, the Reynolds number. 4% is the turbulent intensity of flow. With the aid of pressure sockets at the channel inlet and outlet, the pressure drop values of various Reynolds numbers in the tube bundle are determined. The used inclined manometer has 14 mmH$_2$O measurement capability and it works with alcohol with a density of 0.850 kg/m^3. Connections between inclined manometer and measurement points support with equal length hoses.

Table 1. The used Reynolds numbers for all longitudinal distances and arrangements.

		1	2	3	4	5	6	7	8
S_L=18	inline	989	1505	2026	2751	3672	4313	5139	-
	staggered	1508	1714	2229	3054	4097	4830	5550	-
S_L=21.6	inline	1058	1828	2550	3323	4115	4933	5541	-
	staggered	1066	1838	2547	3287	4057	4826	5618	6352

Using a differential approach to error analysis, a comprehensive analysis of experimental uncertainties is conducted (Holman, 1994). The maximum uncertainty values in the measured measurement parameters are temperature ± 1.18 %, air velocity in the tubes and pressure drop through the model $\pm 3.42\%$, $\pm 1.03\%$. The maximum uncertainties for Reynolds number, Nusselt number are found to be $\pm 1.28\%$ and $\pm 3.02\%$ respectively.

Between the support plate and air, the convective heat transfer coefficient (h) of the support plate and the air was counted up as;

$$Q = \dot{m}.C_p.(T_i - T_0) = h.F_{WA}.\left(T_w - \frac{T_i + T_0}{2}\right) \qquad (1)$$

where Q indicates the heat flow rate, $\dot{m}$ the mass flow rate, T_i the inlet temperature, T_0 outlet temperature, T_w the average wall temperature and F_{WA} the heat transfer area. In order to find the average wall temperature, the temperature was measured at six different points on the support plate and the arithmetic mean was taken. The points used are indicated by x in Fig 2. The Nusselt number based on tube diameter is, then, calculated as;

$$Nu = \frac{h.D}{k} \qquad (2)$$

where k denotes the fluid thermal conductivity. As mentioned before, the pressure values are measured via pressure sockets at the channel inlet and outlet. The difference in these pressure values gives the pressure drop (ΔP). With using pressure drops, the friction factor is determined as;

$$f = \frac{\frac{\Delta P}{dx}.D}{\frac{1}{2}.\rho.U^2} \qquad (3)$$

where ρ is the fluid density, U is inlet velocity, and dx denotes the distances between pressure sockets. Finally, the area goodness factor for thermohydraulic performance is introduced (Kuppan, 2000). The area goodness factor was calculated by dividing the Colburn j-factor by the friction factor.

$$A_{GF} = \frac{Nu}{Re.Pr^{\frac{1}{3}}.f} \qquad (4)$$

where Re and Pr denote Reynolds number and Prandtl number, respectively.

Modeling

Turbulence modeling

The numerical analysis is performed using the commercial code Ansys-Fluent (2009), which is based on FVM. The flow must be time-dependent and turbulent within this Reynolds number range (Aslan et al., 2015; Aslan, 2016). For modelling turbulence, a URANS approach is adopted, for being able yo capture flow large scale unsteadiness that can occur in the wake of the

cylinders. In the previous investigation (Aslan,2016), four different turbulence models were used which were Realizable k-ε, k-ω, SST (Shear Stress Transport), and transition SST. According to previous investigations, Realizable k-ε predictions were far from experimental results, therefore, the remaining three turbulence models except the Realizable k-ε turbulence model are used in the present investigation. Here, k is turbulent kinetic energy, ω is specific dissipation rate (Ansys-Fluent,2009).

Table 2. The used number of cells of quarter modelling strategy

	Inline	Staggered
S_L=18mm	6 703 251	6 632 314
S_L=21.6mm	8 313 400	8 313 300

Wilcox (1998) developed the k- model, with modifications for low Reynolds number effects, compressibility, and shear flow dispersion. Sensitivity to turbulence values and specific rate of dispersion except for the shear layer are powerless points of the Wilcox k-ω model. For addressing these weak points, Menter (1994) developed the SST turbulence model. Accordingly, the correct formulation in the near wall region (Ansys,2009) of the k-ω model was effectively blended with the robust behavior of the k-ε model (Launder and Spalding,1974) in the free stream, where ε is the dissipation rate. Combining the SST turbulence model with two other transport equations from the perspective of momentum thickness Reynolds number, which are for intermittency and the transition onset criteria, a new turbulence model, transition SST, has emerged (Menter et al., 2003; Menter et al., 2004; Lotfi et al., 2014). Near-wall turbulence models are not modelled using the wall function approach (Durbin and Reif, 2011). If the grid resolution is sufficient, the used turbulence equations can represent turbulence close to the wall. When designing the grid, attention was paid to the fact that the y^+ (Ansys-Fluent,2009) value of the non-dimensional wall distance of the cells near the wall was always below 1.

The boundary conditions

To reduce computational effort, two-dimensional numerical analyses are performed to represent three-dimensional numerical analyses using proportion coefficients, as will be described in greater detail below.

There were three distinct preliminary investigations conducted to determine proportion coefficients. In the first preliminary study, a single tube was considered in the channel, and a three-dimensional numerical study was conducted. The strategy for modelling is based on full and semi-models. A symmetric half-length boundary condition was applied to the tube's half-length modelling. Practical examination revealed no difference between the full and half models (less than 1% deviation in Nusselt number). Thus, it was determined that applying the symmetrical boundary condition in half tube length (the xy plane) would not raise any objections. In the second preliminary analysis, a tube bundle was utilised rather

than a single tube, and the flow characteristics of all tubes were examined in two dimensions. Again, both full and half modelling approaches were employed. The symmetry boundary condition utilised in the half model was placed in the centre of the side walls. Due to these comparisons, it was realised that there was no practical difference between the time-averaged results of full and half models, and that the symmetry boundary condition could be applied to the xz plane. Note that this symmetry boundary is perpendicular to the one used in the first preliminary study, so that a quarter of the domain is bounded by two symmetry planes. In the third preliminary study, a numerical investigation of a single tube in a channel in two-dimensional domains was conducted. On the tube wall, two different heat fluxes were applied. The Nusselt number of two distinct heat flux analyses was nearly identical, with only a 1% difference observed. Therefore, it can be concluded that flow characteristics, and not necessarily thermal boundary conditions, play a significant role in determining the Nusselt number.

In accordance with the first and second preliminary validations, a quarter of the channel volume is used as the solution domain in the three-dimensional calculations, which is bounded by two channel walls and two symmetry planes, as depicted in Figure 3. The number of cells in three-dimensional grids is displayed in Table 2. Only for the highest Reynolds number and with the SST turbulence model was a three-dimensional analysis with quarter modelling performed.
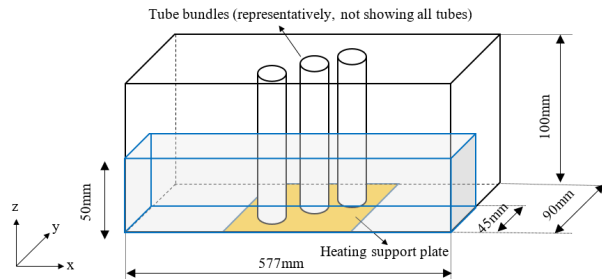

Figure 3. The schematic of quarter modelling strategy with indication of coordinate system

The velocity fields around a cylinder are predicted utilising a two-dimensional half domain with symmetric boundary conditions. While the actual problem involves heat transfer through supporting plates with constant heat flux, the absence of supporting plates in the 2D numerical computations makes it possible to apply constant heat flux to the cylinders. The focus is on capturing the flow characteristics in order to predict the Nusselt number, according to a third preliminary validation. Due to the absence of the third dimension, there are minor differences between three-dimensional and two-dimensional flow characteristics. However, the overall flow behaviour, including flow separation and the formation of von Karman vortex streets, can be observed in both cases.

According to the second preliminary investigation, a constant heat flux is applied to the cylinders in the absence of a supporting plate. In light of the third preliminary, the constant heat flux is not decisive for the prediction of the Nusselt number. Obviously, in two-dimensional numerical calculations, an equivalent heat flux value must be defined for three-dimensional numerical calculations to accurately determine the outlet temperature. If we combine the second (due to determining equivalent constant heat flux at the cylinders) and third (due to the significance of flow characteristics for Nusselt number predictions), preliminary validation two-dimensional numerical computations can be transferred to three-dimensional numerical computations by means of a constant coefficient.

Taking into account the quarter domain described previously, the computational work for a three-dimensional calculation is reduced by a factor of four. Nonetheless, the computational effort required for a three-dimensional calculation is considerable. Due to the large number of tubes and high grid resolution, this is the case. Consequently, it was necessary to find an additional method for performing parametric studies with reasonable effort and time. To accomplish this, the so-called "proportion coefficient" method is utilised. The idea behind this concept is that, for a given geometry, the ratio between the two-dimensional and three-dimensional results remains constant, as expressed by a "proportion coefficient" that is independent of the Reynolds number. Comparing the two-dimensional and three-dimensional results for a single Reynolds number enables the calculation and application of proportion coefficients for different Reynolds numbers. This indicates that, for the remaining cases (Reynolds numbers), three-dimensional calculations are not required. Calculations can be performed in two dimensions and then transferred to three dimensions using proportion coefficients previously determined.

Thus, for obtaining the proportion coefficients, three and two-dimensional calculations are performed for inline and staggered configurations, for two different longitudinal distances (S_L= 18 mm, S_L = 21.6 mm), for a single Reynolds number. To achieve this, the highest Reynolds number is used as a starting point, and three-dimensional results for the quarter domain are obtained. Utilising the SST turbulence model. Comparing the two-dimensional and three-dimensional results yields the proportion coefficients, which are then used to convert the two-dimensional Reynolds numbers to three-dimensional. The proportion coefficients are assumed to be independent of the turbulence model used. Formally, the proportion coefficients were expressed. The obtained proportion coefficients are listed in Table 3.

for the Nusselt number ;

$$Nu_{proportion} = \frac{Nu_{2D}}{Nu_{3D}} \qquad (5)$$

the pressure drop;

$$\Delta P_{proportion} = \frac{\Delta P_{2D}}{\Delta P_{3D}} \tag{6}$$

Table 3. The proportion coefficients

		Inline	Staggered
S_L = 18 mm	Nu	1.18	1.16
	ΔP	0.60	0.91
S_T = 21.6 mm	Nu	1.19	1.21
	ΔP	0.79	0.82

Figure 4 depicts the two-dimensional domains employed. In the inlet section (channel inlet, Fig. 1), preliminary calculations determine the velocity and turbulence rates. The distributions at the exit of the channel entrance are defined as the main solution field's entrance boundary conditions. The input is maintained at a constant temperature due to the energy equation. For all convective-diffusive transport variables, the zero gradient boundary condition at the output of the solution field is applied, i.e., the outflow boundary condition is used. Momentum equations in walls are applied with a non-slip boundary. For the energy equation, adiabatic boundary conditions are applied to all walls, with the exception of tube bundles. In three-dimensional analyses, a uniform heat flux boundary condition is prescribed at the support plate, whereas in two-dimensional analyses, a constant heat flux is applied to the tube surfaces. According to the heat flux in three-dimensional domains, the heat flux in two-dimensional domains is calculated equivalence. Consequently, outlet temperatures are obtained that are comparable for both two- and three-dimensional domains.
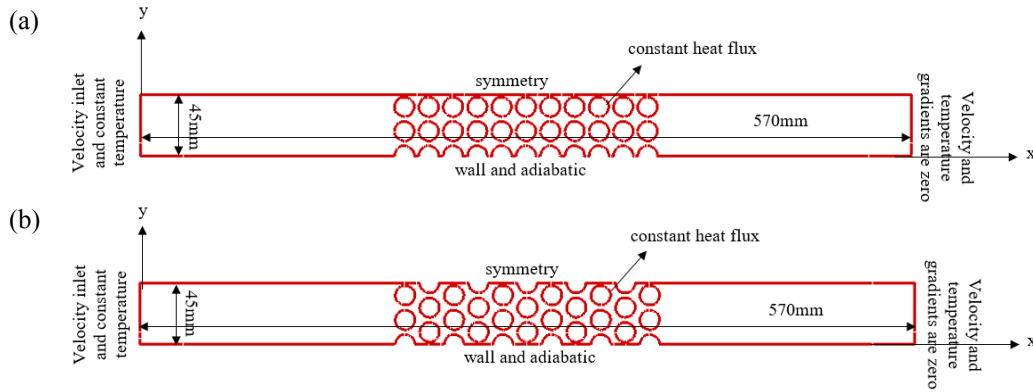

Figure 4. Two-dimensional domains with boundary conditions for (a) inline and (b) staggered arrangements

Before determining the equivalent heat flux in a two-dimensional domain, the total heat in a three-dimensional domain must be determined. Multiple heat flux and heat transfer surface area at the support plate are used to calculate total heat. When the total area of the support plate is subtracted from the total area of the tubes, the heat transfer area at the support plate is obtained. Second, the total heat is partitioned into two-dimensional domains based on the area of all tubes. The area of all tubes is determined by multiplying the perimeter of all tubes by the channel height (100 mm). For all two- and three-dimensional calculations, the turbulent intensity and length scale are 4% and one-third of the hydraulic diameter, respectively.

The grids of numerical modeling

Abed and Afgan (2017) used the FVM for spatial discretization with second-order upwind to convection terms. For time integration, an implicit second-order scheme is used. For pressure velocity coupling, the PISO algorithm is utilised (Ansys, 2009). Default under-relaxation factors which are pressure is 0.3, momentum is 0.7, turbulent quantities are 0.8 and energy is 1.0 are used (Abed and Afgan,2017). For all equations except the energy equation, a 10^{-6} residual value is required as a convergence factor. The residual value 10^{-8} is necessary for the convergence factor of energy equations.

Structured and unstructured mesh strategies are used concurrently in 2-D numerical calculations. In close proximity to the wall, structural topologies are utilised, whereas unstructured topologies are employed in distant areas. Structured grids (boundary layer meshes) are utilised in remote regions near the bottom walls.

In remote areas, we believe that using an unstructured grid with boundary layer meshes provides the same level of accuracy as using a multiblock structured grid. A grid independence study was not conducted to determine mesh resolutions; however, the authors' prior work was utilised. Benim et al. (2008) investigated the flow through a circular cylinder using the LES, DES, RANS, and URANS methods. In this study, the circumference of the cylinder was distinguished between two- and three-dimensional calculations using 240 cells. According to Benim et al. (2008), the meshes employed are adequate for accurately predicting flow characteristics such as drag and pressure coefficients. Different aspects of the produce grids are represented in Fig 5, for arrangements of (a) S_L=18 mm, inline, (b) S_L=18 mm, staggered, (c) S_L=21.6 mm, inline, and (d) S_L=21.6 mm, staggered.
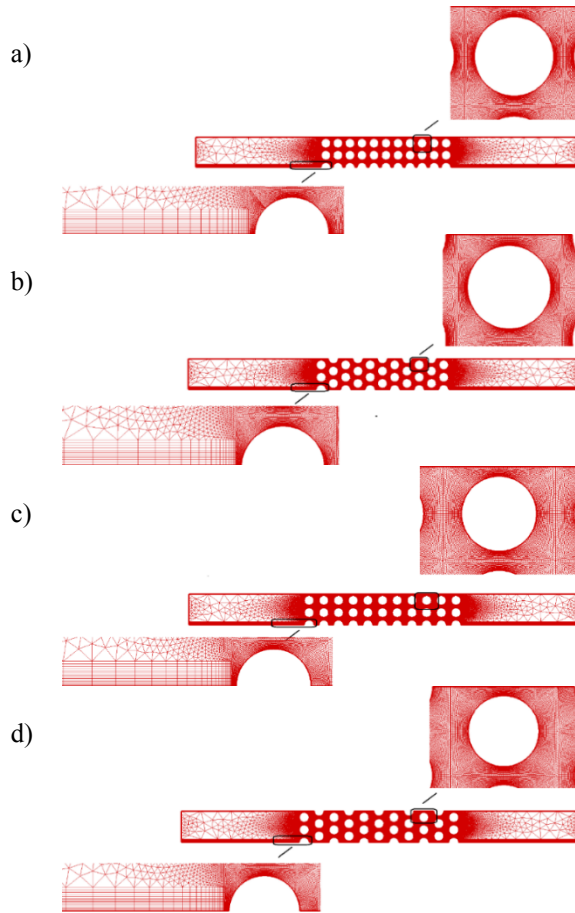
Figure 5. Two dimensional meshes for (a) S_L=18mm, inline, (b) S_L=18mm, staggered,(c) S_L=21.6mm, inline, (b) S_L=21.6mm, staggered

In Table 4, the simulation's employed cell numbers are listed. For the three-dimensional numerical computations, the same mesh strategy as in the two-dimensional case is utilised, with the addition of 72 cells in the third direction. This expanded mesh configuration permits a comprehensive representation of the three-dimensional flow behaviour and allows for more precise predictions of the flow characteristics and heat transfer phenomena.

Table 4. The used number of cells of two-dimensional domain

	Inline	**Staggered**
S_L= 18 mm	150 049	149 908
S_T = 21.6 mm	150 666	150 666

In transient computation, the time step size has been selected in such a way that the cell Courant number takes a value about one. Drag and lift coefficients are monitored with time for four tubes. Two of four tubes (tube-1 and tube-2) are located on inlet side of the model, and the other two tubes (tube-3 and tube-4) are placed on exit side of the model. By looking at the drag and lift coefficiens, the oscilation frequency or periodi for each tube are determined. Time averaged values, which are x-velocity, y-velocity, pressure and temperature, are determined according to largest oscillation period. Using

these time-averaged values, Nusselt number (Eq.1 and Eq.2), friction factor (Eq.3) and area goodness factor (Eq.4) are determined.
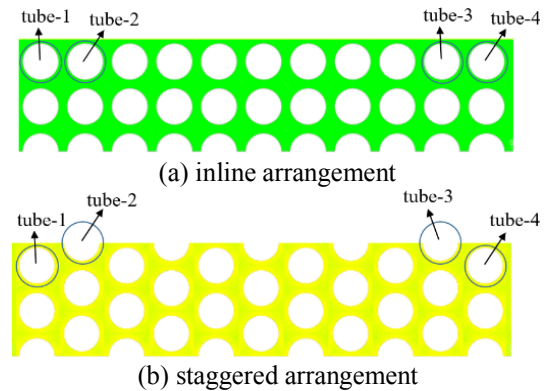

(a) inline arrangement

(b) staggered arrangement

Figure 6. The monitored tubes for drag and lift coefficient and for (a) inline and (b) staggered arrangements.

RESULTS AND DISCUSSIONS

The numerical calculations included Reynolds values between 989 and 6352. Across all employed turbulence models, qualitative flow characteristics remained remarkably consistent. In light of this, only the predictions derived from the SST turbulence model will be considered in the initial section discussing the general flow characteristics. At the conclusion of this section, a quantitative comparison of the predicted Nusselt number, friction factor, and area goodness factor will be carried out, incorporating the results obtained from the various turbulence models utilised. This comparative analysis will shed light on the performance and precision of the various turbulence models in predicting the heat transfer and flow characteristics of the system.

In Fig 7, the time-averaged x-velocity distributions are shown for (a) S_L=18 mm, inline, (b) S_L=18 mm, staggered, (c) S_L=21.6 mm, inline, and (d) S_L=21.6 mm, staggered configurations. At the highest Reynolds number, the distribution of time-averaged x-velocity is presented for each configuration. Flow patterns before tube bundles have not changed significantly in any of four configurations due to the fully developed velocity at the model's inlet. In the tube bundle, the flow strip in the inline is in the form of a linear line. Streams originating from a single source are always divided into two for staggered arrangement. Maximum time average x velocities are found between the tube rows in both configurations.Behind the initial row, the flow pattern produces an extremely repetitive pattern. In the streams surrounding the cylinders, von Karman's vortex street (instable vortex shedding) is observed. This is due to the fact that the back of the rollers have varying Reynolds numbers and modes. Due to the extremely close spacing between cylinders within the tube bundles, this behaviour is dampened. The time-averaged axial velocity regions reveal a low-velocity zone where the main flow is drawn towards the side wall in the middle of the channel (it clears the symmetry plane). This is possible because the jet acts as an ejector between the side wall and the next

cylinder, drawing fluid from the surrounding environment. In Fig 8 these are shown the time-averaged pressure distributions for (a)S_L=18 mm, inline, (b)S_L=18 mm, staggered, (c)S_L=21.6 mm, inline, and (d)S_L=21.6 mm, staggered configurations. Again, time-averaged

pressure distributions at the highest Reynolds numbers are presented in Fig 8 for each configuration. Significant pressure variations can be achieved for all configurations. Staggered arrangements and small longitudinal distance (S_L=18 mm) produce higher pressure drop values.

Figure 7. The SST predictions of time-averaged x-velocity distributions for (a) S_L=18mm, inline (Re = 5139), (b) S_L=18mm, staggered (Re = 5550), (c) S_L=21.6mm, inline (Re =5541) and (d) S_L=21.6mm, staggered (Re = 6352)

Figure 8. The SST predictions of time-averaged pressure distributions for (a) S_L=18 mm inline (Re=5139), (b) S_L=18 mm staggered (Re=5550), (c) S_L=21.6 mm inline (Re=5541) and (d) S_L=21.6 mm staggered (Re=6352)

Time-averaged temperature distributions are presented in Fig 9 for (a)S_L=18 mm, inline, (b)S_L=18 mm, staggered,

(c)S_L=21.6 mm, inline, and (d)S_L=21.6 mm, staggered configurationsEstimates of the time-averaged

temperatures are displayed for all configurations at the highest Reynolds numbers. With a constant heat flux, the temperature of the cold fluid entering the model gradually rises for all configurations. There is a recirculation zone behind the tubes where warmer zones can be observed. Nusselt numbers are derived from the time-averaged results of an experiment and a numerical analysis.

Fig 10 shows the measured and calculated Nusselt numbers (Nu) as a function of Reynolds number (Re) for the configurations of (a)S_L=18 mm, inline (Aslan,2016), (b)S_L=18 mm, staggered (Aslan,2016), (c)S_L=21.6 mm, inline, and (d)S_L=21.6 mm staggered. As the Reynolds number increases, flow characteristics become more turbulent, as expected, the Nusselt numbers of experiments and numerical predictions increase with the Reynolds number. For staggered arrangements, streams from a raw one are always divided into the next two (see Figure 7), therefore temperature gradients at near cylinders of staggered arrangements are greater than temperature gradients at near cylinders of inline arrangements. Nusselt numbers in the staggered arrangements [Fig 10(b) and Fig 10(d)] are higher than the inline arrangements [Fig 10(a) and Fig 10(c)], for both longitudinal distances.
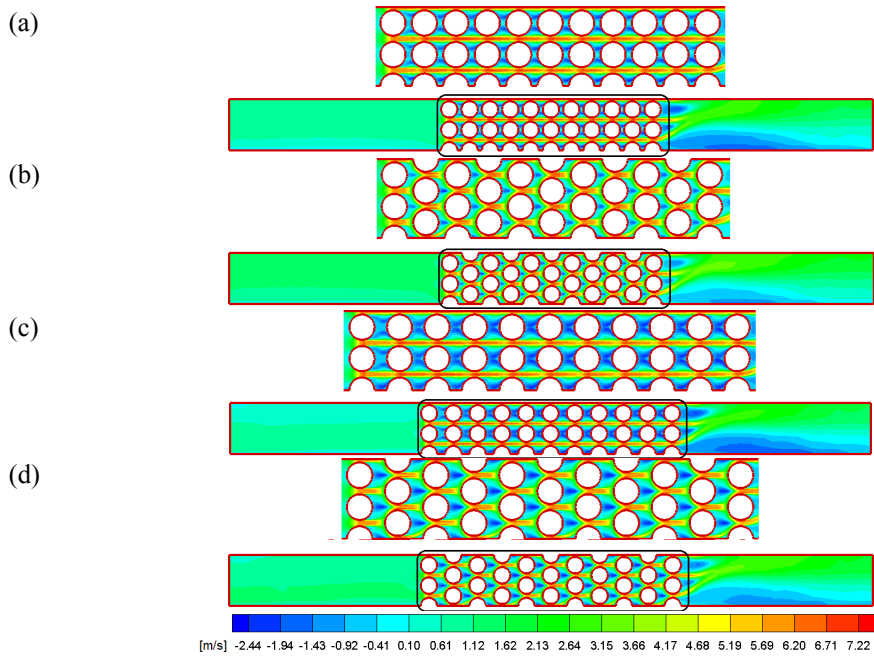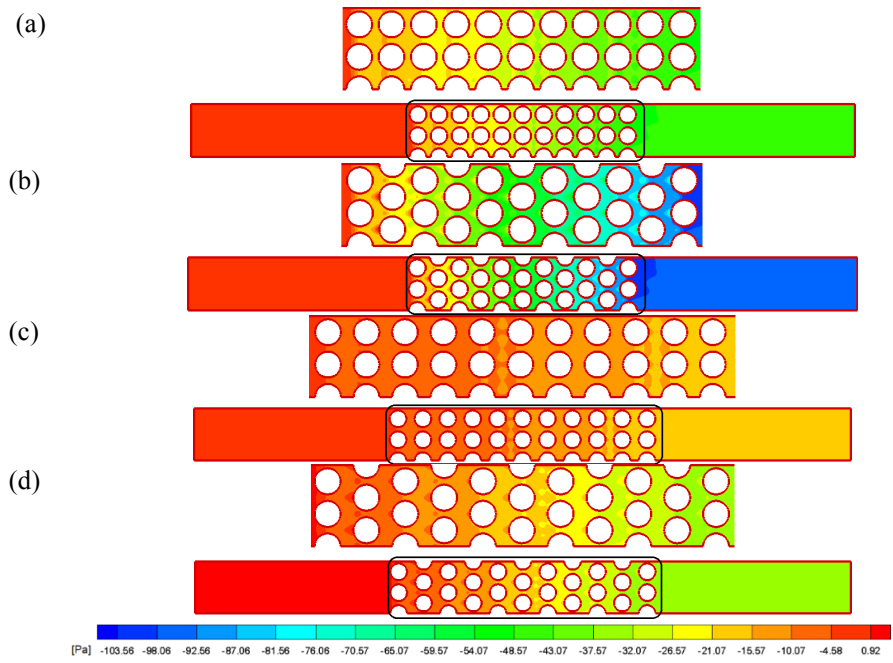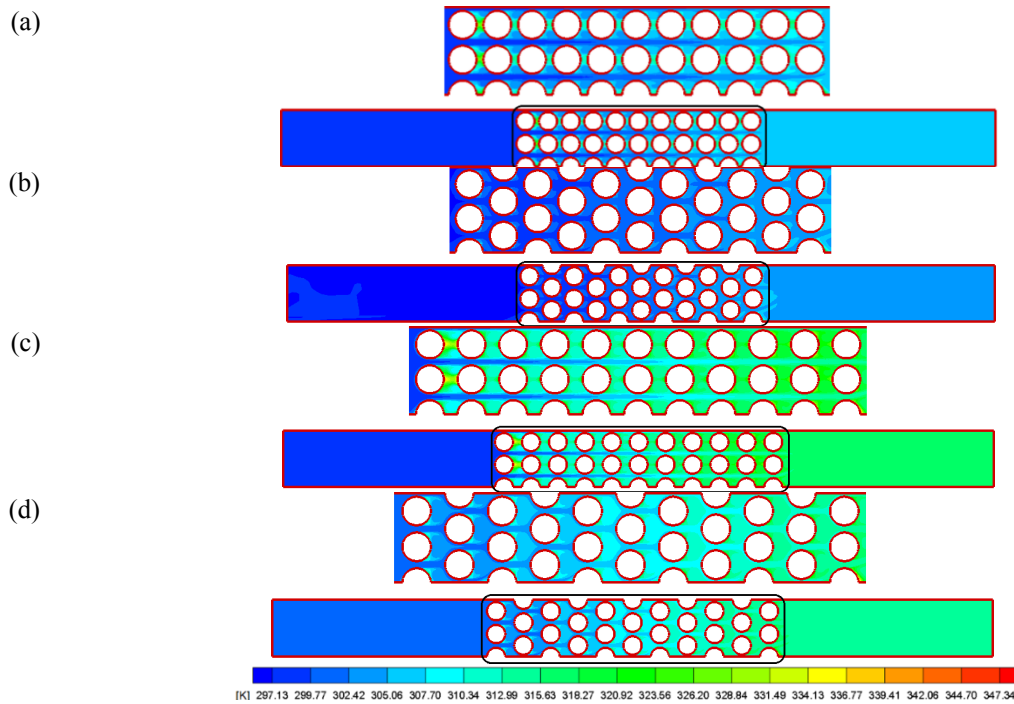

Figure 9. The SST predictions of time-averaged temperature distributions for (a) S_L=18 mm inline (Re=5139), (b) S_L=18 mm staggered (Re=5550), (c) S_L=21.6 mm inline (Re=5541) and (d) S_L=21.6 mm staggered (Re = 6352)

Furthermore, higher Nusselt numbers are observed to occur for the smaller longitudinal distance (S_L = 18 mm) for both arrangements [Fig 10(a) and Fig 10(b)].

At a small longitudinal distance (SL = 18mm), the flow behind the tube experiences the presence of adjacent tubes without undergoing complete mixing. Consequently, there is a greater degree of flow mixing than in cases where the tube distances are greater. This phenomenon occurs due to the close proximity of the tubes, which causes interactions and flow pattern disturbances. Incomplete mixing at shorter tube distances can have substantial effects on heat transfer and fluid dynamics, influencing variables such as the Nusselt number and flow characteristics. In order to gain a comprehensive understanding of the system's performance and optimise heat transfer efficiency, it is necessary to consider and analyse the flow behaviour at different longitudinal distances. Accordingly, larger temperature gradients occur at smaller longitudinal distances. For both arrangements of S_L = 18 mm, the SST turbulence model predicts the nearest results to the measurements. For the inline arrangement of S_L = 18 mm, under and over predictions are observed for the k-ω and transition SST turbulence models, respectively [Fig 10(a)]. The prediction of the k-ω turbulence model is not very good, particularly at high Reynolds numbers for the staggered arrangement of S_L=18 mm [Fig 10(b)]. For the long longitudinal distance (S_L=21.6 mm) of the inline arrangement, the SST and k-ω turbulence models predict analogous results, which are quite near to the experimental result, while predictions of transition SST are also found reasonable [Fig 10(c)]. Over predictions are observed for all turbulence models in the staggered arrangement of the long longitudinal distance (S_L=21.6 mm) [Fig 10(d)]. The utilization of a long longitudinal distance (SL=21.6 mm) facilitates a greater presence of free stream flow around the tube, which impacts the heat transfer characteristics. In comparison to experimental results, the SST turbulence model tends to overestimate the Nusselt number. At low Reynolds numbers, this overestimation is especially pronounced. Notable similarities exist between the predictions of all

turbulence models, particularly at low Reynolds numbers. This suggests that the choice of turbulence model has less of an effect on the predictions when Reynolds numbers are low. As the Reynolds number rises, however, the disparities between the turbulence models become more pronounced. When analysing heat transfer performance and predicting the Nusselt number, it is crucial to consider the appropriate turbulence model and the effect of Reynolds numbers on the precision of predictions.

Friction factor as a function of Reynolds number is shown for the configurations (a) S_L=18 mm, inline (Aslan,2016), (b) S_L=18 mm, staggered (Aslan,2016), number (c) S_L=21.6 mm, inline and (d) S_L=21.6 mm,
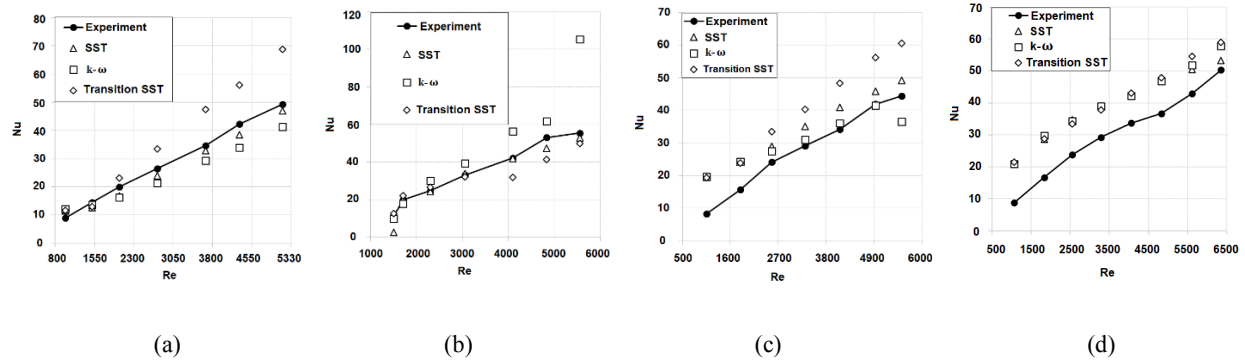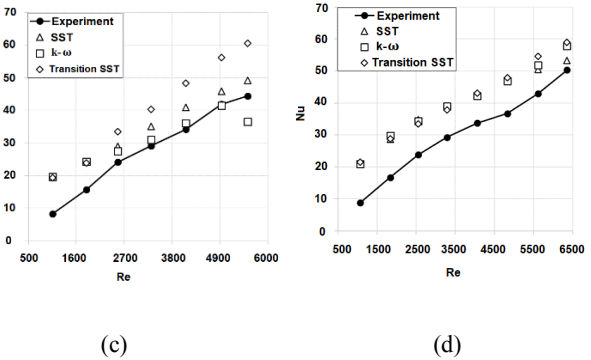
staggered in Figure 11. As expected, friction factors increase for all configurations as pressure drop increases more than dynamic pressure as Reynolds number increases. At both longitudinal distances, the friction factor values for staggered arrangements are greater than those for inline arrangements. This is because the pressure against the flow is greater in staggered configurations. In addition, as mentioned previously, the rising number of Nusselt is a result of this (Figure 10). As the longitudinal distance increases at the same Reynolds number, the pressure drop increases; consequently, the friction factor increases for both configurations as the longitudinal distance increases [Fig 11(c) and Fig 11(d)].

(a)   (b)   (c)   (d)

Figure 10. Nusselt number as a function of Reynolds number (a) S_L=18mm, inline, (b) S_L=18mm, staggered, (c) S_L=21.6mm, inline, and (d) S_L=21.6mm, staggered

Predictions of the SST turbulence model is quite good according to experiment result for both arrangements of S_L=18 mm, whereas the other turbulence models also perform reasonably well [Fig 11a) and Fig 11(b)].

The estimation of the transition SST model is so close to experimental results for the inline arrangement of S_L=21.6 mm. SST and k-ω turbulence models predict quite well at low Reynolds numbers. However, with increasing Reynolds number, predictions of SST and k-ω turbulence models are far from experiments. For the staggered arrangement of S_L=21.6 mm, all turbulence models behave similarly, and their predictions are quite good compared to the experimental results [Fig 11(d)]. However, some deviations are observed at high Reynolds numbers.

Convective heat transfer and pressure drop are not taken into account separately when designing heat exchangers. Both are considered concurrently. Consequently, a new parameter titled area goodness factors is created. The ratio of Colburn factor j to friction factor is the area goodness factor. If the performance value is high, convective heat transfer will be high and the friction factor will be low, resulting in efficient heat transfer and low operating costs. Fig 12 presents the measured and predicted area goodness factor as a function of the Reynolds number for the configurations of (a) S_L=18 mm, inline (Aslan,2016), (b) S_L=18 mm, staggered

(Aslan,2016),(c) S_L=21.6 mm, inline and (d) S_L=21.6 mm, staggered. Time-averaged results from experiments are numerical calculation used to get the area goodness factor. Reynolds number decreases the area goodness factor for all configurations. In the case of small longitudinal distances, inline arrangement results in a greater area goodness factor than staggered arrangement. For long longitudinal distances, however, inline arrangement produces a lower area goodness factor than staggered arrangement. When we observe the inline arrangement, the area goodness factor of S_L=18 mm is greater than the area goodness factor of S_L=21.6 mm. In the same manner, when we look at the staggered arrangement, a small longitudinal distance (S_L=18 mm) produces a bigger area goodness factor than a long longitudinal distance (S_L=21.6 mm). For all cases, especially, for low Reynolds numbers, predictions of all turbulence models are not good enough, however, with increasing Reynolds numbers, turbulence model predictions are close to experimental results. For the inline arrangement of S_L=18 mm [Fig 12(a)], the prediction of the SST turbulence model is close to experimental results after Re=1837. For the same arrangement and longitudinal distance, under and over-estimation are observed for k-ω and transition SST, respectively. For inline arrangement and staggered arrangement of S_L=21.6 mm, all turbulence models behave similarly for a staggered arrangement of S_L=18 mm [Fig 12(b)], prediction of transition SST turbulence models is quite good after Re=4057.
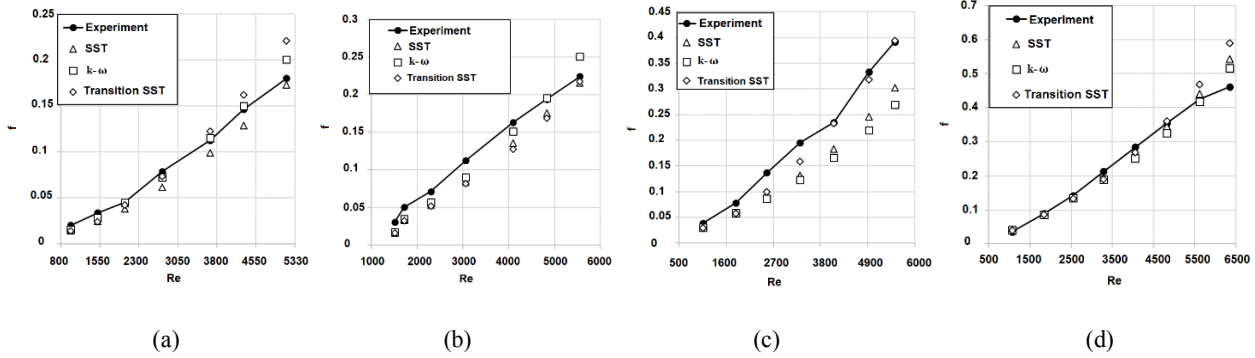
(a) (b) (c) (d)

Figure 11. Friction factor as a function of Reynolds number (a) S_L=18mm, inline, (b) S_L=18mm, staggered (c) S_L=21.6mm, inline and (d) S_L=21.6mm, staggered

Generally, all turbulence models make over estimations for the same arrangement and longitudinal distance, only prediction of the SST turbulence model is lower than experimental results at minimum Reynolds number.
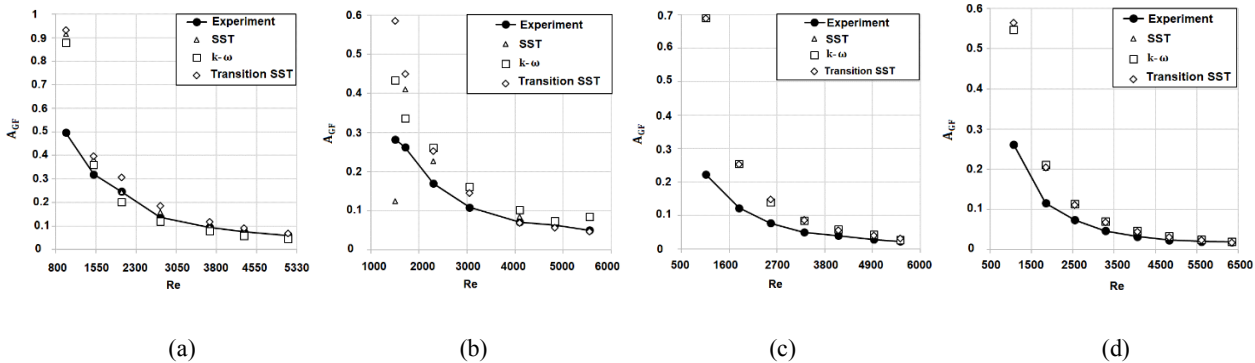

(a) (b) (c) (d)

Figure 12. Area goodness factor as a function of Reynolds number (a) S_L=18mm, inline, (b) S_L=18mm, staggered (c) S_L=21.6mm, inline and (d) S_L=21.6mm, staggered

CONCLUSIONS

This study examines the convective heat transfer and pressure drop characteristics of a heat exchanger with two different longitudinal distances (SL=18 mm and SL=21.6 mm) and tube bundles arranged inline and staggered on supporting plates. Experimental and numerical methods are used to investigate these properties. The Reynolds numbers range from 989 to 6352, with a fixed Prandtl number of 0.7. Three turbulence models, namely k-ω, SST, and transition SST, are utilized within the framework of the URANS approach. The experimental results serve as a benchmark for evaluating the precision of the numerical predictions.

To reduce the computational burden of large meshes, 2D calculations are performed instead of 3D calculations, and proportion coefficients are used to approximate the 3D behaviour based on the 2D results.

Across all geometric configurations, the Nusselt number and friction factor values are observed to increase with Reynolds number, while the area goodness factor decreases. The staggered configuration has a greater Nusselt number and friction factor than the inline configuration. Reducing the longitudinal distance between rows of tubes increases the Nusselt number but decreases the pressure drop. For short longitudinal distances, the inline arrangement produces a greater area goodness factor than the staggered arrangement, whereas the opposite is true for long longitudinal distances.

In terms of turbulence models, the SST model provides the closest agreement with experimental results for both geometric patterns at small longitudinal distances. The k- and transition SST models also provide accurate forecasts. For the large longitudinal distance of the staggered arrangement, all turbulence models exhibit similar behaviour and are in excellent agreement with experimental data. In the case of the inline arrangement with a longitudinal distance of 21.6 mm, the k-ω model performs best in predicting the Nusselt number, while the transition SST model provides the closest results for the friction factor. Lastly, for the inline configuration with a distance of 18 mm along the longitudinal axis, the SST model closely matches the experimental results for the area goodness factor.

REFERENCES

Abed, N., and Afgan, I. (2017). A CFD study of flow quantities and heat transfer by changing a vertical to

diameter ratio and horizontal to diameter ratio in inline tube banks using URANS turbulence models. *International Communications in Heat and Mass Transfer,* 89,18-30.

Aburoma, M.M. , Cho, S.M., and Sawyer, R.H. (1975). *Thermal/hydraulic design considerations for Clinch River breeder reactor plant intermediate heat exchangers*, ASME, 75-WA/HT-101.

Ansys-Fluent (2009) *Ansys-Fluent 12.0 User's Guide.* Ansys Inc.

Aslan, E., Taymaz, I., Benim, A.C.(2015). Investigation of LBM curved boundary treatments for unsteady flows. *European Journal of Mechanics B/Fluids,* 51,68-74

Aslan, E. (2016).Numerical investigation of the heat transfer and pressure drop on the tube bundle support plates for inline and staggered arrangements. *Progress in Computational Fluid Dynamics,* 56(1),38-47

Barmasian, H.R., and Hassan, Y.A. (1997). Large eddy simulation of turbulent crossflow in the tube bundles. *Nuclear Engineering and Design,* 172,103-122.

Beale, S.B., and Spalding, D.B. (1999). A numerical study of unsteady fluid flow in inline and staggered tube banks. *Journal of Fluids and Structures,* 13,723-754.

Benim, A.C., Cagan, M., and Gunes, D. (2004). Computational analysis of heat transfer in turbulent pipe flow. *International Journal of Thermal Science,* 43,725-732.

Benim, A.C., Ozkan, K., Cagan, M., and Gunes, D. (2007). Computational investigation of turbulent jet impinging onto rotating disk. *International Journal of Numerical Methods for Heat and Fluid Flow,* 17, 284-301.

Benim, A.C., Chattopadhyay, H., and Nahavandi, A. (2011). Computational analysis of turbulent forced convection in a channel with a triangular prism. *International Journal of Thermal Science,* 50,1973-1983.

Benim, A.C., Brillert, D., and Cagan, M. (2004). Investigation into the computational analysis of direct-transfer pre-swirl systems for gas turbine cooling. *ASME Turbo Expo,* 4,453-460.

Benim,A.C., Geiger, M., Doehler, S., Schoenenberger ,M., and Roemer, H. (1995). Modelling the flow in the exhaust hood of steam turbines under consideration of turbine-exhaust hood interaction, *in Proc. 1st European. Conf. Turbomachinery - Fluid Dynamic and Thermodynamic Aspects: Computational Methods,* pp.343-357.

Benim, A.C., Pasqualotto, E., and Suh, S.H. (2008). Modelling turbulent flow past a circular cylinder by

RANS, URANS, LES and DES. *Progress in Computational Fluid Dynamics, An International Journal,* 8,299-307.

Bouris, D., Papadakis, G., and Bergeles, G. (2001). Numerical evaluation of alternate tube configurations for particle deposition rate reduction in heat exchanger tube bundles. *International Journal of Heat and Fluid Flow,* 22 ,525-536.

Brandt, F. (1985).*Wärmeübertragung im Dampferzeugen und Wärmetauschen, FDBR-Fachverband Dampfkessel-Behälten-und Rohrleitungsbau*, Essen: Vulkan-Verlag.

Chattopadhyay, H., and Benim, A.C. (2011). Turbulent heat transfer over a moving surface due to impinging slot jets. *Journal of Heat Transfer* ,133 ,104502-1.

Dagsöz, A.K. Bestimmung des Wörmeübergangs an Rohrbündel Tragplatten für Flucthende und Versetze Rohraordnungen. ITU Makine Fakültesi Isı Tekniği ve Ekonomi Araştırma Kurumu Bülteni 1975; 13.

Durbin, P.A., and Reif, B.A.P. (2011). *Statical theory and modelling for turbulent flows*, (2nd ed.).Chichester,Wiley.

Grimisson,E.D. (1937). Correlation and utilization of new data on flow resistance and heat transfer for crossflow of gases over tube banks. *Trans. ASME,* 59,583-594.

Hamid, M.O.A., Zhang, B., and Yang, L. (2014). Application of field synergy principle for optimization fluid flow and convective heat transfer in a tube bundle of a pre-heater. *Energy,* 76, 241-253.

Hilpert, R. (1933). *Wärmeabgabe von geheizten Drähten und Rohren im Luftstrom.* Fors. Ingenieurwesen,(4):215-224.

Holman, J.P. (1994). *Experimental methods for engineers* (6th ed.).McGraw-Hill Int.

Horvat, A., Leskovar, M., and Mayko, B. (2006). Comparison of heat transfer conditions in tube bundle cross-flow for different tube shaped. *International Journal of Heat and Mass Transfer,* 49 ,1027-1038.

Ibrahim, T.A., and Goma, A. (2009). Thermal performance criteria of elliptic tube bundle in cross flow. *International Journal of Thermal Science* ,48 , 2148-2158.

Khan, M.G., Fartaj, A., and Ting, D.S. (2004). An experimental characterization of cross-flow cooling of air via an in-line elliptical tube array. *International Journal of Heat Fluid Flow* ,25,636-648.

Kukulka, D.J., and Smith, R (2014). Heat transfer evaluation of an enhanced heat transfer tube bundle.*Energy* ,75,97-103.

Kuppan T. Heat exchanger design handbook. New York: Marcel Deker Inc, 2000.

Kwak, K.M., Torii, K., and Nishino, K. (2003). Heat transfer and pressure loss penalty for the number of tube rows of staggered finned-tube bundles with a single transverse row of winglets. *International Journal of Heat Mass Transactions*, 46, 175-180.

Launder, B.E., and Spalding, D.B. (1974). The numerical computation of turbulence flows. *Computer Methods Applied Mechanical Engineering,* 3,269-289.

Launder, B.E., and Massey, T.H. (1978).The numerical prediction of viscous flow and heat transfer in tube banks.*Journal of Heat Transfer,* 100,565-571.

Lavasani, A.M., Bayat, H., and Maarefdoost, T. (2014). Experimental study of convective heat transfer from in-line cam shapped tube bank in crossflow. *Applied Thermal Engineering,* 65 ,85-93.

Li, X., Zhu, D., Yin, Y., Liu, S., and Mo, X. (2018). Experimental study on heat transfer and pressure drop of twisted oval tube bundle in cross flow. *Experimental Thermal Fluid Science,* 99,251-258.

Liao, L., and Liu, Z.H. (2011). Enhanced Boiling Heat Transfer of the Compact Staggered Tube Bundles under Sub-Atmospheric Pressures. *Heat Transfer Engineering* ,28,444-450.

Lin, C.N., Liu, Y.W., and Leu, J.S. (2008). Heat Transfer and Fluid Flow Analysis for Plate-Fin and Oval Tube Heat Exchangers With Vortex Generators. *Heat Transfer Engineering* ,29,588-596.

Lotfi, B., Zeng, M., Sunden, B., and Wang, Q. (2014). 3D numerical investigation of flow and heat transfer characteristics in smooth wavy fin-and-elliptical tube heat exchangers using new type vortex generators. *Energy* ,73,233-257.

Maithani, R., Kumar, A., Zadeh, P.G., Safaei ,M.Z., and Gholamalizadeh, E. (2020). Empirical correlations development for heat transfer and friction factor of a solar rectangular air passage with spherical-shaped turbulence promoters. *Journal of Thermal Analysis and Calorimetry,* 139,1195–1212.

Maqableh, A.M., Khadrawi, A.F., Al-Nimr, M.A., Ammoruah, S.A., and Benim, A.C. (2011). Heat transfer characteristics of parallel and counter flow micro-channel heat exchangers with varying wall resistance. *Progress in Computational Fluid Dynamics,* 11,318-328.

Matos, R.S., Laursen, T.A., Vargas, J.V.C., and Bejan, A. (2004). Three-dimensional optimization of staggered finned circular and elliptic tubes in forced convection. *International Journal of Thermal Science,*43,447-487.

Mavriodu, S.G., and Bouris, D.G. (2012). Numerical evaluation of a heat exchanger with inline tubes of different size for reduced fouling rates. *International Journal of Heat and Mass Transfer,* 55 ,5185-5195.

Menter, F.R. (1994). Two equation eddy viscosity turbulence models for engineering applications. *AIAA Journal,* 32, 1598-1695.

Menter, F.R., Kuntz, M., and Langtry, R.B., (2003). Ten years of experience with the SST turbulence model. *Heat and Mass Transfer,* 4,625-632.

Menter, F.R., Langtry, R.B., Likki, S.R., Suzen, T.B., Huang, P.G., and Volker, S. (2006). A Correlation-Bases Transition Model Using Local Variables-Part-1: Model Formulation. *Journal of Turbomachinery,* 128 ,413-422.

Mizushima, J., and Suehiro, N. (2005). Instability and transition of flow past two tandem circular cylinders. *Physics Fluids* ,14,104-107.

Oclon, P., Lopata, S., Novak, M., and Benim, A.C. (2015). Numerical study on the effect of inner tube fouling on the thermal performance of high-temperature fin-and-tube heat exchanger. *Progress in Computational Fluid Dynamics* ,15,290-306.

Oengoeren, A., and Ziada, S. (1992).Unsteady fluid forces acting on a square tube bundle in air cross-flow. *in Proc. 1992 International Symposium on Flow-Induced Vibration and Noise*,55-74.

Ozturk, N.A., Ozalp, C., Canpolat, C., and Sahin, B. (2016). PIV measurement of flow through normal triangular cylinder arrays in the passage of a model plate-tube heat exchangers. *International Journal of Heat Fluid Flow* ,61(B),531-544.

Pourdel, H., Afrouzi, H.H., Akbari, O.A., Miansari, M., Toghraie, D., Marzban, A., and Koveiti, A. (2019). Numerical investigation of turbulent flow and heat transfer in flat tube. *Journal of Thermal Analysis and Calorimetry,* 135,3471-3483.

Taymaz, I., Aslan, E., and Benim, A.C. (2015). Numerical investigation of incompressible fluid flow and heat transfer across a bluff body in a channel flow. *Thermal Science*,19,537-547.

Wilcox, D.C. (1988). *Turbulence Modelling for CFD.* DCW Industries.

Yahiaoui, T., Ladjede, O., Imine, O. and Adjlout, L. (2016). Experimental and CFD investigations of turbulent cross flow in staggered tube bundle equipped with grooved cylinders. *J Braz Soc Mech Sci Eng*,38,163–175.

You, Y., Xiao, S., Pan, N., and Deng, Z. (2017). Full Model Simulation of Shell side Thermal Augmentation

of Small Heat Exchanger with Two Tube Passes. *Heat Transfer Engineering,* 39,1024-1035.

Zhao, H., Liu, Z., Zhang, C., Guan, N., and Zhao, H. (2016). Pressure drop and friction factor of a rectangular channel with staggered mini pin fins of different shapes. *Experimental Thermal Fluid Science* ,71,57-69.

Zheng, Z., Yang, W., Cai, Y., Wang, Q., and Zeng, G. (2020). Dynamic simulation on ash deposition and heat transfer behavior on a staggered tube bundle under high-temperature conditions. *Energy,* 190,116390.

Erman Aslan received his B.Sc., M.Sc., and Ph.D. in Mechanical Engineering from Sakarya University. He was a researcher for his Ph.D. at Dusseldorf University of Applied Sciences, Germany. His research area is Lattice Boltzmann method, CFD, forced convection, aerodynamics and heat transfer. He is Associate Prof. at Kocaeli University.

Imdat Taymaz earned BSc degree in Mechanical Engineering from Istanbul Technical University in 1983. He got M.Sc. of Mechanical Engineering at ITU in 1985 and Ph.D. at Sakarya University in 2001. He has interest in the following research areas as internal combustion engines, alternative fuels, fuel cells, heat transfer. He is Professor at Sakarya University.

Kemal Cakir is Assistant Professor at Sakarya University. He got M.Sc. of Mechanical Engineering at ITU and Ph.D. at Sakarya University. His main research interest is experimental heat transfer.

Elif Eker Kahveci is Assistant Professor at Sakarya University. She received M.Sc. and Ph.D. in Mechanical Engineering from Sakarya University, Turkey. Her research is about fuel cells, CFD, heat transfer

TRNSYS MODEL OF THE COMBI BOILER DOMESTIC HOT WATER CIRCUIT WITH A FOCUS ON THE PARAMETER DEFINITION OF THE PLATE HEAT EXCHANGER

Okan Gök*, Ayşe Uğurcan Atmaca**, Aytunç Erek*, and Hürrem Murat Altay***

* Mechanical Engineering Department, Faculty of Engineering, Dokuz Eylül University Tınaztepe Yerleşkesi 35390 Buca, İzmir, Türkiye, gok.okan@ogr.deu.edu.tr; aytunc.erek@deu.edu.tr
** Aerospace Engineering Department, Faculty of Engineering, Dokuz Eylül University Tınaztepe Yerleşkesi 35390 Buca, İzmir, Türkiye, ugurcan.atmaca@deu.edu.tr
*** Bosch Termoteknik Isıtma ve Klima Sanayi Ticaret Anonim Şirketi, 45030 Manisa, Türkiye, murat.altay@tr.bosch.com

Abstract: Combi boilers used for both space and domestic hot water heating are one of the common household appliances. Modelling the domestic hot water circuit of a combi boiler for the preliminary evaluation of the laboratory testing is of crucial importance since it decreases the time, cost, and energy spent on the trials. There are various modelling approaches established by the authors of this paper. Domestic hot water circuit of the appliance is modelled previously making use of the Transient System Simulation Tool (TRNSYS 18) and a good agreement is achieved with the experimental and numerical data for the economic mode simulations. The drawback of the current TRNSYS model is the dependence on the experimental data for some of the parameter definitions of the components selected from the TRNSYS library, i.e. UA (multiplication of the overall heat transfer coefficient and the heat transfer area) input of the plate heat exchanger and heat retention effect of the heat cell block. In this paper, a constant value is assigned to the parameter definition of UA instead of a time dependent varied profile. Mean absolute errors covering the steady-state and transient operating regions for the domestic hot water inlet and outlet temperature difference in economic mode simulations stay nearly the same around 0,46°C, 0,82°C, and 0,53°C for 5 l/min, 7 l/min, and 8,7 l/min, respectively, under constant and variable UA approaches. Comfort operating scheme model is established with a couple of experimental data as of the principal application of the constant UA approach. Mean absolute error of the overall domestic hot water inlet and outlet temperature difference profile decreases to 0,5°C in the comfort mode simulation.
Keywords: Combi boiler, Transient system simulation, Plate heat exchanger (PHE), Domestic hot water (DHW), Comfort and economic (eco) operating modes, TRNSYS model, UA input.

PLAKALI ISI EŞANJÖRÜNÜN PARAMETRE TANIMI ODAKLI KOMBİ SICAK KULLANIM SUYU HATTININ TRNSYS MODELİ

Özet: Mahal ve sıcak kullanım suyu ısıtılması için kullanılan kombiler, yaygın olarak kullanılan ev aletlerindendir. Laboratuvar testlerinin ön değerlendirmesi için bir kombinin sıcak kullanım suyu devresinin modellenmesi, deneyler için harcanan zamanı, maliyeti ve enerjiyi azalttığı için oldukça önemlidir. Bu makalenin yazarları tarafından oluşturulan çeşitli modelleme yaklaşımları bulunmaktadır. Önceki çalışmalarda, cihazın sıcak kullanım suyu devresi *Zamana Bağlı Sistem Simülasyon Aracı* (TRNSYS 18) kullanılarak modellenmiştir ve ekonomik mod simülasyonları için deneysel ve sayısal veriler kullanılarak iyi bir uyum ortaya konmuştur. Mevcut TRNSYS modelinin dezavantajı, TRNSYS model kütüphanesinden seçilen bileşenlerin, plakalı ısı eşanjörünün UA (toplam ısı transfer katsayısı ve ısı transfer alanının çarpımı) girdisi ve ısı hücresi bloğunun ısı tutma etkisi gibi bazı parametre tanımlarının deneysel verilere bağımlı olmasıdır. Bu makalede, plakalı ısı eşanjörünün UA parametresi zamana bağlı değişken bir profil yerine sabit bir değer olarak tanımlanmıştır. Kombinin ekonomik çalışma modu simülasyonlarında, sıcak kullanım suyunun giriş ve çıkış sıcaklık farkı için kararlı ve kararsız süreçleri kapsayan ortalama mutlak hatalar, sabit ve değişken UA yaklaşımları altında 5 l/dk, 7 l/dk ve 8.7 l/dk için sırasıyla 0.46°C, 0.82°C ve 0.53°C olarak neredeyse sabit kalmıştır. Konfor çalışma modunun modeli, sabit UA yaklaşımının önemli bir uygulaması olarak birkaç deneysel veri ile oluşturulmuştur. Konfor modu simülasyonunda, sıcak kullanım suyu giriş ve çıkış sıcaklık farkı profilinin ortalama mutlak hatası 0.5°C'ye düşmektedir.
Anahtar Kelimeler: Kombi, Zamana bağlı sistem simülasyonu, Plakalı ısı değiştiricisi (PID), Sıcak kullanım suyu (SKS), Konfor ve ekonomik (eco) çalışma modları, TRNSYS modeli, UA girdisi.

INTRODUCTION

Combi boilers are one of the mostly used appliance groups for the residence since they are used for both space and domestic hot water (DHW) heating functions. Combi boilers are simple devices since they include a primary heat exchanger, a secondary heat exchanger, a pump, and a diverter valve as given in Figure 1. Primary heat exchanger is the heat cell (HC) including the combustion of the natural gas at which the energy of the hot combustion products is transferred to the central heating (CH) water. The CH water is sent to the radiators to warm up the surroundings when the space heating function is active. The space and DHW heating function cannot be activated at the same time, hence when the user DHW demand is created, space heating function stops. At the time of the user DHW demand, the diverter valve changes the direction of the flow and the CH water is sent through the secondary heat exchanger named as plate heat exchanger (PHE). Therefore, DHW is provided users after the energy of the hot CH water is transferred to the DCW in the PHE.
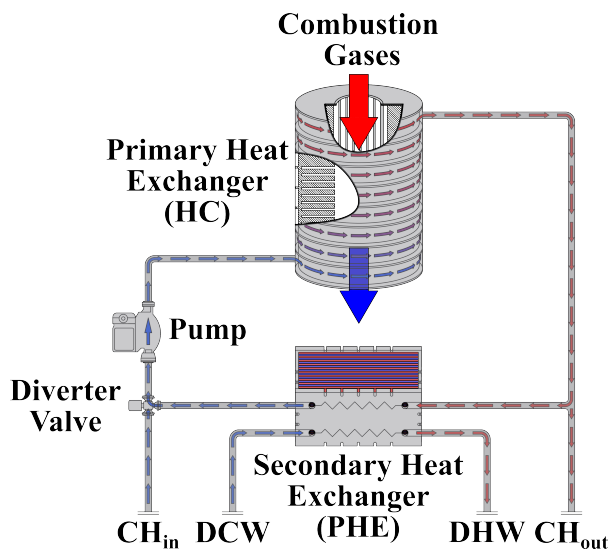

Figure 1. Schematic view of the combi boiler heater with the basic equipment

The subject of this paper is modelling the DHW heating circuit of the combi boiler type heating appliances. This study is a continuation of the previous studies established by the authors of these studies. First of the milestone studies of the research group is the one-dimensional (1D) model of the DHW heating circuit (Atmaca et al., 2015). 1D transient heat transfer equations were solved simultaneously to calculate the temperature profiles of the CH water at the inlet and outlet of the HC and the temperature difference of the DHW between the PHE inlet and outlet and the agreement was found satisfactory at various operating conditions especially for the steady-state region. Secondly, a commercial 1D thermal-fluid system modelling software, Flowmaster® was used to create the model of the DHW function of the combi boiler (Atmaca et al., 2016). CH inlet and outlet temperatures from the HC resulted in approximately 10 K higher values than the experimental data even in the steady-state region. Since the heat transfer rates and the DHW temperature difference between the inlet and outlet of the

PHE were compared in main, the Flowmaster® model as well was found appropriate to be used in the preliminary evaluations. The essential drawback with this model was the parameter definition concerned with the HC, i.e. implementation of the heat retention effects of the HC. Lastly, DHW heating circuit was modelled using the Transient System Simulation Tool (TRNSYS 18) (Klein et al., 2017) and the model achieved a good agreement with the experimental data for both the steady-state and transient temperature profiles of the economic (eco) mode simulations at various operation conditions (Gök et al., 2022). Subsequently, both experimental and numerical validations were displayed elaborately for the CH inlet and outlet temperatures from the HC and the DHW inlet and outlet temperature difference from the PHE at 5 l/min, 7 l/min, and 8,7 l/min DHW user demands in economic mode simulations (Gök et al., 2023). However, the TRNSYS model needed improvement since it was highly dependent on the experimental data.

When compared to the previous studies of the authors regarding the use of TRNSYS, this current research has two main objectives as to decrease the dependence of the TRNSYS model on the experimental data and to define appropriate parameter definition of the model for the comfort mode validation. The TRNSYS model needs experimental data for the UA parameter definition of the plate heat exchanger and the heat retention effect of the HC block. In the firstly established TRNSYS models (Gök et al., 2022 and Gök et al., 2023), UA profile of the PHE was inserted into the model with respect to the transient behavior of the appliance. When compared to the previous 1D DHW circuit model, the temperature profiles of the CH water and DHW were estimated with less mean absolute errors (MAE), mean square errors (MSE), and root mean square errors (RMSE) for the overall time duration including the transient and steady-state regions. Besides, in this study, the effects of the insertion of the transient UA profile and an average UA value into the model on the MAE, MSE, and RMSE are compared and the influence of this UA parameter definition is discussed in detail. Moreover, comfort mode validation is made with regard to this crucial finding.

Part of the literature studies conducted by the authors of this paper is summarized in the aforementioned paragraphs in order to highlight the objectives of the paper clearly. There are various studies as well in the literature concerning DHW heating, combi boilers, and TRNSYS models of the systems other than the formerly summarized studies of the authors. Five different domestic hot water heater concepts were investigated by Boait et al. (2012) and they highlighted the higher efficiency of the instantaneous hot water systems when compared to the systems with storage tanks. Moreover, the authors also discussed the temperature ranges of DHW to prevent scalding and to mitigate the risk of Legionella in the system. Pärisch et al. (2019) investigated tankless water heaters (instantaneous water heaters) using hot water as the energy source. The authors of this paper as well gave the critical temperature limits with respect to typical system characteristics, i.e. exchange frequency of water within the system, the

volume of the water between the heater and each tap, etc. They focused on the comfort properties of DHW under transient conditions rather than other challenging design parameters of capacity and energy efficiency. A new test procedure proposal for comfort evaluations was given with future work discussion. Pomianowski et al. (2020) prepared a review paper on the recent developments covering the production, storage, circulation, and distribution of DHW from the viewpoints of energy use and efficiency. They pointed out the attitude of the latest studies focusing on the DHW production. Haissig and Woessner (2000) explained the adaptive fuzzy control (AFC) algorithm in detail. In comparison with a traditional proportional-integral-derivative (PID) controller which was commonly used in combi-boilers, set-point error and control effort were reduced between 18%-70% and 23%-41%, respectively due to the development of AFC. Lastly, there are review studies covering DHW heating systems with various perspectives. İbrahim et al. (2014) presented a literature review of the DHW production systems categorizing them into six groups as wood, oil/gas, electric, heat pump, solar and instantaneous systems.

As of the previous studies concerned with the combi boilers, there are many other researches in addition to previously given studies (Atmaca et al., 2015; Atmaca et al., 2016; Gök et al., 2022; and Gök et al., 2023). Ucar and Arslan (2021) stated that the combustion unit including the main heat exchanger had the highest contribution to the total exergy destruction with reference to the advanced exergy analysis for the space heating function of 24 kW commercial condensed combi boiler. Hence space heating efficiency could be improved to 14.32% due to the improvements made on the combustion process and main heat exchanger. Fridlyand et al. (2021) used EnergyPlus to establish a simple simulation tool to calculate the energy consumption of the tankless combi boilers since EnergyPlus is a widely used and open source energy simulation program. The proposed Lumped Heat Capacity combi model could be used to compare the effects of the various control strategies and to evaluate the amount of the energy savings of the modern combi concepts when compared to the regular/traditional appliances. Quintã et al. (2019) constructed the mathematical model of the tankless gas water heaters via lumped space approach. There were challenging targets concerned with the efficiency, comfort, and emissions of the flue gas. Therefore, the proposed model was useful to test /simulate various appliance concepts and control algorithms in order to optimize the efficiency, the comfort level of the users, and the emissions of the harmful gases.

In the last part of the literature survey, TRNSYS models are summarized. In the study of Jordan and Vajen (2001), four categories were specified to generate different types of loads. Effects of the DHW flow rate and the draw-off time of the day under realistic and simplified DHW profiles with respect to two different designs of the discharge unit on the fractional energy savings were analyzed. Andrés and López (2002) constructed a new

physical model of a solar domestic water heater with a horizontal storage and mantle heat exchanger making use of TRNSYS. The main distinction of their model was the place of the hot fluid inlet at the upper of the mantle heat exchanger annulus. The comparison for the delivered daily energy between the model results and the experimental data yielded error less than 3%. Nordlander and Persson (2003) built the first simulation study of the pellet stoves to be used in house heating with TRNSYS using the type 140 and type 210 in order to model the convection and storage mechanism with the combustion phenomenon. Experimental measurements were used for the model specification in order to determine some of the component parameters and the validation. Persson et al. (2009) created the dynamic model of small pellet boilers and stoves for house heating via TRNSYS. The methodology of the paper was comprised of laboratory measurements of boilers and stoves, modelling and parameter definition, and model validation. Although the agreement between the model results and measurements was found generally satisfactory, improvements were required for large water volumes. Bourke and Bansal (2012) expressed the thermal efficiency of the gas instantaneous water heater with respect to the operating conditions by an equation in order to be used in the TRNSYS model to include the efficiency variations of this water heater and to yield more accurate energy consumption calculations. Persson et al. (2019) established a boiler model combining two of the existing models in TRNSYS as Type 210 and Type 341 which is a modified version of Type 340. The pellet burner was modelled using the Type 210. The flue gas heat exchanger and boiler water volume were established under Type 341. They could model the thermal behavior of the boilers, namely stratification and the thermal response, more accurately with respect to previously established models. Braas et al. (2020) used TRNSYS in their study to model four sub-station types including two instantaneous and two storage systems for the single family and multifamily houses in order to establish realistic DHW load profiles. Harrabi et al. (2021) analyzed the performance of the solar collector for DHW production with the help of TRNSYS. An additional storage tank as well was considered with the tank of the collector.

There are various TRNSYS modelling studies regarding the space and DHW heating (Antoniadis and Martinopoulos, 2019; Villa-Arrieta and Sumper, 2018; and Lu et al., 2021). All these exemplified studies highlight that TRNSYS is an effective and valuable tool for the transient system modelling. Moreover, Shrivastava et al. (2017) presented a literature review regarding the solar water heaters with respect to the system analyses simulations and they focused on the TRNSYS software throughout the paper due to the wide use of the program in the simulations. They also showed the necessity of the simulations since they decrease the testing time and cost with the preliminary evaluations, simplify the complicated phenomenon, and enable efficient source utilization. Hence the outstanding motivation of this study is the importance of the

construction and development of the combi boiler DHW circuits for the preliminary system evaluations to decrease the number of test trials and improving the reliance of the simulation model on the experimental data to analyze the system performance for a wide range of operating conditions.

For the variable and constant UA comparisons, the temperature profiles of CH water inlet and outlet from the HC and DHW inlet and outlet temperature difference of the PHE calculated making use of TRNSYS model are declared with the experimental data. Mean absolute error (MAE), mean square error (MSE), and root mean square error (RMSE) are tabulated for both UA insertion approaches. Moreover, for the comfort mode validation after showing the applicability of the constant UA approach, the DHW inlet and outlet temperature difference of the PHE from TRNSYS model is compared with the results calculated by the previously established 1D model (Atmaca et al., 2015) with respect to the experimental data. The same regression metrics for the comfort mode simulation of the TRNSYS model and 1D model are presented. As a result, comfort mode validation according to the constant UA approach yields a more satisfactory agreement with the experimental data for the transient region than the 1D model.

OPERATIONAL SCHEMES OF A COMBI BOILER

Two operating modes are examined in this study as economic (eco) and comfort modes for the DHW heating function. The distinction between these two operating modes is apparent from the temperature profile comparisons of DHW at the PHE outlet as given in Figure 2. In the eco mode, when the users request DHW, the appliance starts ignition and there is a transient region in the temperature profile of the DHW outlet since all of the system components are at the ambient temperature and store some of the released energy until the system reaches the steady-state operating condition.

In the comfort mode, hot CH water is kept within the system to decrease the transient region in the DHW outlet temperature and hence the user comfort is improved. According to the operation algorithm of the appliance, the CH water in the HC is heated regularly until its temperature reaches an upper set point, i.e. 60°C, whenever the temperature decreases below another lower set point as exemplified in Figure 3. The appliance keeps hot CH water within the system to provide the DHW directly for the higher comfort level of the users although keeping hot CH water all the time within a temperature range is disadvantageous in terms of efficiency.
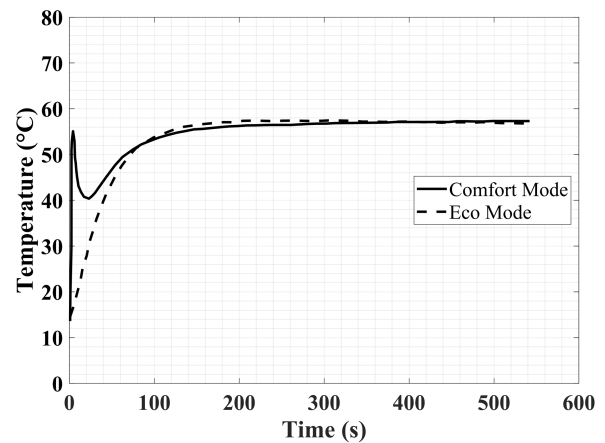

Figure 2. Comparison of the DHW outlet temperature profile between the eco and comfort operating schemes (Atmaca et al., 2015).
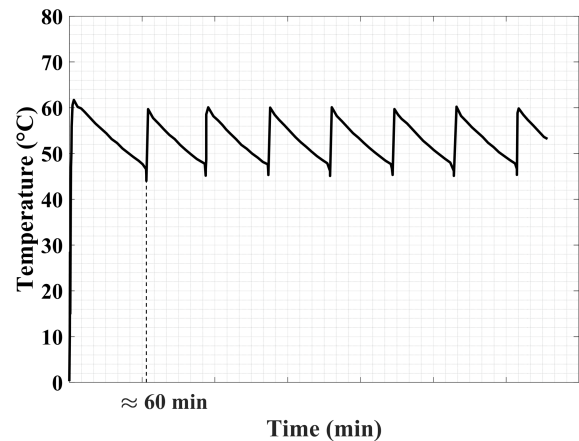

Figure 3. Variation of the CH water temperature throughout the preheat cycles in the comfort mode (Atmaca et al., 2015).

MODELLING APPROACHES

Main model of this study is established with the help of TRNSYS. Variable and constant UA approaches are compared according to the results obtained from this model. However, for the comfort operating mode validations, the results obtained from previously established 1D model as well are used to show the superiority of the TRNSYS model. Hence, 1D HC and PHE modelling equations are introduced briefly with reference to Atmaca et al. (2015).

1D Model Governing Differential Equations

1D model of the DHW circuit is constructed with five equations, namely the flue gas cooling, the CH water heating in the HC, the HC wall heating, the CH water cooling in the PHE, and the DHW heating. Differential control volumes of the HC and the PHE on which the governing equations are derived are given in Figure 4 (a) and (b), respectively, as well as the flow directions of each fluid domain. The details concerned with the solution algorithm of these five equations are described by Atmaca et al. (2015).
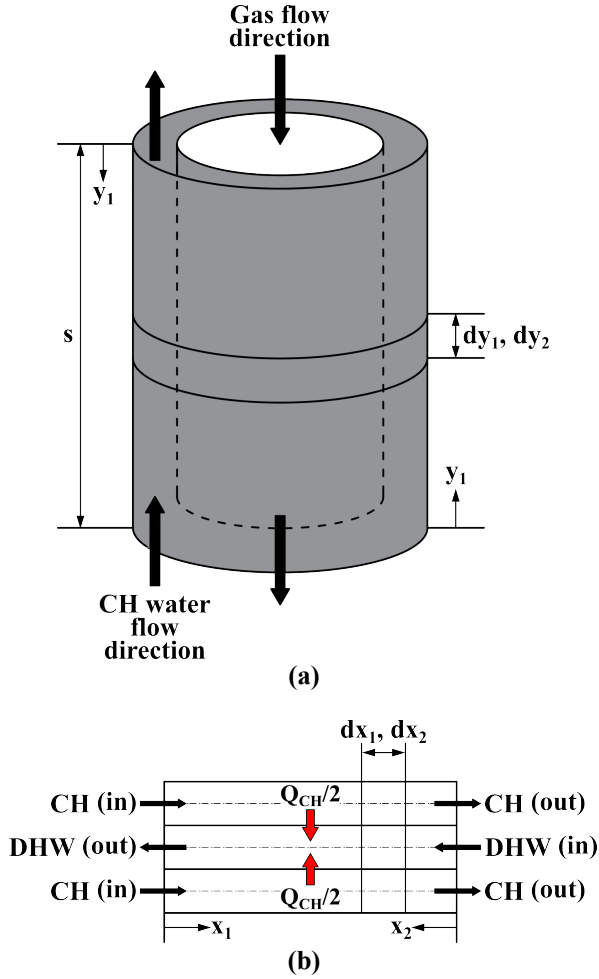
Figure 4. Differential control volumes on which the governing equations are derived and the flow directions of (a) the HC and (b) the PHE (Atmaca et al., 2015).

The first three equations belong to the HC and describe the cooling of the flue gas, the heating of the CH water in the HC, and the heating of the HC wall. The total thermal resistances between the HC wall and the flue gas, and the HC wall and the CH water are determined theoretically. The fourth equation shows the cooling of the CH water and the fifth equation declares the heating of the DHW in the PHE. The multiplication of the overall heat transfer coefficient and the heat transfer area (UA) for the PHE is determined experimentally to be used in the numerical calculations. The terms on the left side of the equation shows the rate of change of thermal energy stored within the control volumes. Hence, due to these terms, the variation of the temperature from the transient regions to steady-state regions could be calculated.

$$\rho_g A_{c,g} c_{p,g} \frac{\partial T_g}{\partial t} = -\dot{m}_g c_{p,g} \frac{\partial T_g}{\partial y_1} - \frac{A_{s,g} U_g}{s} (T_g - T_w) \quad (1)$$

$$\rho_{wt} A_{c,wt(1)} c_{p,wt} \frac{\partial T_{wt(1)}}{\partial t}$$
$$= -\dot{m}_{wt(1)} c_{p,wt} \frac{\partial T_{wt(1)}}{\partial y_2}$$
$$+ \frac{U_{wt(1)} A_{s,wt(1)}}{z} (T_w - T_{wt(1)})$$
$$- h_\infty \frac{A_o}{z} (T_{wt(1)} - T_\infty) \quad (2)$$

$$\rho_w A_{c,w} c_w \frac{\partial T_w}{\partial t} = k_w \frac{\partial^2 T_w}{\partial y_2^2} A_{c,w} + \frac{U_g A_{s,g}}{s} (T_g$$
$$- T_w) - \frac{U_{wt(1)} A_{s,wt(1)}}{s} (T_w$$
$$- T_{wt(1)}) \quad (3)$$

$$\rho_{wt} \frac{V_{chwc}}{l_{PHE}} c_{p,wt} \frac{\partial T_{wt(2)}}{\partial t}$$
$$= -\dot{m}_{wt(2)} c_{p,wt} \frac{\partial T_{wt(2)}}{\partial x_1}$$
$$- 2 \frac{U_{PHE} A_{PHE}}{l_{PHE}} (T_{wt(2)} - T_{wt(3)}) \quad (4)$$

$$\rho_{wt} \frac{V_{dhwc}}{l_{PHE}} c_{p,wt} \frac{\partial T_{wt(3)}}{\partial t}$$
$$= -\dot{m}_{wt(3)} c_{p,wt} \frac{\partial T_{wt(3)}}{\partial x_2}$$
$$+ 2 \frac{U_{PHE} A_{PHE}}{l_{PHE}} (T_{wt(2)} - T_{wt(3)}) \quad (5)$$

The boundary condition of the flue gas equation is the adiabatic flame temperature as follows;

$$T_g(0, t) = T_{adia} \quad (6)$$

The boundary condition of the second and fourth equations are interconnected to each other since the CH water entering the HC is the CH water leaving the PHE and the CH water at the inlet of the PHE comes from the HC outlet as formulated below;

$$T_{wt(1)}(0, t) = T_{wt(2)}((l_{PHE}/dx_1), t) \quad (7)$$
$$T_{wt(2)}(0, t) = T_{wt(1)}((z/dy_2), t) \quad (8)$$

The wall heating equation includes the heat transfer term by conduction resulting in second order differential equation. Therefore, two boundary conditions are given as the convection surface condition (Incropera et al., 2007) and expressed by

$$\left(-k_w \frac{\partial T_w}{\partial y_2}\right)_{y_2=0} = h_\infty (T_\infty - T_w(0, t)) \quad (9)$$

$$\left(-k_w \frac{\partial T_w}{\partial y_2}\right)_{y_2=s/dy_1} = h_\infty (T_\infty - T_w((s/dy_1), t)) \quad (10)$$

The boundary condition of the DHW heating equation in the HC comes from the test conditions given as

$$T_{wt(3)}(0, t) = 10°C \quad (11)$$

The initial conditions for all of the equations are the same as the test conditions as

$$T_{g,wt(1),w}(y_{1,2}, 0) = 10°C \quad (12)$$
$$T_{wt(2),wt(3)}(x_{1,2}, 0) = 10°C \quad (13)$$

TRNSYS Model

TRNSYS v18 (Transient System Simulation Tool) is a dynamic simulation software consisting of different

modules for modelling various electrical and thermal systems such as heating/cooling, HVAC, and alternative energy sources etc., developed by a group of academicians at the University of Wisconsin, USA (Klein et al., 2017). TRNSYS v18 is composed of two parts. The first part named as the kernel reads and processes the inputs defined by the user or the selected model, iteratively solves the system/model equations, determines the convergence, and creates the system variables. The name of the second part is the user interface that contains the models of the system components called "Type" in its existing libraries.

In this study, the TRNSYS model as shown in Figure 5 is created by selecting the types in the TRNSYS library according to the characteristics of each combi-boiler component in order to simulate the DHW circuit of the combi-boiler. The black, red, and blue line indications given in Figure 5 represent the three main subsections of the TRNSYS model, namely the component adjustment and the controlling tools, the CH water flow circuit, and the DHW flow circuit, respectively. Unlike the designation of the lines in Figure 5, in the schematic display of the combi-boiler DHW circuit in Figure 1, red and blue arrows represent the hot and relatively cold water of the CH water and DHW, respectively.

created as the output of this module. The variation of the HC load, i.e. heat retention effect of the heat cell block in the CH water circuit, and the power modulation are obtained from the Type 62 - Calling External Programs: Excel™ module by using the simulation time and nominal power values provided by the Equa module. Nominal power values for DHW flow rates of 5 l/min, 7 l/min and 8.7 l/min are presented as Equa module outputs. Besides, they are the inputs of the Type 62 module as given in Table 1. The time-dependent percentage power modulation values are presented in the plots of the Result and Discussion section for each DHW flow rate. Using the power modulation variations and the nominal power values, the amount of energy obtained from the combustion gases in the heat cell of the combi boiler is calculated through the following equation

$$\dot{Q}_{comb,in} = P\varphi \tag{14}$$

In the previously established TRNSYS model (Gök et al., 2022 and Gök et al., 2023), the multiplication of the overall heat transfer coefficient and the heat transfer area (symbolized by the UA designation) of the PHE as well is the output provided by the Type 62 - Calling External Programs: Excel™ module. The required measurements in order to define the time-dependent power modulation,
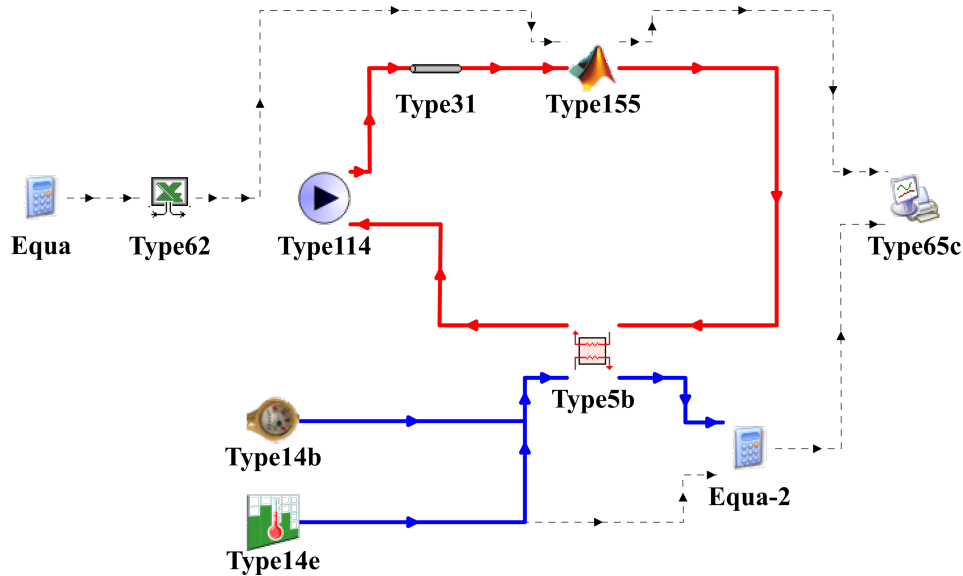

Figure 5. Flow diagram created in the TRNSYS interface for the DHW circuit model of the combi boiler.

These subsections are used to define the DHW circuit, CH water loop, and the inputs/outputs specifications for the control and connection of the model components. Therefore, the components of the DHW heating function simulation model selected from the TRNSYS existing library are presented in Table 1 with this extent covering their parameters, inputs, and outputs. The first subsection of the DHW circuit model for the adjustment and control tools is indicated by the dashed black lines. When the components in the TRNSYS model presented in Figure 5 are evaluated in hierarchical flow order, the module providing the first input to the simulation is Equa. The simulation time value and the nominal power input of the combi boiler depending on the DHW user demand are

UA input, and the HC load profile are explained thoroughly in the Experimental Test Rig section. The variation of the UA input in the transient and steady-state operating regions is given in Figure 6 for various operating conditions of 5 l/min, 7 l/min, and 8,7 l/min DHW user demands. In this study, the results are calculated using constant UA inputs and the comparison between the constant and variable UA input approaches is one of the main outcomes.

In Figure 6, there are two UA input variation lines for the 8,7 l/min DHW flow rate as the eco and comfort modes. Eco mode variations of the UA input are derived directly from the experimental data as used in the previous

TRNSYS model (Gök et al., 2022 and Gök et al., 2023). However, the UA input variation for the comfort mode is estimated under constant UA approach which is described in the subsequent regarding section. Therefore, in the previous TRNSYS model, UA input definition is made using the output of Type 62 and then becomes the input of Type 5b – Counterflow Heat Exchanger, whereas in the current TRNSYS model, the constant UA is directly defined as the input of Type 5b.

The last components of first main subsection indicated by the dashed black line are Equa-2 and Type 65c - Online Plotter. Using the Type 65c, the calculated temperature difference of the DCW and DHW, the CH water inlet temperature, and the CH water outlet temperature from the HC are printed. The temperature difference between the DHW and the DCW of the PHE is calculated in Equa-2 module as follows

$$\Delta T_{DHW} = T_{DHW} - T_{DCW} \qquad (15)$$

The second subsection displayed by the red lines is the CH water flow circuit in which the combustion of the natural gas is replaced by the heat input definition. The selected components from the TRNSYS existing library given in the red circuit are Type 114 - single speed pump model providing fluid drive and used to define the CH water mass flow rate, Type 31 - pipe model representing the piping in the CH water circuit, Type 5b - counterflow heat exchanger model (representing the plate heat exchanger) in which the heat is transferred from the CH water circuit to the DHW circuit, and Type 155 - MATLAB model for the heat cell component where heat input is defined simply instead of the natural gases combustion. Moreover, the heat retention effects of the heat cell block are calculated in Type 155. In line with the difference between the heat input provided by the natural gas combustion and the heat retention of the heat cell which is defined as the HC load, the amount of the energy transferred to the CH water and the temperature of the CH water at the HC outlet are calculated in Type 155 as

$$\dot{Q}_{CH,net} = \dot{Q}_{comb,in} - \dot{Q}_{HC,load} \qquad (16)$$

$$T_{CH,HC,out} = T_{CH,HC,in} + \frac{\dot{Q}_{CH,net}}{(\dot{m}_{CH} c_{p,wt})} \qquad (17)$$

Time dependent data of the heat retention effects for the HC transferred from the Type 62 outputs is the input of Type 155. Implementation of the heat retention effects is of crucial importance for the transient temperature profile of the DHW and the CH water. The time-dependent heat cell load profiles for the various DHW user demands are given in Figure 7. The main reason for this time-dependent load profile definition requirement is the lack of mass content to store heat in the components used for the simulations in TRNSYS software. In Figure 7, the load is calculated as minus at some regions due to the instantaneous power modulation of the appliance. There are two load profiles for 8,7 l/min DHW flow rate for the

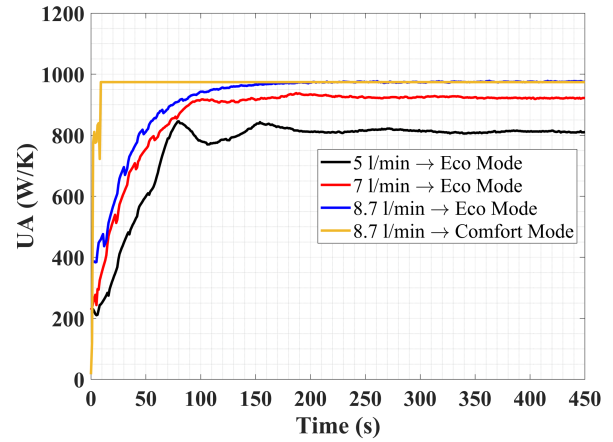eco and comfort modes both of which are explained in the regarding subsequent section.

Figure 6. Variation of the UA input for the Type 5b - Counterflow Heat Exchanger module
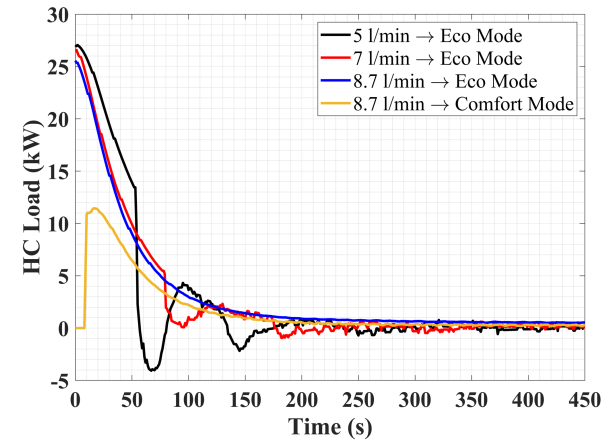

Figure 7. Time-dependent variation of the load profile for representing the heat retention effects of the heat cell

The third main sub-section designated by the blue lines is for obtaining the DHW by heating the DCW according to the user demand. In the blue circuit, Type 14b and Type 14e modules are time dependent forcing functions and used for mass flow rate specification and temperature declaration components, respectively. The provided time-dependent data from Type 14b and Type 14e outputs are transferred to Type 5b. Furthermore, the blue circuit passes on the load side of Type 5b and the red circuit passes on the source side of this module. All aforecited modelling details are summarized in Table 1.

EXPERIMENTAL TEST RIG

Experimental measurements are collected from the test rig given in Figure 8. CH inlet and outlet temperatures from the HC and DHW inlet and outlet temperatures from the PHE are measured for the experimental verification. Moreover, these temperature measurements are not only used in the validations, but for the parameter definition of some of the components as well in the TRNSYS model.

Table 1. Summary of the Type selection and definition of the DHW circuit model in TRNSYS

Type Name	Parameters		Inputs		Outputs	
Equa	–		–		Time (s)	Simulation Time
					P (kW)	17.6 24.6 27.5
Type 62	–		Time (s)	Simulation Time	$\dot{Q}_{comb,in}$ (kW)	Time dependent
			P (kW)	17.6 24.6 27.5	$\dot{Q}_{HC,load}$ (kW)	Time dependent
Type 114	$\dot{m}_{rated}$ (kg/s)	0.3742	$\dot{m}_{CH,pump,in}$ (kg/s)	0.3742	$\dot{m}_{CH,pump,out}$ (kg/s)	0.3742
	$c_{p,water}$ (kJ/kg.K)	4.19				
	P_{rated} (kW)	0.03	$T_{CH,pump,in}$ (°C)	Calculated Value	$T_{CH,pump,out}$ (°C)	Calculated Value
Type 31	$D_{pipe,inner}$ (m)	0.0165	$\dot{m}_{CH,pipe,in}$ (kg/s)	0.3742	$\dot{m}_{CH,pipe,out}$ (kg/s)	0.3742
	L_{pipe} (m)	1				
	$\rho_{pipe,inner}$ (m)	1000				
	$c_{p,water}$ (kJ/kg.K)	4.19	$T_{CH,pipe,in}$ (°C)	Calculated Value	$T_{CH,pipe,out}$ (°C)	Calculated Value
	$T_{CH,pump,initial}$ (°C)	10				
Type 155	–		$\dot{m}_{CH,HC,in}$ (kg/s)	0.3742	$\dot{m}_{CH,HC,out}$ (kg/s)	0.3742
			$T_{CH,HC,in}$ (°C)	Calculated Value		
			$\dot{Q}_{comb,in}$ (kW)	Time dependent	$T_{CH,HC,out}$ (°C)	Calculated Value
			$\dot{Q}_{HC,load}$ (kW)	Time dependent		
Type 14b	$t_{initial}$ & t_{final} (s)	0…500	–		$\dot{V}_{DHW}$ (l/min)	5 7 8.7
	$\dot{V}_{DHW}$ (l/min)	5 7 8				
Type 14e	$t_{initial}$ & t_{final} (s)	0…500	–		T_{DCW} (°C)	10
	T_{DCW} (°C)	10				
Type 5b	–		$\dot{m}_{CH,PHE,in}$ (kg/s)	0.3742	$\dot{m}_{CH,PHE,out}$ (kg/s)	0.3742
			$T_{CH,PHE,in}$ (°C)	Calculated Value		
			$\dot{V}_{DHW}$ (l/min)	5 7 8.7	$T_{CH,PHE,out}$ (°C)	Calculated Value
			$T_{DHW,PHE,in}$ (°C)	10	$\dot{V}_{DHW}$ (l/min)	5 7 8.7
			UA (W/K)	812 923.9 974.7	T_{DHW} (°C)	Calculated Value
Equa-2	–		T_{DCW} (°C)	10	ΔT_{DHW} (°C)	Calculated Value
			T_{DHW} (°C)	Calculated Value		
Type 65c	–		$T_{CH,HC,in}$ (°C)	Calculated Value	–	
			$T_{CH,HC,out}$ (°C)	Calculated Value		
			ΔT_{DHW} (°C)	Calculated Value		

First of all, power profiles are recorded for all of the investigated DHW flow rates and they are inserted into 1D model and TRNSYS models including variable and constant UA approaches. Secondly, UA variation is calculated based on these abovementioned temperature measurements under the variable UA parameter approach. The amount of heat transferred to the DHW could be calculated from the adjusted DHW flow rate and the inlet and outlet temperature difference of DHW from the PHE. Since the inlet and outlet temperatures of the CH water and DHW from the PHE are measured, the logarithmic mean temperature difference could be

calculated. Hence, the variation of UA is obtained. In 1D modelling approach, a separate test rig was used to define the UA of the PHE and an average UA value at the steady-state operating condition is used for each investigated case (Atmaca et al., 2015). Lastly, the load profile is defined similarly by subtracting the heat gain of the DHW from the measured power of the appliance. This difference is used to represent the stored energy by the HC block. Therefore, heat retention effect of the HC which is a key parameter in order to obtain the transient temperature profile of the CH water and DHW could be inserted into the model.
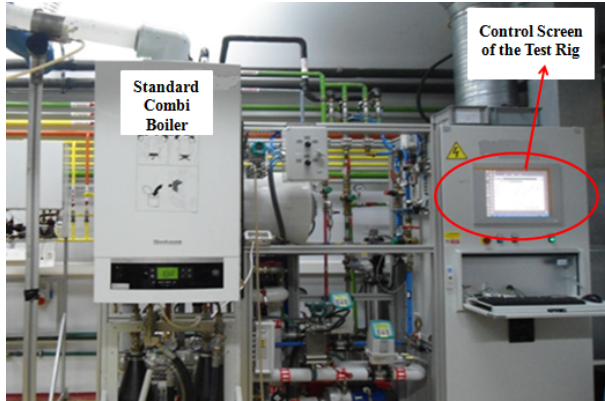

Figure 8. Combi boiler test rig for the temperature measurements of the CH water and DHW

RESULTS AND DISCUSSION

The preliminary results between the 1D modelling approach and the TRNSYS model yielded the superiority of the TRNSYS model over the 1D model with the decreased MAE, MSE, and RMSE for the overall temperature profile covering the transient region (Gök et al., 2022 and Gök et al., 2023). The most important disadvantage of the TRNSYS model is the use of the experimental UA variation and the load profile to represent the heat retention effects of the HC. First of all, UA variation is replaced with a constant UA value which is determined as the average of the UA values from the steady-state region in the TRNSYS model. The concluding remarks are interpreted with reference to some important regression metrics as mean absolute error (MAE) which is the average of the absolute errors between the estimated values and measured data, mean square error (MSE) defined as the average of the square of the errors, and root mean square error (RMSE) expressed as the square root of the MSE. They are all formulated as follows;

$$MAE = \frac{1}{n}\sum_{i=1}^{n}\left|y_{exp,i} - y_{theo,i}\right| \tag{18}$$

$$MSE = \frac{1}{n}\sum_{i=1}^{n}\left(y_{exp,i} - y_{theo,i}\right)^2 \tag{19}$$

$$RMSE = \sqrt{\frac{1}{n}\sum_{i=1}^{n}\left(y_{exp,i} - y_{theo,i}\right)^2} \tag{20}$$
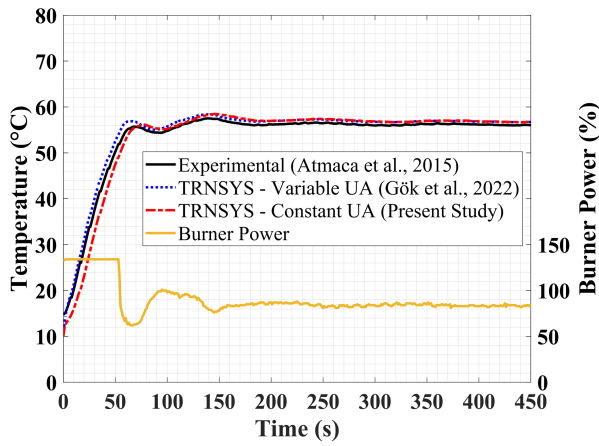
Comparison of the Variable and Constant UA Approaches for the PHE

This section focuses only the parameter definition of the multiplication of the overall heat transfer coefficient and the heat transfer area, designated simply as UA, of the PHE in eco working mode. Figure 9 (a), (b), and (c) shows the comparison between the constant and variable UA approaches with respect to the experimental data for the CH water inlet temperature of the HC, CH water outlet temperature of the HC, and DHW inlet and outlet temperature difference of the PHE, respectively, at 5 l/min DHW user request. It is obvious that both approaches result in a good agreement with the experimental data.

At the DHW user request of 5 l/min, MAE of the steady state temperature profile is around 0.7 ˚C for CH water inlet temperature and approximately 0.4 ˚C for the CH water outlet temperature and DHW inlet and outlet temperature difference under both approaches. For the overall temperature profile of the same DHW flow rate including the transient region, constant UA approach results in slightly higher MAE of CH water inlet and outlet temperatures, but the maximum of these errors is 1.6 ˚C which is still acceptable for this kind of modelling tools and assumptions as tabulated in Table 2 and Table 3. However, as of the most critical performance indicator of the combi boiler DHW heating function, the MAE of the DHW inlet and outlet difference is about 0.5 ˚C for both of the approaches as displayed in Figure 9 (c) with the great consistency in the temperature variations.

Similarly, Figure 10 (a), (b), and (c) make comparison between these two approaches according to the experimental data at the 7 l/min DHW user demand for the CH water inlet temperature of the HC, CH water outlet temperature of the HC, and DHW inlet and outlet temperature difference. MAE values of the steady-state temperature profiles are around 0.5˚C, 1˚C, and 0.4˚C for the CH water inlet temperature, CH water outlet temperature, and DHW inlet and outlet temperature difference, respectively, under both approaches. For the overall temperature profiles of the same DHW flow rate, the MAE values calculated by constant UA approach either decrease or slightly increase when compared to the errors of the variable UA assumption.

User requests at the DHW flow rates of 5 l/min and 7 l/min result in power modulation according to the control algorithm of the appliance as plotted in the secondary axes of Figure 9 and Figure 10. However, the last comparison given in Figure 11 and made for the 8.7 l/min DHW user request does not include any power modulations. Figure 11 (a), (b), and (c) presents the comparative plots of the CH water inlet temperature of the HC, CH water outlet temperature of the HC, and DHW inlet and outlet temperature difference, respectively, for 8,7 l/min DHW flow rate.
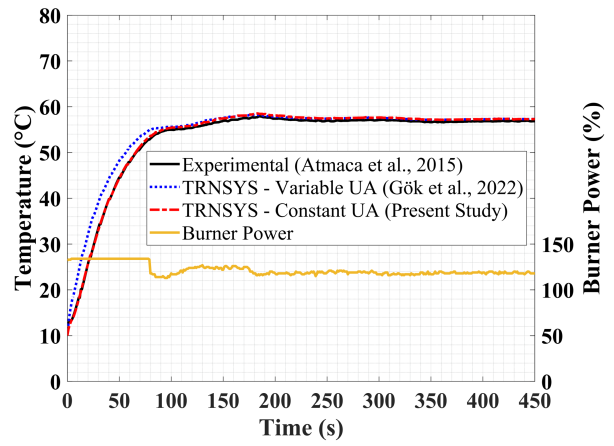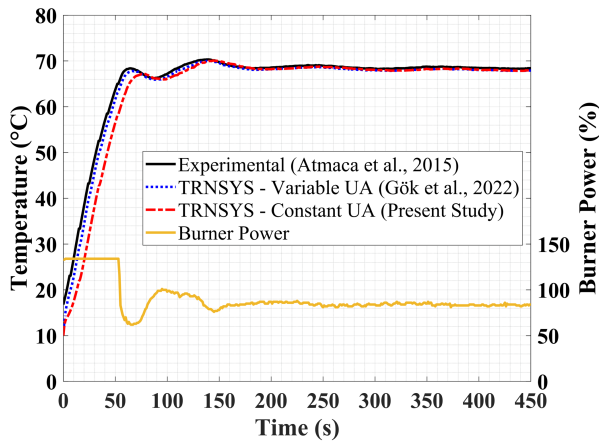
Figure 9. Comparison of the variable and constant UA approaches for (a) the CH water inlet temperature, (b) the CH water outlet temperature, and (c) the DHW inlet and outlet temperature difference of the PHE at 5 l/min DHW request

Figure 10. Display of the difference between the variable and constant UA approaches for (a) the CH water inlet temperature, (b) the CH water outlet temperature, and (c) the DHW inlet and outlet temperature difference at 7 l/min DHW user request
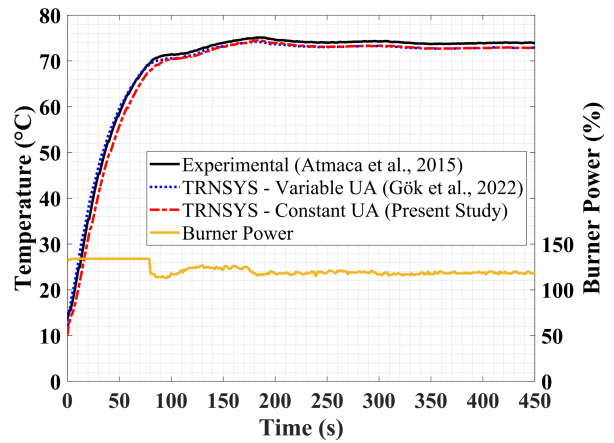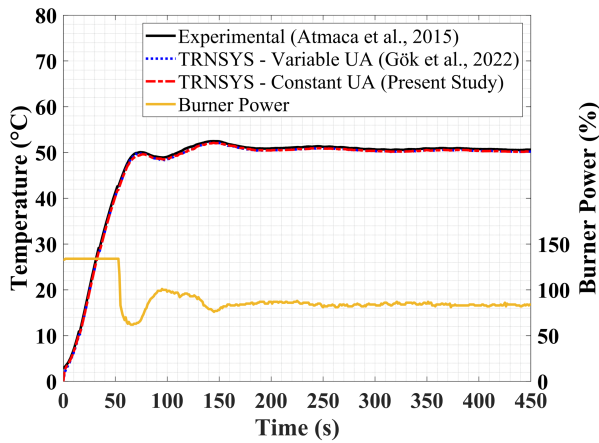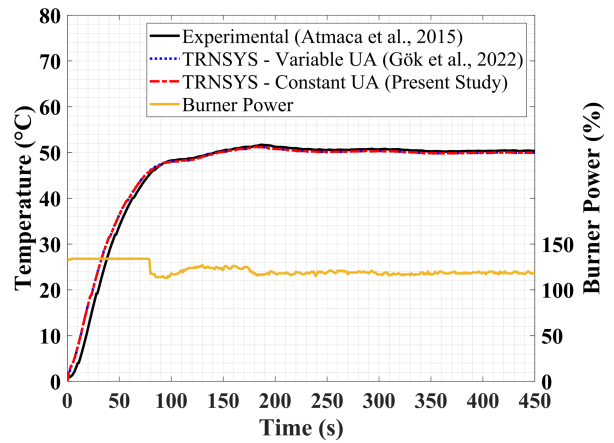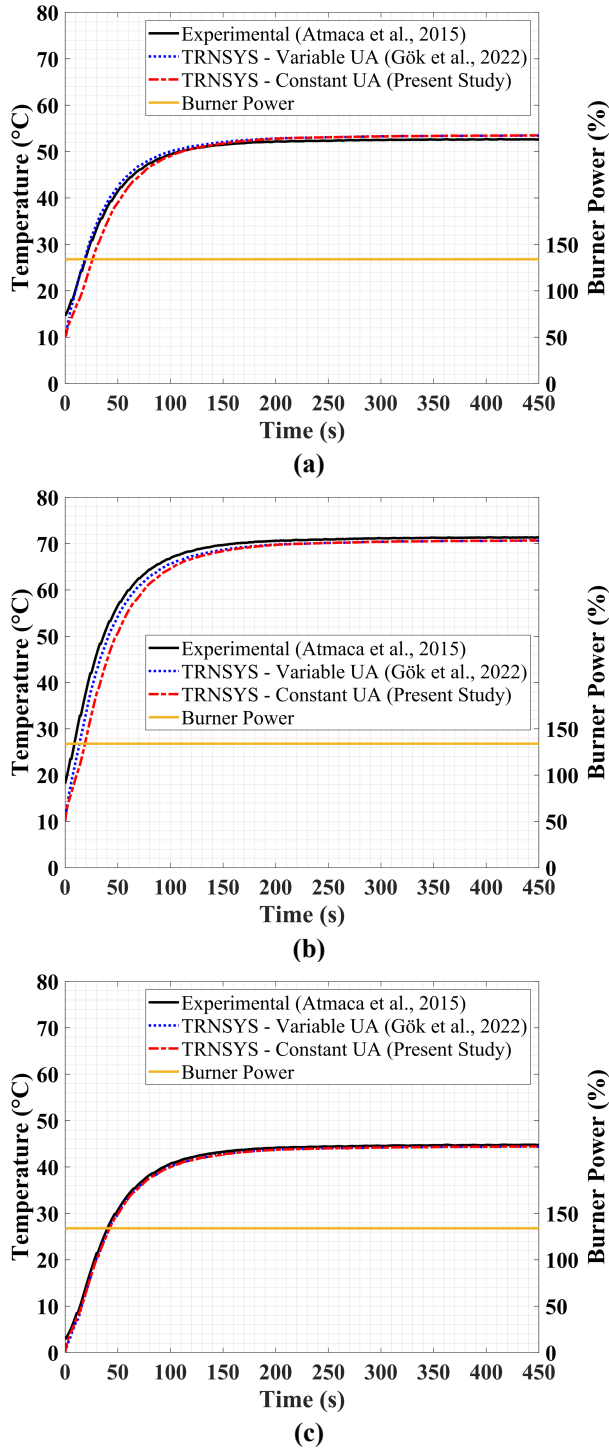
Figure 11. Comparative results of the variable and constant UA approaches for (a) the CH water inlet temperature, (b) the CH water outlet temperature, and (c) the DHW inlet and outlet temperature difference of the PHE at 8.7 l/min DHW request

The MAE values stay the same for the steady-state temperature profiles with respect to both of the approaches at the 8,7 l/min DHW user request simulation. CH water inlet temperature yields averagely 0,8°C error and CH water outlet temperature results in approximately 0,7°C for the same flow rate. Moreover, the MAE of the DHW inlet and outlet temperature difference is 0,4°C showing a good agreement between the modelling results and the experimental data. For the temperature profile covering the transient region as well,

the MAE values for the CH inlet and outlet water increase, but they stay within an acceptable error range as given in Table 3. However, the temperature difference between the DHW inlet and outlet yields a good match with an approximate MAE value of 0.5 °C. To sum up all these discussions based on the constant and variable UA approaches, Table 2 is given for the error comparisons of the steady-state temperature profiles at various DHW flow rates and Table 3 displays the errors of the temperature profiles including the transient regions as well. In addition to MAE, the other metrics as MSE and RMSE are tabulated since they could be interpreted as in the same way of MAE.

Table 2. MAE, MSE, and RMSE comparisons between the variable and constant UA approaches with reference to steady-state region (between 200-500 seconds)

	Error	5 l/min		7 l/min		8,7 l/min (eco mode)	
		Var. UA	Const. UA	Var. UA	Const. UA	Var. UA	Const. UA
$T_{CH,in}$	MAE	0.697	0.749	0.466	0.524	0.769	0.766
	MSE	0.490	0.569	0.220	0.281	0.594	0.591
	RMSE	0.700	0.755	0.469	0.530	0.770	0.769
$T_{CH,out}$	MAE	0.426	0.373	1.030	0.972	0.731	0.734
	MSE	0.184	0.150	1.064	0.955	0.536	0.542
	RMSE	0.428	0.387	1.032	0.977	0.732	0.736
ΔT_{DHW}	MAE	0.403	0.405	0.435	0.435	0.372	0.377
	MSE	0.164	0.166	0.193	0.191	0.139	0.143
	RMSE	0.405	0.407	0.439	0.437	0.373	0.378

Table 3. MAE, MSE, and RMSE comparisons between the variable and constant UA approaches including the transient and steady-state region (0-500 seconds)

	Error	5 l/min		7 l/min		8,7 l/min (eco mode)	
		Var. UA	Const. UA	Var. UA	Const. UA	Var. UA	Const. UA
$T_{CH,in}$	MAE	0.928	1.224	1.215	0.492	0.774	1.051
	MSE	1.156	3.046	4.074	0.281	0.715	2.307
	RMSE	1.075	1.745	2.019	0.530	0.846	1.519
$T_{CH,out}$	MAE	0.771	1.630	1.019	1.345	1.279	2.039
	MSE	1.543	11.722	1.246	2.609	2.982	10.178
	RMSE	1.242	3.424	1.116	1.615	1.727	3.190
ΔT_{DHW}	MAE	0.464	0.464	0.814	0.818	0.528	0.536
	MSE	0.249	0.250	1.840	1.853	0.366	0.355
	RMSE	0.499	0.500	1.356	1.361	0.605	0.596

Validation of the Comfort Mode Operation

All these discussions are made with respect to the eco mode simulations. Up to now, it could be stated that constant UA approach would be utilized achieving a good agreement with the experimental data. Hence, for the comfort mode model validation, constant UA approach could be used. The available data in the literature includes the experimental DHW inlet and outlet temperature difference accompanied by the 1D modelling results (Atmaca et al., 2015). Making use of these data, TRNSYS model is validated both numerically and experimentally under constant UA approach in the

comfort mode. When the DHW user demand is created in comfort mode, the appliance cannot start ignition directly since there is hot CH water in the system already. This late ignition time could be caught from the power profile given in Figure 12 as well. During this late ignition time, the DHW is heated by the heat retention of the HC preventing excessive temperature increase of the DHW which is also an uncomfortable case for the users resulting in scalding.

Hence there are two important respects to be inserted into the model appropriately regarding the comfort mode simulations as the variation of the UA profile during the late ignition time and the variation of the load profile when the ignition starts. The upper peaks in Figure 12 are arisen from the heat retention effects although ignition does not start directly and the lower peaks are observed subsequently since the system starts cooling during the late ignition time. There is no load profile introduced into the model during the late ignition time since the HC is assumed to provide the CH water at 60°C of outlet temperature due to its stored heat at the time of preheat cycles exemplified in Figure 3. As of the UA profile, the same assumption for the CH water outlet temperature from the HC which is 60°C is used. Since the DHW inlet and outlet temperatures of the PHE are measured experimentally at 8,7 l/min DHW user request, the CH inlet temperature of the HC could be obtained with the CH water outlet temperature assumption. Hence, UA profile during the late ignition time could be calculated and inserted into the model to evaluate the transient profile of the DHW temperature difference between the inlet and outlet of the PHE. By the way, the UA profile after the late ignition time is inserted into the model as a constant value defined for the DHW user request of the same flow rate in eco mode since the applicability of the constant UA approach is shown in the previous section.

Definition of the CH water outlet temperature at 60°C during the late ignition time due to the stored heat at the time of preheat cycles is a reasonable assumption as exemplified in Figure 3. Moreover, the assumed CH outlet temperature of 60°C is also supported from the temperature limitations stated by the literature studies. The DHW temperature limit is 60°C in order to produce a mixed fluid with the cold tap water not exceeding 48°C. Although there is an upper limit to prevent scalding for the DHW temperature, there is another problem bringing a lower limit as the colonization of bacteria, *Legionella*. The temperature of the water in the system should be above 60°C in order to reduce the risk of the bacteria (Boait et al., 2012). That's why, UA profiles and load profiles of 8,7 l/min DHW user request are given separately for the eco and comfort modes in Figure 6 and Figure 7, respectively.
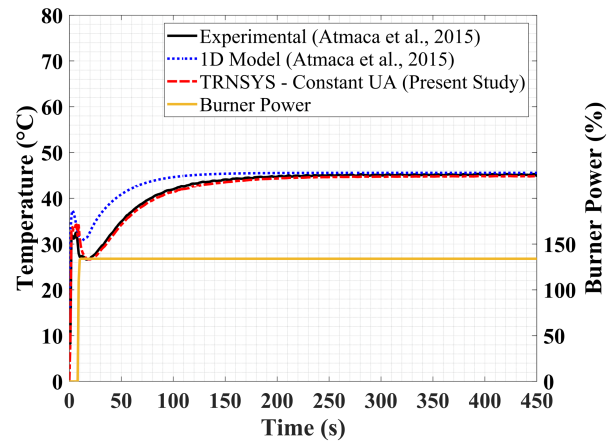

Figure 12. Validation of the comfort mode operation for 8.7 l/min user demand

After the late ignition time of 9 seconds, the appliance starts working and the power profile is recorded which is constant for the DHW user demand of 8,7 l/min. Heat transfer rate to the DHW is calculated from the flow rate of the DHW and DHW inlet and outlet temperature difference of the PHE. Hence the load profile after the late ignition time could be obtained in the comfort mode as the difference between the burner power and heat transfer rate of the DHW. The comfort mode load profile of 8,7 l/min DHW user request after the late ignition time has similar trend to the load profile of the same DHW flow rate in the eco mode, but the load profile of the comfort mode is smaller than that of the eco mode since the system components are still hot in the transient region.

In Figure 12, 1D modelling comfort mode calculations of Atmaca et al. (2015) as well are displayed in addition to the experimental data. For the steady-state region MAE values of the TRNSYS are decreased when compared to that of the 1D model. Generally speaking, the predictions of the both models yield a good agreement with the experimental data for the steady-state region. The greatest achievement of the model is the decrease of MAE value from 1.7°C of 1D model to 0.5°C of TRNSYS model for the temperature profile covering the transient region as well. As it is seen also from Figure 12, TRNSYS model predicts the lower and upper peaks of the DHW inlet and outlet temperature difference profile with a considerably small error when compared to the results obtained from the 1D model. The estimations regarding these peaks are of vital importance to the Waiting Time Test of the combi boiler comfort tests declared by the standards (BS EN 13203-1:2006, 2006). The reason for the better agreement of the TRNSYS modelling results is the experimental load profile inserted into the HC model in comparison with the 1D model. With the extension of a such model with various load profiles covering various operating conditions, a preliminary laboratory testing simulation tool could be proposed.

CONCLUSIONS

This study is a part of an ongoing research focusing on the DHW heating circuit models of the combi boilers. Previously 1D model has been established and validated experimentally. A commercial software has been used to model the DHW heating circuit as well and the applicability of such kind of modelling tool has been discussed. It is concluded that 1D model needs improvement since the discrepancy between the calculated results and the experimental data is to be diminished in the transient region although the agreement of the numerical results with the experimental data is found satisfactory for the steady-state region. Lastly, a TRNSYS model has been constructed for the same DHW circuit with the implementation of the variable load profile of the HC and the variable UA profile of the PHE based on the experimental measurements for various operating conditions of eco working mode. The outcomes from the TRNSYS model are categorized into three sections. Firstly, experimental validation of the TRNSYS model has been made for the eco working mode simulations. Secondly, the TRNSYS model has been validated numerically as well by solving 1D modelling equations of the HC and the PHE. MEA, MSE, and RMSE values of the TRNSYS model and 1D model have been compared with respect to the experimental data for all eco mode simulations. It has been apparently proved that TRNSYS model improves the error values especially for the transient region due to the insertion of the experimental UA variation and the load profiles.

In this study, the main objective is to improve the TRNSYS model decreasing its dependency on the experimental data. Therefore, the UA parameter definition of the PHE is investigated. Unlike the aforementioned TRNSYS model, this modified model uses constant UA approach instead of the variable UA profile. All results obtained under the variable UA approach are compared with the results of the constant UA assumption. The MAE values of the DHW inlet and outlet temperature difference, which is the most critical output of the model, are nearly the same under variable and constant UA approaches with respect to the experimental data for both steady-state temperature distribution and the overall temperature profile covering the transient region as well. MAE values for the same temperature difference profile including the overall time region are 0.46°C, 0.82°C, and 0.53°C for 5 l/min, 7 l/min, and 8,7 l/min, respectively, for the eco mode simulations under both of the UA approaches. Some of the MAE values for the intermediate temperature values such as CH water inlet and outlet temperatures increase under constant UA approach, but the error stays still within the acceptable error range. As a result, it is concluded that the constant UA approach could be used in the parameter definition of the PHE thereby decreasing the reliance of the TRNSYS model on the experimental data. For some of the simulations to test new designs, it is customary to have limited experimental data. Hence, the applicability of the model could be increased while decreasing the dependence of the parameter definitions

on the experimental data. Actually, the selection of these approaches as constant or variable is a critical determination for some the TRNSYS components affecting the final outcomes, i.e. Type 140 – Constant UA and Type 141 – Varying UA.

Lastly, making use of the constant UA approach, the comfort mode validation is completed. The results of DHW inlet and outlet temperature difference obtained from TRNSYS and the previously established 1D model are compared as well with respect to experimental data. The upper and lower peaks in the transient DHW inlet and outlet temperature difference profile of the comfort mode are estimated better with the TRNSYS model. The superiority of the TRNSYS model is more obvious when the MAE values are compared with that of 1D model in the comfort mode validation. MAE value calculated for the DHW inlet and outlet temperature difference in comfort mode operating scheme decreases from 1.7 °C to 0.5 °C with the TRNSYS model. Definition of the UA profile during the late ignition time is made based on the heat retention of the HC. The better agreement of the TRNSYS model with the experimental data is due to the experimental parameter definition. With the implementation of the constant UA approach in the PHE, the reliance of the model on the experimental data is decreased, but the load profile is still inserted to the model to take the transient effects into account. To sum up, the TRNSYS model could be used for the performance estimations of the DHW circuit in both eco and comfort simulations. Therefore, the number of the testing could be decreased with the preliminary evaluations interpreted from the simulation results. As of the future targets, the load profiles could be inserted into the model for various operating conditions or it could be modelled and inserted into the model by a mathematical expression for the wide use of the DHW circuit TRNSYS models.

ACKNOWLEDGEMENT

NOMENCLATURE

ρ	Density, kg/m^3
c_p	Specific heat, J/kg·K
T	Temperature, ˚C
$\dot{m}$	Mass flow rate, kg/s
A_s	Heat transfer surface area, m^2
A_c	Flow cross-sectional area, m^2
A_o	Outer heat transfer surface area, m^2
A_{PHE}	Heat transfer area of each plate, m^2
h	Convective heat transfer coefficient, W/m^2·K
U	Overall heat transfer coefficient, W/m^2·K
l_{PHE}	Length of the PHE, m
s	HC height, m
t	Time, s
z	CH water flow length around the HC, m
k	Thermal conductivity, W/m·K

V_{chwc}	Volume of the CH water at each hot water channel of the PHE, m^3
V_{dhwc}	Volume of the DHW at each cold-water channel of the PHE, m^3
dx_1	Control volume length in x_1 direction, m
dx_2	Control volume length in x_2 direction, m
dy_1	Control volume height in y_1 direction, m
dy_2	Control volume height in y_2 direction, m
Q_{CH}	Amount of heat transferred from CH water to DHW, kJ
T_{adia}	Adiabatic flame temperature, ˚C
P	The appliance power at the steady-state operating region (without power modulation)
φ	Coefficient corresponding to the power modulation
P_{rated}	Rated power of the pump, kW
$\dot{V}$	Volume flow rate, l/min
$\dot{Q}$	Rate of heat transfer, kW
n	Total number of the measurements or calculations from a specified point
UA	Multiplication of the overall heat transfer coefficient and the heat transfer area, W/K
y	Measured or calculated parameter, i.e. temperature

Subscripts

g	Hot combustion gases
wt (1)	CH water in the HC
wt (2)	CH water in the PHE
wt (3)	DHW in the PHE
w	HC wall
wt	Water
∞	Surrounding air
comb	Combustion
pipe	Pipe in the CH circuit
in	Inlet
out	Outlet
load	Heat retention effect of the heat cell block in the CH water circuit (load definition)
initial	Initial value at simulation start
final	Final value at the simulation stop
rated	Nominal value
net	Net amount
exp	Experimental
theo	Theoretical
i	i^{th} number of the measurement or calculation
pump	Pump in the CH circuit

Abbreviations

CH	Central heating
DHW	Domestic hot water
DCW	Domestic cold water
PHE	Plate heat exchanger
HC	Heat cell
CV	Control volume
MAE	Mean absolute error
MSE	Mean square error
RMSE	Root mean square error

REFERENCES

Andrés A. C. and López J. M. C., 2002, TRNSYS model of a thermosiphon solar domestic water heater with a horizontal store and mantle heat exchanger, *Solar Energy*, 72(2), 89-98.

Antoniadis C. N. and Martinopoulos G., 2019, Optimization of a building integrated solar thermal system with seasonal storage using TRNSYS, *Renewable Energy*, 137, 56-66.

Atmaca A. U., Erek A., and Altay H. M., 2015, Investigation of Transient Behaviour of Combi Boiler Type Appliances for Domestic Hot Water, *Applied Thermal Engineering*, 82, 129-140.

Atmaca A. U., Erek, A., and Altay, H. M., 2016, Comparison of Two Numerical Approaches to the Domestic Hot Water Circuit in a Combi Boiler Appliance, *Energy and Buildings*, 127, 1043–1056.

Boait P. J., Dixon D., Fan D., and Stafford A., 2012, Production efficiency of hot water for domestic use, *Energy and Buildings*, 54, 160–168.

Bourke G. and Bansal P., 2012, New test method for gas boosters with domestic solar water heaters, *Solar Energy*, 86 (1), 78-86.

Braas H., Jordan U., Best I., Orozaliev J., and Vajen K., 2020, District heating load profiles for domestic hot water preparation with realistic simultaneity using DHWcalc and TRNSYS, *Energy*, 201, 117552.

BS EN 13203-1:2006, 2006, Gas-fired domestic appliances producing hot water- Appliances not exceeding 70 kW heat input and 300 l water storage capacity - Part 1: Assessment of performance of hot water deliveries.

Fridlyand A., Guada A. B., Kingston T., and Glanville P., 2021, Modeling modern, residential, combined space and water heating systems using EnergyPlus, *ASHRAE Transactions*, 127, 135-142.

Gök O., Atmaca A. U., Altay H. M., and Erek A., 2022, The Use of TRNSYS as a Simulation Tool for the Domestic Hot Water Performance Evaluations of the Combi Boilers, *Proceedings of the 2nd International Conference on Energy, Environment and Storage of Energy,* Kayseri, 96-97.

Gök O., Atmaca A. U., Altay H. M., and Erek A., 2023, Model of the Combi Boiler Appliance in TRNSYS for Domestic Hot Water Circuit: Experimental and Numerical Validations of Economic Mode Simulations, *International Journal of Energy Studies,* 8(1), 15-38.

Haissig C. M. and Woessner M., 2000, An adaptive fuzzy algorithm for domestic hot water temperature

control of a combi-boiler, *HVAC&R Research*, 6:2, 117-134.

Harrabi I., Hamdi M., Bessifi A., and Hazami M., 2021, Dynamic modeling of solar thermal collectors for domestic hot water production using TRNSYS, *Euro-Mediterranean Journal for Environmental Integration*, 6:21.

Ibrahim O., Fardoun F., Younes R., and Louahlia-Gualous H., 2014, Review of water-heating systems: General selection approach based on energy and environmental aspects, *Building and Environment*, 72, 259-286.

Incropera F. P., Dewitt D. P., Bergman T. L., and Lavine A. S., 2007, *Fundamentals of heat and mass transfer* (6th ed.). USA: John Wiley & Sons, Inc.

Jordan U. and Vajen K., 2001, Influence of the DHW load profile on the fractional energy savings: A case study of a solar combi-system with TRNSYS simulations, *Solar Energy*, 69, 197-208.

Klein S. A. et al, 2017, TRNSYS 18: A Transient System Simulation Program, Solar Energy Laboratory, University of Wisconsin, Madison, USA, http://sel.me.wisc.edu/trnsys.

Lu M., Zhang C., Zhang D., Wang R., Zhou Z., Zhan C., Zai X., and Jing Q., 2021, Operational optimization of district heating system based on an integrated model in TRNSYS, *Energy & Buildings*, 230, 110538.

Nordlander S. G. and Persson T. G., 2003, Evaluation and computer modelling of wood pellet stoves with liquid heat exchanger, *ISES World Conference*, Gothenburg.

Pärisch P., Van der Veer N., Kirchner M., Giovannetti F., and Lampe C., 2019, Comfort assessment of tankless water heaters: Review and Suggestions, *IEA SHC International Conference on Solar Heating and Cooling for Buildings and Industry*.

Persson T., Fiedler F., Nordlander S., Bales C., and Paavilainen J., 2009, Validation of a dynamic model for wood pellet boilers and stoves, *Applied Energy*, 86(5), 645-656.

Persson T., Wiertzema H., Win K. M., and Bales C., 2019, Modelling of dynamics and stratification effects in pellet boilers, *Renewable Energy*, 134, 769-782.

Pomianowski M. Z., Johra H., Marszal-Pomianowska A., and Zhang C., 2020, Sustainable and energy-efficient domestic hot water systems: A review, *Renewable and Sustainable Energy Reviews*, 128, 109900.

Quintã A. F., Ferreira J. A. F., Ramos A., Martins N. A. D., and Costa V. A. F., 2019, Simulation models for tankless gas water heaters, *Applied Thermal Engineering*, 148, 944–952.

Shrivastava R. L., Kumar V., and Untawale S. P., 2017, Modeling and simulation of solar water heater: A TRNSYS perspective, *Renewable and Sustainable Energy Reviews*, 67, 126–143.

Ucar M. and Arslan O., 2021, Assessment of improvement potential of a condensed combi boiler via advanced exergy analysis, *Thermal Science and Engineering Progress*, 23.

Villa-Arrieta M. and Sumper A., 2018, A model for an economic evaluation of energy systems using TRNSYS, *Applied Energy*, 215, 765–777.

ANALYTICAL STUDY OF HEMISPHERICAL ICE SUBLIMATION IN ENCLOSURES WITH HUMIDITY AND FORCED CONVECTION

Mehmet Anil GULSAN*, Sedat TOKGOZ**, Seyhan UYGUR ONBASIOGLU***
*Department of Mechanical Engineering, Istanbul Technical University
34437 Gumussuyu, Istanbul, Turkey
anilgulsan@gmail.com, ORCID: 0000-0003-4667-6041
**Department of Aeronautical Engineering, Gebze Technical University
Istanbul, Turkey
sedattokgoz@gtu.edu.tr, ORCID: 0000-0002-0836-2861
***Department of Mechanical Engineering, Istanbul Technical University
34437 Gumussuyu, Istanbul, Turkey
onbasiogl1@itu.edu.tr, ORCID: 0000-0002-8386-2647

Abstract: In real life, sublimation of ice under certain conditions results in non-uniform formation of ice cubes with irregular shapes. During extracting these irregularly shaped cubes from enclosed spaces, the openings through which the cubes move can be plugged. A deep analysis of the sublimation process should be applied to make the shape of the ice cubes homogeneous and smooth-edged. Although there is an analytical method for the sublimation of spherical ice in literature, the hemispherical shape has not been studied. Furthermore, if ice formation and sublimation occur simultaneously within a place confined by a wall, novel approaches are necessary. In the current study, an analytical method has been proposed for the sublimation from a hemispherical ice sample as a combination of the models for the spherical and circular flat surfaces. The sublimation rate calculated by this new analytical method has been compared to the results from the weighing experiments and visualizations where the sublimation over time was measured by processing a series of images of ice cubes. There is a good agreement between the calculated values and the mass loss observed in the visualized images and the weighted samples. Thus, it is concluded that the sublimation rate is correlated with the velocity, temperature, and relative humidity of the air flowing over the ice cubes undergoing sublimation.
Keywords: Sublimation, visualization, transient mass transfer, ice

NEMLİ VE ZORLANMIŞ TAŞINIMLI KAPALI HACİMLERDE YARIKÜRESEL BUZ SÜBLİMASYONUNUN ANALİTİK İNCELENMESİ

Özet: Gerçek hayatta, buzun belirli koşullar altında süblimleşmesi, düzensiz şekilli buz küplerinin oluşumuyla sonuçlanır. Düzensiz şekilli bu küplerin kapalı alanlardan çıkarılması sırasında küplerin hareket ettiği açıklıklar tıkanabilir. Buz küplerinin şeklinin homojen ve düzgün kenarlı olması için süblimasyon prosesinin derinlemesine analizi gerçekleştirilmelidir. Literatürde küresel buzun süblimleşmesine yönelik analitik bir yöntem bulunmasına rağmen yarım küre şekli çalışılmamıştır. Ayrıca, duvarla sınırlandırılmış bir hacimde buz oluşumu ve süblimleşme aynı anda meydana geliyorsa, yeni yaklaşımlar gereklidir. Bu çalışmada, küresel ve dairesel düz yüzey modellerinin bir kombinasyonu olarak yarım küre şeklindeki bir buz örneğinden süblimleşme için analitik bir yöntem önerilmiştir. Bu yeni analitik yöntemle hesaplanan süblimleşme miktarı, süblimleşmenin bir dizi buz küpü görüntüsünün işlenmesiyle elde edildiği görselleştirme deneyleri ve tartım yapılarak elde edilen sonuçlarla karşılaştırıldı. Hesaplanan değerler ile görselleştirme sonuçlarında ve tartım yapılmış numunelerde gözlemlenen kütle kaybı arasında iyi bir uyum vardır. Elde edilen sonuçlara göre süblimleşme miktarının, süblimleşmeye uğrayan buz küplerinin üzerinden akan havanın hızı, sıcaklığı ve bağıl nemi ile ilişkili olduğu sonucuna varılmıştır.
Anahtar Kelimeler: Süblimleşme, görselleştirme, zamana bağlı kütle transferi, buz

NOMENCLATURE

A	equation coefficient [-]	A_s	surface area of circular flat surface [m^2]
		B	equation coefficient [-]
		D	diameter of sphere [m]

D_{AB} diffusion coefficient of water vapor (A) in air (B) [m^2/s]

g gravity [m/s^2]

Gr Grashof number for heat transfer [-]

Gr_m Grashof number for mass transfer [-]

h convection heat transfer coefficient [W/m^2K]

h_m convection mass transfer coefficient [m/s]

K equation coefficient [-]

k thermal conductivity of air [kW/mK]

L characteristic length [m]

L_s latent heat of sublimation [kJ/kg]

M molecular weight of water [kg/kmol]

m mass of water ice sample [kg]

n equation coefficient [-]

Nu_s Nusselt number of spherical surface [-]

Nu_f Nusselt number of circular flat surface [-]

P perimeter length of flat surface [m]

p equation coefficient [-]

P_s saturation pressure [kPa]

Pr Prandtl number [-]

r radius of sphere [m]

R_u universal gas constant [kJ/kmolK]

Ra Rayleigh number for heat transfer [-]

Ra_m Rayleigh number for mass transfer [-]

Re Reynolds number [-]

Sc_s Schmidt number of spherical surface [-]

Sc_f Schmidt number of circular flat surface [-]

Sh Sherwood number [-]

T absolute temperature [K]

T_∞ ambient temperature [K]

T_f film temperature [K]

T_r surface temperature of the sphere [K]

T_w wall temperature of the circular flat surface [K]

Greek Symbols

α equation coefficient [-]

β equation coefficient [-]

ν kinematic viscosity of air [m^2/s]

ρ average density of water vapor [kg/m^3]

ρ_∞ density of water vapor in the remote environment [kg/m^3]

ρ_r density of water vapor in the immediate vicinity of the sphere [kg/m^3]

ρ_s saturation density of vapor [kg/m^3]

ρ_w density of water vapor in the immediate vicinity of the circular flat surface [kg/m^3]

φ relative humidity [-]

INTRODUCTION

Not only for the snow analysis in meteorology, but also in novel refrigeration systems and cryogenics, sublimation is an important topic (Chen et al., 2014; Schmidt, 1972; Schmidt and Gluns, 1992). The findings in this area may be applied to the dissolution of solids, for instance for controlling the smoothness of surfaces during synthesis or for optimizing crystalline shapes during drug dissolution (Jambon-Puillet et al., 2018). As it is summarized in Zhao et al. (2020), theoretical studies on the sublimation process itself are rare, in contrary to being the fundamental phenomenon in de-icing and defrosting processes, food preservation, and porous media fabrication. In literature, investigations on naphthalene, solid carbon dioxide, benzoic acid (Aoki et al., 2002; Garner and Grafton, 1954; Hong and Song, 2007; Smolik and Vitovec, 1983), ice (Neumann et al., 2009; Schmidt, 1972; Schmidt and Gluns, 1992; Thorpe and Mason, 1966), and subcooled water droplets (Reitzle et al., 2019; Ruberto et al., 2017) are present. However, there is a lack of study on the sublimation during ice formation in domestic refrigerators.

In the current study, the sublimation rate of ice in an enclosed space under forced air flow conditions is visualized by an image processing method and also calculated from weighing experiments. Thus; the parameters of the sublimation rate are studied and a basic approach has been handled to understand the irregularities on the surfaces of the ice cubes resulting in plugging within the passages of the refrigerator. Since hemispherical ice samples are geometrically similar to the ice cubes formed in refrigerators, these shapes have been used as the domain geometry. As stated in Jambon-Puillet et al. (2018) sublimation from hemispherical shapes usually takes longer compared to other types of geometry and both weighing experiments and visualization processes depend on several parameters. Here, in addition to the ones reported in the literature, the temperature difference between the ice sample surface and the enclosure has been taken into account, as well as the humidity of the air within the enclosure. Moreover, the effect of the extreme temperature difference between the ice sample surface and enclosure on the sublimation rate is investigated with an analytical model for a variety of φ levels as a special case. Then the heat and mass transfer have been correlated to the velocity of the air over the ice samples, and the enclosure temperature. The results have been extended to predict ice plugging in a variety of conditions before it occurs and prevent it without any malfunctions.

ANALYTICAL METHOD FOR THE HEMISPHERE

Most of the analytical sublimation models study ice crystals, snow, and snowflakes in cold regions. They investigate sublimation rates on different geometries, especially on spherical and flat geometries. However, there is no sublimation model for the hemispherical geometry, presented in literature. A model developed for the sublimation of the spherical samples is not convenient with a hemispherical sample. In order to develop the model fully, the spherical and the flat surfaces should be investigated, separately.

In the present study, the model proposed for spherical bodies in literature Thorpe and Mason (1966) has been modified for the hemispherical geometry. By this modification, the model for the spherical surface of the hemisphere has been combined with the model for the
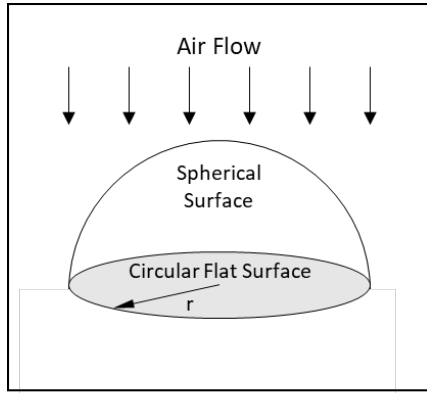

Figure 1. Hemispherical sublimation model.

The modified analytical model has been based on the spherical geometry studied by Thorpe and Mason (1966) where the temperature differences between the ice surface and environment were neglected. They used the diffusivity value (between water and air at 0°C) 7% lower than the reference value, which is 0.22 x 10^{-4} m²/s.

However, in the current study, air temperature in the test section has an oscillation within ±3°C of the reference value. This difference is considered in the modification. On the other hand, the reference diffusivity value was taken as the same with Thorpe and Mason (1966) to keep the test-validated method as possible. The transient heat and mass transfer equations (Eq. 1 and Eq. 2) have been combined with the Clausius-Clapeyron equation (Eq. 3) as in Thorpe and Mason (1966). Finally, a model for the hemispherical surface (Eq. 12), also including temperature differences between the ice surface and the ambient, is formed. Then total sublimation rate was calculated, summing up the sublimation rate for the hemisphere and the circular flat surface (Eq. 23).

Equations for the sublimation rate in terms of heat transfer, and mass transfer given in Thorpe and Mason (1966) are as the followings

$$L_s \frac{dm}{dt} = 2\pi k r (T_r - T_\infty) Nu_s \tag{1}$$

$$\frac{dm}{dt} = 2\pi D_{AB} r (\rho_\infty - \rho_r) Sh_s \tag{2}$$

where Nu_s and Sh_s defined in Eq. (15a) and Eq. (15b).

On the other hand, the Clausius-Clapeyron equation with an ideal gas approximation is:

$$\frac{d\rho_s}{\rho_s} = \left(\frac{L_s M}{R_u T^2}\right) dT - \frac{dT}{T} \tag{3}$$

flat surface. This modification has also considered that the circular flat surface of the hemisphere is not directly exposed to the freestream but it is located in the wake region facing the downstream (Figure 1).

where boundary conditions are

$$T = T_\infty \ \rightarrow \ \rho_s = \rho_s(T_\infty) \tag{4}$$

$$T = T_r \ \rightarrow \ \rho_s = \rho_s(T_r) \tag{5}$$

Integrating Eq. (3) and applying boundary conditions (4 and 5) gives:

$$ln\left(\frac{\rho_s(T_r)}{\rho_s(T_\infty)}\frac{T_r}{T_\infty}\right) = \frac{L_s M}{R_u}\left(\frac{T_r - T_\infty}{T_\infty T_r}\right) \tag{6}$$

If water vapor density in the immediate vicinity of the ice surface is considered to be equal to the saturated vapor density at ambient temperature (i.e. $\rho_s = \rho_s(T_r)$), using Eq. (2)

$$\rho_r = \rho_s(T_r) = \rho_\infty - \frac{1}{2\pi D_{AB} r Sh_s}\frac{dm}{dt} \tag{7}$$

can be obtained.

Combining Eqs. (6) and (7) results in

$$ln\left[\left(\frac{\rho_\infty}{\rho_s(T_\infty)} - \frac{1}{2\pi D_{AB} r Sh_s \rho_s(T_\infty)}\frac{dm}{dt}\right)\frac{T_r}{T_\infty}\right]$$
$$= \frac{L_s M}{R_u}\left(\frac{T_r - T_\infty}{T_\infty T_r}\right) \tag{8}$$

Here, $\rho_\infty/\rho_s(T_\infty)$ is equal to φ, at ambient temperature T_∞. Thus;

$$\left(\varphi - \frac{1}{2\pi D_{AB} r Sh_s \rho_s(T_\infty)}\frac{dm}{dt}\right)\frac{T_r}{T_\infty} = e^{\frac{L_s M}{R_u}\left(\frac{T_r - T_\infty}{T_\infty T_r}\right)} \tag{9}$$

is obtained.

If a series expansion is performed for the right-hand side of the above equation:

$$\left(\varphi - \frac{1}{2\pi D_{AB} r Sh_s \rho_s(T_\infty)}\frac{dm}{dt}\right)\frac{T_r}{T_\infty} = 1 + \frac{L_s M}{R_u}\left(\frac{T_r - T_\infty}{T_\infty T_r}\right) +$$
$$\frac{1}{2}\left(\frac{L_s M}{R_u}\right)^2\left(\frac{T_r - T_\infty}{T_\infty T_r}\right)^2 + \cdots \tag{10}$$

Since the third and the following terms can be considered as a truncation error because of their relatively small values,

$$\left(\varphi - \frac{1}{2\pi D_{AB} r Sh_s \rho_s(T_\infty)}\frac{dm}{dt}\right)\frac{T_r}{T_\infty} = 1 + \frac{L_s M}{R_u}\left(\frac{T_r - T_\infty}{T_\infty T_r}\right) \tag{11}$$

is obtained.

Combining Eq. (1) and Eq. (11) and rearranging and dividing by 2, the sublimation rate for the hemispherical surface can be calculated:

$$\frac{dm}{dt} = \frac{\pi r\left(\varphi - \frac{T_\infty}{T_r}\right)}{\left(\frac{1}{D_{AB}Sh_s\rho_s(T_\infty)}\right) + \left(\frac{L_s^2 M}{R_u k Nu_s T_r^2}\right)} \quad (12)$$

Nu_s and Sh_s appearing in Eq. (12) have been calculated by substituting the experimental mass change into Equations (1) and (2). Mass transfer due to natural convection from the lower surface of the hemisphere has been calculated from the relevant correlations and subtracted from the total mass measured during the experiments. Sherwood numbers from the experimental data for the hemisphere under study have been compared to the correlations reported in the literature (Figure 2).
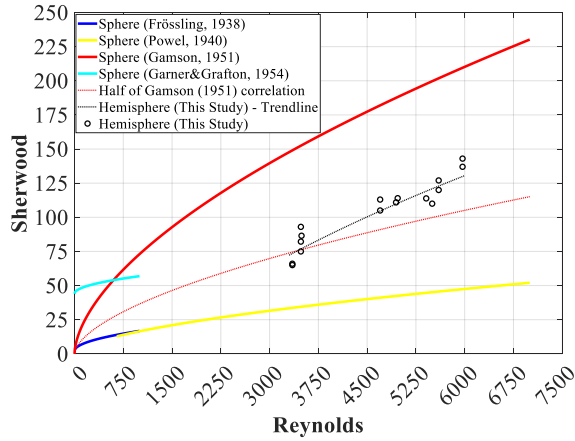
Figure 2. Comparison of the Sherwood correlation for the hemisphere with the Sh correlations for the sphere in the literature.

It is seen that Sherwood numbers from the current experimental results coincide with the half of the correlation for spherical surfaces by Gamson (1951). The maximum variation is 24.2% at Reynolds 6000 between the trendline of experimental results and the half of the Gamson (1951) correlation.

On the other hand; the wind factor curve was generated using weighing results as in previous studies (Pasternak and Gauvin, 1960; Pitter et al., 1974; Thorpe and Mason, 1966). For spherical bodies, the correlations below have been used:

$$Nu_s = B + \beta Re^n Pr^p \quad (13)$$

$$Sh_s = A + \alpha Re^n Sc^p \quad (14)$$

where Reynolds number is based on the diameter (Garner and Grafton, 1954; Pitter et al., 1974; Thorpe and Mason, 1966).

For the coefficients appearing in correlations, there are different values in the literature. For the quiescent environment (Re = 0), A = B = 2 is proposed by Langmuir (1918) and validated by Frossling (1938) and Ranz and Marshall (1952). For low Reynolds number cases (10<Re < 200), A = B = 1.88 is obtained by Thorpe and Mason (1966).

In the presented study, the range is as 3300<Re<6000. Thus, the wind factor, F values in Pasternak and Gauvin (1960), Pitter et al. (1974), Thorpe and Mason (1966) have been used to determine A, B, α, and β coefficients of Nu_s and Sh_s correlations.

In Powell (1940) for 650≤Re≤45000, also in Pasternak and Gauvin (1960) for 500 < Re < 5000, and in Gamson (1951) without regarding to the Reynolds number, it is given as p=1/3 and n=0.5. Considering p and n independent of geometric shapes, and the moderate range of the Reynolds numbers in the current study, p=1/3 and n=0.5 are assumed. Thus, the following equations in terms of wind factor are obtained (Figure 3).

$$Nu_s = 3.432 Re^{1/2} Pr^{1/3} - 94.942$$
$$3300<Re<6000 \quad (15a)$$

$$Sh_s = 3.432 Re^{1/2} Sc^{1/3} - 94.942$$
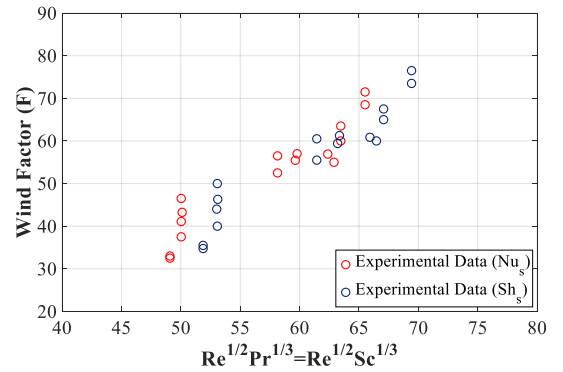$$3300<Re<6000 \quad (15b)$$

Figure 3. Investigation of heat and mass transfer correlations as a single equation by using wind factor.

Eq. (15b) is identical to the correlation $Sh=0.85Re^{0.59}Sc^{0.33}$ which is validated by the experimental data illustrated in Figure 2. The discrepancy between the resulted correlation, and the one obtained as the half of Gamson's has emerged due to the uncertainty of the experiments. The natural convection from the flat surface of the hemisphere may be another reason for this difference.

The sublimation rate from the flat surface can be written in terms of the Nusselt number, and Sherwood number (Goldstein et al.,1973; Incropera, 2011; Lloyd and Moran, 1974):

$$L_s \frac{dm}{dt} = (T_w - T_\infty)\frac{4Nu_f k}{D}\frac{\pi.D^2}{4} = 2\pi r k Nu_f (T_w - T_\infty)$$

$$\frac{dm}{dt} = (\rho_\infty - \rho_w) \frac{4Sh_f D_{AB}}{D} \frac{\pi . D^2}{4}$$
$$= 2\pi r D_{AB} Sh_f (\rho_\infty - \rho_w)$$

(16)

(17)

With Clausius Clapeyron equation (Eq. 3) and ideal gas equation of state, the sublimation rate from the circular flat surface (Figure 1) is obtained as:

$$\frac{dm}{dt} = \frac{2\pi r\left(\varphi - \frac{T_\infty}{T_w}\right)}{\left(\frac{1}{D_{AB}Sh_f \rho_S(T_\infty)}\right) + \left(\frac{L_s^2 M}{R_u k Nu_f T_w^2}\right)}$$

(18)

For the flat surface, natural convection correlations (Goldstein et al., 1973; Incropera, 2011; Lloyd and Moran, 1974) have been used:

$$Nu_f = 0.54 Ra^{1/4}$$

(19)

$$Sh_f = 0.54 Ra_m^{1/4}$$

(20)

As the characteristic length, L, is equal to r/2 for the circular surface; heat and mass transfer Rayleigh numbers appearing in the equations are:

$$Ra = GrPr = \frac{g\beta|T_s - T_\infty|}{\nu^2}\frac{D^3}{64}Pr$$

(21)

$$Ra_m = Gr_m Sc = \frac{g(\rho_s - \rho_\infty)}{\rho\nu^2}\frac{D^3}{64}Sc$$

(22)

Finally, the total sublimation rate of hemispherical ice is defined as:

$$\frac{dm}{dt} = \frac{\pi r\left(\varphi - \frac{T_\infty}{T_r}\right)}{\left(\frac{1}{D_{AB}Sh_s \rho_S(T_\infty)}\right) + \left(\frac{L_s^2 M}{R_u k Nu_s T_r^2}\right)} + \frac{2\pi r\left(\varphi - \frac{T_\infty}{T_w}\right)}{\left(\frac{1}{D_{AB}Sh_f \rho_S(T_\infty)}\right) + \left(\frac{L_s^2 M}{R_u k Nu_f T_w^2}\right)}$$

(23)

where the first term represents the spherical surface of the hemisphere and the second term corresponds to the sublimation rate from the bottom flat surface.

Here, the effects of the flow separations and vortices at the wake of the hemisphere and acting on the flat bottom surface have been neglected.
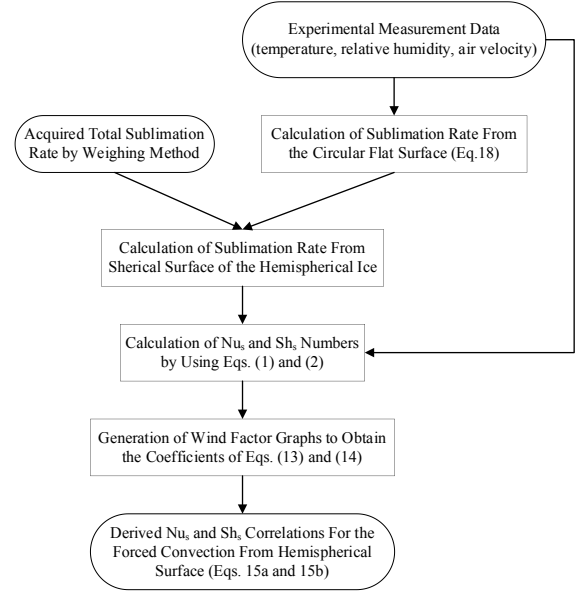

Figure 4. Flow chart for Nu_s and Sh_s correlations.

Once the required correlations were formed (Figure 4), Eq. (23) was analytically solved with a time step of 60 seconds which is the data sampling interval of the experiments. Since, it was confirmed by the recorded images of the ice sample (see the next section) that the ice shape changed homogeneously, throughout the spherical surface, the numerical procedure has not considered a varied sublimation rate.

EXPERIMENTAL SETUP

For the test rig, a wind tunnel has been installed on the refrigerator shelf within a well-insulated cabinet. The wind tunnel directs the air to flow over the hemispherical ice cube. As illustrated in Figure 5; the tunnel consists of an axial fan (A), flow straightener (B), and ice sample (C). The dimensions of the air tunnel are 90 mm x 90 mm x 300 mm. To enable optical access, tunnel walls were made up of transparent plexiglass. K-type thermocouples (T) and MSI HTG3500 relative humidity sensors (H) have been used to collect data from experiments with a data acquisition system. The thermocouples have been placed onto the tunnel entry and immediate vicinity of the flat surface of the ice sample. The flat surface temperature values have been used as identical to those of the spherical surface. In other words, the temperature distribution whole over the surfaces has been assumed as uniform. Also, φ data from the refrigerator ambient and inside of the tunnel has been measured. Both temperature and humidity data have been recorded with a sampling rate of 0.017 Hz (recording every 60 seconds). The velocity inside the tunnel has been controlled by changing the rotational speed of the DC-controlled fan.
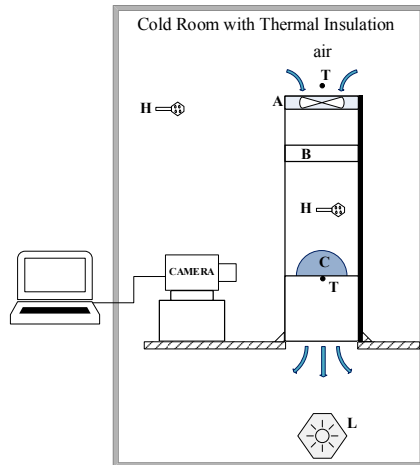
Figure 5. The experimental setup. A: Axial fan B: Flow straightener C: Ice sample H: Humidity sensors L: LED T: Thermocouples

Visualizations of the ice cubes were performed using a USB-controlled RGB camera with 15 megapixels resolution was placed at a 100 mm distance from the tunnel wall, for the image acquisition. Except for the observation window facing the camera, the walls of the tunnel were painted black in order to increase the contrast between the ice and the background of the images. A LED light (L) was used for illumination. NI Vision Builder ® software was used to periodically (1 image per hour) record the images of the hemispherical ice. An image processing algorithm in MATLAB® was developed to analyze the recorded images. The algorithm was used to determine the number of pixels forming the ice for each image and to detect the difference between successive images. Using this approach, it is possible to determine the change in the shape and the volume of the ice cube over time. In Figure 6, the purple field in the comparison image represents the change in the ice sample due to the sublimation. These results are compared to the results of weighing measurements that are discussed below.
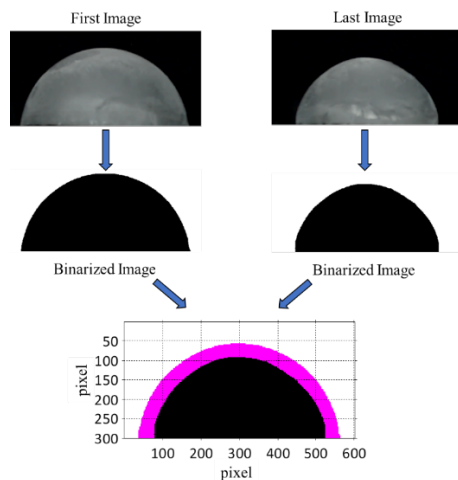

Figure 6. An example of the process of visualization for the -18°C forced convection with 1m/s air velocity case. The left image is recorded at the start of the measurements, while the image on the right is recorded after 72 hours. The difference

in the projection of the two ice cubes is indicated by purple at the bottom graph.

The average air velocity in the test section has been measured by using particle image velocimetry (PIV). A HiSense Mk II camera with a resolution of 1344 x 1024 pixels was used for recording the PIV images. The light source for illumination was a double-pulsed Nd:YAG laser (New Wave Solo-III) with 50 mJ/pulse energy at a wavelength of 532 nm. The flow was seeded with paraffin oil smoke with a mean diameter of 1.5 μm. The vector fields were calculated using an interrogation window size of 32×32pixels and 50% of overlap. An average of 100 instantaneous vector fields were used to compute the average air velocity in the test section.

Mass loss due to sublimation was detected by also weighing the ice samples with KERN DE35K0.5D digital scale having a resolution value of ±0.5 g. Weighing measurements were performed at room temperature, rapidly so as not to allow additional sublimation or melting, after taking out the ice samples from the controlled (cold) room. At the beginning of each experiment, ice samples were weighted to check the initial mass of each sample. Also, they were weighted at the end of each experiment, and sublimated mass was calculated from the difference between two consecutive weighing measurements. The weighing was not continuous throughout the measurement duration. Thus, the results of the weighing measurements include only the initial and the final mass for each sample. Residual mass is calculated from the difference between these two values at the end of the weighting process. Each experiment was repeated twice to avoid possible errors and provide consistency between the image results.

CASE CONDITIONS AND MEASUREMENTS

In addition to the parameters such as temperature, air velocity, size of ice particles, and geometrical shape used in previous studies (Neumann et al., 2009; Thorpe and Mason, 1966), also ice storage time in the refrigerator is investigated. Since the purpose is to prevent the plugging within the ice-extracting channels, duration is an important parameter.

The hemispherical ice samples that were used in this study are 50 grams each and have 30 mm of radius. The ice sublimation rates were studied at two different ambient temperatures (-18°C and -24°C), which are the set temperatures of the refrigerator. To adjust the airspeed, 3 different voltage values of the axial fan were used, which are 6V, 9V, and 12V corresponding to 0.7m/s, 1m/s, and 1.2m/s. The experiments were carried out at two different durations, 72 and 144 hours. Although the value is between 50% and 70% for the refrigerators, the φ in the cold room could not be kept constant as also stated in Reitzle et al. (2019). Thus, φ was not able to be used as a controlled parameter for the experiments, but it was acquired for using in the analytical calculations (Eq. 23).

Residual mass which is the ratio of the remaining ice mass to the initial ice mass has been calculated from the weighing measurements and observed during the visualizations. Then, this ratio has been compared to the one calculated by the analytical method (Eq. 23). It is seen that the differences between the calculations, visualizations, and analytical method developed in the current are lower than 8% (Figure 7).
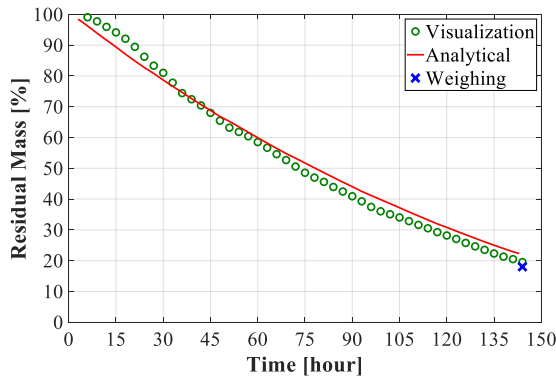

Figure 7. Ice sublimation results for -18 °C temperature; 1.2 m/s air velocity and 144 hours.

RESULTS

The effects of different parameters on the sublimation rate of hemispherical ice (Figure 8) have been measured and observed. Although the volumes of the ice cubes reduced significantly over time, the geometries mainly remained hemispherical during the

sublimation process (see Figure 6). This is further confirmed by the samples weighed at the end of each experimental campaign, where the shapes of the ice cubes were axially symmetric. This shows that the sublimation of the hemispherical ice cubes occurs homogeneously over the hemispherical surface in our experimental setup, probably due to the shape of the test rig.

The sublimation rate depends on ambient temperature and air velocity. An increase in the ambient temperature at a constant air velocity results in a higher sublimation rate. On the other hand, the almost linear characteristics of the curves in Figure 8 show that the sublimation rate does not change with time. The sublimation rate is directly proportional to the air velocity at a constant ambient temperature.

According to the experimental results; in order to decrease the ice sublimation rate, the φ in the environment should be high and the temperature of the environment and air velocity values should be low.

Error analysis of experimental measurements has been given in Figure 9. Errors between the weighing and analytical study are lower than 6%. That shows the good correlation of these two methods. The errors of visualization are relatively higher compared to the other two methods, but all of the errors are lower than 10%. Also, it should be noted that the visualization method can be developed to give more accurate results with better a camera and equipment.
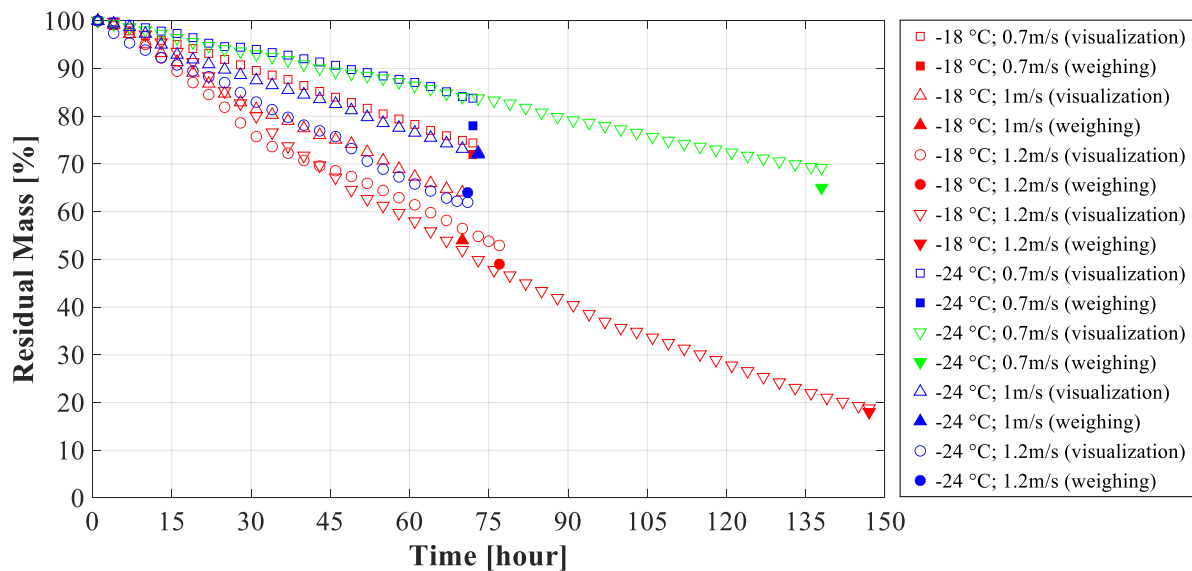

Figure 8. Change of the measured and observed residual mass with respect to time.
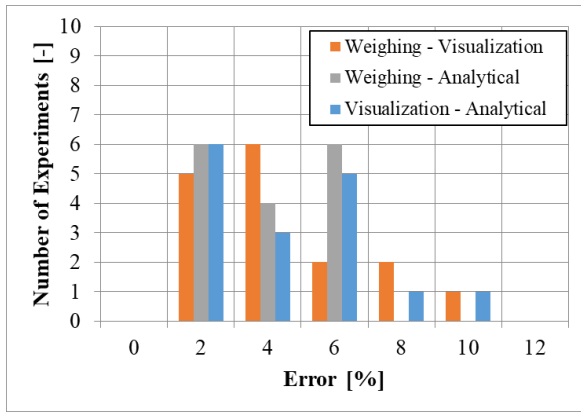
Figure 9. Error analysis of experimental measurements and analytical calculations

The theoretical sublimation amount of the hemispherical ice sample calculated using the analytical sublimation model (initially 50 grams) within one day are given in Figure 10, Figure 11, and Figure 12 for different temperature differences, relative humidities, and air velocities. The "residual mass rate" shows the residual mass of ice as a daily percentage by referencing the initial mass. As the φ decreases, residual mass changes parabolically with respect to the temperature in Figure 10. Also, if the surface temperature and the ambient temperature are identical, obviously there will be no sublimation or solidification if the air is saturated.
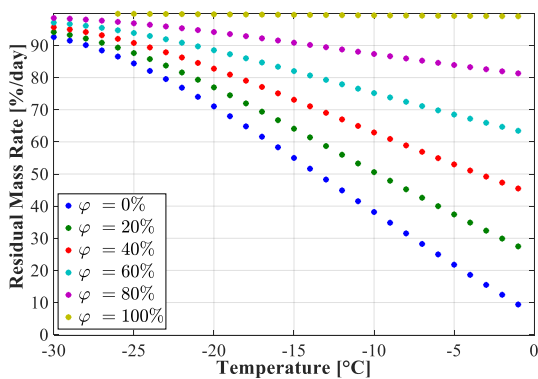

Figure 10. Residual mass rates at different temperatures and φ values for air velocity 1 m/s, and $T_r = T_w = T_\infty$ - 3 °C).

Analytical results of the sublimation model with relatively high-temperature differences between the ice sample and ambient are given in Figure 11 as a specific case. It is seen that *φ* values are less effective than the ones at 3 °C temperature difference illustrated in Figure 10.

In Figure 12, the residual mass rate for different air velocities is illustrated. The sublimation rate increases as the air velocity increases at a constant temperature. However, the amount of increment depends on temperature. For example, a residual mass difference between 0.6 m/s and 0.8 m/s air velocities is 6.2% at -10°C, while it is 2.74% at -20°C. Also, it is seen that the amount of increment is inversely proportional to the airspeed. The residual mass difference decreases from

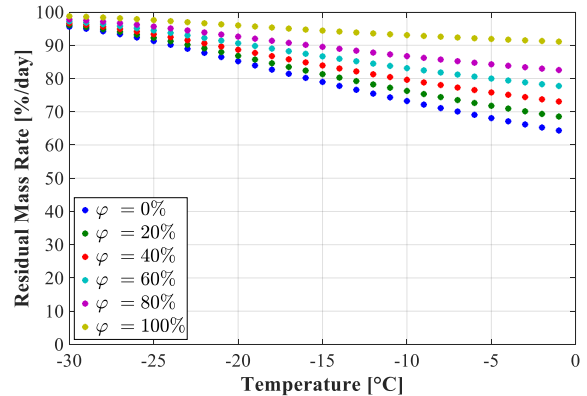6.2% (between 0.6 m/s and 0.8 m/s) to 4.22% (between 1.4 m/s and 1.6 m/s), as the velocity increases at -10°C.

Figure 11. Residual mass rates at different temperatures and φ values for air velocity 1 m/s, $T_r = T_w = T_\infty$ - 100°C.
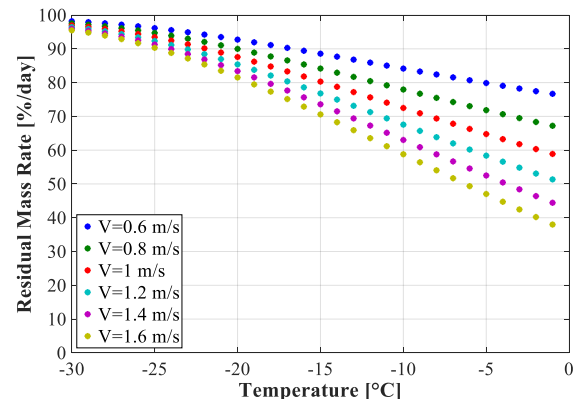

Figure 12. Residual mass rates at different temperatures and air velocity values in forced convection (*φ* =50% in the environment, $T_r = T_w = T_\infty$).

CONCLUSION

A new transient analytical model for the sublimation from a hemispherical ice sample is proposed as a combination of the models for the spherical and circular flat surfaces in this paper. The novel analytical method has been compared to two separate experimental methods, under forced convection conditions. Image processing-based visualization and weighing methods were carried out simultaneously to observe the sublimation phenomena. Experiments were performed at various temperatures, as well as different air velocities corresponding to 3300 < Re < 6000. The results of the analytical method are in good agreement with the calculated residual ice mass, via visualization and the weighted samples. The analytical model was employed to predict ice plugging depending on the sublimation rate of the ice sample under various conditions and to prevent it without undesired formations. Such an analytical method will be used to understand the irregularities on the surfaces of the hemispherical ice cubes, resulting from the parameters affecting the sublimation rate.

REFERENCES

Aoki, K., Sawada, M., & Akahori, M. (2002). Freezing due to direct contact heat transfer including sublimation. *Int. Journal of Refrigeration*, *25*(2), 235–242. https://doi.org/10.1016/s0140-7007(01)00084-6

Chen, L., & Zhang, X.-R. (2014). A review study of solid–gas sublimation flow for refrigeration: From basic mechanism to applications. *Int. J. of Ref.*, *40*, 61–83. https://doi.org/10.1016/j.ijrefrig.2013.11.015

Frossling, N. (1938). Uber die Verdunstung fallender Tropfen. *Gerlands Beitrage Geophysik*, 52:170–216.

Gamson, B.W. (1951). Heat and mass transfer fluid solid systems. *Chem. Eng. Prog. 47* (1): 19-28

Garner, F. H., & Grafton, R. W. (1954). Mass transfer in fluid flow from a solid sphere. *Proceedings of the Royal Society of London. Series A. Mathematical and Physical Sciences*, *224*(1156), 64–82. https://doi.org/10.1098/rspa.1954.0141

Goldstein, R. J., Sparrow, E. M., & Jones, D. C. (1973). Natural convection mass transfer adjacent to horizontal plates. *Int. J. of Heat and Mass Transfer*, *16*(5), 1025–1035. https://doi.org/10.1016/0017-9310(73)90041-0

Hong, K., & Song, T.-H. (2007). Development of optical naphthalene sublimation method. *Int. J. of Heat and Mass Transfer*, *50*(19-20), 3890–3898. https://doi.org/10.1016/j.ijheatmasstransfer.2007.02.017

Incropera, F. P. (2011). *Fundamentals of heat and mass transfer* (7th ed.). John Wiley.

Jambon-Puillet, E., Shahidzadeh, N., & Bonn, D. (2018). Singular sublimation of ice and snow crystals. *Nature Com.*, *9* (1). https://doi.org/10.1038/s41467-018-06689-x

Langmuir, I. (1918). The Evaporation of Small Spheres. *Physical Review*, *12*(5), 368–370. https://doi.org/10.1103/physrev.12.368

Lloyd, J. R., & Moran, W. R. (1974). Natural Convection Adjacent to Horizontal Surface of Various Planforms. *Journal of Heat Transfer*, *96*(4), 443–447. https://doi.org/10.1115/1.3450224

Neumann, T. A., Albert, M. R., Engel, C., Courville, Z., & Perron, F. (2009). Sublimation rate and the mass-transfer coefficient for snow sublimation. *Int. J. of Heat and Mass Transfer*, *52*(1-2), 309–315.

https://doi.org/10.1016/j.ijheatmasstransfer.2008.06.003

Pasternak, I. S., & Gauvin, W. H. (1960). Turbulent heat and mass transfer from stationary particles. *The Canadian Journal of Chemical Engineering*, *38*(2), 35–42. https://doi.org/10.1002/cjce.5450380202

Pitter, R. L., Pruppacher, H. R., & Hamielec, A. E. (1974). A Numerical Study of the Effect of Forced Convection on Mass Transport from a Thin Oblate Spheroid of Ice in Air. *J. of the Atmospheric Sciences*, *31*(4), 1058–1066. https://doi.org/10.1175/1520-0469(1974)031<1058:ansote>2.0.co;2

Powell, R.W. (1940). Further experiments on the evaporation of water from saturated surfaces. *Trans. Inst. Chem. Eng.* 18: 36

Ranz, W. and Marshall, W. (1952). Evaporation from drops. *Chem. Engineering Progress,* 48 (3): 141-146.

Reitzle, M., Ruberto, S., Stierle, R., Gross, J., Janzen, T., Weigand, B. (2019). Direct numerical simulation of sublimating ice particles. *Int. J. of Thermal Sciences*, 145, 105953. https://doi.org/10.1016/j.ijthermalsci.2019.05.009

Ruberto, S., Reutzsch, J., Roth, N., & Weigand, B. (2017). A systematic experimental study on the evaporation rate of supercooled water droplets at subzero temperatures and varying relative humidity. *Experiments in Fluids*, 58(5). https://doi.org/10.1007/s00348-017-2339-5

Schmidt R. and Gluns D. (1992). Sublimation of snow--the basics. *Proceedings, International Snow Science Workshop, Breckenridge, Colorado, USA* pp. 11-17

Schmidt R. A. (1972). Sublimation of wind-transported snow: a model. *U.S. Dept. of Agriculture, Forest Service, Rocky Mountain Forest and Range Experiment Station.*

Smolík, J., & Vítovec, J. (1983). Transient heat and mass transfer in the two-phase system: Subliming solid-vapour-gas mixture. *Int. J. of Heat and Mass Transfer*, 26(7), 975–980. https://doi.org/10.1016/s0017-9310(83)80122-7

Thorpe, A. D., & Mason, B. J. (1966). The evaporation of ice spheres and ice crystals. *British Journal of Applied Physics*, 17(4), 541–548. https://doi.org/10.1088/0508-3443/17/4/316

Zhao, Y., Guo, Q., Lin, T., & Cheng, P. (2020). A review of recent literature on icing phenomena: Transport mechanisms, their modulations and controls. *Int. J. of Heat and Mass Transfer*, 159, 120074. https://doi.org/10.1016/j.ijheatmasstransfer.2020.120074

EXPERIMENTAL INVESTIGATION OF THE EFFECTS OF WATER ADDITION INTO THE INTAKE AIR ON COMBUSTION PARAMETERS, ENERGY BALANCE AND DEVELOPING AN EMPIRICAL COMBUSTION DURATION RELATION IN AUTOMOBILE   DIESEL ENGINE

Mustafa TUTİ[*], **Zehra ŞAHİN**[**] and **Orhan DURGUN**[***]
[*]Karadeniz Technical University, Faculty of Marine Science, Naval Architecture and Marine Eng., Trabzon, mtuti@ktu.edu.tr, ORCID: 0000-0002-2309-3735
[**]Karadeniz Technical University, Faculty of Engineering, Mechanical Engineering Dep., Trabzon, zsahin@ktu.edu.tr, ORCID: ORCID: 0000-0002-7140-2061
[***]Avrasya University, Faculty of Engineering and Architecture, Mechanical Engineering Dep., Trabzon, odurgun@ktu.edu.tr, ORCID: 0000-0001-6381-0690

Abstract: The effect of the water addition into the intake air (WAIA) on cylinder pressure, temperature, heat release rate (HRR), combustion duration (CD), and energy balance in an automotive diesel engine have been investigated experimentally. Also, an empirical correlation has been developed for estimating CD using the HRR. This relation has been developed by applying the multiple curve fitting method, taking into account experimental results for different water ratios such as (2, 4, 6, 8, and 10) %, different engine loads, and different engine speeds such as (2000, 2500, 3000, 3500, and 4000) rpms. The test results showed that cylinder pressure values generally increased at (2000, 2500, and 3500) rpm, but they decreased at (3000 and 4000) rpm for all of the selected water ratios. Also, maximum cylinder temperature values have occurred at crank angles farther from TDC for WAIA. Cylinder temperature values mostly decreased at (2000, 2500, and 3000) rpms, but they generally increased at (3500 and 4000) rpms for WAIA. Also, maximum cylinder temperature values were occurred at crank angles farther from TDC for WAIA. HRR values generally decreased at (2000, 2500, 3500, and 4000) rpms, but they generally increased at 3000 rpm. It has been determined that the CDs were generally shortened at all of the engine speeds under full loads with water addition. CD values for NDF and (2.42, 4.22, 5.95, 8.32, 9.46) % water ratios have been determined as (13.10, 12.96, 12.93, 12.68, 12.95, and 13.576) °CA, respectively, at 2000 rpm. The effective power values according to the chemical energy of the fuel generally decrease with WAIA at 2000 rpm. However, the effective power values according to the chemical energy of the fuel increase for high WRs at 4000 rpm.

Keywords: Diesel engines, Water addition into the intake air, Heat release rate, Combustion duration, Energy balance

BİR OTOMOBİL DİZEL MOTORUNDA EMME HAVASINA SU EKLENMESİNİN YANMA PARAMETRELERİ VE ENERJİ DENGESİ ÜZERİNDEKİ ETKİLERİNİN DENEYSEL İNCELENMESİ VE YANMA SÜRESİ İÇİN AMPİRİK BAĞINTI GELİŞTİRME

Özet: Sunulan çalışmada; bir otomobil dizel motorunda emme havasına su eklenmesinin (EHSE) silindir basıncı, silindir sıcaklığı, açığa çıkan ısı oranı değerleri, enerji dengesi ve yanma süresi üzerindeki etkileri deneysel olarak incelenmiştir. Ayrıca, açığa çıkan ısı oranı eğrilerinden hesaplanan yanma süreleri için çoklu eğri uydurma yöntemi kullanılarak ampirik bir bağıntı geliştirilmiştir. Bu bağıntı geliştirilirken, farklı yükler altında (2000, 2500, 3000, 3500 ve 4000) d/d devir sayılarında ve % (2, 4, 6, 8, ve 10) su oranlarında yapılan deneysel veriler kullanılmıştır. Yapılan çalışma sonunda, EHSE'nin silindir basınçlarını (2000, 2500 ve 3500) d/d devir sayılarında artırdığı ve (3000 ve 4000) d/d devir sayılarında azalttığı ve maksimum basınçların üst ölü noktaya (ÜÖN'ye) daha yakın krank mili açılarında (KMA) oluştuğu belirlenmiştir. EHSE'nin silindir sıcaklıklarını (2000, 2500 ve 3000) d/d devir sayılarında azalttığı ve (3500 ve 4000) d/d devir sayılarında arttırdığı ve maksimum sıcaklıkların ÜÖN'ye daha yakın krank mili açılarında oluştuğu görülmüştür. EHSE ile açığa çıkan ısı oranı değerleri (2000, 2500, 3500 ve 4000) d/d sayılarında azalmış, ancak 3000 d/d devir sayısında artmıştır. EHSE ile, yanma süresi tam yük altında seçilen tüm çalışma koşullarında genel olarak azalmıştır. Örneğin 2000 d/d devir sayısında, saf dizel yakıtı ve % (2.42, 4.22, 5.95, 8.32, 9.46) su oranlarında yanma süreleri (13.10, 12.96, 12.93, 12.68, 12.95, and 13.576) KMA şeklinde hesaplanmıştır.

EHSE ile, motorda harcanan yakıtın kimyasal enerjisine göre değerlendirme yapıldığında efektif gücün 2000 d/d devir sayısında genellikle azaldığı ancak 4000 d/d devir sayısında arttığı belirlenmiştir.

Anahtar kelimeler: Dizel motorları, Emme havasına su eklenmesi, Açığa çıkan ısı oranı, Yanma süresi, Enerji dengesi

NOMENCLATURE

CA	Crank angle
HRR	Heat release rate [J/deg.]
n	Engine speed [rpm]
NDF	Neat diesel fuel
TDC	Top dead center
T_b	Brake torque
WAIA	Water addition into the intake air
WR	Water ratio
CD	Combustion duration [°CA]

INTRODUCTION

Diesel engines, known as the most efficient thermal machines, face two kinds of challenges: the crisis of petroleum and the increasingly stringent emission regulations (Gzahal, 2009). For this reason, scientists and engine manufacturers work intensively on structural and alternative fuel developments related to diesel engines to minimize these undesired effects. Clean combustion strategies, high-pressure fuel injection systems such as common-rail, the new developments in valve and control systems, and, turbocharging etc., can be listed as some examples of these structural studies. The use of different alternative fuels to replace fossil fuels in diesel engines can be given as examples of alternative fuel developments. Biodiesel and bioethanol are among the most studied alternative fuels in this context (Maawa et al., 2020; Han et al., 2020). In addition, water adding method in diesel engines has gained importance in recent years as the use of water significantly reduces NO_x, which is the most crucial pollutant of diesel combustion (Subramanian, 2011; Şahin et al., 2018; Tauzia et al., 2010). As well known from relevant literature; water use allows for controlling combustion temperature, which affects NO_x production (Gzahal, 2009).

Since the 1950s, many different studies have been carried out on the addition of water in diesel engines (Mahmood et al., 2019). Nowadays, the number of studies on the addition of water in diesel engines has increased due to the rising environmental pollution and depletion of crude oil resources. It can be seen from the literature review that, although many different techniques for water adding have been used in diesel engines, generally, three methods were applied. These methods can be classified as (a) water/diesel emulsion, (b) water injection directly into the cylinder (DWI) using a separate injector, and (c) water addition/injection into the intake air (WAIA) (Maawa et al., 2000; Şahin et al., 2018; Shojoei et al., 2019; Ayhan and Ece, 2020).

(a) Water/diesel emulsion method is applied by blending and homogenizing diesel fuel and water (here, a suitable surfactant is generally added to this mixture). This water/surfactant/diesel fuel mixture is injected into the cylinder using the conventional injection system at the end of the compression stroke. This technique requires almost no modification to the engine. Zhu et al. (2019) summarized the disadvantages of this method as follows: (1) One of the main disadvantages of this method is the limitation of the amount of using water that can be added to fuel. (2) An excess of water may be injected into the cylinder either too early or too late in the combustion process in this method, which results in the cooling of the entire cylinder and lead to increased ignition delay, engine noise, and retarded combustion. (3) This method may cause problems at low loads, for example, at the initial operating conditions of the diesel engine. These disadvantages may limit the use of water/diesel emulsion technique in vehicle diesel engines. However, there are many studies in the literature applying this method (Gowrishankar et al., 2020; Jhalani et al., 2019; El Shenawy et al., 2019). Besides these studies, water emulsification has also been applied with different alternative fuels (Maawa et al., 2020; Khanjani and Soboti, 2021; Elsanusi et al., 2017) in recent years. For example, when biodiesel is used in diesel engines, it increases NO_x emissions compared to diesel fuel because biodiesel contains oxygen. For this reason, it is desired to prevent the increase of NO_x emissions by applying biodiesel/diesel fuel blends with water emulsion recently (Maawa et al., 2020; Elsanusi et al., 2017). Maawa et al. (2020) carried out an experimental study by using conventional diesel fuel, blended biodiesel 20% (B20), and B20 emulsified with three different water ratios. They determined that the emulsification of biodiesel/diesel with water decrease effectively exhaust emissions, especially NO_x emissions, with no penalty in engine performance. In this study, the B20 with emulsified 30% water reduced the NO_x emissions by approximately 26.17% compared to diesel fuel. Elsanousi et al. (2017) investigated the effects of biodiesel/diesel fuel blends with different ratios of water emulsion on engine performance and exhaust emissions in a light-duty diesel engine. In this study, diesel fuel and two different canola oil biodiesel (20, 40 % vol.) /diesel fuel blends were emulsified with three different water ratios such as 5%, 10%, and 15%. They reported that as the increasing water content in emulsion fuel, BTF increases and NO_x and smoke emissions decrease significantly. However, emulsion fuel containing a higher water increase considerably CO emissions. There are a lot of similar studies in the literature (Maawa et al., 2020; Khanjani and Soboti, 2021; Elsanusi et al., 2017). In these studies, the effects of water/diesel fuel emulsions (or water/diesel fuel/different alternative fuel emulsions) on engine performance and exhaust emissions were investigated.

(b) Water injection directly into the cylinder using a separate injector. In this technique, the water amount and distribution in the cylinder can be controlled at the appropriate time. However, this method is expensive and difficult to apply (Gowrishankar et al., 2020). Hence, there is a limited number of researches about this method in the literature (Ayhan and Ece, 2020; Sun et al., 2022; Zhang et al., 2017). Zhang et al. (2017)

studied the effects of DWI during compression stroke on the indicated thermal efficiency optimization in a common-rail diesel engine. They found that the application of this method increases indicated thermal efficiency by up to 4.08 %. A similar study was carried out on a marine diesel engine based on the three-dimensional simulation model by Sun et al. (2022). In this study, the effect of DWI at the compression stroke on engine performance and NO_x emissions was investigated. They found that for the W/F ratio is 2.0, the indicated power and NO_x emissions decrease 3.2% and 55.6%, respectively.

(c) WAIA is also applied using an adapted carburetor or a low-pressure injector. This method can be easily and economically realised. In addition to these advantages of WAIA method, it can increase the volumetric efficiency, and it forms a more homogeneous water/air mixture distribution in the combustion chamber, too (Subramanian, 2011; Gowrishankar et al., 2020). In this method, although the injection time of water is not changed, the injection time of diesel fuel can be adjusted to obtain optimum operating conditions. In the literature, there are also various studies applying this method (Subramanian, 2011; Şahin et al. 2018). Subramanian (2011) experimentally compared the effects of water/diesel emulsion and water injection into intake air (WAIA) on the combustion, performance, and emission characteristics of a DI diesel engine under similar operating conditions. The water-diesel ratio for both methods was selected as 0.4:1 by mass. He found that water/diesel fuel emulsion and WAIA drastically reduce NO_x and smoke emissions. In this study, he reported that the water emulsion in reducing smoke and NO_x levels is more effective than WI. However, it was determined that CO and HC levels of water emulsion were higher than WAIA. Water injection into the intake air method was applied for biodiesel (Tesfa et al., 2012). Tesfa et al. (2012) experimentally investigated water injection into intake air (WAIA) in a four-cylinder, direct injection (DI) turbocharged diesel engine running with pure biodiesel. The results indicated that WAIA at a rate of 3 kg/h results in a 50% decrease in NO_x emissions without causing any significant alteration in the specific fuel consumption. Also, it was observed that WAIA has little effect on cylinder pressure and heat release rate.

There are a lot of studies investigating the effects of the above-mentioned methods on diesel engine performance characteristics, combustion, and exhaust emissions. From these researches, it can be seen that the water adding in diesel engines reduces NO_x and smoke emissions simultaneously without any considerable fuel penalty (Subramanian, 2011; Şahin et al., 2018). However, there are few studies on the effects of water adding on combustion characteristics and CD. For these reasons, in the present study, the effects of WAIA on combustion characteristics and duration have been experimentally investigated in an automotive diesel engine. Also, an empirical correlation has been developed for estimating CD using the HRR curves,

which were determined from measured cylinder pressure values. This relation has been developed by applying the multiple curve fitting method, taking into account experimental results for different water ratios such as (2, 4, 6, 8, and 10) %, different engine loads, and different engine speeds such as (2000, 2500, 3000, 3500, and 4000) rpms. As these experiments were carried out in an automotive diesel engine currently used in motor vehicles is very important for providing new information to the industry. In addition, energy balance was investigated at 2000 and 4000 rpms under full load for different water ratios in this study.

MATERIALS AND METHODS

Engine and Experimental Set-up

Neat diesel fuel (NDF) and water adding tests were conducted in a current turbocharged-automotive diesel engine. Table 1 shows the main technical specifications of this engine and Figure 1 presents a schematic view of the test system. A water brake was used for loading the engine, and the brake moment was electronically measured. Cylinder gas pressure was measured by using an AVL GH13P type quartz pressure sensor without cooling. The main specifications of this sensor are given in Table 2.

Experimental Study

In the present study, tests were carried out at (2000, 2500 3000, 3500, and 4000) rpms engine speeds and for approximately (2, 4, 6, 8, and 10 %, by vol.) WRs under six different loads. However, only full load results have been given in the present paper. Firstly, NDF tests were conducted as NDF values were required for comparing water addition results. After NDF tests were completed, the adapted carburetor was mounted on the intake manifold of the engine. Figure 1 presents the technical view of the adapted carburetor. Information about the adapted carburetor was given in the authors' previous studies (Şahin et al. 2018; Şahin et al. 2014). In addition, to introduce water into the intake air and to measure the amount of the added water, a small water tank, a scaled glass bulb, and a flexible pipe were used and this water adding unit is shown in Figure 1. Any other modification on the experimental system and engine was not done. The main steps of the experiments are briefly given in the following paragraph.

Table 1. Technical specifications of the engine.

Engine	Renault K9K 700 turbocharged-automotive diesel engine
Displacement	1.461 liter
Cylinder number	4
Bore & stroke	76 & 80.5 mm
Compression ratio	18.25: 1
Maximum power	48 kW @ 4000 rpm
Maximum torque	160 Nm @ 1750 rpm
Connecting rod length	130 mm
Injection system	Common rail injection system[*]
Nozzle hole numbers and	5 and 0.12 mm

diameter	

*The injection pressures up to 2000 bar

Table. 2. Main specifications of the pressure transducer

Sensor type and model	Piezoelectric (GH13P)
Measuring range [bar]	0-150
Sensitivity [pC/bar]	15.25
Natural frequency [kHz]	115
Linearity	< ±0.3 %

The test engine was run for nearly (20-30) minutes before the tests, and when the cooling water temperature reached the level of (70 ±5) oC, that is steady-state conditions were reached, NDF and various WRs experiments were performed. For example, at 2000 rpm, firstly, the engine load was adjusted to 150 Nm. Then, the mean jet opening of the carburetor was adjusted to the 1st opening, which gives ~2 % WR. After ~2 % WR tests were carried out for loading moments between (150-75) Nm by reducing the engine load at 15 Nm steps and simultaneously adjusting the gas throttle position suitably to obtain a constant 2000 rpm. Thus, ~2 % WR tests under six different engine loads were performed. After that, for obtaining ~4 % WR, the main jet opening of the carburetor was adjusted to the 2nd opening, and this opening was again retained and fixed at the same 2000 rpm. Thus, tests for ~4 % WR were carried out under the above-selected six different engine loads. Then, the similar experimental procedure for approximately (~6 %, ~8 %, and ~12 %) WRs at 2000 rpm was performed. The similar tests were performed for the same loads and WRs at (2500, 3000, 3500, and 4000) rpms.

Energy Balance Calculation

The energy balance calculation in the used test engine is divided into the control volume as shown in Figure 1b. Here, the energy items entering the control volume were the enthalpy of the intake air, $Q_{in,a}$; the energy of turbocharged system, W_K; the fuel chemical energy, Q_f; and energy of water added to the intake air, Q_{H_2O}. The energy items leaving the control volume were the effective power, N_e; energy loss during the exhaust gas flow, Q_{exh}; the heat transfer rate to the cooling fluids, Q_w; energy spent on all of the unaccounted heat losses, Q_{ol}. Thus, the energy balance formula is written as follows.

$$Q_{in,a} + Q_f + Q_{H_2O} + W_K = N_e + Q_{exh} + Q_w + Q_{ol} \qquad (1)$$

$$Q_{ol}(kW) = (Q_{in,a} + Q_f + Q_{H_2O} + W_K) - (N_e + Q_{exh} + Q_w)$$

In relation 1, $Q_{in,a}$ is the energy of the enthalpy of the intake air at the intake temperature. This value has been ignored since the range in intake air temperature is small. Q_f is the fuel chemical energy, Q_{H_2O} is the energy of water added to the intake air, and W_K is the

compression work of the compressor. These values were computed as follows.

$$Q_f(kW) = \frac{B_t \cdot H_{LHV}}{3600} \qquad (1a)$$

$$Q_{H_2O}(kW) = \frac{\dot{m}_{H_2O} \cdot H_{H_2O}}{\mu_{H_2O}} \qquad (1b)$$

where, B_t (kg/h) is the total fuel consumption, H_{LHV} (kJ/kg) is the lower heating values of the fuel, $\dot{m}_{H_2O}$ (kg/s) is the flow rate of water addition to the intake air. H_{H_2O} (kJ/kmol) is the formation enthalpy of water and μ_{H_2O} is the molecular mass of water. B_t was calculated as follows.

$$B_t(\frac{kg}{h}) = \frac{m_f \cdot 3600}{1000 \cdot \Delta t} \qquad (1c)$$

Here, m_f is the mass of consumed diesel fuel during Δt (s), and here it was taken as 30 g. The amount of the water consumed during this time interval (m_{H2O}) was determined by using a scaled glass bulb as can be seen in Figure 1a.

$$W_K(kW) = 0.6 W_T \qquad (1d)$$

where W_T is the turbine work and calculated as follows:

$$W_T(kW) = \dot{m}_{exh}(c_{p,Tout}T_{T_{out}} - c_{p,Tin}T_{T_{in}}) \qquad (1e)$$

where $\dot{m}_{exh}$ is the flow rate of exhaust gases, and in this study $\dot{m}_{exh}$ is calculated as $\dot{m}_{exh} = (\dot{m}_f + \dot{m}_a + \dot{m}_{H_2O})$. In relation 1e, $c_{p,Tin}$ is the specific heat capacity of exhaust gases at $T_{T_{in}}$ (K) the inlet exhaust gases temperature to the turbine and $c_{p,Tout}$ is the specific heat capacity of exhaust gases at $T_{T_{out}}$ (K) the outlet exhaust gases temperature from the turbine, respectively.

$$N_e(kW) = 0.1013 \frac{T_b \cdot \omega}{P_0} \sqrt{\frac{T_0 \cdot X_{hum}}{293}} \qquad (1f)$$

$$\dot{Q}_{exh}(kW) = \frac{\left(\dot{m}_{exh} \cdot c_{p,exh} \cdot (T_{exh} - T_0)\right)}{3600} \qquad (1g)$$

$$\dot{Q}_{cw}(kW) = \frac{\dot{m}_{cw} \cdot c_{p,cw} \cdot (T_{out} - T_{in})}{60} \qquad (1h)$$

In formula 1e, T_b (Nm) is the torque, was measured in the test system. T_0 (K) is the ambient temperature and P_0 (MPa) is the ambient pressure. These values were measured in the experiment. X_{hum} is the humidity correction which is determined depending on dry and wet thermometer temperatures. In formula 1f, $c_{p,exh}$ (kJ/kgK) is the specific heat capacity of the exhaust gas at T_{exh} (K) exhaust temperature. In relation 1g, $\dot{m}_{CW}$ (kg/h) is the flow rate of cooling water, $c_{p,cw}$ (kJ/kgK) represent the specific heat capacity, T_{in} (K) and T_{out} (K) are the inlet and outlet temperature of cooling water.

Heat Release Rate (HRR) Analysis

In this paper, using the following relationship, HRR values has been calculated (Heywood, 1988).

$$\frac{dQ}{d\theta} = \frac{\gamma}{\gamma\text{-}1} P \frac{dV}{d\theta} + \frac{1}{\gamma\text{-}1} V \frac{dP}{d\theta} \qquad (2)$$

where $dQ/d\theta$ (J/deg.) is the heat release rate, γ is the specific heats ratio, V (cm^3) is the cylinder volume, and P (bar) is cylinder pressure. Here, HRR analysis has been conducted along the crank angle steps during the time interval of inlet valve closure and exhaust valve opening. The mean cylinder temperature values were calculated from the ideal gas equation. The specific heat ratio values were calculated at selected crank angles depending on the temperature values, computed from the ideal gas equation.

Deriving of Quadratic Empirical Relation for CD

The heat release rate (HRR) curves, which were calculated from measured pressure values, were shown in Figures (2a, 3a, 4a, 5a, and 6a) and these values have been used to determine the CDs. That is, in the present study, HRR values have been determined by using measured cylinder pressures and corresponding volume values. Then, HRR curves have been drawn for NDF and five different WRs under various loads at (2000, 2500, 3000, 3500, and 4000) rpms. Thus, every one of the CDs was determined separately for operating conditions by using these HRR curves.

Here, CD is defined as the time interval between crank angles corresponding to 10% and 90% values of HRR (Shojoei et al., 2019; Boldaji et al., 2018; Singh et al., 2015). Finally, an empirical relation for the CD, which takes into account the effects of water rate, the loading level and the engine speed, is developed. Here a multiple variable quadratic curve-fitting method was applied to the experimental CD values which were originally developed by Durgun and Kafali (1991). Naturally, the load ranges for the used speeds are different from each other, as shown in Table 3. The same load values must be used to develop the empirical relation for the burning duration. For this reason, identical selected load values are marked in yellow colour in Table 3, and these values are used in curve fitting computations. CD values, determined from HRR curves, for selected engine speeds and WRs under (120, 105, 90, and 75) Nm loads are shown in Table 4, Table 5 and Table 6, respectively. Using the CD values under (120, 105, 90, and 75) Nm loads, an empirical relation has been developed depending on the water ratio (WR), load value (L) and the number of revolutions (n).
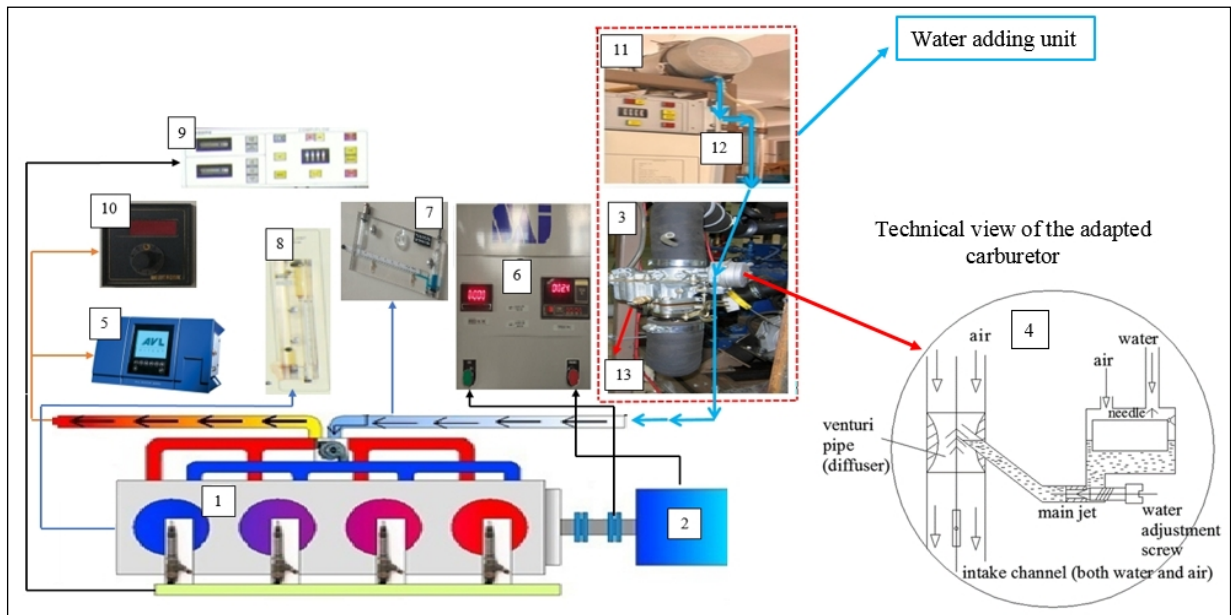

Figure 1a. Schematic view of the experimental setup. 1-Diesel engine, 2-hydraulic dynamometer, 3-carburator, 4-detailed drawing of the carburator, 5-gas analyzer, 6-load measurement indicator, 7-inclined manometer, 8-coolont flow meter, 9-fuel measurement unit, 10-digital display for temperatures, 11-water tank, 12-scaled glass bulb, 13-water adjustment screw
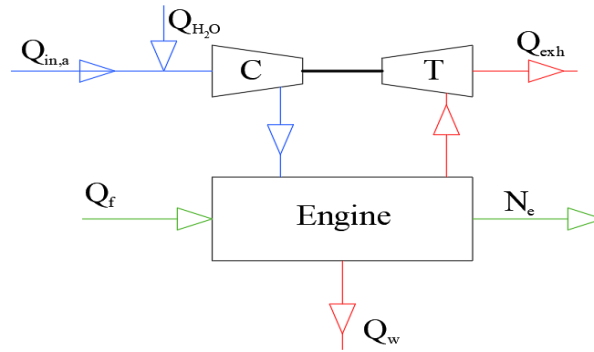
Figure 1b. Schematic of the energy balance of the used test engine. The abbreviations in this figure: C and T are shown as compressor and turbine, respectively.

Here, CD (°CA) is the combustion duration, WR (%) is the water ratio, n (rpm) is the engine number of revolutions, and L (Nm) is the load value.

Table 3. Selected load values corresponding to the various engine speeds

Speed (rpm)	150 Nm	135 Nm	120 Nm	105 Nm	90 Nm	75 Nm	60 Nm	45 Nm
2000	X	X	X	X	X	X	-	-
2500	X	X	X	X	X	X	-	-
3000	-	X	X	X	X	X	X	-
3500	-	-	X	X	X	X	X	X
4000	-	-	X	X	X	X	X	X

In this way, the effects of three parameters, such as n, WR, and, L were taken into account in the empirical CD formula. Here, as explained in the above paragraph, multiple regression was applied to the experimental data to develop the CD relation. However, here, the multiple regression was carried out in the form of nested loops, which is easier.

The aimed empirical CD formula can be a function of the water ratio, engine speed and load value as follows:

$$CD = f(WR, n, L) \tag{3}$$

The calculation process of this multiple curve fitting method consists of the following steps:

Step 1: While applying this method, firstly, the engine speed and the load were taken as constant. Thus, for the CD, a quadratic curve was fitted depending on the water ratio values for every situation. In this way, a quadratic relation is obtained for CD as follows:

$$CD = a_0 \cdot (WR)^0 + a_1 \cdot (WR)^1 + a_2 \cdot (WR)^2 \tag{4}$$

Using the CD data at (2000, 2500, 3000, 3500, and 4000) rpms under selected loads (120, 105, 90, 75) Nm given in Tables 4-8, the following relations are obtained.

Table 4. The determined CD values for 5 different WRs at 5 different engine speeds under 120 Nm

120 Nm	2000 rpm	2500 rpm	3000 rpm	3500 rpm	4000 rpm
WR (%)	CD (°CA)	CD (°CA)	CD (°CA)	CD (°CA)	CD (°CA)
NDF	12.798	21.077	20.752	21.300	24.858
2	12.648	21.221	21.177	21.022	24.02
4	12.941	21.431	21.017	21.254	24.921
6	12.507	20.823	21.243	21.579	24.641
8	12.647	20.848	20.314	21.611	24.942
10	12.841	21.033	20.088	21.611	24.560

Table 5. The determined CD values for 5 different WRs at 5 different engine speeds under 105 Nm

105 Nm	2000 rpm	2500 rpm	3000 rpm	3500 rpm	4000 rpm
WR (%)	CD (°CA)	CD (°CA)	CD (°CA)	CD (°CA)	CD (°CA)
NDF	17.301	21.980	25.488	20.526	22.462
2	17.760	21.972	25.263	20.526	22.200
4	16.416	21.830	25.505	20.044	21.618
6	17.752	21.972	25.053	20.571	21.900
8	17.021	21.727	25.457	20.263	22.219
10	17.697	21.983	25.553	20.338	22.463

Table 6. The determined CD values for 5 different WRs at 5 different engine speeds under 90 Nm

90 Nm	2000 rpm	2500 rpm	3000 rpm	3500 rpm	4000 rpm
WR (%)	CD (°CA)	CD (°CA)	CD (°CA)	CD (°CA)	CD (°CA)
NDF	20.477	22.778	25.698	23.369	20.417
2	20.059	22.747	25.425	23.107	20.134
4	20.175	22.524	25.698	23.141	20.117
6	20.451	22.699	25.568	22.945	19.832
8	20.318	21.911	25.505	22.681	20.100
10	20.454	22.382	25.521	23.369	20.417

Table 7. The determined CD values for 5 different WRs at

75 Nm	2000 rpm	2500 rpm	3000 rpm	3500 rpm	4000 rpm
WR (%)	CD (°CA)	CD (°CA)	CD (°CA)	CD (°CA)	CD (°CA)
NDF	21.663	23.310	25.006	25.996	18.900
2	20.393	23.087	25.006	25.055	18.029
4	21.070	23.523	25.022	25.545	18.015
6	20.769	23.097	25.232	25.976	18.012
8	21.265	23.274	25.473	25.489	18.616
10	20.945	23.323	25.085	25.789	19.100

Following equations can be written for n_1, n_2, n_3, n_4, and n_5;

$$n_1 = 2000, \quad CD_1 = a_{0,1} + a_{1,1}.\left(WR\right) + a_{2,1}.\left(WR\right)^2 \quad (5)$$

$$n_2 = 2500, \quad CD_2 = a_{0,2} + a_{1,2}.\left(WR\right) + a_{2,2}.\left(WR\right)^2 \quad (6)$$

$$n_3 = 3000, \quad CD_3 = a_{0,3} + a_{1,3}.\left(WR\right) + a_{2,3}.\left(WR\right)^2 \quad (7)$$

$$n_4 = 3500, \quad CD_4 = a_{0,4} + a_{1,4}.\left(WR\right) + a_{2,4}.\left(WR\right)^2 \quad (8)$$

$$n_5 = 4000, \quad CD_5 = a_{0,5} + a_{1,5}.\left(WR\right) + a_{2,5}.\left(WR\right)^2 \quad (9)$$

After obtaining CD_1, CD_2, CD_3, CD_4 and CD_5, it has been passed to the calculation step 2.

Step 2: Quadratic curves were fitted to coefficients (a_0, a_1, a_2) in equations 5-9 depending on the engine speed as given in Eqs. 10-12.

$$a_0 = b_0 + b_1.n + b_2.n^2 \quad (10)$$

$$a_1 = c_0 + c_1.n + c_2.n^2 \quad (11)$$

$$a_2 = d_0 + d_1.n + d_2.n^2 \quad (12)$$

These relations were written in Table 8 according to the selected loads for each engine speed. Thus, the coefficients of the relations (13-24) have been calculated. Then, it has been passed to step 3.

Step 3: As can be seen in Table 9, quadratic curves were fitted to the coefficients ($b_{0,120}$, $b_{0,105}$, $b_{0,90}$, $b_{0,75}$,... $d_{2,120}$, $d_{2,105}$, $d_{2,90}$, $d_{2,75}$), in relations (13-24), depending on the engine loads.

Table 8. The quadratic curve equations for a_0, a_1, and a_2 for each engine speed under four different loads

L=120 Nm	Relation number	L=105 Nm	Relation number
$a_{0,120} = b_{0,120} + b_{1,120}.n + b_{2,120}.n^2$	(13)	$a_{0,105} = b_{0,105} + b_{1,105}.n + b_{2,105}.n^2$	(16)
$a_{1,120} = c_{0,120} + c_{1,120}.n + c_{2,120}.n^2$	(14)	$a_{1,105} = c_{0,105} + c_{1,105}.n + c_{2,105}.n^2$	(17)
$a_{2,120} = d_{0,120} + d_{1,120}.n + d_{2,120}.n^2$	(15)	$a_{2,105} = d_{0,105} + d_{1,105}.n + d_{2,105}.n^2$	(18)
L=90 Nm		L=75 Nm	
$a_{0,90} = b_{0,90} + b_{1,90}.n + b_{2,90}.n^2$	(19)	$a_{0,75} = b_{0,75} + b_{1,75}.n + b_{2,75}.n^2$	(22)
$a_{1,90} = c_{0,90} + c_{1,90}.n + c_{2,90}.n^2$	(20)	$a_{1,75} = c_{0,75} + c_{1,75}.n + c_{2,75}.n^2$	(23)
$a_{1,90} = c_{0,90} + c_{1,90}.n + c_{2,90}.n^2$	(21)	$a_{2,75} = d_{0,75} + d_{1,75}.n + d_{2,75}.n^2$	(24)

Table 9. The quadratic curves for the the coefficients ($b_{0,120}$, $b_{0,105}$, $b_{0,90}$, $b_{0,75}$,.. $d_{2,120}$, $d_{2,105}$, $d_{2,90}$, $d_{2,75}$), in relations (13-24), depending on the engine loads

b		c		d	
$b_0 = e_0 + e_1.L + e_2.L^2$	(25)	$c_0 = h_0 + h_1.L + h_2.L^2$	(28)	$d_0 = t_0 + t_1.L + t_2.L^2$	(31)
$b_1 = f_0 + f_1.L + f_2.L^2$	(26)	$c_1 = p_0 + p_1.L + p_2.L^2$	(29)	$d_1 = u_0 + u_1.L + u_2.L^2$	(32)
$b_2 = g_0 + g_1.L + g_2.L^2$	(27)	$c_2 = s_0 + s_1.L + s_2.L^2$	(30)	$d_2 = v_0 + v_1.L + v_2.L^2$	(33)

At the end, by writing the coefficients (b_0, b_1,... d_2) (25-33) in the equation (3), the following empirical formula for CD has been arranged as follows:

$$CD = A.\left(WR\right)^0 + B.\left(WR\right)^1 + C.\left(WR\right)^2 \quad (34)$$

where A, B, and C have been given in Table 10. A program has been prepared in MATLAB to calculate the coefficients (A, B, and C) in the relation (34) by using experimentally determined CD values at different engine speeds and WRs under (120, 105, 90, and 75) Nm load conditions. The numerical values of the A, B, and C coefficients of the relation (34) are given in Table 10. The mean absolute percent error (MAPE) of the CD was determined as 5.18% for relation (34).

Table 10. Relations for A, B, and C coefficients in relation 34 and the numerical values of these coefficients

$$A = \left\{ \begin{array}{l} \left[e_0+e_1.L+e_2.L^2\right] + \\ \left[f_0+f_1.L+f_2.L^2\right].n+ \\ \left[g_0+g_1.L+g_2.L^2\right].n^2 \end{array} \right. \quad (34a)$$

$$B = \left\{ \begin{array}{l} \left[h_0+h_1.L+h_2.L^2\right] + \\ \left[p_0+p_1.L+p_2.L^2\right].n + \\ \left[s_0+s_1.L+s_2.L^2\right].n^2 \end{array} \right. \quad (34b)$$

$$C = \left\{ \begin{array}{l} \left[t_0+t_1.L+t_2.L^2\right] + \\ \left[u_0+u_1.L+u_2.L^2\right].n + \\ \left[v_0+v_1.L+v_2.L^2\right].n^2 \end{array} \right. \quad (34c)$$

$$A = \left\{ \begin{array}{l} \left[-64.63+0.90.L-0.004.L^2\right] + \\ \left[0.04-6.42.10^{-5}.L-8.69.10^{-7}.L^2\right].n+ \\ \left[-4.47.10^{-6}-5.35.10^{-8}.L+5.73*10^{-10}.L^2\right].n^2 \end{array} \right.$$

$$B = \left\{ \begin{array}{l} \left[-27.78+0.53.L-0.003.L^2\right] + \\ \left[0.02-3.80.10^{-4}.L+1.86.10^{-6}.L^2\right].n+ \\ \left[-3.24.10^{-6}+6.11.10^{-8}.L-2.96.10^{-10}.L^2\right].n^2 \end{array} \right.$$

$$C = \left\{ \begin{array}{l} \left[2.47-0.05.L+2.33.10^{-4}.L^2\right] + \\ \left[-0.002+3.47.10^{-5}.L-1.72.10^{-7}.L^2\right].n+ \\ \left[3.04.10^{-7}-5.76.10^{-9}.L+2.83.10^{-11}.L^2\right].n^2 \end{array} \right.$$

RESULTS AND DISCUSSION

The Effects of WAIA on Cylinder Pressure, Temperature, HRR and CD

In this section, the effects of WAIA on the cylinder pressure, cylinder temperature, and HRR are presented in Figures 2-6 and evaluated for (2000, 2500, 3000, 3500, and 4000) rpms under only full load conditions for brevity. These figures show that the cylinder pressure-crank angle, cylinder temperature-crank angle, and heat release rate-crank angle (HRR-CA) diagrams are fairly similar to each other and follow the typical behaviour of NDF under different operating conditions. Here, the HRR has been determined by averaging over 100 consecutive cycles for NDF and five different WRs with CA under full load at five selected different engine speeds. The effects of WAIA on the CDs, which were determined from HRR, were investigated and shown in Figures 7 (a-e).

a) 2000 rpm: The effects of WAIA on the cylinder pressure, temperature, and HRR at 2000 rpm are shown in Figures 2 (a-b-c), respectively. Also, the effects of WAIA on the CD are shown in Figure 7 (a). As can be seen in Figure 2(a), the WAIA cylinder pressure profiles are similar to NDF and the effects of water addition on cylinder pressure seem insignificant. For example, at this engine speed, for NDF the peak cylinder pressure is 156.57 bar and it occurs at 11.15 °CA, while for (2.415, 4.215, 5.945, 8.321, and 9.462) % WRs the peak cylinder pressures become (158.16, 157.05, 156.81, 158.25, and 156.96) bar, respectively and they take place at (10.68, 10.54, 10.72, 10.70, and 11.05) °CA, respectively. The maximum cylinder pressure values for the selected five WRs are slightly higher than that of NDF and the peak cylinder pressure angles occur earlier than that of NDF. This can be attributed to a longer ignition delay because of the cooling effect of water on the inlet air temperature. This observation agrees with the relevant literature (Subramanian, 2011; Tesfa et al., 2012; Gowrishankar and Krishnasamy, 2022; Abu-Zaid, 2004).

As can be seen in Figure 2 (b), WAIA decreases cylinder temperatures. For NDF the peak cylinder temperature is 2168.03 K and it occurs at 21.09 °CA, while for (2.415, 4.215, 5.945, 8.321, and 9.462) % WRs the peak cylinder temperature values become (2055.32, 2039.91, 2052.84, 2068.79 and 2028.79) K, respectively and they take place at (21.513, 21.690, 21.188, 21.850 and 21.283) °CA, respectively. With WAIA, the cylinder temperature values during the compression process will be lower than NDF as water that is injected into intake air will vaporize and cools the air. This will also result in a reduction in combustion temperature. As it is known from the literature that applying the water adding method in engines decreases cylinder temperature values which is naturally an expected result (Subramanian, 2011; Şahin et al., 2014; Ithnin et al., 2015). In addition, the effect of water on cylinder temperature is explained in reference Zhao et al. (2018), as follows: When WAIA method is applied, the liquid water could evaporate in the cylinder during the intake and compression phases. Thus, the cylinder temperature drops since the latent heat of the evaporation of water is larger (Zhao et al., 2018).

Figure 2 (c) shows the variations of HRR for NDF and five different WRs under full load. As can be seen in this figure, HRR values with WAIA are lower than that of NDF at the beginning of the combustion, around of the TDC. However, they have increased toward the end of the combustion process. Similar results have been obtained in the literature (Subramanian, 2011; Zhang et al., 2017; Vigneswaran et al., 2021). For NDF, the maximum value of HRR is 55.27 J/deg. and it occurs at 8.44 °CA, while for (2.415, 4.215, 5.945, 8.321, and 9.462) % WRs the maximum values of HRR become (55.01, 53.96, 54.39, 55.22, and 54.20) J/deg. respectively and they take place at (8.88, 8.45, 8.60, 8.89, and 8.77) °CA, respectively. We could see in Figure 2 (c) that, the maximum values of the HRR for all selected WRs are lower than that of NDF and the maximum HRR angles occur later than that of NDF. With the WAIA, we

can say that the combustion starts a little later and the combustion might continue during the expansion stroke. However, combustion has been completed earlier with water addition. This can be observed from the CD values given below: For example, using the HRR values, the CDs are also determined and 10 %–90 % of the maximum heat release rate was used as the CD (Park and Oh, 2022; Gentz et al., 2015; Hosseini and Checkel, 2006). As can be seen in Figure 7(a), WAIA has decreased CDs at 2000 rpm generally. For NDF, the CD is 13.10 °CA, while for (2.415, 4.215, 5.945, 8.321, and 9.462) % WRs the CD values become (12.96, 12.93, 12.68, 12.95, and 13.576) °CA respectively.

Thus, with the shortening of the CD, approximately the same amount of fuel is burned closer to TDC, which shows the enhancing effect of WAIA on combustion. The burn of the fuel around TDC without forming knocking has a useful effect on reducing of fuel consumption (Heywood, 1988). BSFC decreases at 2000 rpm at low loads, and the maximum decrease rate obtained in BSFC was 2.68% for approximately 6% water under 120 Nm load (Şahin et al., 2018; Şahin et al., 2014; Tuti et al., 2021). Also, it can be thought that the homogeneous combustion, which might be occurred by WAIA, causes the burning process of the fuel to be accelerated, which decrease CD. Similar explanations and results have been given in the literature (Zhang et al., 2017; Park and Oh, 2022).

b) 2500 rpm: The effects of WAIA on the cylinder pressure, temperature, and HRR at 2500 rpm are presented in Figures 3 (a-b-c), respectively. Also, the effects of WAIA on the CD are shown in Figure 7 (b). As can be seen in Figure 3(a); for NDF the peak cylinder pressure is 164.08 bar and it occurs at 9.94 °CA, while for (1.889, 4.215, 6.192, 8.551, and 9.687) % WRs the peak cylinder pressure values become (164.101, 164.088, 164.99, 164.29, and 164.38) bar, respectively and they take place at (9.77, 9.58, 9.77, 9.76, and 9.75) °CA, respectively. The maximum cylinder pressure values for the selected five WRs are higher than that of NDF and the peak cylinder pressure angles occur earlier than that of NDF. As dictated above, it is thought that higher cylinder pressure values with WAIA occurred due to the increased ignition delay. In fact, the water addition has a restricted effect on the cylinder pressure as 2000 rpm.
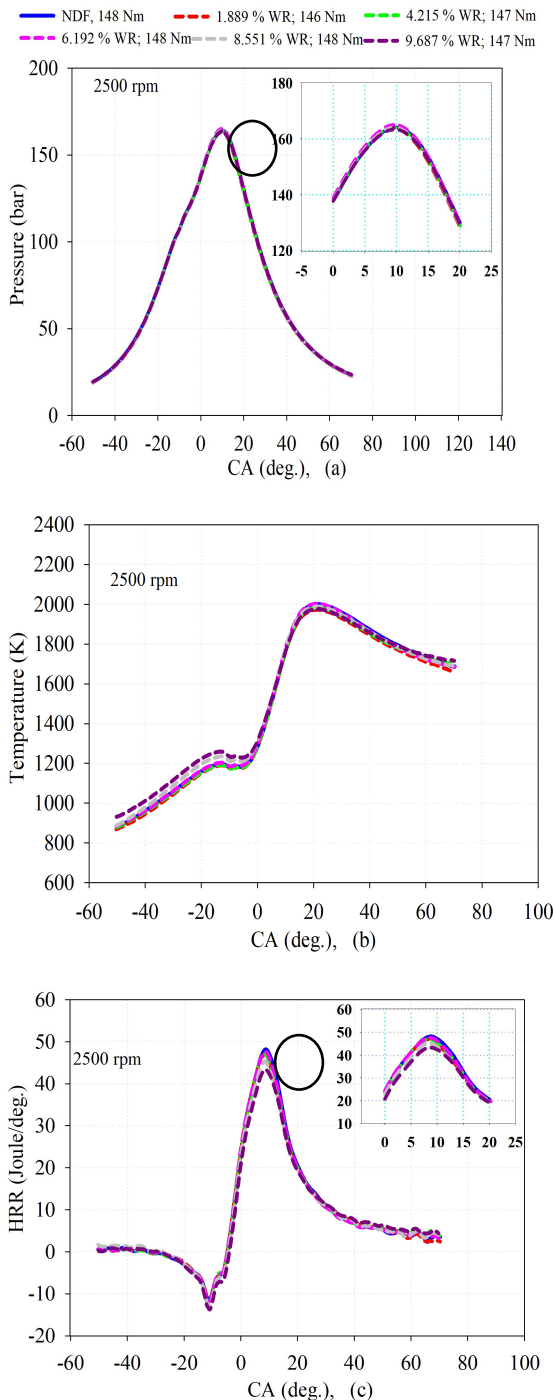
As can be seen in Figure 3 (b), WAIA decreases cylinder temperature values. For NDF the peak cylinder temperature is 2000.74 K and it occurs at 21.57 °CA, while for (1.889, 4.215, 6.192, 8.551, and 9.687) % WRs the peak cylinder temperature values become (1972.86, 1984.01, 2002.86, 1988.47, and 1976.19) K, and they take place at (21.42, 21.22, 21.79, 21.40, and 21.75) °CA, respectively. Thus, it can be said that WAIA decreases cylinder temperature values generally. It is known from the literature that added water may absorb the heat of vaporization during compression and combustion processes, and this reduces the cylinder temperature values (Subramanian, 2011; Zhang et al., 2017; Park and Oh, 2022).
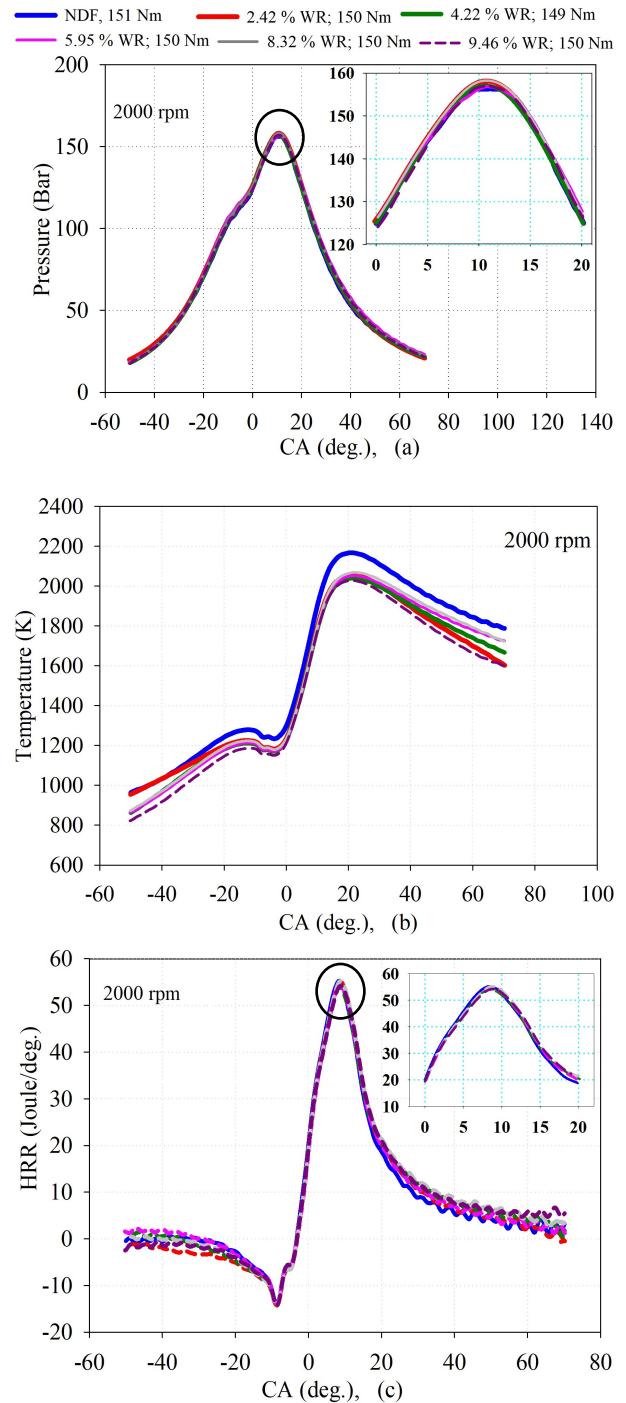
Figures 2 (a-b-c). Cylinder pressure, cylinder temperature and HRR variations for different WRs in respect to CA at 2000 rpm, respectively.

As can be seen in Figure 3 (c), HRR values with WAIA are lower than that of NDF at the beginning of the combustion, around TDC. After that, as combustion was advanced, HRR characteristics followed nearly that of NDF, and HRR values have been very close to NDF. At 2500 rpm, it could be observed that the combustion process with WAIA has not actually improved as expected. Thus, WAIA increases BSFC somewhat at this engine speed. For example, the increase ratios of BSFC for (2.065, 4.013, 6.196, 8.261, and 9.400) % WRs under 149 Nm full load have been (1.088, 2.177, 1.630, 0., and

2.719)% respectively. Similar results have been found under low loads. For NDF, the maximum value of HRR is 48.21 J/deg. and it occurs at 8.82 °CA, while for (1.889, 4.215, 6.192, 8.551, and 9.687) % WRs the maximum values of HRR become (46.96, 47.13, 47.64, 45.31, and 43.33) J/deg. respectively and they take place at (8.27, 8.45, 8.64, 8.26, and 8.63) °CA, respectively. As can be seen in Figure 7 (b), for NDF, the CD is 15.19
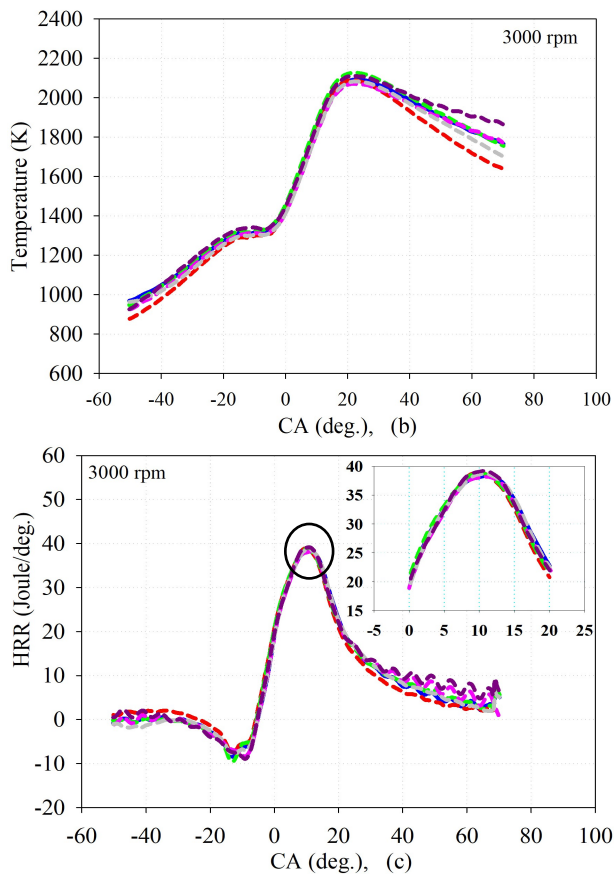

Figures 3 (a-b-c). Cylinder pressure, cylinder temperature and HRR variations for different WRs in respect to CA at 2500 rpm, respectively.

°CA, while for (1.889, 4.215, 6.192, 8.551, and 9.687) % WRs the CDs are (14.66, 14.17, 14.04, 14.35, and 14.62) °CA respectively. Thus, it can be said that WAIA has decreased slightly CDs at 2500 rpm.

c) 3000 rpm: The effects of WAIA on the cylinder pressure, temperature, HRR, and CD at 3000 rpm are shown in Figures 4 (a-b-c) and Figure 7 (c), respectively. As can be seen in Figure 4 (a) for NDF the peak cylinder pressure is 155.99 bar and it occurs at 8.35 °CA, while for (2.142, 4.694, 6.402, 8.050, and 9.418) % WRs the peak cylinder pressure values become (154.45, 157.55, 154.57, 155.11 and 156.92) bar, respectively and they take place at (8.78, 8.35, 8.56, 8.34 and 8.34) °CA, respectively. Thus; cylinder pressure values increase for 4.694% and 9.418% WRs and they decrease for other WRs. However, the peak cylinder pressure values show only minor differences in magnitude for selected operating conditions at this engine speed.

As can be seen in Figure 4 (b), WAIA decreases cylinder temperature values. For NDF the peak cylinder temperature is 2091.44 K and it occurs at 22.34 °CA, while for (2.142, 4.694, 6.402, 8.050, and 9.418) % WRs the peak cylinder temperate values become (2089.40, 2126.81, 2070.62, 2083.20, and 2110.92 K, respectively and they take place at (21.38, 22.34, 21.63, 22.32, and 21.86) °CA, respectively. Thus, peak cylinder temperature values generally decrease. Whereas for (4.694 and 9.418) % WRs, cylinder temperature values increase. As can be seen from the evaluation of the heat analysis graphs below, the maximum values of HRR at this engine speed are generally higher and occur closer to the TDC than that of NDF. Thus, it could be said that combustion takes place closer to the TDC and occurs faster especially for (4.694 and 9.418) % WRs, which may result in increased cylinder temperature values. As shown in Figure 7 (c), the lowest CD has taken place for 4.694% WR at approximately 2.37% reduction level. Hence, the highest combustion temperature increment has reached approximately 1.69% approximately, for this WR.

226
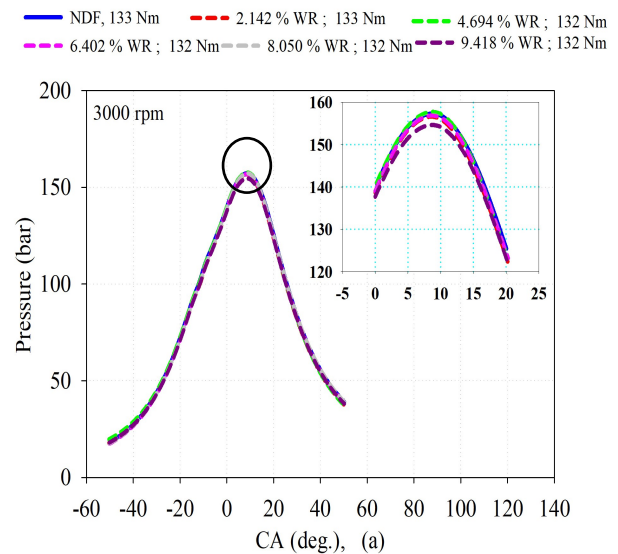
Figures 4 (a-b-c). Cylinder pressure, cylinder temperature and HRR variations for different WRs in respect to CA at 3000 rpm, respectively.

As can be seen in Figure 4 (c), HRR values with WAIA are slightly higher than that of NDF at the beginning of the combustion, around the TDC. After that, as combustion was advanced during the expansion stroke, HRR values become slightly higher than that of NDF. For NDF, the maximum values of HRR are 38.27 J/deg. and it occurs at 11.06 °CA, while for (2.142, 4.694, 6.402, 8.050, and 9.418) % WRs the maximum values of HRR become (38.95, 38.79, 38.17, 38.70, and 39.19) J/deg. respectively, and they take place at (9.68, 9.71, 10.81, 10.60, and 10.60) °CA, respectively. It has been observed from this experimental data that the maximum values of HRR for selected WRs become generally higher than that of NDF, and the burning of the diesel fuel takes place closer to the TDC. For NDF, the CD is 18.96 °CA, while for (2.142, 4.694, 6.402, 8.050, and 9.418) % WRs the CD values become (18.69, 18.51, 18.42, 18.66, and 18.71) °CA respectively, as can be seen in Figure 7 (c). WAIA has decreased CDs slightly at 3000 rpm. It is thought that this reduction takes place due to the improvement of combustion because of the formation of a more homogeneous and faster fuel-air mixture with the water addition.

d) 3500 rpm: The effects of WAIA on the cylinder pressure, cylinder temperature, HRR, and CD at 3500 rpm are shown in Figures 5 (a-b-c) and Figure 7 (d), respectively. As can be seen in Figure 5(a); for NDF the

peak cylinder pressure is 158.16 bar, and it occurs at 6.82 °CA, while for (2.142, 3.689, 6.402, 8.050, and 12.245) % WRs the peak cylinder pressure values become (158.75, 158.05, 159.28, 159.65, and 159.54) bar, and they take place at (6.31, 6.84, 6.56, 6.56, and 6.82) °CA, respectively. The maximum cylinder pressure values for selected WRs are higher than that of NDF, and the peak cylinder pressure values occur earlier than that of NDF. In other words, combustion took place in a shorter time with WAIA, as can be seen in Figure 7 (d). The reasons for this increase in cylinder pressure for this engine speed are almost similar to the other selected engine speeds as explained above. In fact, at this speed, the effect of water addition on cylinder pressure has become at a low level as the increase values of cylinder pressures are under 1 %.

As can be seen in Figure 5 (b), WAIA increases slightly cylinder temperature values. For NDF the peak cylinder temperature is 2048.08 K, and it occurs at 22.04 °CA, while for (2.142, 3.689, 6.402, 8.050, and 12.245) % WRs the peak cylinder temperature values become (2048.19, 2026.37, 2051.18, 2056.11, and 2053.64) K, respectively and they take place at (22.07, 22.10, 21.79, 21.79, and 21.51) °CA, respectively. It could be observed from this data that the cylinder temperature values increased in general with WAIA at 3500 rpm. The possible reason for this temperature increment might be the burning of the injected diesel fuel in a shorter time.

In Figure 5(c), the variations of HRR have been indicated for NDF and five different WRs under full load. As can be seen in this figure, HRR values with WAIA take lower values than that of NDF at the beginning of the combustion, around the TDC. However, they have increased towards the end of the combustion process. For NDF, the maximum value of HRR is 31.38 J/deg., and it occurs at 10.50 °CA, while for (2.142, 3.689, 6.402, 8.050, and 12.245) % WRs the maximum values of HRR become (30.65, 30.52, 31.29, 31.17, and 30.91) J/deg. and they take place at (9.46, 9.47, 9.72, 9.72, and 8.92) °CA, respectively. We can notice in Figure 5(c), the maximum values of the HRR for all of the selected WRs are lower than that of NDF and the maximum HRR values occur at smaller crank angles than that of NDF. For NDF, the CD is 21.51 °CA, while for (2.142, 3.689, 6.402, 8.050, and 12.245) % WRs the CD values become (21.28, 20.93, 20.72, 21.01, and 21.31) °CA respectively. Here, the maximum decrement ratio of the CD was at the level of rate 3.67 % at 6.402 % WR. The reduction in HRR was also low at the level of 0.03 % for this WR. Thus, it can be advised to apply this WR at 3500 rpm.

e) 4000 rpm: The effects of WAIA on the cylinder pressure, temperature, HRR, and CD at 3000 rpm are shown in Figures. 6 (a-b-c) and Figure 7 (e), respectively. As can be seen in Figure 6 (a) for NDF the peak pressure is 157.99 bar and it occurs at 5.42 °CA, while for (1.860, 4.467, 5.705, 8.321, and 9.236) % WRs the peak cylinder pressure values become (153.68, 153.04, 154.74, 157.22 and 156.05) bar, and they take place at (5.42, 6.05, 5.42, 4.85, and 5.72) °CA, respectively. As can be seen in

227

Figure 6 (a), the maximum cylinder pressure values are lower than NDF for all of the selected WRs and they occur earlier than that of NDF. Contrary to the other engine speeds, cylinder pressures have decreased at 4000 rpm, which is the nominal speed of this engine. It is well known that automotive diesel engines run in a very short time at this engine speed in practice application. In the literature; Subramanian (2011) also stated that the usage of water in diesel engines reduces the maximum cylinder pressure. Ayhan and Ece (2020) have studied the effect of electronically controlled direct water injection into the cylinder at compression stroke on engine performance, combustion, and exhaust emissions, and they found that water injection decreases cylinder pressure at 2200 rpm, which was the nominal engine speed of their engine.

As can be seen in Figure 6 (b), WAIA generally decreases cylinder temperature values. For NDF the peak temperature is 1846.58 K and it occurs at 21.32 °CA, while for (1.860, 4.467, 5.705, 8.321, and 9.236) % WRs the cylinder peak temperature values become (1857.42, 1838.21, 1823.01, 1861.15, and 1874.60) K, and they take place at (21.60, 21.32, 22.59, 21.64, and 23.01) °CA, respectively. Peak cylinder temperature values increase for (1.860, 8.321, and 9.236) % WRs but they decrease for (4,467 and 5,705) % WRs. It has been observed in Figures 6 (a and b) and during the experiments that the cylinder temperature and the pressure variations are not quite consistent at 4000 rpm. As mentioned above, this speed is a very little used engine speed under the normal operating period of automotive diesel engines, and the running of the engine is not stable.

In Figure 6 (c), the variations of HRR have been shown for NDF and five different WRs under full load. As can be seen in these figures HRR values with WAIA are close to that of NDF generally and lower at the beginning of the combustion, around TDC. After that, as combustion was advanced, HRR curves followed nearly NDF characteristics, and HRR values have been almost equal to NDF values. For NDF, the maximum values of HRR are 24.98 J/deg. and it occurs at 8.71 °CA, while for (2.142, 3.689, 6.402, 8.050, and 12.245) % WRs the maximum values of HRR become (24.21, 24.35, 24.64, 25.29, and 24.94) J/deg. respectively, and they take place at (9.00, 9.31, 8.71, 9.02, and 8.66) °CA, respectively. Here, it could be observed that the maximum values of the HRR in all selected WRs were generally lower than that of NDF. It could be also seen from these curves that the combustion process could not be improved with the application of WAIA as expected, for 4000 rpm. For NDF, the CD is 24.32 °CA, while for (1.860, 4.467, 4.467, 5.705, 8.321, and 9.236) % WRs the CDs become (24.25, 24.12, 24.02, 26.44, and 28.88) °CA. For (1.860, 4.467, and 5.705)% WRs, the decrease ratios in the CD values are (0.28, 0.81, and 1.23) %, but for (8.321 and 9.236) % WRs, the increase ratios in the CD values become (8.73 and 18.76) %, respectively. In fact, the variation ratios in CD are at low levels and they take place within the error limits.
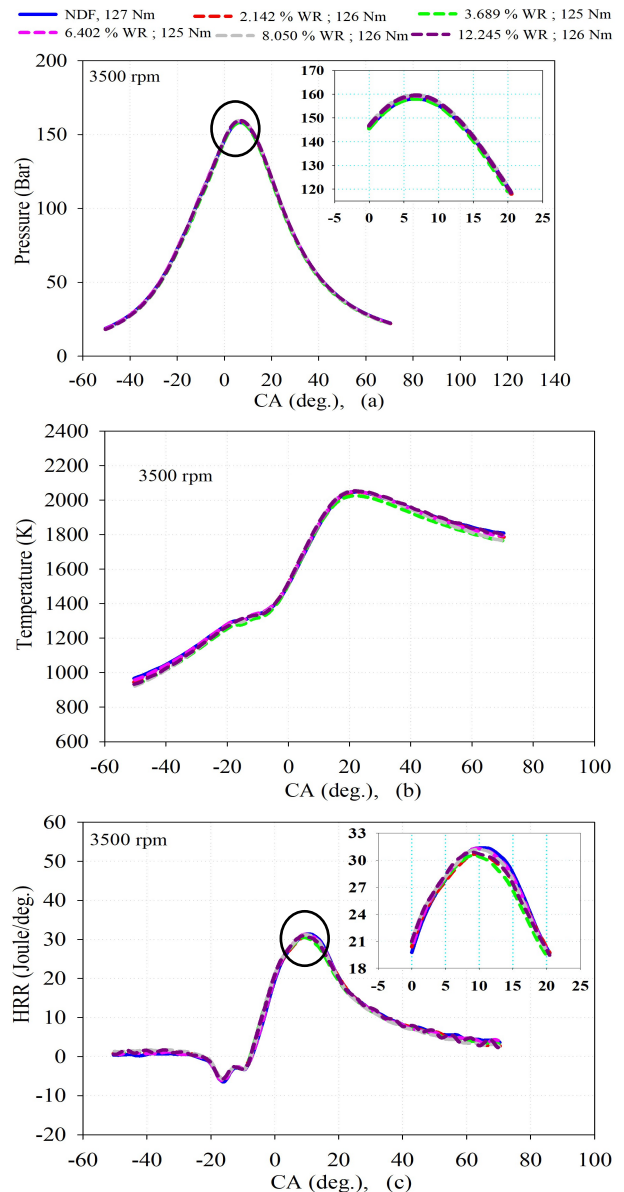
Figures 5 (a-b-c). Clinder pressure, cylinder temperature and HRR variations for different WRs in respect to CA at 3500 rpm, respectively
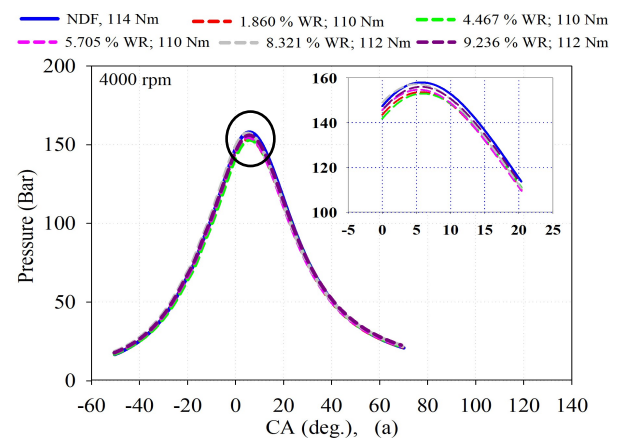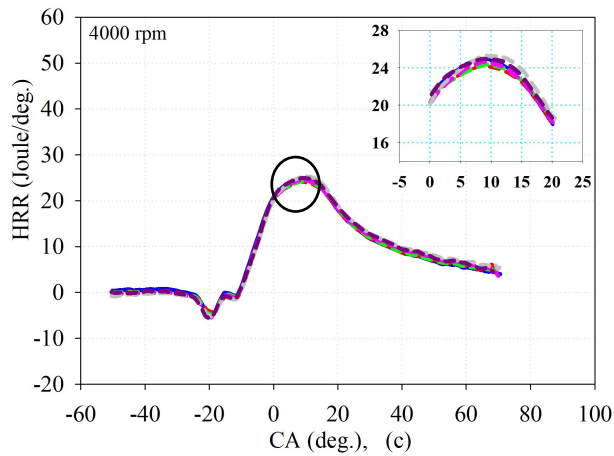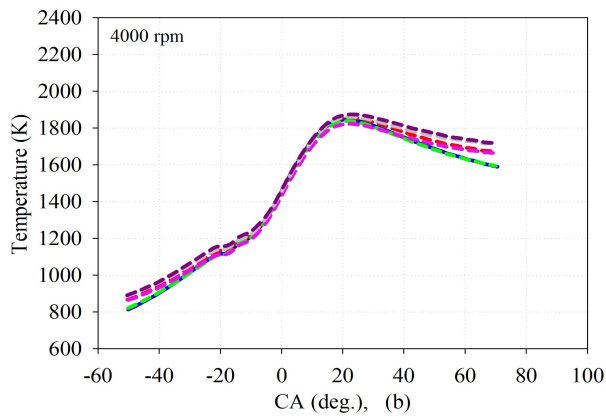
Figures 6 (a-b-c). Cylinder pressure, cylinder temperature and HRR variations for different WRs in respect to CA at 4000 rpm, respectively.

Here; using the developed empirical correlation, CDs were also calculated for NDF and (2.5, 5, and 7.5) % WRs at 2250 rpm, (80, 70, and 60) Nm load conditions, which were not tested, and the calculated values are presented in Table 9. As a result, we can say that by using the developed empirical correlation, the CD can be determined at any desired condition for this engine. Also, this correlation can be used for different diesel engines, and it could give useful information for the combustion duration of these engines. As can be seen from Table 9, the CDs are decreased with the WR in all of the selected operating conditions.

Table 9. Computed CD by using the developed empirical correlation for three WRs under three load at 2250 rpm.

WR (%)	2250 rpm		
	80 Nm	70 Nm	60 Nm
	CD (°CA)	CD (°CA)	CD (°CA)
NDF	22.799	22.778	22.111
2.5	22.651	22.670	22.071
5	22.590	22.609	22.012
7.5	22.617	22.595	21.933
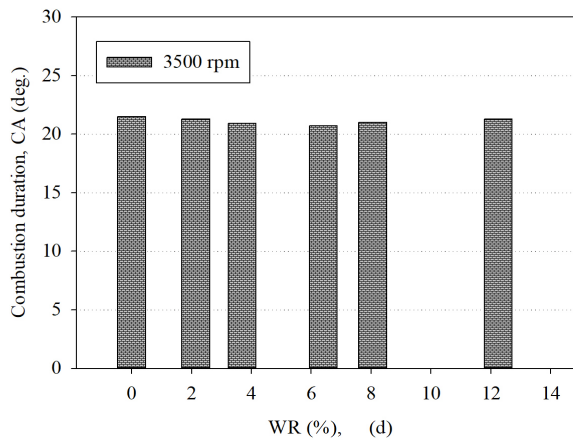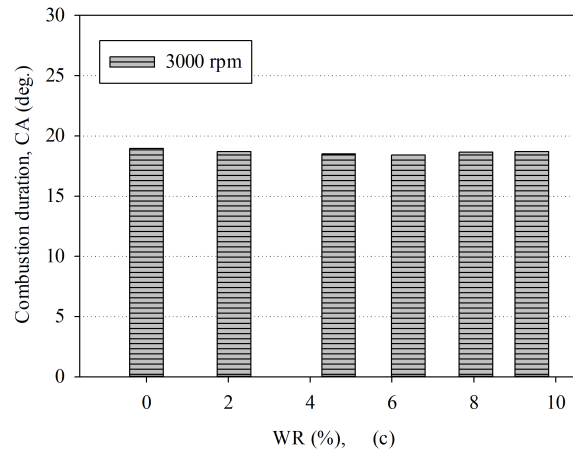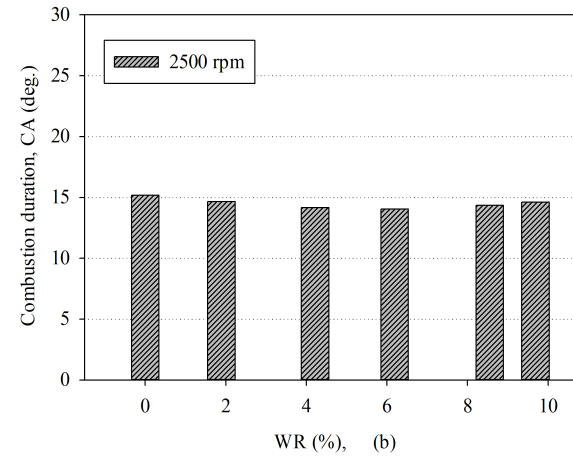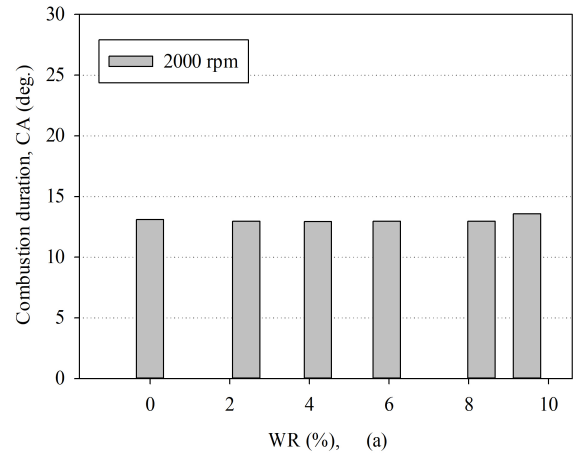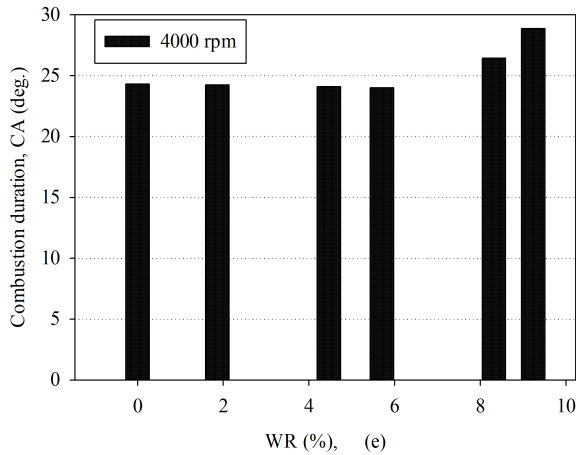
Figures 7 (a-b-c-d-e). CD variations for different WRs at 2000, 2500, 3000, 3500, and 4000 rpms under full load, respectively.

The Effects of WAIA on Energy Balance

In this section, the effects of WAIA on the energy balance analysis are presented in Figures 8 at 2000 and 4000 rpms under only full load conditions. Here, the energy balance evaluations were made according to the fuel chemical energy. As can be seen in Figure 8 (a), the effective power values according to the chemical energy of the fuel generally decrease with WAIA at 2000 rpm. The effective power values according to fuel chemical energy for NDF and (2.419, 4.215, 5.945, 8.321, and 9. 482) % WRs have become 34.707 and (33.969, 34.253, 34.769, 34.344, and 34.189) respectively. Here, it could be observed that the effective power values according to fuel chemical energy in all selected WRs were generally lower than that of NDF. For only 5.945 % WR, this value is higher than that of NDF. Exhaust losses generally decrease with WAIA. As can be seen from Figure 2(b) given above, the cylinder temperatures and also exhaust temperatures decrease with the addition of water, which reduces exhaust losses. However, the exhaust losses increase for 9.462 % WR. The combustion continues in the expansion process because of the increase in burning duration with this water ratio.
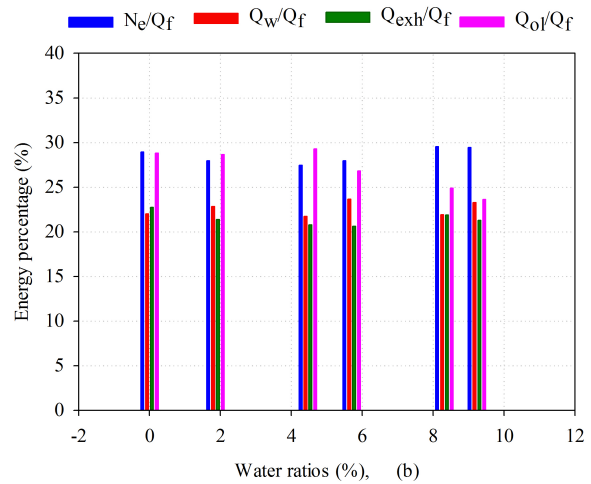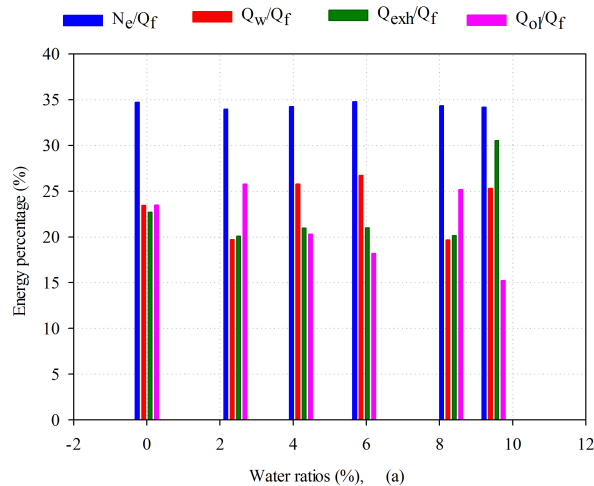

Figure 8. The energy balance of the used test engine for different WRs under full load condition, **(a)** 2000 rpm, and **(b)** 4000 rpm, respectively

For this reason, the exhaust temperature may be slightly higher, increasing the exhaust losses. The heat losses to cooling water generally tend to increase with the addition of water although the change of these values is not very smooth. The other losses are generally reduced with the WAIA.

The influence of the WAIA on the energy balance at 4000 rpm is shown in Figure 8b. It can be seen from this figure that the effective power values according to the chemical energy of the fuel decrease until 8.32 % WR but, after this ratio, these values slightly start to increase at 4000 rpm. Similarly, CDs and the values of HRR increase for (8.321 and 9.236) % WRs. The addition of water into the intake air between approximately (6-10) percent is thought to improve combustion at 4000 rpm, which increases effective power from the interpretation of these results. The water addition to the intake air slightly reduces the exhaust losses but, it increases the heat losses to cooling water at this engine speed according to the chemical energy of the fuel. Although the exhaust temperature slightly increased with the addition of water at 4000 rpm, the exhaust losses decrease according to the added fuel energy. The reason for this is that the injected fuel mass is more with the addition of water at this engine speed. With the water addition into intake air at 4000 rpm, the air in the intake channel also cools well because of the evaporation of water. This can increase the volumetric efficiency of the engine. This explanation agrees with the literature (Zhanming et al., 2022; Subramanian, 2011). Thus, depending on the electronic control unit, more fuel may be injected. In fact, the change in exhaust losses according to fuel chemical energy is not very high with a minimum value of 21.74% and a maximum value of 22.74%. WAIA generally decreases the other losses. The other losses are generally reduced with the water addition into the intake.

CONCLUSION

In the present study, the effects of water addition into intake air on the cylinder pressure, cylinder temperature, HRR, and CD were experimentally investigated and compared with NDF in an automotive diesel engine. Based on the experimental results, the main obtained results can be summarized as follows:

1. Cylinder pressure values generally increased at (2000, 2500, and 3500) rpms, but they decreased at (3000 and 4000) rpms for all of the selected WRs. The crank angles in which the maximum cylinder pressure values occurred have been closer to TDC with WAIA.

2. Cylinder temperature values mostly decreased at (2000, 2500, and 3000) rpms, but they generally increased at (3500, and 4000) rpms for WAIA. Also; maximum cylinder temperature values occurred at crank angles farther from TDC with WAIA.

3. The characteristic behaviour of the HRR-crank angle curve for water adding has been very similar to that of the NDF at all of the selected engine speeds. HRR values generally decreased at (2000, 2500, 3500, and 4000) rpms, but generally increased at 3000 rpm.

4. The CD values were generally shortened at all of the engine speeds under full loads with water addition. CD values for NDF and for (2.42, 4.22, 5.95, 8.32, and 9.46) % WRs have been determined as (13.10, 12.96, 12.93, 12.68, 12.95, and 13.576) °CA respectively at 2000 rpm.

5. Using the HRR curves, an empirical correlation has been developed for estimating the CD for the test engine. This quadratic relation has been developed by applying the multiple least squares curve fitting method, considering experimental results for different WRs, different engine loads and different engine speeds. By using this empirical formula CD at any condition can be estimated for this test engine. Similar correlations can be performed for different diesel engines, and this way, generalised results can be obtained.

Using the developed empirical relation, the CD can be estimated for any operation condition which is different from the experiments. For example; at 2250 rpm under 80 Nm load condition, CDs have been determined as (22.80, 22.65, 22.59, and 22.62) °CA for NDF and WRs of (2.5, 5, 7.5) %.

6. The effective power values according to the chemical energy of the fuel generally decrease with WAIA at 2000 rpm. However, the effective power values according to the chemical energy of the fuel generally decrease until 8.32 % WR but, after this ratio, these values slightly start to increase at 4000 rpm. WAIA decreases generally the exhaust losses at 2000 rpm, but it increases the exhaust losses at 4000 rpm. The heat losses to cooling water generally tend to increase with the water addition into the intake air.

REFERENCES

Abu-Zaid M., 2004, Performance of single cylinder, direct injection diesel engine using water fuel emulsions, *Energy Conv. and Management*, 45, 697-705.

Ayhan V. and Ece Y.M., 2020, New application to reduce NOₓ emissions of diesel engines: Electronically controlled direct water injection at compression stroke, *Applied Energy*, 260, 114328.

Boldaji R.M. and Sofianopoulos A., Mamalis S., Lawler B., 2018, Effects of mass, pressure, and timing of injection on the efficiency and emissions characteristics of TSCI combustion with direct water injection, *SAE Technical Papers*, 2018-01-0178.

Durgun O. and Kafali K., 1991, Blockage correction, *Ocean Engineering*, 18, 2699-82.

Elsanusi O.A., Roy M.M. and Sidhu M.S., 2017, Experimental invest. on a diesel engine fueled by diesel-biodiesel blends and their emulsions at various engine operating conditions, *Applied Energy*, 203, 582–93.

El Shenawy E.A., Elkelawy M., Mohamood H.A.E, Shams M.H., Panchal H. and Sadasivuni K.K., 2019, Investigation and performance analysis of water-diesel emulsion for improvement of performance and emission characteristics of partially premixed charge compression ignition (PPCCI) diesel engines, *Sustainable Energy Technologies and Assessments*, 36, 100546.

Ghazal O.H., 2019, Combustion analysis of hydrogen-diesel dual fuel engine with water injection technique, *Case Studies in Thermal Engineering*,13,100380.

Gentz G., Thelen B., Litke P., Hoke J. and Toulson E., 2015, Combustion visualization, performance, and CFD modeling of a pre-chamber turbulent jet ignition system in a rapid comp. machine, *SAE Int J Engines*, 8, 538–46.

Gowrishankar S. and Krishnasamy A., 2022, A relative assessment of emulsification and water injection methods to mitigate higher oxides of nitrogen emissions from biodiesel fueled light-duty diesel engine, *Fuel*, 308, 121926.

Gowrishankar S., Rastogi P. and Krishnasamy A., 2020, Investigations on NOₓ and smoke emissions reduction potential through water-in-diesel emulsion and water fumigation in a small-bore diesel engine, *SAE Technical Paper*, 2020-32-2312.

Han J., Somers L.M.T., Cracknell R., Joedicke A., Wardle R. and Mohan V.R.R., 2020 Experimental investigation of ethanol/diesel dual -fuel combustion in a heavy -duty diesel engine, *Fuel*, 275,117867.

Heywood J.B., 2018, Internal Combustion Engine Fundamentals (2nd edit), McGrow-Hill Book Company.

Hosseini V. and Checkel M.D., 2006, Using reformer gas to enhance HCCI combustion of CNG in a CFR engine, *SAE Technical Paper*, 01, 13.

Ithnin A.M., Ahmad M.A., Bakar M.A.A., Rajoo S. and Yahya W.J., 2015, Combustion performance and emission analysis of diesel engine fuelled with water-in-diesel emulsion fuel made from low-grade diesel fuel, *Energy Conv. and Management*, 90, 375–82.

Jhalani A., Sharma D., Soni S.L. and Sharma P.K., 2019, Effects of process parameters on performance and emissions of a water-emulsified diesel-fueled compression ignition engine, *Energy Sources, Part A: Recovery, Utilization, and Environmental Effects*,1-13.

Khanjani A. and Sobati M.A., 2021, Performance and emission of a diesel engine using different water/waste fish oil (WFO) biodiesel/diesel emulsion fuels: Optimization of fuel formulation via response surface methodology (RSM), *Fuel*, 288, 119662.

Maawa W. N., Mamat R., Najafi G. and Goey LPH. D., 2020, Performance, comb., and emission characteristics of a CI engine fueled with emulsified diesel-biodiesel blends at different water contents, *Fuel*, 267,117265.

Mahmood A.S., Qatta H.I., Hussein N.F. and Ismael A.A., 2019, Effect of using diesel-water emulsion as a fuel on diesel engine emissions: An experimental study. *International Journal of Energy and Envirn.*,10, 321-8.

Park J. and Oh J., 2022, Study on the characteristics of performance, comb., and emissions for a diesel water emulsion fuel on a combustion visualization engine and a commercial diesel engine, *Fuel*, 311, 122520.

Singh S.B., Dhar A. and Agarwal A.K., 2015, Technical feasibility study of butanol-gasoline blends for powering medium-duty transportation spark ignition engine, *Renewable Energy*, 76, 706-716.

Shojaei T.R., Khalife E., Tabatabaei M., Najafi B. and Mirsalim M., 2019, Effect of nano-cerium oxide and water additives on B5 combustion emissions, *Zanco Journal of Pure and Applied Sciences*, 31, 34–9.

Subramanian KA., 2011, A comparison of water–diesel emulsion and timed injection of water into the intake manifold of a diesel engine for simultaneous control of NO and smoke, *Energy Conv. & Mana.*, 52, 849–57.

Sun X., Ning J., Liang X., Jing G., Chen Y. and Chen G., 2022, Effect of direct water inj. on comb. and emissions charact. of marine diesel engines, *Fuel*, 309, 122213.

Şahin Z., Tuti M. and Durgun O., 2014, Experimental investigation of the effects of water adding to the intake air on the engine performance and exhaust emissions in a DI automotive diesel engine*, Fuel*, 115, 884 –895.

Şahin Z., Durgun O. and Tuti M., 2018, An experimental study on the effects of inlet water injection of diesel engine heat release rate, fuel consumption, opacity, and NO_x emissions, *Exergetic, Energetic and Environmental Dimensions*, 981-96.

Tauzia X., Maiboom A. and Shah SR., 2010, Experimental study of inlet manifold water injection on combustion and emissions of an automotive direct injection diesel engine. *Energy*, 35, 3628–39.

Tesfa B., Mishra R., Gu F. and Ball A.D., 2012, Water injection effects on the performance and emission characteristics of a CI engine operating with biodiesel, *Renewable Energy*, 37, 1, 333-344.

Tuti M., Şahin Z. and Durgun O., 2021, Experimental investigation of the effects of water addition into the intake air on cylinder pressure, temperature, heat release rate and combustion duration in an automotive diesel engine, *23rd Congree on Thermal Science and Technology*, September 8-10, Gaziantep, Türkiye, 785–95.

Vigneswaran R., Balasubramanian D. and Sastha B.D.S., 2021, Performance, emission and combustion characteristics of unmodified diesel engine with titanium dioxide (TiO_2) nano particle along with water-in-diesel emulsion fuel, *Fuel*, 285, 119115.

Zhang Z., Kang Z., Jiang L., Chao Y., Deng J., Hu Z., Li L. and Wu Z., 2017, Effect of direct water injection during compression stroke on thermal efficiency optimization of common rail diesel engine, *Energy Procedia*, 142, 1251-1258.

Zhanming C., Long W., Xiaochen W., Hao C., Limin G. and Nan G., 2022, Experimental study on the effect of water port injection on the combustion and emission characteristics of diesel/methane dual-fuel engines, *Fuel*, 312, 122950.

Zhao R., Zhang Z., Zhuge W., Zhang Y. and Yin Y., 2018, Comparative study on different water/steam injection layouts for fuel reduction in a turbocompound diesel engine, *Energy Conv. & Manag.*, 171, 1487-501.

Zhu S., Hu B., Akehurst S., Copeland C., Lewis A. and Yuan H., 2019, A review of water injection applied on the internal combustion engine, *Energy Conv. & Management*, 184,139–158.

NUMERICAL ANALYSIS AND DIFFUSER VANE SHAPE OPTIMIZATION OF A RADIAL COMPRESSOR WITH THE OPEN-SOURCE SOFTWARE SU2

Mustafa Kürşat UZUNER*, Altuğ Melik BAŞOL**, Bob MISCHO***, Philipp JENNY****
*Özyeğin University Graduate School of Science and Engineering, Cekmekoy, Istanbul, Türkiye
kursat.uzuner@ozu.edu.tr, ORCID: 0000-0003-2880-7300
**Özyeğin University Graduate School of Science and Engineering, Cekmekoy, Istanbul, Türkiye
altug.basol@ozyegin.edu.tr, ORCID: 0000-0002-7289-7246
***MAN Energy Solutions Schweiz AG, Zurich, Switzerland, bob.mischo@man-es.com
****MAN Energy Solutions Schweiz AG, Zurich, Switzerland, philipp.jenny@man-es.com, ORCID: 0009-0005-8770-8689

Abstract: In recent years, the usage of open-source computational fluid dynamics tools is on a rise both in industry and academia. SU2 is one of these open-source tools. Unlike other open-source alternatives, SU2 is equipped with boundary condition types, solvers and methods that are especially developed for the analysis and design of turbomachinery. The aim of this work is to explore and investigate the capabilities of SU2 in the prediction of performance parameters of radial compressors. Two different single stage shrouded compressor geometries, one with a vaneless diffuser and the other with a vaned diffuser have been investigated with steady state CFD. The compressors were designed by MAN Energy Solutions Schweiz AG. Computational results with SU2 showed a satisfactory agreement with both the experimental data and reference CFD solutions obtained with Fidelity Flow, which is formerly known as Numeca Fine TURBO. Only at the relatively higher mass flow rates the difference between references and SU2 were higher compared to other operating points. After performance parameters were successfully calculated with SU2, the optimization tools that come with SU2 were also used. A 2D adjoint optimization study on the vane of the vaned diffuser was carried out. The study was carried out at a single operating point that is close to choke conditions. The loss generated by the large separated flow region at the suction side of the diffuser vane was reduced by 0.55 % in the optimized geometry using minimal modifications on the existing vane geometry to keep the performance of the compressor intact at other operating points. However, the resulting modification increased the total pressure loss by 0.86 % at one of the design operating points. This performance penalty could be due to the discontinuity in the vane geometry generated by the optimizer. Overall, the study shows that SU2 has the basic numerical schemes and models that are required for the analysis of radial turbomachinery flows and geometry optimization.
Keywords: Computational Fluid Dynamics, Open-source, SU2, Turbomachinery, Compressor, Optimization

AÇIK KAYNAK AKIŞKANLAR DİNAMİĞİ YAZILIMI SU2 İLE RADYAL BİR KOMPRESÖRÜN PERFORMANS ANALİZİ VE OPTİMİZASYONU

Özet: Son yıllarda açık-kaynak hesaplamalı akışkanlar dinamiği yazılımlarının kullanımı hem akademi hem de endüstride gittikçe yaygınlaşmaktadır. SU2, bu açık kaynak akışkanlar dinamiği araçlarından biridir. Diğer açık kaynak araçlarda görülmeyen turbomakine simülasyonu ve tasarımına özel sınır koşulları, çözücüler ve metotlar SU2 içerisinde mevcuttur. Bu çalışmanın amacı, bir radyal kompresörün performans parametrelerinin SU2 ile belirlenmeye çalışılarak SU2'nin kabiliyetlerinin incelenmesidir. Bunun için tek aşamalı, kanatçıklı ve kanatçıksız difüzörlü olmak üzere iki farklı radyal kompresör kullanılmıştır. Bu kompresörler MAN Energy Solutions Schweiz AG tarafından tasarlanmıştır. SU2, deneysel veriler ve Fidelity Flow ile elde edilen sonuçlarla kıyaslandığında yeterli benzerlikte sonuçlar vermiştir. Yalnızca yüksek debili çalışma koşullarında referanslar ile aradaki farkın diğer noktalara göre açıldığı gözlemlenmiştir. Performans parametrelerinde başarılı sonuçlar elde edildikten sonra SU2 içerisinde hazır olarak bulunan optimizasyon araçlarının kabiliyetleri de denenmiştir. Kanatçıklı difüzörün kanatçığı üzerinde iki boyutlu bir adjoint optimizasyon yapılarak optimizasyon kabiliyetleri incelenmiştir. En kötü performansın görüldüğü, boğulma koşullarına yakın bir çalışma noktası optimizasyon için seçilmiştir. Optimizasyon sırasındaki şekil bozunumları başka çalışma noktalarında performansı aynı tutabilmek için olabildiğince küçük tutulmuştur. Kanatçığın basınç tarafında görülen akım ayrılmasının sebep olduğu kayıp optimizasyon sonucu %0.55 azaltılmıştır. Ancak, optimize edilmiş kanatçık profili bir

başka tasarım çalışma noktasında denendiğinde toplam basınçta görülen kaybın %0.86 arttığı gözlemlenmiştir. Bu performans kaybının muhtemel ana sebebi olarak optimizasyon sonucu kanatçıkta oluşan kesiklilik gösterilebilir. Genel olarak bu çalışma, SU2'nin radyal turbomakine analizi ve optimizasyonu için gerekli temel nümerik şemalara ve modellere sahip olduğunu göstermektedir.

Anahtar Kelimler: Hesaplamalı Akışkanlar Dinamiği, Açık Kaynak, SU2, Turbomakine, Kompresör, Optimizasyon

NOMENCLATURE

Polytropic Efficiency (Total to Total)	$\eta = \dfrac{R}{cp}\dfrac{\log\left(\frac{P_{t_5}}{P_{t_1}}\right)}{\log\left(\frac{T_{t_5}}{T_{t_1}}\right)}$
	(1: Inlet) (5: Outlet)
Work Input Coefficient [-]	$\mu_0 = \Delta h_{t_{1-5}}/u_2^2$
Pressure Rise Coefficient [-]	$\mu_y = \eta\mu_0$
Volume Flow Coefficient [-]	$\Phi = \dfrac{\dot{m}}{\rho_{t_1} u_2 D_2^2}$
Gas Constant $\left[\frac{J}{kgK}\right]$	$R = 287.4$
Heat Capacity $\left[\frac{J}{kgK}\right]$	$cp = 1006$
Impeller Tip Rotational Speed $[\frac{m}{s}]$	$u_2 = \dfrac{D_2\omega}{2}$
Impeller Tip Diameter [m]	D_2
Mass Flow Rate $\left[\frac{kg}{s}\right]$	$\dot{m}$
Total Density at Inlet Conditions $\left[\frac{kg}{m^3}\right]$	ρ_{t_1}
Rotational Speed $\left[\frac{rad}{s}\right]$	ω
Total Pressure $[Pa]$	P_t
Total Temperature $[K]$	T_t
Total Enthalpy Difference $\left[\frac{J}{kg}\right]$	Δh_t

Total values are calculated by area averaging.

INTRODUCTION

Computational Fluid Dynamics (CFD) plays a key role in the design of turbomachinery. Even though there are a variety of commercial codes that serve the needs of the designers, open source CFD tools have started to gain attention in recent years. However, most of the open source CFD tools are built for general purpose applications and do not contain turbomachinery specific features. The open-source flow simulation and design software SU2 is different in that sense. It is equipped with turbomachinery specific features such as nonreflecting boundary conditions and special mesh interfaces. In open literature, several contributions on turbomachinery analysis conducted with SU2, are available. A very

similar work, which performs an analysis of a centrifugal compressor with vaneless diffuser shows the predictive capability of SU2 when compared to ANSYS and experimental data (de Castro, 2019). An important output of this work is related to the mesh topology dependency of SU2. Different grid topologies, namely C-grid and O-grid, are tested, and SU2 is found out to be working better with O-grid topology when a second order accurate solution is desired. Another example where turbomachinery capabilities of SU2 are compared to experimental data and ANSYS-CFX is also available (Yan *et.al,* 2023). The single passage steady, full-annulus unsteady and aeroelasticity capabilities of SU2 are investigated on NASA Stage 35, TUDa-GLR-OpenStage, and a linear cascade SC1. Results are compared with ANSYS-CFX and experimental data. Overall, SU2 showed satisfactory agreement in these comparisons up to near-stall operating points. Additionally, an analysis of a one-and-a half stage, stator-rotor-stator, axial turbomachinery (Mollá, 2017), and an analysis of a simple radial inflow turbine (Keep *et.al,* 2017) are also performed with SU2. These works mostly incorporate mixing-plane and non-reflecting boundary condition features with periodic boundary faces (Giles, 1990). SU2 can also be utilized for design purposes as well with its simple 2D capabilities (de Koning, 2015). Additionally, it can be used with its built-in optimization tools for design (Vitale *et.al,* 2020) and use special features such as harmonic balance as well (Rubino *et.al,* 2020).

Adjoint methods are commonly used for optimization in computational fluid dynamics and has been pioneered by Jameson in the aerospace field (Giles and Pierce, 2000). Adjoint equations are derived from the governing equations and the sequence of discretization change the type of adjoint method. There are two adjoint methods, continuous and discrete. For continuous adjoint, adjoint equations are formulated before the governing equations are discretized, and for discrete adjoint, adjoint equations are formulated after the governing equations are discretized (Ntanakas and Meyer, 2014). In terms of turbomachinery optimization, the use of adjoint methods is widely seen as well. A gradient based shape optimization of NASA Rotor 37 can be found where the shock related tonal noise is minimized when maximizing the isentropic efficiency (Katsapoxaki *et.al,* 2023). Moreover, the SRV2 radial compressor is optimized to increase the total-to-total efficiency at highest efficiency meanwhile conserving its wide operating range (Châtel *et.al,* 2022). Optimization is conducted with a gradient-based method, where gradients are found with the adjoint approach. Another optimization study on SRV2-O compressor is present where the volute designed for this compressor is optimized using adjoint optimization (Hottois *et.al,* 2023). Other studies where turbomachinery targeted optimization method developments are also

available. A new volumetric parametrization approach for gradient-based shape optimization focused on turbomachinery stages is introduced, where the need for an extra mesh deformation tool is eliminated (Trompoukis *et.al,* 2023). In another study, the robustness of the optimized design is aimed to be improved by considering the effect of uncertainties with a Surrogate-Assisted Gradient-Based (SAGB) optimization method (Luo *et.al,* 2022). Additionally, a multi-row discrete adjoint solver development combining manual and automatic differentiation is also available (Wu *et.al,* 2023).
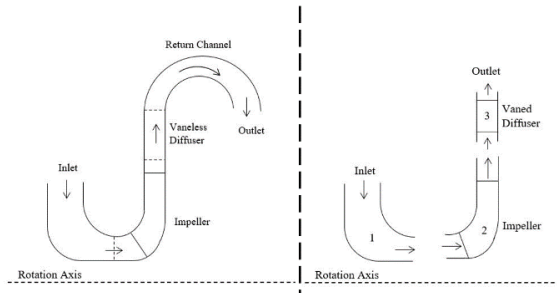
Figure 1. Compressor Flow Paths for each Case

SU2 has its own Adjoint Optimization tool integrated in the package, and both continuous and discrete methods are available. There are two shape deformation methods used in SU2, which are Hicks-Henne (Hicks and Henne, 1978) and FFD (Free Form Deformation) (Koshakji *et.al,* 2013) methods. Both methods work by changing the design variables to see how the changed geometries would perform. FFD deforms a specified space around the object interested whereas other methods deform the geometry directly (Koshakji *et.al,* 2013). Hicks-Henne deformation method is only available with 2D cases whereas FFD is applicable to both 2D and 3D cases.

However, a detailed investigation of the SU2's flow analysis capabilities, the computational cost of its solvers and their parallel scalability against other proven commercial codes is still needed to identify regions for further improvements. In the first part of this study, the capabilities of the solvers in SU2 are tested on two single stage radial compressor geometries, one with a vaneless and the other with a vaned diffuser. The compressor stages used in this work are proprietary designs of MAN Energy Solutions Schweiz AG. The company provided experimental and reference CFD data obtained with 'Fidelity Flow' for comparison with the SU2 results. In the second part of this study the shape optimization capabilities of SU2 are evaluated. In this regard, the existing compressor vane geometry from the vaned diffuser case is considered as the baseline design, and it is optimized using the adjoint optimization tools in SU2 in 2D. The performance improvements is compared to the baseline design.

NUMERICAL METHODOLOGY

Two different single stage radial compressor geometries have been considered. Schematics of the meridional flow

paths of the compressors are shown in Figure 2. Both compressors contain shrouded impellers. One of the geometries, Case1, included a vaneless and the other one, Case2, was equipped with a vaned diffuser. The meshes were generated using 'Fidelity Automesh Autogrid'.

The zones (inlet-impeller-diffuser) of the compressor in Case 2 are meshed separately. In all meshes a multi-block structured O-grid mesh topology was utilized. A close view of the mesh around the impeller are shown in Figure 2 and Figure 3.
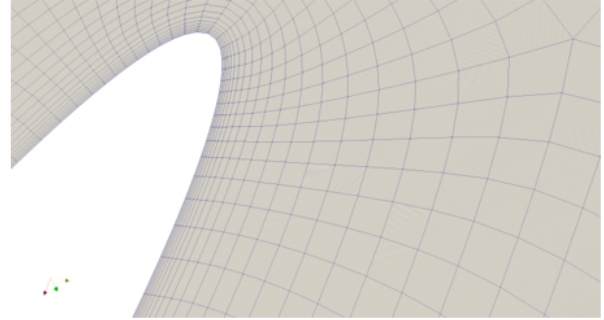

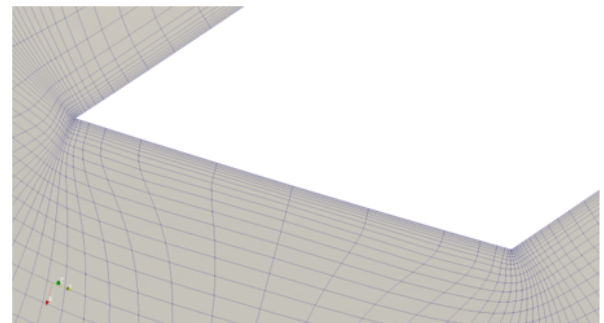**Figure 2.** Close-up View of Impeller Leading Edge Mesh

Figure 3. Close-up View of Impeller Trailing Edge Mesh

The different mesh zones in Case 2 are solved in either stationary or rotating frame of references. The interfaces between the different mesh zones were treated with the mixing plane interface condition. At the inlet zone a uniform total pressure, total temperature and flow directions were specified as inlet boundary conditions. At the diffuser zone outlet, averaged static pressure at the outlet was applied. At the walls, no slip boundary conditions were defined. At the periodic faces, periodic boundary conditions were specified.

The compressor in Case 1 was meshed as a single zone. Due to the vaneless diffuser, the entire domain could be run in rotating frame of reference. So, no interface treatment was necessary in Case 1. Apart from that, same type boundary conditions were specified at the domain boundaries as in Case 2.

For the closure of the RANS equations, different turbulence models are available in SU2. In this study, k-omega SST (Menter, 1994) turbulence model was used.

SU2 offers different schemes for the discretization of the RANS equations. In this study, Backward Euler scheme was used for the temporal discretization. The implicit character of the scheme enables to use relatively large time steps compared to explicit schemes and offers a superior convergence behavior compared to explicit schemes. For the spatial discretization first and second order Roe schemes are available in SU2. However, second order scheme led to numerical instability at the cutback impeller trailing edge. Local mesh refinement at the trailing edge region could also not resolve the numerical instability and therefore the first order accurate Roe scheme was used in all the computations. Air, modeled as perfect gas, was used as the working fluid. For convergence, the mass imbalance between the inlet and outlet were monitored, and simulations with imbalance less than 0.5% is assumed to be converged.

To determine the required mesh resolution for a grid insensitive solution a mesh dependency study was carried out. The mesh dependency study was carried out only for Case 2. Accordingly, three different meshes were generated. Statistics of the meshes used in the study are given in Table 1.

Table 1. Total Number of Cells used in the generated grids.

Mesh 1	Mesh 2	Mesh 3
0.4m	1.6m	3.9m

Mesh dependency study is done by comparing the total enthalpy difference, Δh_{tot}, and flow coefficient, Φ, by taking the corresponding values from experiment as the reference. The percent changes for Δh_{tot} and Φ as the mesh cell count increases are considered. As it can be seen from Figure 4 and Figure 5, the difference between Mesh 1 and Mesh 2 is higher compared to Mesh 2 and Mesh 3. The percent changes for Δh_{tot} and Φ are 3.77 and 2.68 as the mesh changes from Mesh 1 to Mesh 2, and 0.98 and 0.4 as the mesh changes from Mesh 2 to Mesh 3, respectively. Therefore, since the changes from Mesh 2 to Mesh 3 are below 1%, Mesh 2 is determined to have the required resolution for capturing the necessary flow characteristics.

For the geometry with the vaneless diffuser, same mesh settings with Mesh 2 are incorporated. Therefore, a separate mesh dependency study for the vaneless diffuser geometry is not conducted. For the optimization study, the same mesh settings are applied to the 2D diffuser vane blade.
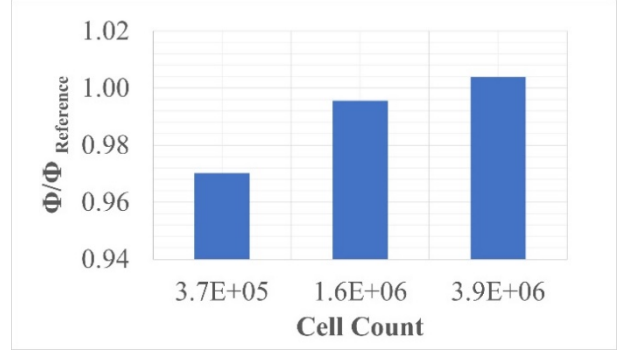

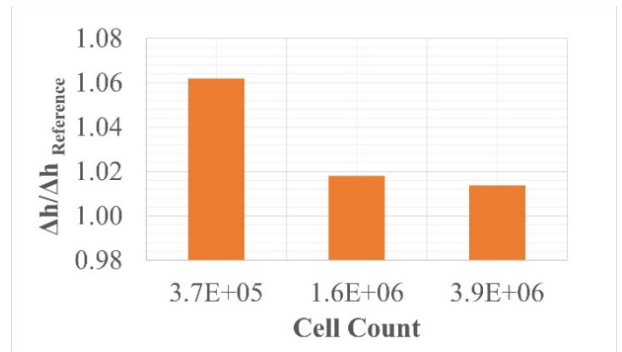**Figure 4.** Change of Flow Coefficient with respect to Cell Count

Figure 5. Change of Enthalpy Difference Between Inlet and Outlet with respect to Cell Count

RESULTS

Both compressor geometries Case 1 and 2 were solved at a single rotational speed and at constant total conditions at the inlet boundary. However, the static pressure at the diffuser outlet were varied to evaluate the performance of the compressor at different mass flow rates.

Operating points close to the stall condition could not be simulated precisely because SU2 is not equipped with an outlet boundary condition type that allows to impose mass flow rate, which is a shortcoming for turbomachinery flow simulations. For flat compressor characteristics close to the stability limit, ability to specify outlet mass flow rate as boundary condition is a necessity. When the static pressure is imposed at the outlet boundary, numerical/physical pressure oscillations eventually lead to strong mass flow fluctuations and no fixed stable operating point may be found.

For two operating points, one with low and one with high polytropic efficiency, flow fields are compared between SU2 and 'Fidelity Flow'. With 'Fidelity Flow', a second order central spatial scheme with a Jameson type dissipation and an explicit q-stage Runge-Kutta local time stepping scheme was used. Since SU2 was only able to work with a first order scheme, the difference between these solvers is very apparent in the flow field comparison. The comparison stations are chosen from diffuser zone as shown in Figure 6.
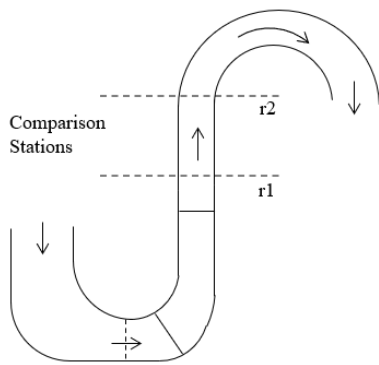
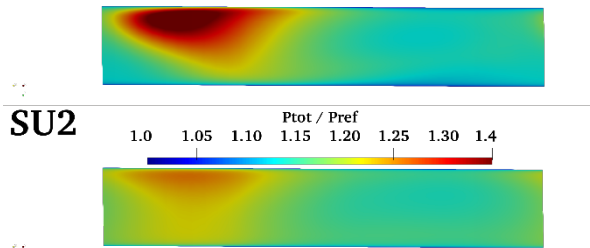**Figure 6.** Stations in Case 1 for Flow Field Comparison

Fidelity Flow

SU2

		Ptot / Pref				
1.0	1.05	1.10	1.15	1.20	1.25	1.30	1.4

Figure 7. Total Pressure Comparison at Station r1 for Low η

Fidelity Flow

SU2

	Ttot / Tref			
1.0e+00	1.10	1.15	1.20	1.3e+00
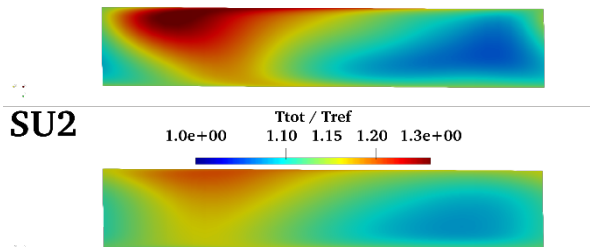
Figure 8. Total Temp. Comparison at Station r1 for Low η

Fidelity Flow

SU2

	Ptot / Pref						
1.10e+00	1.12	1.13	1.14	1.15	1.16	1.17	1.18	1.20e+00
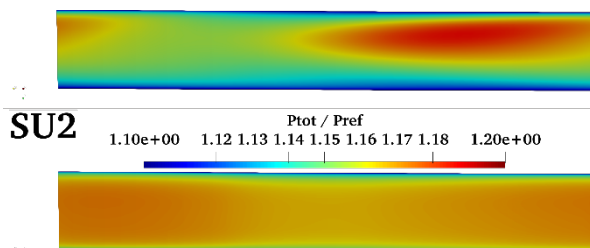
Figure 9. Total Pressure Comparison at Station r2 for Low η

Fidelity Flow

SU2

	Ttot / Tref				
1.1e+00	1.08	1.1	1.12	1.14	1.16	1.2e+00
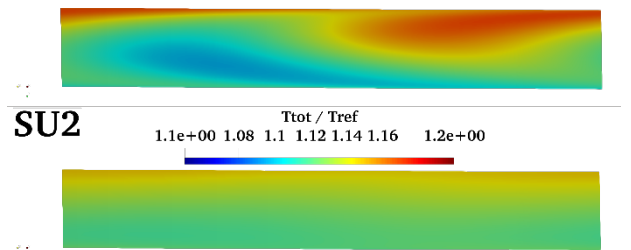
Figure 10. Total Tempe. Comparison at Station r2 for Low η

Fidelity Flow

SU2

	Ptot / Pref			
1.4	1.45	1.5	1.55	1.6
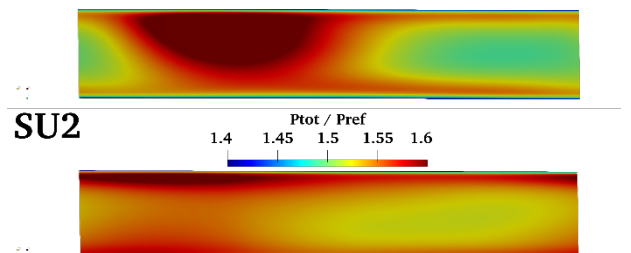
Figure 11. Total Pressure Comp. at Station r1 for High η

Fidelity Flow

SU2

	Ttot / Tref				
1.1	1.16	1.17	1.18	1.19	1.2
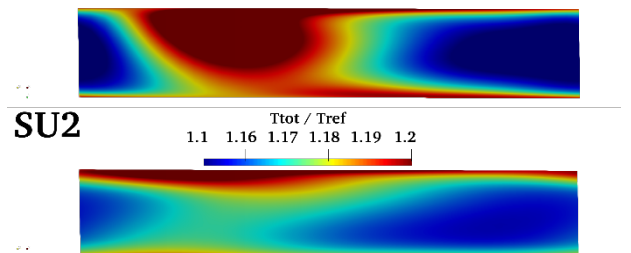
Figure 12. Total Temp. Comparison at Station r1 for High η

Fidelity Flow

SU2

	Ptot / Pref						
1.4	1.42	1.44	1.46	1.48	1.5	1.52	1.6
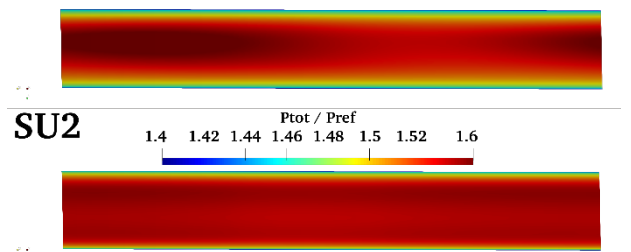
Figure 13. Total Pressure Comparison at Station r2 for High η

Fidelity Flow

SU2

Ttot / Tref
1.1 1.16 1.17 1.18 1.19 1.2
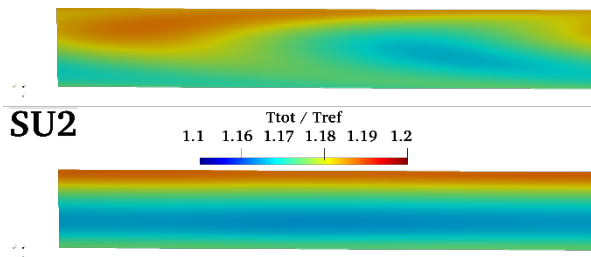
Figure 14. Total Temp. Comparison at Station r2 for High η

Even though the integral parameters such as efficiency do not change significantly, the differences between using a lower and higher order spatial discretization scheme are visible in the flow field contours shown in between Figure 7 and Figure 14. Trailing edge of the impeller corresponds to middle of these contours. As it can be seen from these figures, SU2 shows a much significant diffusion in terms of flow structures as the flow travels from r1 to r2. Even though SU2 captures some of the flow structures it is not as good as 'Fidelity Flow' results. This is an expected behavior since SU2 results are obtained by using a first order spatial scheme, whereas 'Fidelity Flow' results are obtained by using a second order spatial scheme.

Figure 15 and Figure 16 show the comparison of SU2 results with Fidelity Flow results and experimental data for Case 1. As shown in Figure 15, SU2 predicts the outlet pressure of the compressor very close to Fidelity Flow results. In Figure 16, other performance parameters of the compressor such as polytropic efficiency, work input coefficient and pressure rise coefficients are compared between the different solvers and experimental data. Both CFD and experimental data are taken from values obtained at the inlet and outlet plane of the vaneless diffuser. The definitions of the parameters are given in the nomenclature. Here, one can also observe that the predictions of SU2 agree well with 'Fidelity Flow' results. When compared with the experimental data SU2 shows comparable results. The agreement between SU2 results and experimental data for pressure rise coefficient is better compared to polytopic efficiency and work input coefficient. This is due to not including cavity flows in the CFD model to keep the model simple. Cavity flows would induce higher losses, which is why in experimental data efficiency is lower and work input coefficient is higher compared to CFD results. Because of this, the difference between experimental data and CFD results are somewhat compensated for pressure rise coefficient and are much more similar.

All the operating points given in Figure 15 and Figure 16 showed similar convergence characteristics with SU2. Overall SU2 would need around 2000 to 2500 iterations to reach a converged solution. Convergence was checked by using the mass flow rates at the inlet and outlet.
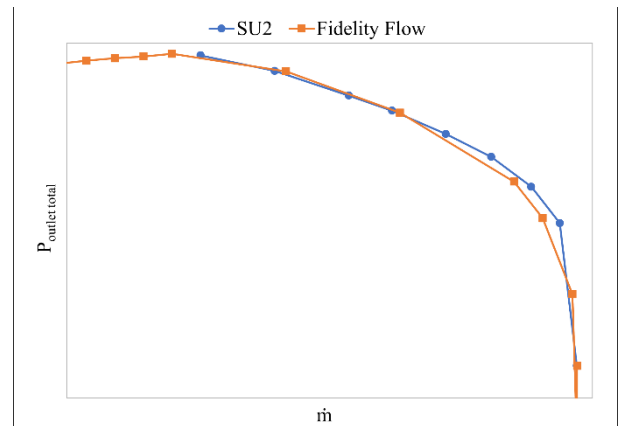
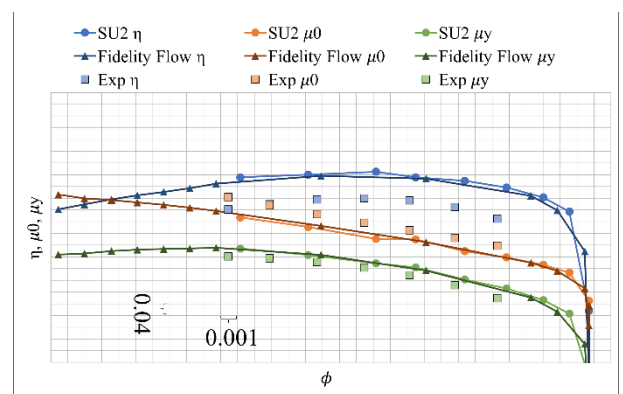

Figure 15. Outlet P_{total} vs $\dot{m}$ for Case 1

Figure 16. η, μ_0 and μ_y vs ϕ for Case 1

Next, the performance parameters of Case 2 predicted with SU2 are compared with 'Fidelity Flow' results. As shown in Figure 17 and Figure 18, one can say that there is a satisfactory match between the two CFD solutions. However, the agreement between the two solutions is relatively lower compared to Case 1. In Figure 18, SU2 shows good accuracy for the most part when compared to 'Fidelity Flow' result. A similar issue that was apparent in Case 1 when comparing the experimental data and CFD results can also be seen here as well. For efficiency, SU2 and Fidelity Flow results agree more compared to work input and pressure rise coefficients. The difference at work input coefficient indicates that SU2 underpredicts losses compared to 'Fidelity Flow'. This difference then transferred on to pressure rise coefficient since all these parameters are linked together.
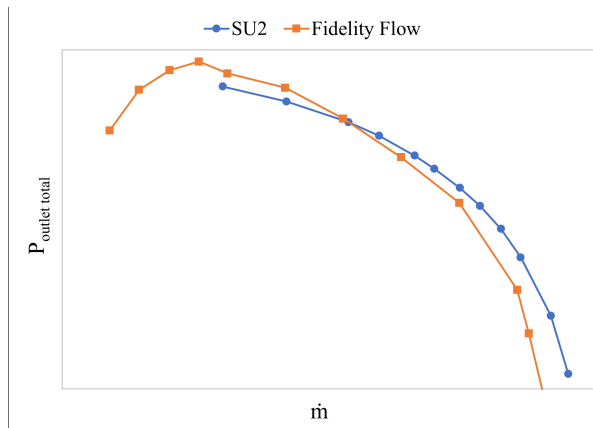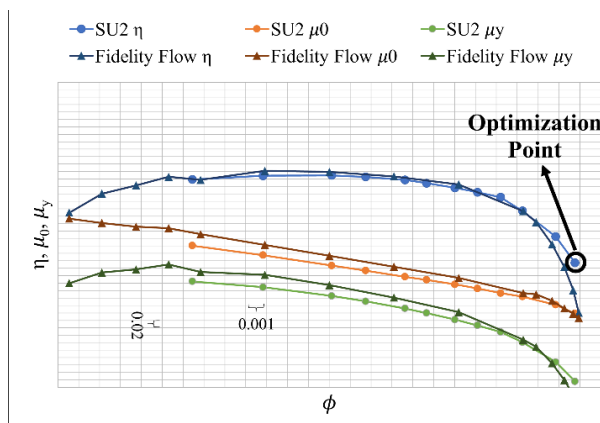
238

Figure 17. Outlet P_{total} vs $\dot{m}$ for Case 2

Figure 18. η, μ_0 and μ_y vs ϕ for Case 2

DIFFUSER VANE SHAPE OPTIMIZATION

The geometry of the vane in the vaned diffuser case is prismatic, which means that the profile of the diffuser blade does not change in spanwise direction, so it is possible to follow a 2D modelling approach. The flow field comparison around diffuser vane is shown in Figure 19. As it can be seen from Figure 19, flow field section taken from 3D solution at the mid span of the vane and 2D flow field solution are very similar. Therefore, the optimization of the diffuser vane is done in 2D. Since FFD has a broader applicability and great potential in a possible future 3D case, FFD method is used as the deformation method.

At the operating condition with the worst polytropic efficiency, there is a separation region that cover a considerable portion of the diffuser vane blade suction side, which is shown in Figure 20. This separated flow region is selected for the optimization problem with the aim of reducing the pressure loss at the diffuser for that operating condition.
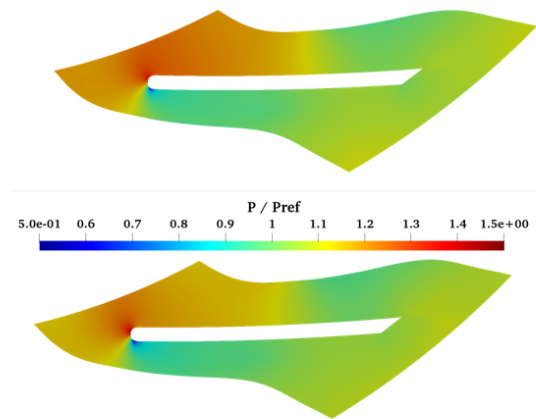
Figure 19. Mid-span Section of 3D Solution (Top) and 2D Solution (Bottom) Flow Field Comparison

For objective and constraint functions, drag and lift were working without any modification in the code. However, due to a bug in the source code total pressure and mass flow rate could not be used as objective functions, which are much more suitable for a turbomachinery optimization study. To use these objective functions, the source code had to be altered slightly. The adaptation consisted of minor name changes. SU2 would print out total pressure and mass flow with a slightly different name in its history file and would not recognize these as the same with the corresponding objective functions, which would disrupt the optimization routine at the very first design iteration. By making these history output and objective/constraint function names consistent, total pressure and mass flow could be used as objective/constraint functions. Drag and total pressure are the two objective functions performed better compared to others and were more suitable for the optimization study. Drag is used for constraint function as to somewhat limit the shape deformation. Specifying *Drag > 0* as the constraint helps the optimizer keep shape deformations more subtle. Total pressure at the outlet is given as the main objective function. Drag direction in SU2 is determined from the freestream angle of attack. Giving a zero angle of attack for the freestream and positioning the blade exactly parallel in that direction and constraining the optimization with positive drag prevented unreasonable deformations. Curvature of the surface inside the FFD box is selected as the design variable. The deformation is done by changing the curvature of the surface that is covered in the FFD box.

The optimization is carried out for a single operating condition and that operating condition is shown in Figure 18. The point where the efficiency is the lowest is chosen as the operating point for optimization. Since this is a 3D case simplified to a 2D one, the boundary conditions are taken from the 3D case and applied to the stand alone 2D vane geometry. Due to optimization being done on a single operating point, major changes in geometry are avoided. To achieve this, only the portion where a

significant flow separation happens is chosen as the geometry portion that is to be optimized. Only the portion where flow separation is seen at the suction side of the blade is included inside the FFD box, excluding the pressure side, and leading edge and trailing edge portions of the blade. The streamlines around the vane are shown in Figure 20. The blue streamlines show the separated flow region for the selected optimization condition. Also, the FFD box used for the optimization study is shown in Figure 20 as well.
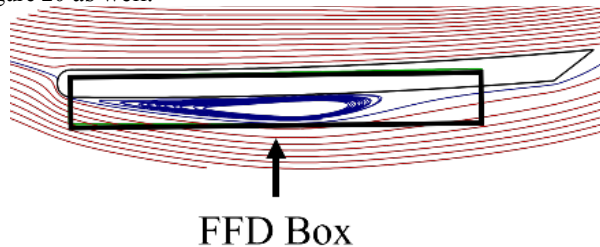
Figure 20. Streamlines Around the Diffuser Vane and the FFD Box for the Optimization Study

As for the optimization results, a total of 20 design iterations were carried out. The change in total pressure loss between inlet and outlet with each design iteration is shown in Figure 21.
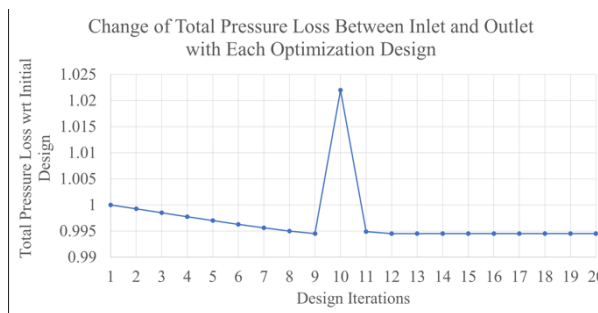
Figure 21. Change of Total Pressure Loss Between Inlet and Outlet with Each Design Iteration

As it can be seen from Figure 21, at 10th design iteration there is a jump. This is due to SU2 trying to continue changing the shape of the interested area in the same way as it was changing the shape in the previous design iterations. However, because of this, the total pressure loss between diffuser inlet and outlet increases. Thus, SU2 changes the direction it changed the shape so far for the next design iteration. After some design iterations SU2 converges to an optimum design that is very similar to 9th design iteration. This indicates that after the 9th design iteration, SU2 reached the shape deformation limit for the given objectives and constraints.

Since the optimization is done to a very small portion of the blade the change in total pressure at the outlet is very minor. However, the total pressure loss between diffuser inlet and outlet is decreased by 0.55%. Considering that this geometry was designed for an interval of operating points, the increase in total pressure for one of the worst

operating points with minimal change in the geometry is expected to be small.

In Figure 22, initial and optimized blade profiles are shown, with a closeup of the most deformed area. Also, in Figure 23, Mach contour around this most deformed area is shown. With the optimized blade profile, it can be said that flow separation starting location is slightly moved downstream.

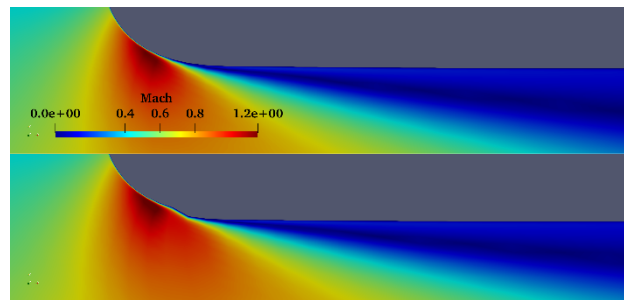**Figure 22.** Initial (Black) and Optimized (Red) Vane Blade Profiles

Figure 23. Mach Contour Near the Most Deformed Location, Original (Top) vs Optimized (Bottom) Profiles

Moreover, the effect of the geometry optimization on the compressor performance at the operating point with highest efficiency is also tested. When the original and optimized vane geometries are compared, it was found out that the optimized vane geometry resulted in a 0.86% increase in the total pressure loss at the vane outlet. Compared to the achieved decrease in the total pressure loss at the operating point used in the optimization study this increase seen at the operating with the highest efficiency is slightly more significant. This shows the importance of conducting optimization studies considering the entire operating curve of the compressor.

CONCLUSION

In this study the capabilities of SU2 for analyzing compressible turbomachinery flows were tested on two different centrifugal compressor geometries. The performance parameters derived from simulation results were compared against experimental data and against 'Fidelity Flow', a commercial solver for turbomachinery flows. Results showed that SU2 predicted the performance parameters of the compressors with minor differences relative to the predictions of the commercial tool. In addition to the performance parameters, the

numerical accuracy of SU2 is also tested on a more detailed flow field analysis. There, significant differences were observed between the predictions of SU2 and 'Fidelity Flow'. The first order accurate discretization scheme in space is thought of as the primary factor for the more diffused flow field solutions with SU2.

The capabilities of the adjoint optimization toolbox included in SU2 is also investigated as well. Even though it required some amount of work to obtain a functioning and meaningful optimization case setup, in the end it was possible to carry out an optimization study on the diffuser vane with SU2. The optimized vane geometry reduced the losses by 0.55% generated by the flow separation downstream of the vane leading edge. However, testing the geometry optimized for the specific operating point close to choke conditions at another operating point with the best efficiency resulted to a performance deterioration. This points out the necessity for a multi-point optimization algorithm for turbomachinery applications. Also, shape deformation tool within the optimization toolbox should be improved to increase the capability of the tool in handling geometrical discontinuities in the optimized geometry.

Additionally, SU2 has very limited turbomachinery specific post-processing capabilities. It only has two turbomachinery specific outputs, and these are kinematic and thermodynamic values at spanwise locations at the inlet and outlet of the corresponding zones. Kinematic values consist of Mach, velocity, and absolute and relative flow angles. Thermodynamic values consist of pressure, temperature, enthalpy and total counterparts of these, and density. Especially for radial turbomachinery a more extended post-processing capability that enables to generate meridional, constant angular and spanwise cut planes is a necessity.

In conclusion, SU2 is a promising open-source software for handling compressible turbomachinery flows. It works with a simple text-based input file, which makes it a user-friendly application for first-time users. Also, its turbomachinery specific settings make it more usable, especially for internal flow applications compared to other open-source alternatives. Optimization package included in SU2 is also a nice to have tool for simple optimization cases. However, it required some source code modifications to be able to use turbomachinery specific objective functions.

REFERENCES

de Castro İ.C., 2019, Assessment of SU2 for radial compressor performance prediction, [Online]. Available: http://resolver.tudelft.nl/uuid:604be835-1715-42e9-bd87-a856322f71d4

Yan C., Wang B., He X., Zhao F., Zheng X., Vahdati M. and Zheng X., 2023, Extension and Validation of the Turbomachinery Capabilites of SU2 Open-SOurce CFD Code, *Turbomachinery Technical Conference and Exposition, Boston.*

Mollá V.F., 2017, 3D-simulation of multi-stage turbomachinery by means of a non-reflecting mixing plane interface, [Online]. Available: http://resolver.tudelft.nl/uuid:324b6057-aeab-4ad8-ab24-5aa1a62819a0

Keep J.A., Vitale S., Pini M. and Burigana M., 2017, Preliminary verification of the open-source CFD solver SU2 for radial-inflow turbine applications, *Energy Procedia*, vol. 129, pp. 1071-1077.

Giles M., 1990, Nonreflecting boundary conditions for Euler equation calculations, *AIAA*, pp. 2050-2058.

de Koning R.C.V., 2015, Development of a Parametric 3D Turbomachinery Blade Modeler, [Online]. Available: http://resolver.tudelft.nl/uuid:9bbcf030-af4b-42c8-a7e5-2157bde13706

Vitale S., Pini M., Colonna P., 2020, Multistage Turbomachinery Design Using the Discrete Adjoint Method Within the Open-Source Software SU2, *Journal of Propulsion and Power*, pp. 1-14.

Rubino A., Vitale S., Colonna P., Pini M., 2020, Fully-turbulent adjoint method for the unsteady shape optimization of multi-row turbomachinery," *Aerospace Science and Technology*, vol. 106.

Giles M.B., Pierce N.A., 2000, An introduction to the Adjoint Approach to Design, *Flow, Turbulence and Combustion*, vol. 65, pp. 393-415.

Ntanakas G.D., Meyer M., 2014, Towards Unsteady Adjoint Analysis for Turbomachinery Applications, *European Conference on Computational Fluid Dynamics (ECFD VI), Barcelona.*

Katsapoxaki P., Hottois R., Tran T.S., Schram C., Coussement G., Verstraete T., 2023, Adjoint-Based Aeroacoustic Optimization of NASA Rotor 37, *Proceedings of ASME Turbo Expo 2023: Turbomachinery Technical Conference and Exposition*, Boston.

Châtel A., Verstraete T., 2022, Aerodynamic Optimization of the SRV2 Radial Compressor Using an Adjoint-Based Optimization Method, *Proceedings of ASME Turbo Expo 2022: Turbomachinery Technical Conference and Exposition*, Rotterdam.

Hottois R., Châtel A. Verstraete T., 2023, Adjoint-Based Design Optimization of a Volute for a Radial Compressor, *Int. J. Turbomach. Propuls. Power*, vol. 8, no. 4.

Trompoukis X.S., Tsiakas K.T., Asouti V.G., Giannakoglou K.C., 2023, Continuous Adjoint-Based Shape Optimization of a Turbomachinery Stage using a

3D Volumetric Parameterization, *International Journal for Numerical Methods in Fluids*, vol. 95, no. 7, pp. 1054-1075.

Luo J., Chen Z., Zheng Y., 2022, A Gradient-Based Method Assisted by Surrogate Model for Robust Optimization of Turbomachinery Blades, *Chinese Journal of Aeronautics*, vol. 35, no. 10, pp. 1-7.

Wu H., Da X., Wang D., Huang X., 2023, Multi-Row Turbomachinery Aerodynamic Design Optimization by an Efficient and Accurate Discrete Adjoint Solver, *Aerospace*, vol. 10, no. 2.

Hicks R.M., Henne P.A., 1978, Wing Design by Numerical Optimization, *J. of Aircraft*, vol. 15, no. 7.

Koshakji A., Quarteroni A., Rozza G., 2013, Free Form Deformation Techniques Applied to 3D Shape Optimization Problems, https://www.epfl.ch/labs/mathicse/wp-content/uploads/2018/10/44.2013_AK-AQ-GR.pdf .

Menter F.R., 1994, Two-equation Eddy-viscosity Turbulence Models for Engineering Applications", *AIAA*, vol. 32, no. 8, pp. 1598-1605.

ISI BİLİMİ VE TEKNİĞİ DERGİSİ İÇİN MAKALE HAZIRLAMA ESASLARI

Isı Bilimi ve Tekniği Dergisi'nde, ısı bilimi alanındaki özgün teorik ve deneysel çalışmaların sonuçlarının sunulduğu makaleler ve yeterli sayıda makaleyi tarayarak hazırlanmış olan literatür özeti makaleler yayınlanmaktadır. Makaleler, Türkçe veya İngilizce olarak kabul edilmektedir. Makaleler ilk sunumda serbest formatta hazırlanabilir. Ancak yayın için kabul edilmiş olan makaleler dergimizin basım formatına tam uygun olarak yazarlar tarfından hazırlanmalıdır. Aşağıda, ilk sunuş ve basıma hazır formatta makale hazırlamak için uyulması gereken esaslar detaylı olarak açıklanmıştır.

İLK SUNUŞ FORMATI

İlk sunuşta, makale A4 boyutundaki kağıda tek sütun düzeninde, 1.5 satır aralıklı ve sayfa kenarlarından 25'er mm boşluk bırakılarak yazılmalıdır. Yazı boyutu 11 punto olmalı ve **Times New Roman** karakter kullanılmalıdır. Şekiller, tablolar ve fotograflar makale içinde **olmaları gereken yerlere** yerleştirilmelidir. Makale, elektronik olarak editörün e-posta adresine gönderilmelidir.

BASIMA HAZIR MAKALE FORMATI

Hakem değerlendirmelerinden sonra, yayın için kabul edilmiş olan makaleler, dergimizin basım formatına tam uygun olarak yazarlar tarafından hazırlanmalıdır. Makaleler yazarların hazırladığı haliyle basıldığı için, yazarların makalelerini basım için hazır formatta hazırlarken burada belirtilen esasları titizlikle takip etmeleri çok önemlidir. Aşağıda, basıma hazır formatta makale hazırlamak için uyulması gereken esaslar detaylı olarak açıklanmıştır.

Genel Esaslar

Makaleler genel olarak şu başlıklar altında düzenlenmelidir: Makale başlığı (title), yazar(lar)ın ad(lar)ı, yazar(lar)ın adres(ler)i, özet (abstract), anahtar kelimeler (keywords), semboller, giriş, materyal ve metod, araştırma sonuçları, tartışma ve sonuçlar, teşekkür, kaynaklar, yazarların fotoğrafları ve kısa özgeçmişleri ve ekler. Yazılar bilgisayarda tek satır aralıklı olarak, 10 punto Times New Roman karakteri kullanılarak Microsoft Office Word ile iki sütun düzeninde yazılmalıdır. Sayfalar, üst kenardan 25 mm, sol kenardan 23 mm, sağ ve alt kenarlardan 20 mm boşluk bırakılarak düzenlenmelidir. İki sutun arasındaki boşluk 7 mm olmalıdır. Paragraf başları, sütunun sol kenarına yaslanmalı ve paragraflar arasında bir satır boşluk olmalıdır.

Birinci seviye başlıklar büyük harflerle kalın olarak, ikinci seviye başlıklar bold ve kelimelerin ilk harfleri büyük harf olarak ve üçüncü seviye başlıklar sadece ilk harfi büyük olarak yazılır. Bütün başlıklar sutunun sol kenarı ile aynı hizadan başlamalıdır ve takip eden paragrafla başlık arasında bir satır boşluk olmalıdır. Şekiller, tablolar, fotoğraflar v.b. metin içinde ilk atıf yapılan yerden hemen sonra uygun şekilde yerleştirilmelidir. İlk ana bölüm başlığı, Özetten (Abstract'tan) sonra iki satır boşluk bırakılarak birinci sutuna yazılır.

Başlık, Yazarların Adresi, Özet, Abstract ve Anahtar Kelimeler

Yazılar Türkçe veya Ingilizce olarak hazırlanabilir. Her iki durumda da makale özeti, başlığı ve anahtar kelimeler her iki dilde de yazılmalıdır. Eğer makale Türkçe olarak kaleme alınmışsa, Türkçe başlık ve özet önce, İngilizce başlık ve Özet (Abstract) sonra yazılır. Eğer makale İngilizce olarak kaleme alınmışsa önce İngilizce başlık ve özet (abstract) sonra Türkçe başlık ve özet yazılır. Başlık, sayfanın üst kenarından 50 mm aşağıdan başlar ve kalın olarak 12 punto büyüklüğünde, büyük harflerle bütün sayfayı ortalayacak şekilde yazılır. Yazar(lar)ın adı, adresi ve elektronik posta adresi başlıktan sonra bir satır boşluk bırakılarak yazılmalıdır. Yazarların adı küçük, soyadı büyük harflerle yazılmalı ve bold olmalıdır. Yazarların adresinden sonra üç satır boşluk bırakılarak, Özet ve Abstract 10 punto büyüklüğünde bütün sayfa genişliğinde yazılır. Özet ve Abstractan sonra anahtar kelimeler (Keywords) yazılır.

Birimler

Yazılarda SI birim sistemi kullanılmalıdır.

Denklemler

Denklemler, 10 punto karakter boyutu ile bir sütuna (8 cm) sığacak şekilde düzenlenmelidir. Veriliş sırasına göre yazı alanının sağ kenarına yaslanacak şekilde parantez içinde numaralanmalıdır. Metin içinde, denklemlere **'Eş. (numara)'** şeklinde atıfta bulunulmalıdır.

Şekiller

Şekiller 8 cm (bir sütun) veya 16 cm (iki sütun) genişliğinde olmalıdır ve makale içerisinde olmaları gereken yerlere bilgisayar ortamında sutunu (veya bütün sayfa genişliğini) ortalayacak şekilde yerleştirilmelidir. Şekil numaraları (sıra ile) ve isimleri şekil **altına, 9 punto büyüklüğünde** yazılmalıdır.

Tablolar

Tablolar 8 cm (bir sütun) veya 16 cm (iki sütun) genişliğinde olmalıdır. Makale içerisinde olmaları gereken yerlere bilgisayar ortamında sutunu (veya bütün sayfa genişliğini) ortalayacak şekilde yerleştirilmelidir. Tablo numaraları (sıra ile) ve isimleri tablo **üstüne, 9 punto büyüklüğünde** yazılmalıdır.

Fotograflar

Fotograflar, siyah/beyaz ve 8 cm (bir sütun) veya 16 cm (iki sütun) genişliğinde olmalıdır. Fotograflar digitize edilerek, makale içinde bulunmaları gereken yerlere bilgisayar ortamında sutunu (veya bütün sayfa genişliğini) ortalayacak şekilde yerleştirilmelidir ve şekil gibi numaralandırılmalı ve adlandırılmalıdır.

Yazar(lar)ın Fotograf ve Kısa Özgeçmişleri

Yazarların fotografları digitize edilerek, makalenin en sonuna özgeçmişleri ile birlikte uygun bir şekilde yerleştirilmelidir.

SEMBOLLER

Makale içinde kullanılan bütün semboller alfabetik sırada Özetten sonra liste halinde tek sütun düzeninde yazılmalıdır. Boyutlu büyüklükler birimleri ile birlikte ve boyutsuz sayılar (Re, Nu, vb.) tanımları ile birlikte verilmelidir.

KAYNAKLAR

Kaynaklar metin sonunda, ilk yazarın soyadına göre alfabetik sırada listelenmelidir. Kaynaklara, yazı içinde, yazar(lar)ın soyad(lar)ı ve yayın yılı belirtilerek atıfta bulunulmalıdır. Bir ve iki yazarlı kaynaklara, her iki yazarın soyadları ve yayın yılı belirtilerek (Bejan, 1988; Türkoğlu ve Farouk, 1993), ikiden çok yazarlı kaynaklara ise birinci yazarın soyadı ve "*vd.*" eki ve yayın yılı ile atıfta bulunulmalıdır (Ataer *vd*, 1995). Aşağıda makale, kitap ve bildirilerin kaynaklar listesine yazım formatı için örnekler verilmiştir.

Ataer Ö. E., Ileri A. and Göğüş, Y. A., 1995, Transient Behaviour of Finned-Tube Cross-Flow Heat Exchangers, *Int. J. Refrigeration,* 18, 153-160.

Bejan A., 1998, *Advanced Engineering Thermodynamics* (First Ed.), Wiley, New York.

Türkoğlu H. and Farouk B., 1993, Modeling of Interfacial Transport Processes in a Direct-Contact Condenser for Metal Recovery, *Proc. of 73rd Steel Making Conference*, Detroit, 571-578.

Türkoğlu H., 1990, *Transport Processes in Gas-Injected Liquid Baths*, Ph.D. Thesis, Drexel University, Philadelphia, PA, USA.

İnternet, 2004, Türkiye İstatistik Kurumu, *Atıksu İstatistikleri*, http://www.tuik.gov.tr/HaberBulteni.

DİĞER HUSUSLAR

Hakem değerlendirmesinden sonra kabul edilen makaleler, yukarıda açıklandığı şekilde dizilerek basıma hazırlandıktan sonra, bir elektronik kopyası editöre gönderilmelidir. Makalenin basıma hazır kopyası ile birlikte, "Telif Hakkı Devri Formu" da doldurularak göderilmelidir. Telif Hakkı Devir Formu'na ve bu yazım klavuzuna www.tibtd.org.tr adresinden ulaşılabilir.

FOTOĞRAFINIZ

TÜRK ISI BİLİMİ VE TEKNİĞİ DERNEĞİ
ÜYELİK BAŞVURU FORMU

A. Adınız Soyadınız   :

   Ünvanınız   :

   Doğum yeri :   :   Doğum tarihi: /   / 19   T.C. Kimlik No:

   İş Adresiniz   :

   Ev adresiniz :

   Telefonunuz : İş   Ev   Cep

   E-posta   :

B. *Derneğe   □Asil üye   □Fahri üye   olmak istiyorum.

1. Sizi tanıyan dernek üyesi (Üyelik için) :

2. Mezun olduğunuz
    <u>Yüksek Okullar</u>   <u>Yıl</u>   <u>Branşınız</u>   <u>Ünvanınız</u>

3. İlgilendiğiniz konular :

2015 yılı aidatı olarak toplam 25 YTL (Yirmibeş Milyon TL) derneğin

        İş Bankası Maltepe Şubesi Hesap No: 42120867567
        IBAN: TR08 0006 4000 0014 2120 8675 67

    hesabına yatırılmıştır.

                                    Tarih :   İmza :

* Asil üye olmak için beş yıllık deneyim gereklidir.
  Fahri üyelik için yüksekokul mezunu olma şartı yoktur.

Türk Isı Bilimi ve Tekniği Derneği
Gazi Üniversitesi
Mühendislik Fakültesi
Makina Mühendisliği Bölümü
06570 Maltepe/ ANKARA

İÇİNDEKİLER / CONTENTS